CRANFIELD UNIVERSITY

Norbert Donhauser

ELECTROMAGNETIC MEASUREMENT OF BUBBLE VELOCITY IN TWO-PHASE DIELECTRIC FLUID FLOW

PhD Thesis

SCHOOL OF MECHANICAL ENGINEERING

Department of Fluid Engineering and Instrumentation

CRANFIELD UNIVERSITY

SCHOOL OF MECHANICAL ENGINEERING

Department of Fluid Engineering and Instrumentation

PhD Thesis

Academic Years 1994 - 1997

Norbert Donhauser

ELECTROMAGNETIC MEASUREMENT OF BUBBLE VELOCITY IN TWO-PHASE DIELECTRIC FLUID FLOW

Supervisor: Professor M L Sanderson

October 1997

ABSTRACT

This thesis deals with the theoretical and experimental investigation of two-phase flow for a dielectric liquid electromagnetic flowmeter. So far only limited investigations into the possible use of electromagnetic flowmeters for multiphase flow measurement have been made. These have been restricted to electromagnetic flowmeters designed for conducting water based (electrolytic) fluids. The possibility of designing electromagnetic flowmeters for use with insulating (dielectric) fluids such as oil and petrol has been existed for some years. However the measurement of two-phase flow of insulating fluids using electromagnetic flowmeters and the application of this knowledge to the measurement of the separate phases has not yet been a subject for research. An analytical model is developed which evaluates a transformer signal that is produced on the electrodes when a bubble unbalances eddy currents while it passes through the meter. The shape and magnitude of this signal for various positions in the pipe cross-section is investigated. The behaviour of this transformer signal for various electrode shapes is studied as well and it is found that when using large area electrodes the position of the amplitude along the pipe axis remains almost constant. For measuring the speed of bubbles passing through the meter a frequency analysis is carried out and shows that the peak frequency of the signal is proportional to the velocity of the bubbles. A flowmeter is built to carry out experimental work. The first sets of experiments are carried out with plastic beads fixed on a thin string which is attached around two wheels. The speed of the beads is adjusted by an electromotor which powered one wheel. In a second experimental design gas bubbles are injected in a vertical pipe which is filled with dielectric oil. Both types of experiments exhibit the behaviour predicted in theoretical analysis.

ACKNOWLEDGEMENTS

I would like to take this opportunity to thank Professor Mike Sanderson for his guidance and input especially into the experimental side of the work. I am very grateful to Dr John Hemp for his continuous support and interest throughout the research project and his invaluable help of the theoretical part of the work. Many thanks to Will Rawes for sharing his computational expertise, Luke Durcan for many useful discussions and his advice on experimental problems and Chris Evans for building the two experimental rigs.

I would also like to say thanks to all my fellow students in the department for their friendship.

Finally I wish to thank my parents for their continuous encouragement throughout the time for this work.

CONTENTS

ABSTRACT i

ACKNOWLEDGEMENTS ii

CONTENTS iii

NOMENCLATURE vii

LIST OF FIGURES ix

1. INTRODUCTION AND LITERATURE REVIEW

1.1 Objectives 1

1.2 Introduction 2

1.3 Literature review 2

1.3.1 Brief history on the general electromagnetic flowmeters 2

1.3.2 Governing equations for electromagnetic flowmeasurement 5

1.3.3 The nature of dielectric fluids 7

1.3.4 Electromagnetic flowmeters for insulating fluids 9

1.3.5 Electromagnetic flowmeters for two-phase flow 13

2. THE DEVELOPMENT OF AN ANALYTICAL MODEL

2.1 Introduction 16

2.2 The Transformer signal 16

2.3 Transformer signal due to a bubble passing through the meter 17

2.4 Model of a dipole in z-direction 18

2.4.1 Field at infinity 20

2.4.2 Field inside the sphere 21

2.4.3 Field near the sphere 21

2.4.4 Evaluation of the field constants 22

2.4.5 Calculation of the dipole strength 24

2.5 Evaluation of eddy current field 25
2.6 Model of the field and bubble interaction 27
2.6.1 Expansion of the potential in eigenfunctions 28
2.6.2 Field of point charge in the duct 34
2.6.3 Evaluation of the coefficients in equation 2.52 37
2.6.3.1 Evaluation of the integrals 39
2.6.4 Field of the bubble dipole source in the duct 41
2.7 Results for point electrodes 43
2.8 Results for strip electrodes 46
2.9 Results for wide area electrodes 49
2.10 Summary 52

3. NUMERICAL INVESTIGATION OF THE TRANSFORMER SIGNAL

3.1 Introduction 53
3.2 ANSYS for electric field analysis 53
3.3 Model of a dipole within a dielectric medium 54
3.3.1 Operating conditions 54
3.3.2 Results for dipole modelling 59
3.4 Model of a sphere within a dielectric medium 59
3.4.1 Physical model 60
3.4.2 Operating conditions 62
3.4.3 Results for bubble modelling 63
3.6 Summary 66

4.THEORETICAL FREQUENCY ANALYSIS OF THE TRANSFORMER SIGNAL

4.1 Introduction 67
4.2 Frequency analysis 68
4.3 Power spectra for evenly spaced bubbles compared with varying velocities 75
4.4 Power spectra for varying bubble spacings 78

4.5 Power spectra for randomly spaced bubbles 79
4.6 Frequency analysis for transformer signal due to time varying eddy currents 81
4.7 Summary 96

5. PREDICTION OF FLOW SIGNAL DUE TO A BUBBLE PASSING THROUGH THE METER

5.1 Introduction 97
5.2 Development of model 98
5.2.1 Governing equations 98
5.3 Solution of governing equations 100
5.3.1 Evaluation of vector product 100
5.3.2 Solution of Laplace's equation 102
5.3.2.1 Evaluation of constants 103
5.3.2.2 Resulting dipole strength 104
5.4 Summary 105

6. SET-UP AND EXPERIMENTS WITH ARTIFICIAL BUBBLE FLOW

6.1 Introduction 106
6.2 System design of the experimental rig 106
6.3 The electromagnetic flowmeter 108
6.3.1 The flow conduit 108
6.3.2 Detection and guard electrodes 110
6.3.3 Electrode and wire clamp 110
6.3.4 The electrostatic shield 113
6.3.5 Excitation coils 114
6.4 The electronics 117
6.4.1 Excitation electronics 117
6.4.2 Detection and quadrature suppression electronics 120

6.4.2.1 Signal detection unit (I) 121
6.4.2.2 Amplitude and phase shifting unit (II) 122
6.4.2.3 Quadrature deduction stage (III) 123
6.4.3 Bandpass filter design 124
6.4.4 Phase sensitive detection (Lock-in-Amplifier) 126
6.4.5 The signal recording method 128
6.4.6 The ONO-SOKKI analyzer 128
6.5 The used fluid 128
6.6 Experiments carried out 129
6.6.1 Transformer signal behaviour 129
6.6.2 Experimental frequency analysis of the transformer signal 132
6.7 Summary 136

7. EXPERIMENTS FOR INSERTED NITROGEN BUBBLES

7.1 Introduction 137
7.2 Experimental set-up 137
7.3 Experiments carried out 137
7.4 Summary 146

8.0 CONCLUSIONS AND RECOMMENDATIONS FOR FUTURE WORK

8.1 Introduction 147
8.2 Conclusions of work 147
8.3 Recommendations for future work 148

REFERENCES 151

APPENDIX A. Flow Charts and determinant 156
APPENDIX B. Bandpass filter design 159

NOMENCLATURE

a	Inner Pipe Radius	$[m]$
b	Outer Pipe radius	$[m]$
c	Electrostatic Shield Radius	$[m]$
d	Bubble Radius	$[m]$
f	Frequency	$[Hz]$
f_p	Peak Frequency	$[Hz]$
j	Current Density	$[\ Am^{-2}\ ]$
l	Lenght	$[m]$
p	Dipole Strength	$[\ Cm\ ]$
q	Unit Charge	$[C]$
r	Radius	$[m]$
s	Radial Bubble Position	$[m]$
t	Time	$[s]$
v	Velocity	$[\ ms^{-1}\ ]$
v_m	Mean Velocity	$[\ ms^{-1}\ ]$
A	Area	$[\ m^2\ ]$
B	Magnetic Flux Density	$[Tesla = Vsm^{-2}]$
C	Capacitance	$[F]$
C	Flowmeter Configuration Constsnt	$[-]$
D	Electric Flux Density or Displacement Flux Density	$[Cm^{-2}]$
E	Electric Field Intensity	$[Vm^{-1}]$
H	Magnetic Field Intensity	$[\ Am^{-1}\ ]$
I	Current	$[A]$
J	Besselfunction of first kind	$[-]$
L	Inductance	$[H]$
P	Polarization	$[\ Cm^{-2}\ ]$

Q	Charge	$[C]$
R	Resistance	$[\Omega]$
V	Volumetric Flowrate	$[m^3 s^{-1}]$
X_C	Reactance of Capacitance	$[\Omega]$
X_L	Reactance of Inductance	$[\Omega]$
Y	Besselfunction of secon kind	$[-]$
Z	Impedance	$[\Omega]$
Z	Attenuation Factor	$[-]$
α	Void Fraction	$[-]$
χ_e	Susceptibility	$[-]$
ε_0	Permittivity	$[8.854 \cdot 10^{-12} \frac{C}{Vm}]$
ε_b	Relative Permitivity of Bubble	$[-]$
ε_1, K_0	Relative Permitivity of Dielectic Medium	$[-]$
ε_2, K_1	Relative Permitivity of Pipe Material	$[-]$
ε_3	Relative Permitivity of Air	$[-]$
ϕ, U	Scalar Potential	$[V]$
$\Delta\phi$	Potential Difference	$[V]$
φ	Phase Angle	$[rad]$
μ_0	Permeability	$[4\pi 10^{-7} \frac{Vs}{Am}]$
μ_r	Relative Permeability	$[-]$
ρ_s	Surface Charge Density	$[Cm^{-2}]$
ρ_v	Volume Charge Density	$[Cm^{-3}]$
ω	Angle Velocity	$[s^{-1}]$
σ	*Conductivity*	$[Sm^{-2}]$
Φ	Magnetic Flux	$[Wb]$
Ψ	Electric Flux	$[C]$

LIST OF FIGURES

CHAPTER1

Figure 1.1 Basic electromagnetic flowmeter arrangement 3

Figure 1.2 Circulating currents effect 3

Figure 1.3 Incremental surface element in interior of dielectric medium 8

CHAPTER 2

Figure 2.1 Schematic of transformer signal due to loop on detection leads 17

Figure 2.2 Schematic of dipole behaviour in electric field 18

Figure 2.3 Schematic of definition of dipole 25

Figure 2.4 Schematic for resulting electric field 26

Figure 2.5 Schematic of eddy current electric field in z-direction 27

Figure 2.6 Schematic of potential regions 27

Figure 2.7 Schematic of charge in pipe section 34

Figure 2.8 Schematic of Gaussian law 35

Figure 2.9 Definition of position of charge and electric flux density 35

Figure 2.10 Definition of radius and angle on charge 35

Figure 2.11 Potential difference due to dipole of radius a/10 at various positions 43

Figure 2.12 Potential difference due to dipole of radius a/10 at 45° for various radii 44

Figure 2.13 Maximum potential difference at various angles and radii 44

Figure 2.14 Maxima potential difference due to dipole of radius a/5 45

Figure 2.15 Maxima and minima position for point electrodes 45

Figure 2.16 Potential difference for various dipole-radii 46

Figure 2.17 Averageing method for area electrodes 47

Figure 2.18 Schematic of strip electrodes 47

Figure 2.19 Comparison between signal from point- and strip electrodes 48

Figure 2.20 Maxima and minima positions of transformer signal for strip electrodes 49
Figure 2.21 Schematic of area electrodes 50
Figure 2.22 Comparison between signal from point- strip- and area electrodes 51
Figure 2.23 Maxima and minima positions of transformer signal for area electrodes 51
Figure 2.24 Maxima and minima positions of signal for large area electrodes 52

CHAPTER 3

Figure 3.1 Schematic of method of images 54
Figure 3.2a Set boundary conditions of FEM model 56
Figure 3.2b Potential distribution in y-z plane 57
Figure 3.2c Potential distribution in y-x plane 58
Figure 3.3 Comparison of signal obtained numerically and analytically 59
Figure 3.4 Boundary conditions on dielectric surface 61
Figure 3.5 Surface charge on bubble in eddy current electric field 61
Figure 3.6 Potential difference dut to bubble moving along the meter at various positions 63
Figure 3.7 Potential difference dut to bubble moving along the meter at various positions 63
Figure 3.8 Transformer signals produced from bubbles of various diameters 64
Figure 3.9 Transformer signals produced from bubbles of various diameters 64
Figure 3.10 Distribution of maxima signals 65
Figure 3.11 Distribution of maxima signals against y-positions of bubble 65
Figure 3.12 Comparison of analytical and numerical transformer signal 66

CHAPTER 4

Figure 4.1 Transformer signal produced by evenly spaced bubbes 75

Figure 4.2 Spectra for a set of evenly spaced bubbles moving at 0.25 *m/s* 76
Figure 4.3 Spectra for a set of evenly spaced bubbles moving at 0.5 *m/s* 76
Figure 4.4 Spectra for a set of evenly spaced bubbles moving at 1.5 *m/s* 77
Figure 4.5 Relationship between bubble velocity and peak frequency 77
Figure 4.6 Spectra for sets of varying bubble spaces and a bubble speed of 0.5 *m/s* 78
Figure 4.7 Spectra for sets of varying bubble spaces and a bubble speed of 1.5 *m/s* 79
Figure 4.8 Spectra for set of randomly spaced bubbles at a speed of 0.5 *m/s* 80
Figure 4.9 Spectra of averaged bubble spacing and a bubble speed of 0.5 *m/s* 80
Figure 4.10 Distorted signal (velocity: 0.5 *m/s*; spacing:100 *mm*; drive frequency:10 *Hz*) 82
Figure 4.11 Distorted signal (velocity: 0.5 *m/s*; spacing:100 *mm*; drive frequency:100 *Hz*) 82
Figure 4.12 Distorted signal (velocity: 1 *m/s*; spacing:100 *mm*; drive frequency:10 *Hz*) 83
Figure 4.13 Distorted signal (velocity: 1 *m/s*; spacing:100 *mm*; drive frequency:100 *Hz*) 83
Figure 4.14 Distorted signal (velocity: 1.5 *m/s*; spacing:100 *mm*; drive frequency:10 *Hz*) 84
Figure 4.15 Distorted signal (velocity: 1.5 *m/s*; spacing:100 *mm*; drive frequency:100 *Hz*) 84
Figure 4.16 Distorted signal (velocity: 2 *m/s*; spacing:100 *mm*; drive frequency:10 *Hz*) 85
Figure 4.17 Distorted signal (velocity: 2 */s*; spacing:100 *mm*; drive frequency:100 *Hz*) 85
Figure 4.18 Spectra (velocity:0.5 *m/s*; spacing:100 *mm*; drive frequency: 10 *Hz*) 86
Figure 4.19 Spectra (velocity:0.5 *m/s*; spacing:100 *mm*; drive frequency: 100 *Hz*) 86
Figure 4.20 Spectra (velocity:0.5 *m/s*; spacing:100 *mm*; drive frequency: 1000 *Hz*) 87
Figure 4.21 Spectra (velocity:0.5 *m/s*; spacing:100 *mm*; drive frequency: 1500 *Hz*) 87
Figure 4.22 Spectra (velocity:1 *m/s*; spacing:100 *mm*; drive frequency: 10 *Hz*) 88
Figure 4.23 Spectra (velocity:1 *m/s*; spacing:100 *mm*; drive frequency: 100 *Hz*) 88
Figure 4.24 Spectra (velocity:1 *m/s*; spacing:100 *mm*; drive frequency: 1000 *Hz*) 89

Figure 4.25 Spectra (velocity:1 *m/s*; spacing:100 *mm*; drive frequency: 1500 *Hz*) 89
Figure 4.26 Spectra (velocity:1.5 *m/s*; spacing:100 *mm*; drive frequency: 10 *Hz*) 90
Figure 4.27 Spectra (velocity:1.5 *m/s*; spacing:100 *mm*; drive frequency: 100 *Hz*) 90
Figure 4.28 Spectra (velocity:1.5 *m/s*; spacing:100 *mm*; drive frequency: 1000 *Hz*) 91
Figure 4.29 Spectra (velocity:1.5 *m/s*; spacing:100 *mm*; drive frequency: 1500 *Hz*) 91
Figure 4.30 Spectra (velocity:2 *m/s*; spacing:100 *mm*; drive frequency: 10 *Hz*) 92
Figure 4.31 Spectra (velocity:2 *m/s*; spacing:100 *mm*; drive frequency: 100 *Hz*) 92
Figure 4.32 Spectra (velocity:2 *m/s*; spacing:100 *mm*; drive frequency: 1000 *Hz*) 93
Figure 4.33 Spectra (velocity:2 *m/s*; spacing:100 *mm*; drive frequency: 1500 *Hz*) 93
Figure 4.34 Spectra (velocity:1 *m/s*; spacing:66.7 *mm*; drive frequency: 10 *Hz*) 94
Figure 4.35 Spectra (velocity:1 *m/s*; spacing:66.7 *mm*; drive frequency: 100 *Hz*) 94
Figure 4.36 Spectra (velocity:1 *m/s*; spacing:66.7 *mm*; drive frequency: 1000 *Hz*) 95
Figure 4.37 Spectra (velocity:1 *m/s*; spacing:66.7 *mm*; drive frequency: 1500 *Hz*) 95

CHAPTER 5

Figure 5.1 Flow around a bubble 97
Figure 5.2 Fluid velocity around a bubble 101
Figure 5.3 Schematic of dipole direction 104

CHAPTER 6

Figure 6.1 Drawing of experimental rig 107
Figure 6.2 Schematic drawing of flowmeter 109
Figure 6.3 Schematic of signal detection and feedback system 111
Figure 6.4 Schematic of electrode clamps 112
Figure 6.5 Schematic of electrodes 111
Figure 6.6 Schematic of electrostatic shield 113
Figure 6.7 Schematic of coil of geometry 116

Figure 6.8 Schematic of excitation electronics 118

Figure 6.9 Correlation between drive voltage and power amp. current output 119

Figure 6.10 Correlation between voltage current output from power amp. 120

Figure 6.11 Correlation between power amp. current output and maximum mag. field strength in pipe centre 120

Figure 6.12 Schematic of detection and quadrature suppression electronics 121

Figure 6.13 Schematic of method of quadrature suppression 124

Figure 6.14 Schematic of narrow bandpass filter 125

Figure 6.15a Schematic of PSD method regarding flow related signal 127

Figure 6.15b Schematic of PSD method regarding quadrature related signal 127

Figure 6.16 Transformer signal 130

Figure 6.17a Maxima transformer signal 131

Figure 6.17b Maxima transformer signal 131

Figure 6.17c Maxima transformer signal 131

Figure 6.18 Spectrum for bubble speed of 0.1 *m/s* 132

Figure 6.19 Spectrum for bubble speed of 0.2 *m/s* 133

Figure 6.20 Spectrum for bubble speed of 0.25 *m/s* 133

Figure 6.21 Spectrum for bubble speed of 0.32 *m/s* 134

Figure 6.22 Spectrum for bubble speed of 0.4 *m/s* 134

Figure 6.23 Spectrum for bubble speed of 0.45 *m/s* 135

Figure 6.24 Spectra versus bubble velocities 135

CHAPTER7

Figure 7.1 Schematic of experimental rig 138

Figure 7.2 Spectra and corresponding flow regime for zero flow 139

Figure 7.3 Spectra and corresponding flow regime for bubble flow of 0.15 *m/s* 140

Figure 7.4 Spectra and corresponding flow regime for bubble flow of 0.2 *m/s* 141

Figure 7.5 Spectra and corresponding flow regime for bubble flow of 0.24 *m/s* 142

Figure 7.6 Spectra and corresponding flow regime for bubble flow of 0.275 *m/s* 143

Figure 7.7 Spectra and corresponding flow regime for bubble flow of 0.31 *m/s* 144
Figure 7.8 Spectra and corresponding flow regime for bubble flow of 0.395 *m/s* 145
Figure 7.9 Correlation between peak frequency and bubble velocity 146

CHAPTER 1

INTRODUCTION AND LITERATURE REVIEW

1.1 Objectives

The project is concerned with the behaviour of electromagnetic flowmeters in two-phase flow of electrically insulating fluids (such as oil and gas) with the view to developing electromagnetic flowmeters that can measure the velocity of the second phase. The objective was to gain an understanding of the physical effects of bubbles on the quadrature output of electromagnetic flowmeters for dielectric liquids and to evaluate and test a signal processing means for extracting velocity information for the gas phase. This work laid the basis for the development of electromagnetic flowmeters for two-phase flow measurement of insulating fluids.

1.2 Introduction

Electromagnetic flowmeters have been in use for many years in various parts of the, water, food, process, energy production or chemical industries. The meter is also used in medicine, measuring flow in human blood vessels. The electromagnetic flowmeter is mainly used to measure single phase flow. For commercial applications meters are available for fluids with a minimum conductivity of 0.05 $\mu S/cm$. The basic principle for magnetic flow measurement is based on Faraday's law of induction, which states that when a conductor moves in a magnetic field a voltage is generated in this conductor. The general equation for this application is $U = B \cdot l \cdot v$ where U is the induced voltage, B is the magnetic field, l is the length of the moving conductor across the magnetic field and v is the velocity. This is called "Induction Flowmeasurement". The volumetric flow is directly proportional to the voltage.

General advantages of 'Magmeters' are their high measuring reliability, good accuracy (up to ±0.1 % of measurement at maximum velocity), can be cleaned in place, virtually maintenance free because of no mechanical moving parts and therefore no wear and tear. The major advantage of electromagnetic flowmeters over mechanical flowmeters such as Orifice Plates, Vortex Meters, Turbine Meters or others is that they are not intrusive. They do not cause an additional pressure drop because of some obstruction in the flow. Another major advantage of electromagnetic flowmeters is that they are not susceptible to erosion by solid particles in the flow. Also of impotrance is the fact that this meter is a linear device (i.e. the induced voltage is proportional to the flow rate). It gives a signal whose mean may be directly used to give the mean of the flow rate.

Traditionally, electromagnetic flowmeters as well as many other types of flowmeters are used for single-phase flow only. In practice, however, there are many applications, especially in the oil and petroleum industry, where multiphase flow has to be measured.

1.3 Literature review

The subject of electromagnetic flowmeasurement is a rather wide area and large amount of research work has been published over the last century. For this reason the literature review will cover only a brief history of the general subject of electromagnetic flowmeasurement. More weight is put on the work which has been undertaken on using to measure two phase flow.

•

1.3.1 Brief history on the general electromagnetic flowmeasurement

It was Michael Faraday [1] who discovered in 1831 that a fluid, which moves through a magnetic field experiences an induced voltage. The first flowmeter device was designed by William's [2] in 1930. He used a copper sulphate solution which moved through a

nonconducting circular pipe and applied a uniform transverse magnetic field. This arrangement is shown in Figure 1.1. He measured a d.c. voltage between two electrodes, which were mounted opposite each other on to the pipe and perpendicular to the magnetic field. The arising voltage was proportional to the flowrate.

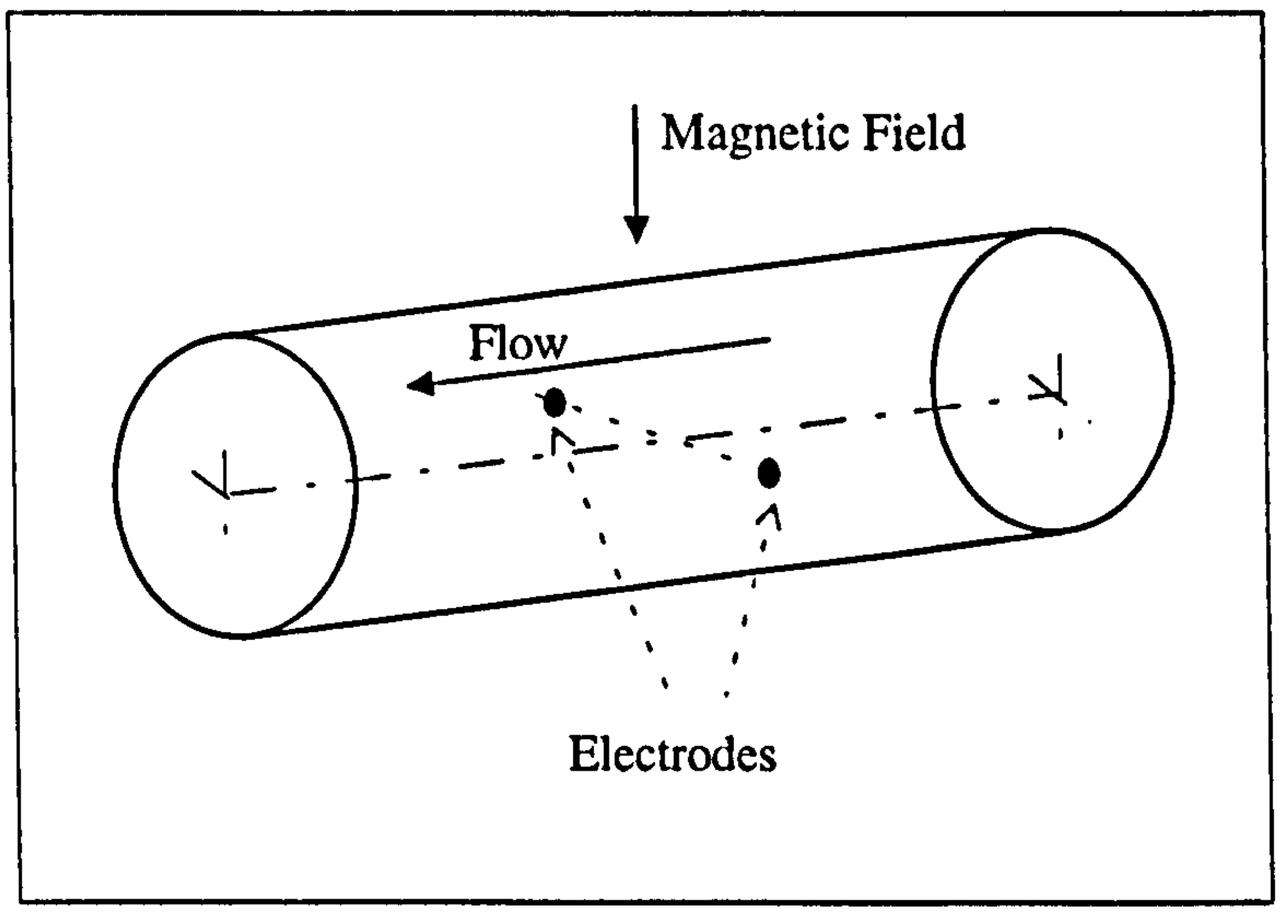

Figure 1.1 (Basic Electromagnetic Flowmeter Arrangement)

William's realised that because the velocity profile is not uniform over the cross section of the pipe, the induced electromagnetic force (e.m.f.) would therefore not be uniform either. The result is that larger e.m.f.'s in the centre of the pipe would drive a current back against the weaker e.m.f.'s near the pipe wall. This effect produces a current circulation. An illustration of this occurrence is given in Figure 1.2.

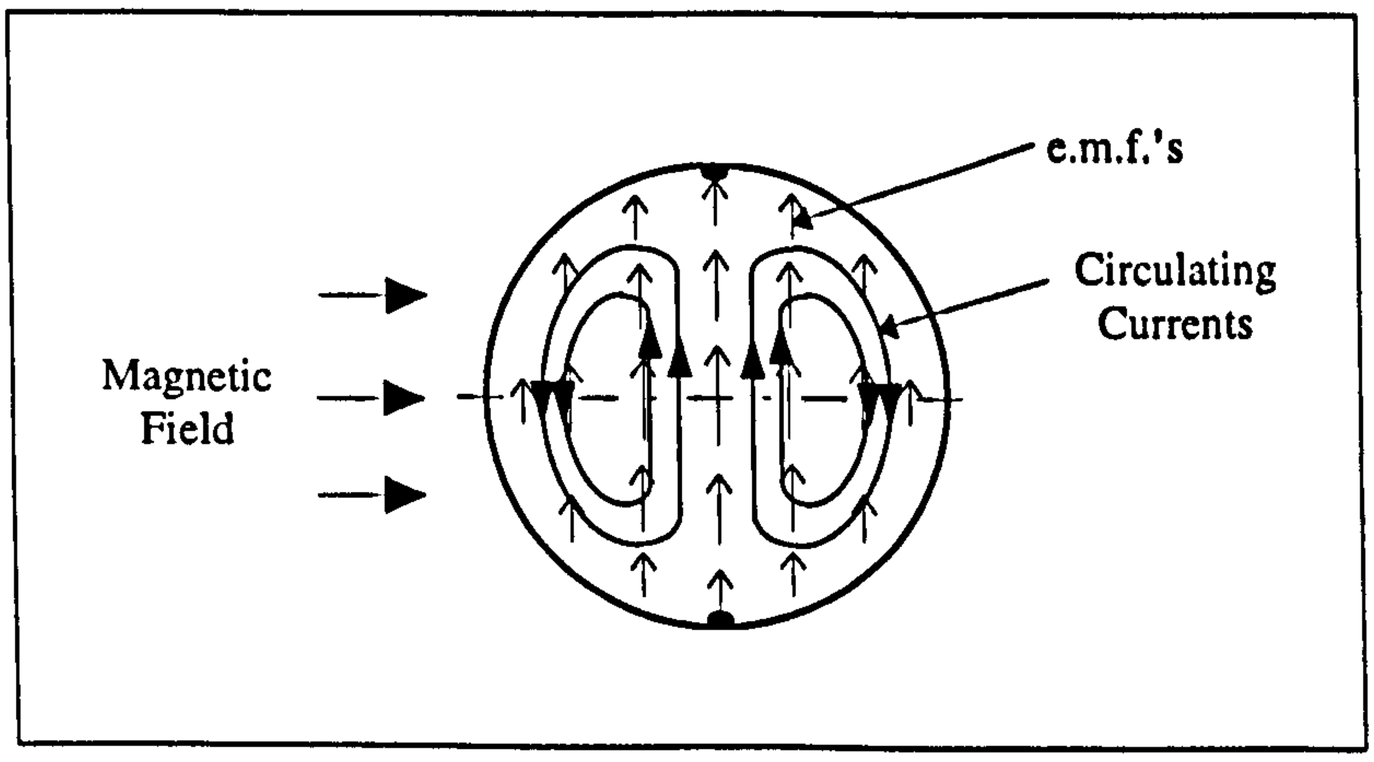

Figure 1.2 (Induced Electromagnetic Force)

The slower moving fluid near the pipe wall 'short-circuits' to some extent the e.m.f. induced in the faster moving fluid in the pipe centre. However, if the velocity distribution is symmetrical about the centre line of the pipe the voltage which appears across the electrodes is the same as it would be if the fluid moved at a uniform velocity. In 1936 Fabre [3] recognised the possibility of making use of this method in measuring blood flow. A further development for electromagnetic blood flow measurement was introduced by Kolin [4] in 1941. He designed a cuff - type flowmeter, which could be mounted around the blood vessel and not damaging it. He also made use of a.c. coil excitation to overcome polarisation on the electrodes. In further medical research other developments took place such as applying a square wave excitation introduced by Denison et al. [5] in 1955 and a trapezoidal wave drive of the coils by Yanof and Salz [6] in 1960. Shercliff [7] gave a comprehensive theoretical contribution including the investigation of conducting and non-conducting walls, circular and rectangular pipe sections, and point and area electrodes, in his book, which he published in 1962. The sensitivity, which is described as $S = \frac{U}{B2av}$ where a is the pipe radius, is only constant when an uniform transverse magnetic field, diametrically opposed electrodes, non-conducting pipe and an axisymmetric velocity profile are provided. Shercliff was the first to introduce the weight function. It gives the sensitivity of the flow induced signal at the electrodes to the velocity at any point in the pipe cross section. An extension of the weight function was given by Bevir [8] in 1970, who introduced the concept of the virtual current that derived the weight vector $\vec{W} = \vec{B} \times \vec{j}$. He described the virtual current (j) as the imaginary current which would flow when a unit current enters through the first electrode and leaves through the second electrode (for no fluid flow). The virtual current theory was applied to investigate a numerous amount of weight functions for different electrode shape and size and various magnetic fields. For a velocity profile which would cause the same flow signal, regardless of its position in the flow conduit, the weight function is aimed to be as uniform as possible. A considerable amount of work improving the sensitivity using weight function theory have been published over the years, such as Ketelsen [9] in 1969, Hemp [10] in 1975, Al-Khazraji and Baker [11] in 1979, Wyatt and O'Sullivan [12] in 1983. It became apparent that

when using large electrodes in an electromagnetic flowmeter the problem of electrode fouling which would affect both the flow signal and transformer signal. Al-Khazraji [13] calculated that the sensitivity for the flow signal would change up to 5% and the transformer signal would change about 10 times of the flow signal for flow velocity of 1 *m/s* and for 100 *mm* diameter flowhead. A way of removing electrode fouling was developed by Cox and Wyatt [14] in 1983, when they introduced insulated electrodes of large area. These non-contacting electrodes were embedded in the flowtube and the result was that this arrangement also reduced the sensitivity by a factor of 14 in comparison to point electrodes. An investigation of eddy currents and transformer signals was carried out by Hemp [15] in 1990. He showed a relation between the axial component E_z of the eddy current *E*-field in the liquid and the electrical potential U induced by a flat profile flow. He could prove with this relation the impossibility of reducing base-line instability by magnetic field shaping. At the same time he found with this relation, a new method for monitoring flowmeter sensitivity.

1.3.2 Governing equations in electromagnetic flow measurement

The foundation for the basic governing equations for the electromagnetic flowmeter theory are Maxwell's equations in the following form

$$\nabla \times \vec{B} = \mu \vec{j} \tag{1.1}$$

$$\nabla \cdot \vec{B} = 0 \tag{1.2}$$

$$\nabla \times \vec{E} = -\dot{\vec{B}} \tag{1.3}$$

and Ohm's law

$$\vec{j} = \sigma\left(\vec{E} + \vec{v} \times \vec{B}\right) \tag{1.4}$$

It is allowable to neglect $\dot{\vec{B}}$ since the influence of this value can be eliminated by means of mechanical and electronic design. The basic relation that the gradient of the potential equals the electric field ($-\nabla U = \vec{E}$) introduces the potential in equation 1.4.

$$\vec{j} = \sigma\left(-\nabla U + \vec{v} \times \vec{B}\right) \tag{1.5}$$

When taking the divergence of this equation and including from equation 1.1 that the divergence of $\vec{j}$ is zero (vector identity), then the following equation appears

$$\nabla^2 U = \nabla \cdot \left(\vec{v} \times \vec{B}\right) \tag{1.6}$$

Applying vector identity to this equation leads to the following expression

$$\nabla^2 U = \vec{B} \cdot \nabla \times \vec{v} - \vec{v} \cdot \nabla \times \vec{B} \tag{1.7}$$

The second term of the above equation can be neglected ($\nabla \times \vec{B} = 0$) since the magnetic field is not affected by the low currents in the fluid. Hence equation 1.7 becomes

$$\nabla^2 U = \vec{B} \cdot \nabla \times \vec{v} \tag{1.8}$$

This equation is known as the 'Flowmeter equation'. Baker [16] derived the solution of equation 1.8 for a circular pipe and for a flow profile which is rotationally symmetrical around the centre line of the pipe as

$$U = \frac{1}{2}\int_0^r \left[\vec{v}\left(\sqrt{\rho r}\right) + \vec{v}\left(a\sqrt{\rho / r}\right)\right] B_0(\rho, \theta) d\rho \tag{1.9}$$

where ρ is the radius for the term to be integrated. The potential difference between diametrically opposed electrodes can be obtained by solving the following integral

$$\Delta U = 2\int_0^a \vec{v}\left(\sqrt{ra}\right) B_0\left(r, \frac{\pi}{2}\right) dr \tag{1.10}$$

For a uniform magnetic field the potential difference can be solved as

$$\Delta U = \frac{4B}{a}\int_0^a rv(r)dr = BDv_m \tag{1.11}$$

with D as pipe diameter and v_m as mean fluid velocity.

1.3.3 The nature of dielectric materials

A dielectric medium in an electric field can be viewed as a free-space arrangement of microscopic electric dipoles. These dipoles are composed of positive and negative charges whose centres do not perfectly coincide. These charges are not free charges, and therefore can not contribute to the conduction process. They are bound in place by atomic and molecular forces and can only shift their positions slightly in response when an external electric field is applied. For this reason these charges within a dielectric medium are called bound charges. Bound charges can be treated as any other sources of the electrostatic field. The feature of all dielectric material (no matter if they are solid, liquid or gas) is their ability to store energy. This storage takes place by shifting the relative positions of the internal, bound positive and negative charges against the original molecular and atomic forces. The source of the energy is a transient current. The negative and positive charges shift in opposite directions (against their mutual attraction) and produce a dipole which is aligned with the electric field. This dipole is described by it's dipole moment $\vec{p}$ and can be calculated as

$$\vec{p} = Q \cdot \vec{d} \tag{1.12}$$

For n dipoles per unit volume there are $n*\Delta V$ dipoles. The total dipole moment is the vector sum,

$$\vec{p}_{sum} = \sum_{i=1}^{n\cdot\Delta V} \vec{p}_i \tag{1.13}$$

Polarisation is defined as the dipole moment per unit volume,

$$\vec{P}_{sum} = \lim_{\Delta V \to 0} \frac{1}{\Delta V} \sum_{i=1}^{n \cdot \Delta V} \vec{p}_i \qquad (1.14)$$

An incremental surface element ΔS is selected in the interior of the dielectric and an electric field $\boldsymbol{E}$ is applied. This is shown in Figure 1.3. The net charge (since there are n molecules/m^3) which crosses the elemental surface in an upward direction is $\Delta Q_{bound} = nQ\vec{d} \cdot \Delta\vec{S}$. In terms of polarisation the last equation can be written as $\Delta Q_{bound} = \vec{P} \cdot \Delta\vec{S}$. The net increase in the bound charge within the closed surface is achieved through the integral

$$Q_{bound} = -\oint_S \vec{P} \cdot d\vec{S} \qquad (1.15)$$

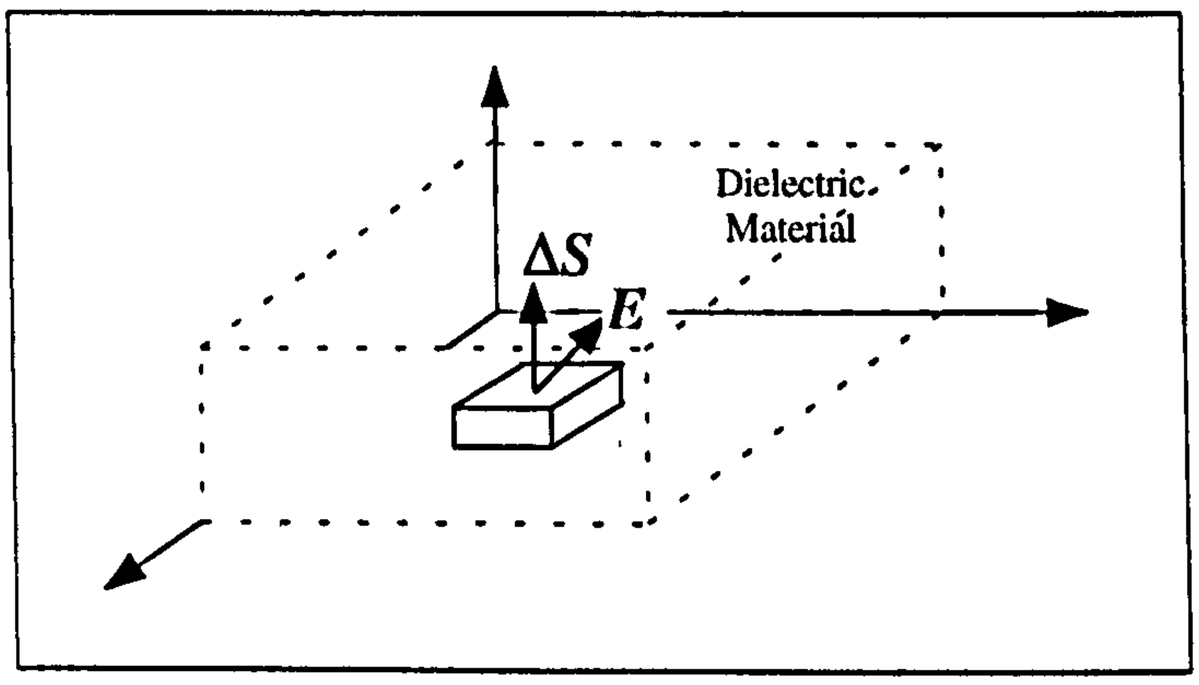

Figure 1.3 (Interior of dielectric)

The general expression for the total charge density (bound plus free charge) is given in Gauss's law as

$$Q_{total} = \oint_S \varepsilon_0 \vec{E} \cdot d\vec{S} \qquad (1.16)$$

The total charge is

$$Q_{total} = Q_{bound} + Q_{free} \qquad (1.17)$$

Consequently the free charge can be expressed by

$$Q_{free} = Q_{total} - Q_{bound} = \oint_S \left(\varepsilon_0 \vec{E} + \vec{P}\right) \cdot d\vec{S} \qquad (1.18)$$

A general equation for the electric flux density ($\boldsymbol{D}$) can now be derived as

$$\vec{D} = \varepsilon_0 \vec{E} + \vec{P} \tag{1.19}$$

Therefore

$$Q_{free} = \oint_S \vec{D} \cdot d\vec{S} \tag{1.20}$$

By making use of the divergence theorem (Maxwell's first equation for electrostatic fields) the above equation can be transformed into the following

$$\nabla \cdot \vec{D} = \rho \tag{1.21}$$

The relationship between the electric field intensity (E) and the polarisation (P) is a function of the type of material. For isotropic materials E and P are linearly related. In an isotropic material the vectors E and P are always parallel. This linear relationship is found as

$$\vec{P} = \chi_e \varepsilon_0 \vec{E} \tag{1.22}$$

with χ_e as the electric susceptibility of the material. The susceptibility can also be expressed as the relative permittivity minus one $\left(\vec{P} = (\varepsilon_r - 1)\varepsilon_0 \vec{E}\right)$. Putting this expression in to equation 1.19 a final form for the electric field flux density can be derived as

$$\vec{D} = \varepsilon_0 \varepsilon_r \vec{E} \tag{1.23}$$

1.3.4 Electromagnetic flowmeter theory for insulating liquids

It was V. Cushing [17, 18, 19] in the late 50's and early 60's who investigated extensively the behaviour of electromagnetic flowmeters with an insulating medium. He worked out a flowmeter theory within he shows that it is possible to measure a potential difference on the electrodes when a nonconducting liquid is used in an electromagnetic flowmeter. He started his investigation by looking at the general law of

induction (an electric field will be induced in a medium moving relative to a magnetic field).

$$\vec{E} = \vec{v} \times \vec{B} \tag{1.24}$$

This induced electric field is proportional to the intensity of the magnetic field and to the relative velocity of the moving medium. This vector equation does not give any information on the dependency and influence of the electrical properties. Cushing therefore concludes and shows how the voltage induced by flow depends on conductivity and dielectric constant of the fluid, as well as on the frequency of induction. He derives an expression (see reference [17]) for the potential that is dependent on the electrical properties of the medium.

$$\nabla^2 U = Z div\left(\vec{B} \times \vec{v}\right) \tag{1.25}$$

where the variable Z, known as attenuation factor, stands for:

$$Z = \alpha + i\beta = Ae^{i\gamma} \tag{1.26}$$

$$\alpha = \frac{1 + (\omega K_0 / \sigma_1)^2 K_1 (K_1 - 1)}{1 + (\omega K_0 K_1 / \sigma_1)^2} \tag{1.27}$$

$$\beta = \frac{\omega K_0 / \sigma_1}{1 + (\omega K_0 K_1 / \sigma_1)^2} \tag{1.28}$$

$$A = \frac{\left\{\left[1 + (\omega K_0 / \sigma_1)^2 K_1 (K_1 - 1)\right]^2 + (\omega K_0 / \sigma_1)^2\right\}^{\frac{1}{2}}}{1 + (\omega K_0 K_1 / \sigma_1)^2} \tag{1.29}$$

$$\gamma = \arctan \frac{\omega K_0 / \sigma_1}{1 + \left(\omega K_0 / \sigma_1\right)^2 K_1 (K_1 - 1)} \tag{1.30}$$

with a further derivation he found an expression for the potential difference at the electrodes as

$$\Delta U = \frac{ZBV}{\pi a} \tag{1.31}$$

where V is the volumetric flowrate

He continuous taking the effect of the pipe configuration into account and finds a final equation for the potential difference on the electrodes for a circular flow pipe where the pipe surface is maintained at zero potential as

$$\Delta U = \frac{2CZBV}{\pi a} \tag{1.32}$$

where the flowmeter configuration constant C is given as

$$C = \frac{R\left[1 - \left(\frac{a}{b}\right)^2\right]}{(R+1) - \left(\frac{a}{b}\right)^2 (R-1)} \tag{1.33}$$

Cushing [20] proposed in 1965 a capacitive pick-up design of the induced potential. The design consisted of a wide area curvilinear electrode which is mounted on the inner pipe wall (touches the fluid) and a driven shield which is placed behind the detection electrode. This driven shield is held at the same potential as the detection electrode by a buffer amplifier of unity gain. The results he gained were promising. He achieved a linear output voltage for a flowrate ranging from 0 to 50 gallons per minute. However,the results on baseline stability with a zero point drift of about 10% of full scale per hour were unsatisfactory.

Hentschel [21] reported in 1973 that for dielectric liquid flow a movement of electrostatic charge is generated and appears as random noise on the electrodes. This electrostatic charge is generated from friction between the pipe wall and the moving liquid as well as the turbulence of the flowing fluid. The magnitude of electrostatic noise depends on fluid velocity, type of liquid, as well as boundary conditions such as pipe wall roughness and arrangement of the electrodes. Hentschel discovered in his investigations that the drive frequency plays a significant role for this kind of noise. He found that with increasing frequency the magnitude of electrostatic noise decreases very considerably.

Al-Rabeh, Baker and Hemp [22] (1978) provided the theoretical principles and a thorough description of governing equations for electromagnetic flowmeasurement applicable to poorly conducting and nonconducting liquids.

Al-Rabeh [23] (1981) designed and carried out experiments on an axial current meter. His results of the output voltage related to the flowrate. But again like in Cushings and Hentschels experiments, the baseline stability was found to be low.

Further work was carried out by Codazzi and Mioque [24] (1986). In their experiments it was observed that a flow related signal existed for flow velocities below 1.5 *m/s*. For higher velocities electrostatic charge noise made it impossible to detect a flow signal.

The recent investigations carried through by Barnes [25] in 1991, whose objective was to assess and narrow the problems associated with the measurement of dielectric liquid flow. His initial experiments did not show a flow induced signal at all, not even for low fluid velocities. The reasons for the failure he concluded were based on three major factors: Flow induced noise (electrostatic charge), because his drive frequency was 278.75 *Hz* only, Non-uniform electrode coupling (electrodes were not firmly attached to the spool piece), and capacitive pick-up from the electro-magnets (500 *V* pk-pk existed on the coils). A capacitive coupling of just 0.2 *pF* is necessary to induce an in-phase potential in the low impedance output leads of 10 *mV*. Also, he pointed out that

this capacitance is very variable due to influencing factors like draughts or changes in humidity.

The latest investigations and efforts to improve the performance of a dielectric electromagnetic flowmeter was implemented by Amare (1994). The emphasis of his work concentrated on overcoming the main problems Barnes experienced. He increased the drive frequency to 1500 *Hz* and minimised the electrostatic noise problem. The associated increase in transformer signal was compensated by applying an electronic quadrature suppression system as well as the method of phase sensitive detection. The very high voltage on the coils (the required magnetic field was 100 *Gauss* the voltage to produce such a magnetic field amounted to 1250 *V* pk-pk) led to an even higher risk of capacitive coupling between the coils and the detection leads. He overcame this problem by designing and building of an eddy current free electrostatic shield. The attenuation for 1500 *Hz* was found to be 60 *dB*. His results were very promising with a linear response of the flow induced signal to the flowrate (range from 0 to 3 *m/s*) and the zero stability of the designed meter was measured to be 2.5% zero drift per hour for full scale voltage and 1% per hour for half the maximum voltage.

1.3.5 Electromagnetic flowmeters for multiphase flow

The first attempt to investigate the behaviour of electromagnetic flowmeters in two-phase flow was carried out by Heineman et al. [27] in 1963. They theoretically developed a form which predicted the vapour volume fraction dependet on voltage output on the meter. Their experimental set-up consisted of two electromagnetic flowmeters placed in series. Only liquid flowed through the first meter and output readings were measured on the electrodes. Before the liquid entered the second meter a gaseous phase was mixed in. With the two output readings from the meters the vapour volume fraction could be calculated with the previously established equation. The gamma attenuation method was used to calculate the void fraction as a reference.

The results were encouraging. For void fractions greater than 20% a deviation of + 9% to -20% compared with the reference results were achieved.

In 1966, Hori et al. [28] carried out an extensive amount of work on electromagnetic flowmeters in two-phase flow. The continuous phase was mercury and water and the second phase was simulated through plastic rods. To simulate different forms of two-phase flow rods of various sizes were placed at various positions in the cross section of the 1 inch flowtube. In this way the flowrate of the continuous liquid phase was kept constant. In their experiments they used two electromagnetic flowmeters put in series. The first meter, upstream of the second, measured the velocity of the single phase. Whereas the arrangement of plastic rods inserted in the flow conduit of the second meter in order to simulate the void and measure the average velocity of the obstructed flow. The void fraction could therefore be calculated by the following equation

$$\alpha = 1 - (U_1/U_2) \tag{1.34}$$

The measured results for the void fractions were slightly lower compared with those calculated from the ratio of the pipe cross section and the cross section of the rods.

Bernier and Brennan [29] in (1982) investigated theoretically and experimentally the behaviour of a transverse electromagnetic flowmeter in two-phase flow. They gave expressions for the potential difference across the electrodes for a homogenous two-phase flow with an uniformly dispersed second phase which has zero velocity, for annular two-phase flow, and two-phase flow with dispersed nonconducting spheres with relative motion. These investigations both theoretically and experimentally led to the conclusion that the calibration of the meter was not dependent on void fraction, flow regime, or flow profile. It was also concluded that the meter measures the average water velocity over a substantial range of void fractions, water flow rates, slip ratios, and flow regimes. The experimental results agreed extremely well (only a 2% deviationwas recorded) with the theoretical predictions. In addition they found that the

flow noise was virtually independent of the void fraction or water flow rate.

In the same year Velt et al. [30] made a different approach in measuring two-phase flow with an electromagnetic flowmeter. Their idea was to consider eddy currents produced by an alternating magnetic field. These eddy currents would be unbalanced by a nonconducting particle moving through the meter and hence generate a signal on the electrodes which would be in phase with the transformer signal. The typical shape for this signal can be described as follows. The voltage rises when the bubble enters the meter then reaches a maximum at a certain distance from the electrode plan, and then falls to zero when reaching z=0. When the bubble passes the position z=0 the same signal occurs in an anti-symmetric form. Their investigations predicted that the magnitude of the signal and position of the peaks along the pipe axis depends on the flowmeter geometry, the magnetic field and the electrode design. The flow rate was calculated by measuring the maximum signal with two meters placed in series and also measuring the time in between.

Krafft [31] in 1994 made use of this idea and further developed this method for a water based main phase and a nonconducting second phase. He investigated the size of the signal depending on the position of the second nonconducting phase in the pipe section as well as the position of maximum and minimum signal occurrence along the pipe axis. He found out that when using large area electrodes the location of maxima and minima is almost constant for any position of the moving bubble in the pipe cross section. In his investigations he also predicted that the spectra peaks at a frequency of $f_p = \frac{v_m / l}{2\pi\sqrt{3}} = 3.68 v_m$. Though his measured values of peak frequencies were all above the calculated ones.

CHAPTER 2

DEVELOPMENT OF AN ANALYTICAL MODEL

2.1 Introduction

In this chapter a theoretical evaluation of the transformer signal in an electromagnetic flowmeter due to a moving gas bubble within a dielectric liquid is made. The objective is to obtain an understanding of the physical effects of a bubble on the output transformer signal of electromagnetic flowmeters for dielectric liquids.

2.2 The Transformer Signal

The existence of the transformer signal has several causes. One major fact that causes this signal is that the electrode wires which constitute a loop which, when not perfectly perpendicular with the applied magnetic field, can pick up induced voltages from the flux of the magnetic field. This phenomena is a result of Faraday's law. A general explanation says that an electromotive force (*emf*), which is simply a voltage that arises, is produced due to relative motion between a steady flux and a closed path or a time varying flux (Φ) linking a stationary closed path, and is described in the following equation and illustrated in Figure 2.1.

$$emf = -\frac{\partial \Phi}{\partial t} = \oint \vec{E} \cdot d\vec{L} = -\int_s \frac{\partial \vec{B}}{\partial t} \cdot d\vec{S} \qquad (2.1)$$

The minus sign indicates that this electromotive force is in a direction to generate a current with a flux, in addition to the initial flux, which reduces the magnitude of the emf. In other words the induced voltage acts to produce an opposing flux and is known

as Lenz's law. Equation (2.1) shows that the transformer signal lags 90° behind the actual flow induced signal. As applied to flowmeters with sinewave excitation it is known as 'quadrature emf'. Even larger transformer signals can arise from electrodes which are not uniform in contact with the liquid. A further increase of this transformer effect arises when bubbles pass through the meter together with the fluid, because the path in the fluid is deflected. This effect is investigated in depth and is explained in the following sections.

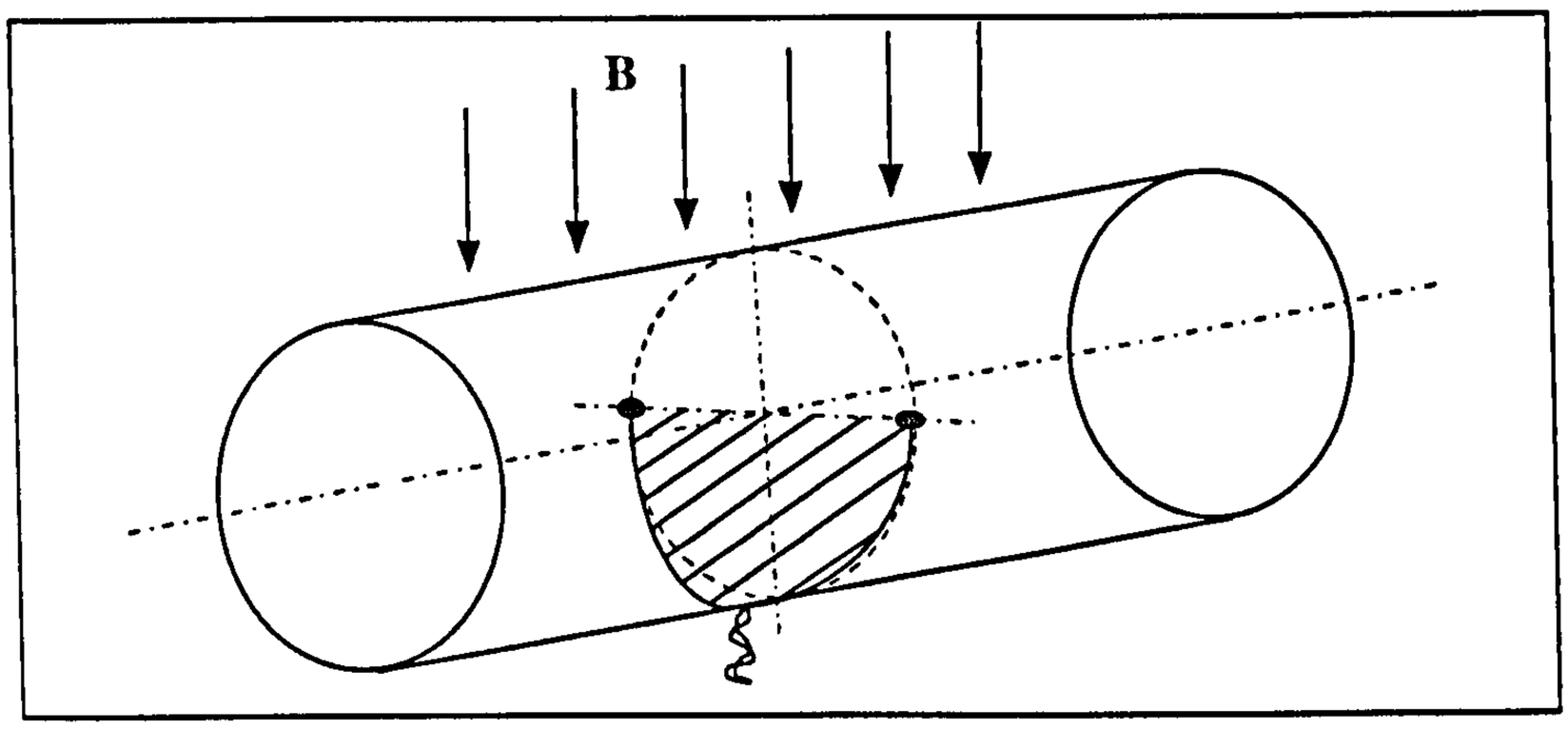

Figure 2.1 (Existance of transformer signal due to loop on detection leads)

2.3 The transformer signal due to a bubble that passes through the meter

The following theoretical approach to the measurement of two-phase flow with a dielectric electromagnetic flowmeter is made. Considering the (displacement) eddy currents in the liquid due to an alternating external magnetic field, as soon as a gas bubble passes through the current field, it is expected to unbalance the eddy currents and therefore produce a 'transformer signal' across the flowmeter electrodes. The following analytical model of eddy current/bubble interaction and resulting signals across the flowmeter electrodes is developed. The magnetic field is assumed to be infinitely long uniform and exactly perpendicular to the y and z axis. End shorting effects were not considered.

2.4 Modelling a dipole in z-direction

A gas bubble of specific permittivity, represented in the form of a sphere, surrounded by a dielectric liquid (oil) is considered in a uniform current field. The undisturbed electric displacement (***D***) field lines are parallel to the z-axis. In Figure 2.2 it is seen that the induced field of the sphere in the region outside the sphere is that of a dipole. The first step is to model a dipole pointing in z-direction. The aim is to gain the strength of the induced dipole.

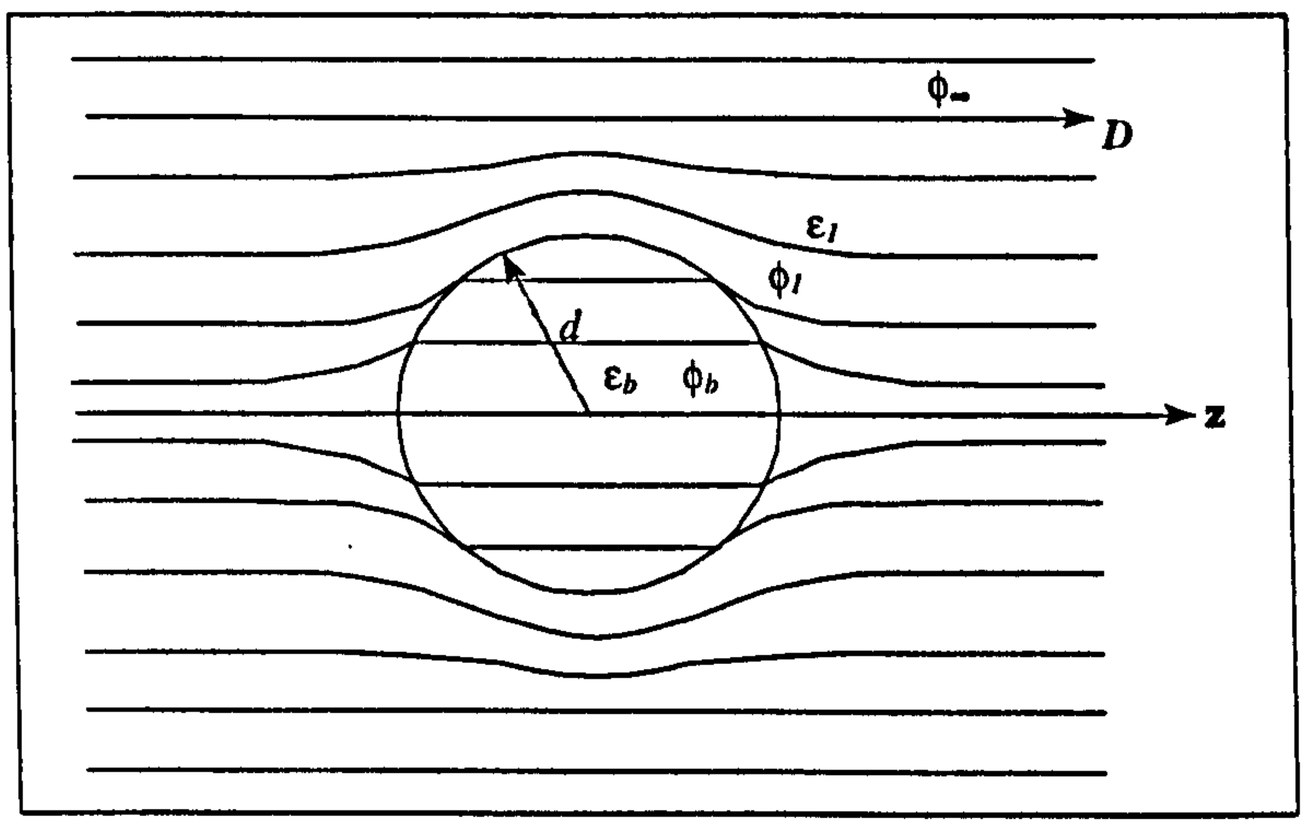

Figure 2.2 (Electric field lines around a gas bubble)

We assume there is no volume charge density or surface charge density on the boundaries (e.g. the surface of the sphere) and therefore Laplace's Equation, in spherical co-ordinates is used to derive a form for the potentials in the different regions.

$$\nabla^2\phi = \frac{1}{r^2}\frac{\partial}{\partial r}\left(r^2\frac{\partial\phi}{\partial r}\right)+\frac{1}{r^2\sin\theta}\frac{\partial}{\partial\theta}\left(\sin\theta\frac{\partial\phi}{\partial\theta}\right)+\frac{1}{r^2\sin^2\theta}\frac{\partial^2\phi}{\partial\varphi^2}=0 \qquad (2.2)$$

Now separating the radial and angular parts of this equation as

$$\phi = R(r)Y(\theta,\varphi) \qquad (2.3)$$

Hence we have the separated equations as

$$\frac{\partial}{\partial r}\left(r^2 \frac{\partial R}{\partial r}\right) - n(n+1)R = 0 \tag{2.4}$$

and

$$\frac{1}{\sin\theta}\frac{\partial}{\partial\theta}\left(\sin\theta \frac{\partial Y}{\partial\theta}\right) + \frac{1}{\sin^2\theta}\frac{\partial^2 Y}{\partial\varphi^2} + n(n+1)Y = 0 \tag{2.5}$$

The form of the separation constant $n(n+1)$, where n is a real integer, is dictated by the necessity that there is a regular solution at the singularities of the equation for Y, which occur at $\theta = 0$ and $\theta = \pi$. In general $Y(\theta,\varphi)$ is known as spherical harmonics. If the boundary is such that $\theta = 0$ and $\theta = \pi$ (i.e. in polar axis) are excluded, then n need not be an integer.

The general solution of the differential equation for the radial part is

$$R(r) = A_n r^n + B_n^{-n+1} \tag{2.6}$$

The spherical surface harmonics can be further separated by means of the following substitution

$$Y(\Theta,\varphi) = \Theta(\theta)\Phi(\varphi) \tag{2.7}$$

The new separation constant is called m^2. For convenience the polar angle variable will be $\mu = \cos\theta$. The resulting equations are

$$\frac{d}{d\mu}\left[(1-\mu^2)\frac{d\Theta}{d\mu}\right] + \left[n(n+1) - \frac{m^2}{1-\mu^2}\right]\Theta = 0 \tag{2.8}$$

$$\frac{d^2\Phi}{d\varphi^2} + m^2\Phi = 0 \tag{2.9}$$

The solutions of these equations are

$$\Theta = C_n P_n^m(\mu) + D_n Q_n^m(\mu) \tag{2.10}$$

$$\Phi = E_m \cos m\varphi + F_m \sin m\varphi \qquad m \neq 0 \tag{2.11}$$

$$\Phi = G\varphi + H \qquad m = 0$$

The functions $P_n^m(\cos\theta)$ and $Q_n^m(\cos\theta)$ are the associated Legendre functions of the first and second kind, respectively. It is necessary to note only that P_n^m is the solution that is finite for $\mu = \pm 1$ and is thus the only solution allowed when the space involved in the problem includes the polar axis.

These solutions yield the following general expression for the potential.

$$\phi = \sum \left[A_n r^n + B_n r^{-n-1}\right]\left[C_n P_n^m(\mu) + D_n Q_n^m(\mu)\right]\left[E_m \cos m\varphi + F_m \sin m\varphi\right] \tag{2.12}$$

Consider now the potential of a dielectric sphere (gas bubble), shown in Figure 2.1, in a uniform field.

2.4.1 Field at infinity

Since the field at infinity is uniform, the potential is given by

$$\phi_\infty = -E_0 z \quad = -E_0 r\cos\Theta \quad = -E_0 r\mu \quad = -E_0 r P_1(\mu) \tag{2.13}$$

2.4.2 Field inside the sphere

Regarding now the region inside the sphere, represented by ϕ_b, the following terms in equation 2.12 are removed.

$B_n r^{-n-1}$: Because if r goes to zero this term goes to zero as well.

$E_m \cos m\varphi + F_m \sin m\varphi$: Because ϕ does not change with the value of the angle φ, (axial symmetry).

Therefore the potential distribution inside the sphere becomes

$$\phi_b = \sum_{n=0}^{\infty} A_n r^n P_n(\mu) \tag{2.14}$$

2.4.3 Field outside the sphere

Finally consider the region outside and near the sphere represented by ϕ_1. The following terms in equation (2.12) is removed.

$A_n r^n$: Because if r goes to infinity this term goes to infinity as well.

$E_m \cos m\varphi + F_m \sin m\varphi$: Because ϕ does not change with the value of the angle φ, (axial symmetry).

Hence the remaining equation for ϕ_1 (near the sphere) become

$$\phi_1 = \sum_{n=0}^{\infty} B_n r^{-n-1} P_n(\mu) - E_0 r P_1(\mu) \tag{2.15}$$

The first term in equation (2.15) represents the dipole source term and the second comes from the uniform field.

2.4.4 Evaluation of the field constants

To evaluate the constants A_n and B_n the coefficients $P_n(\mu)$ had to be equated for the same *n*-values. The boundary conditions are $\phi_b = \phi_1$ and $\varepsilon_b\left(\frac{\partial\phi_b}{\partial r}\right) = \varepsilon_1\left(\frac{\partial\phi_1}{\partial r}\right)$ at $r=d$ and must hold for all values of the angle θ.

Case *n=0*

$$\phi_b = A_0 d^0 P_0(\mu) = B_0 d^{-1} P_0(\mu) = \phi_1$$

$$\therefore \qquad A_0 = \frac{B_0}{d}$$

Also

$$\varepsilon_b \left.\frac{\partial\phi_b}{\partial r}\right|_{r=d} = 0 = \varepsilon_1 B_0(-1)d^{-2}P_0(\mu) = \varepsilon_1 \left.\frac{\partial\phi_1}{\partial r}\right|_{r=d}$$

because: $\left.\begin{array}{l} d \neq 0 \\ P_0(\mu) \neq 0 \\ \varepsilon_1 \neq 0 \end{array}\right\}$ $\therefore \qquad B_0 = 0, A_0 = 0$

Case *(n>1)*

$$\phi_b = A_n d^n P_n(\mu) = B_n d^{-n-1} P_n(\mu) = \phi_1$$

$$\therefore \qquad A_n = \frac{B_n d^{-n-1}}{d^n}$$

Also

$$\varepsilon_b A_n n d^{n-1} P_n(\mu) = \varepsilon_1 B_n(-n-1) d^{-n-2} P_n(\mu)$$

$$\therefore \qquad A_n = \frac{\varepsilon_1 B_n(-n-1) d^{-n-2}}{\varepsilon_b A_n n d^{n-1}}$$

because: $\left.\begin{array}{l} d \neq 0 \\ \varepsilon_b \neq 0 \\ \varepsilon_1 \neq 0 \end{array}\right\}$ $\therefore \qquad B_n = 0 \rightarrow A_n = 0$

Case $n=1$

$$\phi_b = A_1 r^1 P_n(\mu) = B_1 r^{-2} P_1(\mu) - E_0 r P_1(\mu) = \phi_1$$

$$\therefore \qquad A_1 = \frac{B_1 d^{-2}}{d} - \frac{E_0 d}{d} = B_1 d^{-3} - E_0$$

Also

$$\varepsilon_b A_1 1 d^0 P_1(\mu) = \varepsilon_1 \left[B_1(-2) d^{-3} P_1(\mu) - E_0 P_1(\mu) \right]$$

$$A_1 = \frac{\varepsilon_1}{\varepsilon_b} \left[-2 B_1 d^{-3} - E_0 \right]$$

Solving the equations for A_1 and B_1 as

$$A_1 = E_0 \left[\frac{\left(1 - \frac{\varepsilon_1}{\varepsilon_b} \right)}{\left(1 + \frac{2\varepsilon_1}{\varepsilon_b} \right)} - 1 \right] \qquad (2.16)$$

$$B_1 = \frac{E_0\left(1-\frac{\varepsilon_1}{\varepsilon_b}\right)d^3}{\left(1+\frac{2\varepsilon_1}{\varepsilon_b}\right)} \tag{2.17}$$

Having derived the constants A_1 and B_1 equations (2.14) and (2.15) become

$$\phi_b = E_0\left[\frac{\left(1-\frac{\varepsilon_1}{\varepsilon_b}\right)}{\left(1+\frac{2\varepsilon_1}{\varepsilon_b}\right)}-1\right]r\cos\theta \tag{2.18}$$

$$\phi_1 = E_0 r\cos\theta\left[\frac{\left(1-\frac{\varepsilon_1}{\varepsilon_b}\right)d^3}{\left(1+\frac{2\varepsilon_1}{\varepsilon_b}\right)r^3}-1\right] \tag{2.19}$$

2.4.5 Calculation of the dipole strength

Looking at equation 2.19 it is seen that the induced field of the sphere in the region outside of the sphere is that of a dipole. The definition of a dipole is shown in Figure 2.3.

The general definition of a dipole moment is as follows,

$$lim\delta \cdot q = \vec{p}$$

$$\delta \to 0$$

$$q \to \infty$$

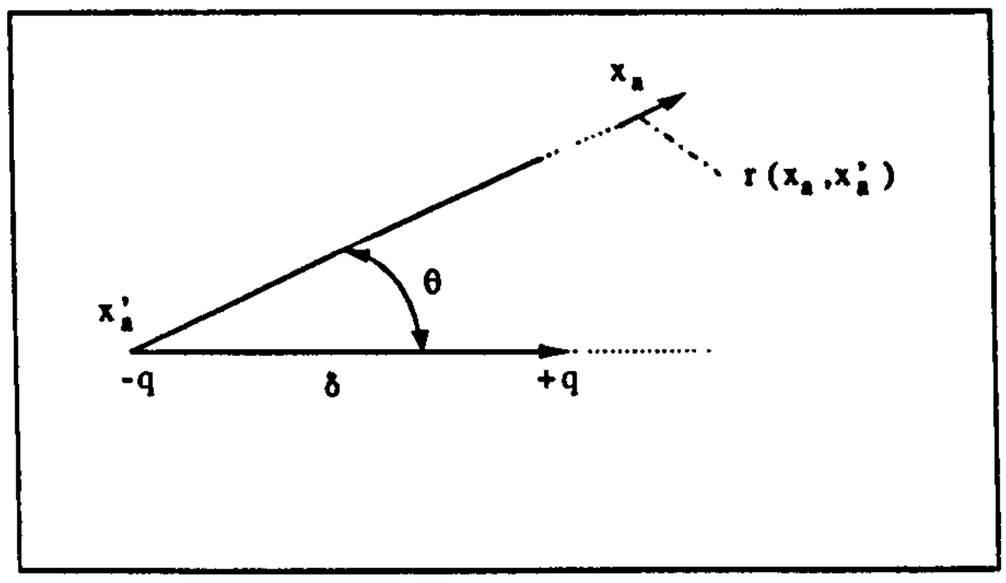

Figure 2.3 (Schematic of dipole definition)

The potential of a dipole is as

$$\phi = \frac{1}{4\pi\varepsilon_0}\frac{\vec{p}\cdot\vec{r}}{r^3} \tag{2.20}$$

Combining equation (2.19) and (2.20) the dipole moment in this case becomes

$$\vec{p} = \vec{E}_0\left[\frac{\left(1-\frac{\varepsilon_1}{\varepsilon_b}\right)}{\left(1+\frac{2\varepsilon_1}{\varepsilon_b}\right)}\right]d^3 4\pi\varepsilon_0 \tag{2.21}$$

2.5 Evaluation of eddy current field

We come now to evaluate the eddy current field E_0 due to the transformer signal using Maxwell's equation for time-varying fields to achieve a solution for E_0. The geometry is shown in figure 2.4.

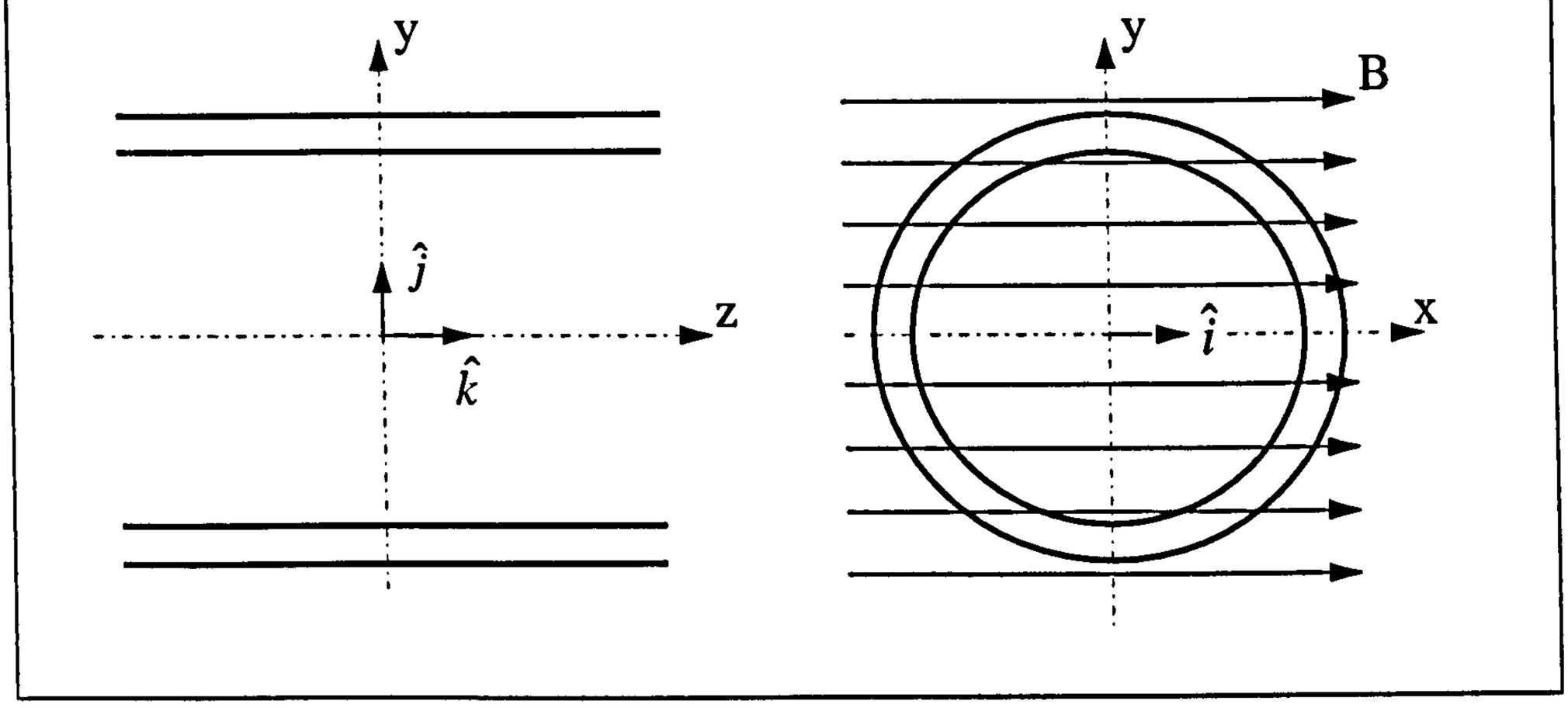

Figure 2.4 (Geometry of Flowmeter Arrangement)

$$\nabla \times \vec{E}_0 = -i\omega\vec{B} \tag{2.22}$$

$$\nabla \times E = \begin{vmatrix} \hat{i} & \hat{j} & \hat{k} \\ \partial/\partial x & \partial/\partial y & \partial/\partial z \\ E_x & E_y & E_z \end{vmatrix} \tag{2.23}$$

Assuming there is no current going in x and y-direction ($\vec{E} = E(y)\vec{\hat{k}}$) (because the walls are parallel to the z-axis), the components E_x and E_y are zero out and therefore equation 2.22 turns into the following form

$$\frac{\partial E_z}{\partial y} = -i\omega\vec{B}$$

Hence E_z becomes $$E_z = -i\omega\vec{B}y \tag{2.24}$$

As it can be seen in equation (2.24) E_z varies linearly with y and becomes maximum near the pipe wall and is zero in the pipe centre. This is also shown in Figure 2.5.

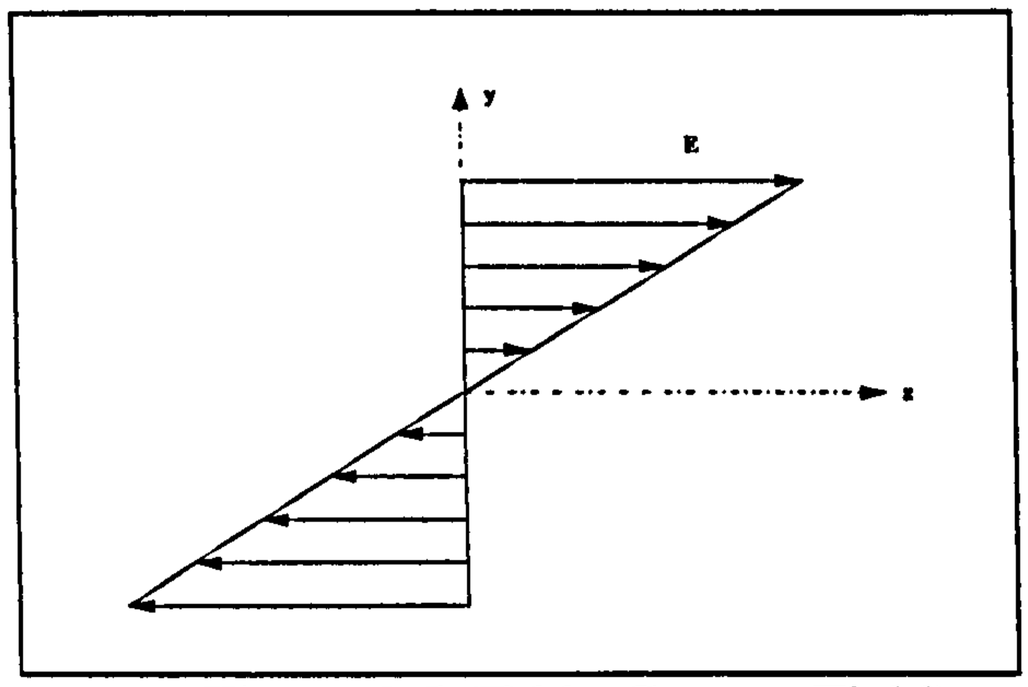

Figure 2.5 (Eddy Current Field)

Having achieved the solution for the electric field, the final expression for the dipole moment becomes

$$\vec{p} = -i\omega By\left[\frac{\left(1-\frac{\varepsilon_1}{\varepsilon_b}\right)}{\left(1+\frac{2\varepsilon_1}{\varepsilon_b}\right)}\right]4\pi\varepsilon_0 d^3 \qquad (2.25)$$

2.6 Model of the field and bubble interaction

Having derived an expression for the dipole moment, now an expression for the potential due to the electric field and bubble interaction in three regions is developed. Region 1 contains the dielectric medium, region 2 is the insulating pipe and region 3 is the medium (air) between the pipe and the grounded shield. In Figure 2.6, this arrangement is shown.

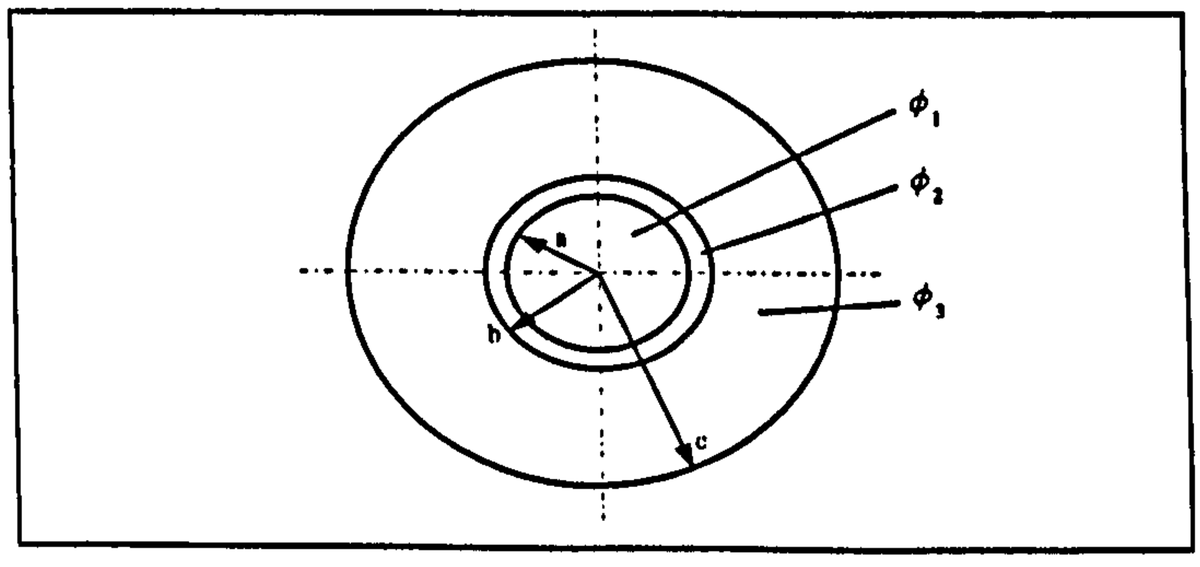

Figure 2.6 (Regions for calculated electrical potentials)

6.1 Expansion of the potential in eigenfunctions

Again, Laplace's equation, this time in cylindrical co-ordinates, is used.

$$\nabla^2\phi = 0 = \frac{1}{r}\frac{\partial}{\partial r}\left(r\frac{\partial\phi}{\partial r}\right)+\frac{1}{r^2}\frac{\partial^2\phi}{\partial\Theta^2}+\frac{\partial^2\phi}{\partial z^2} \qquad (2.26)$$

The following procedure to solve Laplace's equation is used. Starting with the separation of the variables $\phi(r,\Theta,z) = f(r)\cdot g(\Theta)\cdot h(z)$

Putting the variables into equation (2.26) Laplaces equation changes to the following form

$$\frac{1}{r}\frac{d}{dr}(rf'gh)+\frac{1}{r^2}fg''h+fgh'' = 0$$

$$\frac{1}{f}\frac{1}{r}\frac{d}{dr}(rf')+\frac{1}{r^2}\frac{g''}{g}+\frac{h''}{h}=0$$

$$\Rightarrow \qquad \frac{d^2h}{dz^2}-hA^2 = 0$$

$$\Rightarrow \qquad \frac{1}{f}\frac{1}{r}\frac{d}{dr}(rf')+\frac{1}{r^2}\frac{g''}{g}+A^2 = 0 \qquad (2.26.a)$$

where A is a constant.

Continuing the procedure with respect to the second separation constant:

$$\frac{1}{f}r\frac{d}{dr}(rf')+\frac{g''}{g}+A^2r^2=0$$

$$\Rightarrow \qquad \frac{d^2g}{d\Theta^2}+gB^2 = 0$$

$$\Rightarrow \qquad \frac{1}{f} r \frac{d}{dr}\left(rf'\right) + A^2 r^2 - B^2 = 0 \tag{2.26.b}$$

Hence $f(r)$ is in a form of a Bessel function satisfying

$$r \frac{d}{dr}\left(rf'\right) + \left(A^2 r^2 - B^2\right) f = 0 \tag{2.26.c}$$

The three solutions to (2.26a, .b, .c) from Laplace's equation are derived, where A and B are the separation parameters. Equation 26.c is known as Bessel's equation.

For real A and B, then, the integrals are of the form:

$$f(r) = aJ_B(Ar) + bY_B(Ar) \qquad \Rightarrow \text{for } A \neq 0$$

$$f(r) = ar^B + br^{-n} \qquad \Rightarrow \text{for } A = 0$$

$$g(\Theta) = c\cos B\Theta + d\sin B\Theta \qquad \Rightarrow \text{for } B \neq 0$$

$$g(\Theta) = c\Theta + d \qquad \Rightarrow \text{for } B = 0$$

$$h(z) = ke^{Az} + je^{-Az} \qquad \Rightarrow \text{for } A \neq 0$$

$$h(z) = kz + j \qquad \Rightarrow \text{for } A = 0$$

In the present problem neither A nor B are zero, therefore the equation for the potential is as follows

$$\phi = \sum \left(aJ_B(Ar) + bY_B(Ar)\right)\left(c\cos B\Theta + d\sin B\Theta\right)\left(ke^{Az} + je^{-Az}\right) \tag{2.27}$$

Because of the fact that the potential does not approach infinity $(\phi \not\to \infty)$ when moving to infinity along the z-axis $(z \to \infty)$, the term ke^{Az} in equation (2.27) must be zero. For convenience from now on the constants A and B will be renamed m and n respectively. The general solution valid for $z \geq 0$ is

$$\phi = \sum_{n=0}^{\infty}\sum_{m=1}^{\infty}\left\{a_{nm}\left[\left(J_n(mr)+Y_n(mr)\right)\left(\cos n\Theta+\sin n\Theta\right)\right]e^{-mz}\right\} \tag{2.28}$$

Each solution must satisfy the condition $\phi = 0$ on r=c, so that m is limited to a discrete set of values m_l where l is an index number. The entire solution is, in general, a double sum over m_l and n, with coefficients determined so as to satisfy the boundary conditions. The following equations are therefore valid for $z \geq 0$

$$\phi = \sum_{n=0}^{\infty}\sum_{m=1}^{\infty} F_{nl}\phi_{nl}(r,\phi,z) \tag{2.29}$$

where the F_{nl} are constants and the potential in different regions become as follows

in region 1:
$$\phi_{nl} = \underbrace{\left[A_{nl}J_n(m_{nl}r)+Y_n(m_{nl}r)\right]\cos n\Theta}_{\overline{\phi}_{nl1}}e^{-m_{nl}z} \tag{2.30}$$

in region 2:
$$\phi_{nl} = \underbrace{\left[B_{nl}J_n(m_{nl}r)+C_{nl}Y_n(m_{nl}r)\right]\cos n\Theta}_{\overline{\phi}_{nl2}}e^{-m_{nl}z} \tag{2.31}$$

in region 3:
$$\phi_{nl3} = \underbrace{\left[D_{nl}J_n(m_{nl}r)+E_{nl}Y_n(m_{nl}r)\right]\cos n\Theta}_{\overline{\phi}_{nl3}}e^{-m_{nl}z} \tag{2.32}$$

The term $Y_n(m_{nl}r)$ in equation (2.30) is not needed, because for $r=0$ this Bessel function goes to infinity.

The above equations (2.30, 2.31, 2.32) are used to form a matrix in order to achieve the relations between the constants A, B, C, D and E. The following boundary conditions are valid and used.

$$\phi_{nl1}(r=a) = \phi_{nl2}(r=a) \tag{2.33}$$

$$\phi_{nl2}(r=b)=\phi_{nl3}(r=b) \tag{2.34}$$

$$\phi_{nl3}(r=c)=0 \tag{2.35}$$

$$\varepsilon_1\frac{\partial\phi_{nl1}(r=a)}{\partial r}=\varepsilon_2\frac{\partial\phi_{nl2}(r=a)}{\partial r} \tag{2.36}$$

$$\varepsilon_2\frac{\partial\phi_{nl2}(r=b)}{\partial r}=\varepsilon_3\frac{\partial\phi_{nl3}(r=b)}{\partial r} \tag{2.37}$$

Hence the boundary conditions applied to equation (2.30, 2.31, 2.32) became

$$\begin{bmatrix} A_{nl}J_n(m_{nl}a)=B_{nl}J_{nl}(m_{nl}a)+C_{nl}Y_n(m_{nl}a) \\ B_{nl}J_n(m_{nl}b)+C_{nl}Y_{nl}(m_{nl}b)=D_{nl}J_n(m_{nl}b)+E_{nl}Y_n(m_{nl}b) \\ D_{nl}J_n(m_{nl}c)+E_{nl}Y_n(m_{nl}c)=0 \\ \varepsilon_1 A_{nl}m_{nl}J'_n(m_{nl}a)=\varepsilon_2[B_{nl}m_{nl}J'_n(m_{nl}a)+C_{nl}m_{nl}Y'_n(m_{nl}a)] \\ \varepsilon_2[B_{nl}m_{nl}J'_n(m_{nl}b)+C_{nl}m_{nl}Y'_n(m_{nl}b)]=\varepsilon_3[D_{nl}m_{nl}J'_n(m_{nl}b)+E_{nl}m_{nl}Y'_n(m_{nl}b)] \end{bmatrix} \tag{2.38}$$

Having a linear system of equations, the next step is to set it in matrix form. Hence equation (2.37) becomes

$$\begin{bmatrix} J_n(m_{nl}a) & -J_n(m_{nl}a) & -Y_n(m_{nl}a) & 0 & 0 \\ 0 & J_n(m_{nl}b) & J_n(m_{nl}b) & -J_n(m_{nl}b) & -Y_n(m_{nl}b) \\ 0 & 0 & 0 & J_n(m_{nl}c) & Y_n(m_{nl}c) \\ J'_n(m_{nl}a)\varepsilon_1 m_{nl} & -J'_n(m_{nl}a)\varepsilon_2 m_{nl} & -Y'_n(m_{nl}a)\varepsilon_2 m_{nl} & 0 & 0 \\ 0 & J'_n(m_{nl}b)\varepsilon_2 m_{nl} & Y'_n(m_{nl}b)\varepsilon_2 m_{nl} & -J'_n(m_{nl}b)\varepsilon_3 m_{nl} & -Y'_n(m_{nl}b)\varepsilon_3 m_{nl} \end{bmatrix} \begin{bmatrix} A_{nl} \\ B_{nl} \\ C_{nl} \\ D_{nl} \\ E_{nl} \end{bmatrix} = 0 \tag{2.39}$$

The determinant of the matrix is calculated with a computer software program (Maple). By setting the determinant equal to zero the eigenvalues m_{nl} are calculated from a

FORTRAN program. Both the determinant and the flow-chart are listed in Appendix A. The form of the above matrix (2.39) would give an infinite number of solutions for the constants A, B, C, D and E. However by using the following method a set of finite solutions is achieved. Dividing the matrix by the constant A will form a 'new' matrix of the following configuration.

$$\begin{bmatrix} J_n(m_{nl}a) & -J_n(m_{nl}a) & -Y_n(m_{nl}a) & 0 & 0 \\ 0 & J_n(m_{nl}b) & J_n(m_{nl}b) & -J_n(m_{nl}b) & -Y_n(m_{nl}b) \\ 0 & 0 & 0 & J_n(m_{nl}c) & Y_n(m_{nl}c) \\ J'_n(m_{nl}a)\varepsilon_1 m_{nl} & -J'_n(m_{nl}a)\varepsilon_2 m_{nl} & -Y'_n(m_{nl}a)\varepsilon_2 m_{nl} & 0 & 0 \\ 0 & J'_n(m_{nl}b)\varepsilon_2 m_{nl} & Y'_n(m_{nl}b)\varepsilon_2 m_{nl} & -J'_n(m_{nl}b)\varepsilon_3 m_{nl} & -Y'_n(m_{nl}b)\varepsilon_3 m_{nl} \end{bmatrix} \begin{bmatrix} A_{nl}/A_{nl} \\ B_{nl}/A_{nl} \\ C_{nl}/A_{nl} \\ D_{nl}/A_{nl} \\ E_{nl}/A_{nl} \end{bmatrix} = 0$$

(2.40)

For convenience the following substitution is made

$$B_{nl}/A_{nl} = U_{nl}$$
$$C_{nl}/A_{nl} = V_{nl}$$
$$D_{nl}/A_{nl} = W_{nl}$$
$$E_{nl}/A_{nl} = X_{nl}$$

Multiplying the constants V_{nl}, W_{nl}, X_{nl} and Y_{nl} back into the matrix an obviously solvable equation system comes up with the form

$$\begin{bmatrix} U_{nl}J_n(m_{nl}b)+V_{nl}J_n(m_{nl}b)-W_{nl}J_n(m_{nl}b)-X_{nl}Y_n(m_{nl}b)=0 \\ W_{nl}J_n(m_{nl}c)+X_{nl}Y_n(m_{nl}c)=0 \\ -\varepsilon_2 U_{nl}m_{nl}J'_n(m_{nl}a)-\varepsilon_2 V_{nl}m_{nl}Y'_n(m_{nl}a)=-\varepsilon_1 m_{nl}J'_n(m_{nl}a) \\ \varepsilon_2 U_{nl}m_{nl}J'_n(m_{nl}b)+\varepsilon_2 V_{nl}m_{nl}Y'_n(m_{nl}b)-\varepsilon_3 W_{nl}m_{nl}J'_n(m_{nl}b)-\varepsilon_3 X_{nl}m_{nl}Y'_n(m_{nl}b)=0 \end{bmatrix}$$

For further simplification the following substitutions are made

$$J_n(m_{nl}a)=a$$

$$Y_n(m_{nl}a)=b$$

$$J_n(m_{nl}b)=c$$

$$Y_n(m_{nl}b)=d$$

$$J_n(m_{nl}c)=e$$

$$Y_n(m_{nl}c)=f$$

$$m_{nl}J'_n(m_{nl}a)=g$$

$$m_{nl}Y'_n(m_{nl}a)=h$$

$$m_{nl}J'_n(m_{nl}b)=i$$

$$m_{nl}Y'_n(m_{nl}b)=j$$

The solutions for the above equations are calculated as

$$B/A = \qquad U=\frac{\varepsilon_1 g\left(-df\varepsilon_3 i+\varepsilon_2 jef-\varepsilon_2 jde+de\varepsilon_3 j\right)}{(\%1)\varepsilon_2} \tag{2.41}$$

$$C/A = \qquad V=\frac{-\varepsilon_1 g\left(-cf\varepsilon_3 i-i\varepsilon_2 de+c\varepsilon_3 je+i\varepsilon_2 fc\right)}{(\%1)\varepsilon_2} \tag{2.42}$$

$$D/A = \qquad W=\frac{f\varepsilon_1 g(jc-id)}{\%1} \tag{2.43}$$

$$E/A = \qquad X=-\frac{e\varepsilon_1 g(jc-id)}{\%1} \tag{2.44}$$

where

$$\%1=-hcf\varepsilon_3 i-hi\varepsilon_2 de+jg\varepsilon_2 de+hc\varepsilon_3 je+hi\varepsilon_2 fc-jg\varepsilon_2 fc+dgf\varepsilon_3 i-dg\varepsilon_3 je$$

Having found the solutions for the constants, the next step is to determine the constants F_{nl} in the general solution for the potential distribution (2.29) or

$$\phi = \sum_{n} \sum_{l} F_{nl} \overline{\phi}_{nl} e^{-m_{nl} z} \qquad (2.45)$$

where $\overline{\phi}_{nl} = \overline{\phi}_{nl1}, \overline{\phi}_{nl2}, \overline{\phi}_{nl2}$ are defined in equations 3.30 to 3.31 for regions 1,2 and 3.

2.6.2 Field of a point charge in the duct

We first place a unit charge on the x-axis at distance *s* from the flowmeter axis, shown in Figure 2.7.

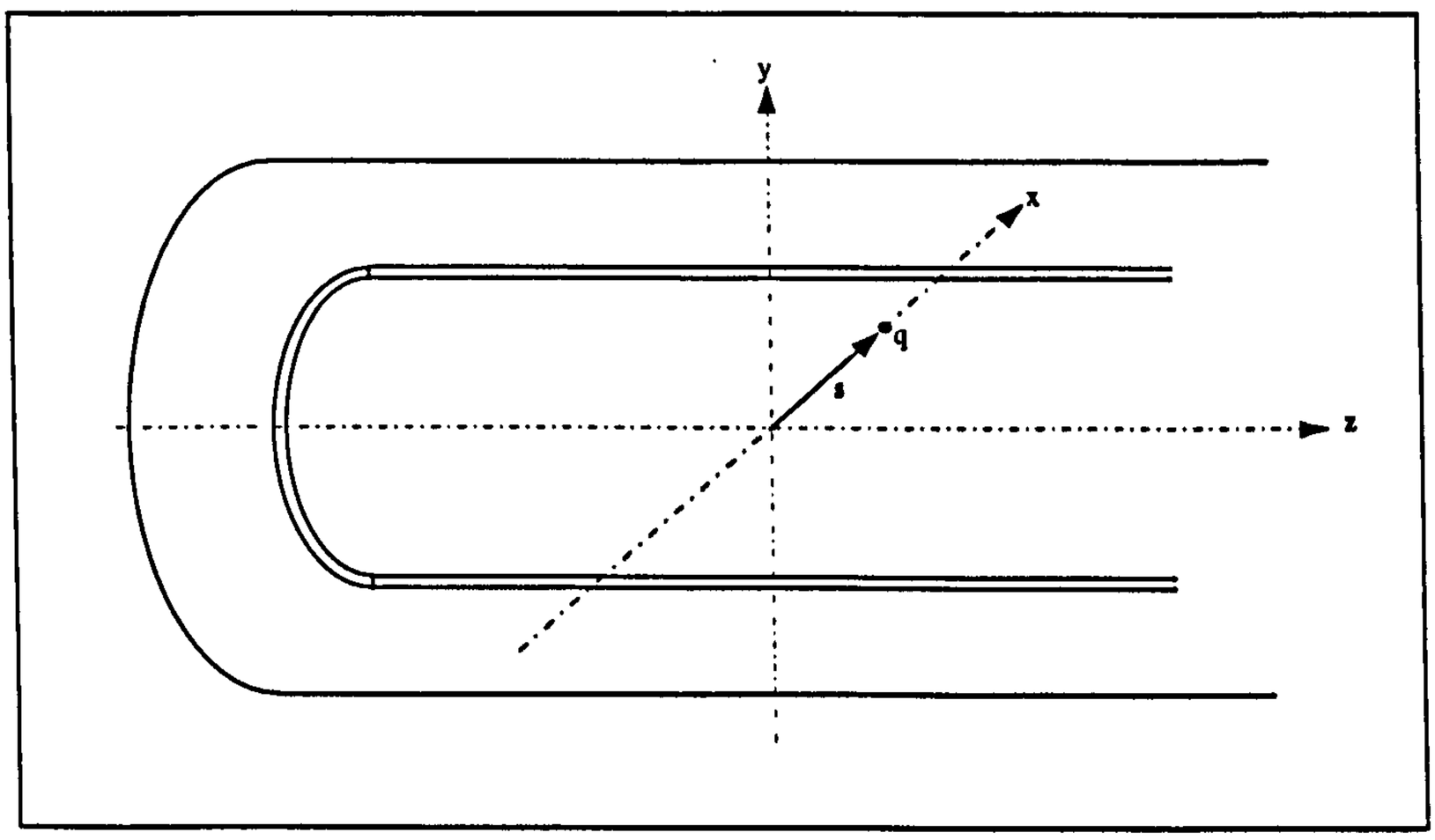

Figure 2.7 (Schematic of Charge in pipe section)

To find the field of the charge we use the well known equation to define the relation between an electric field and its potential (2.46) as well as Gaussian theorem to establish a solution for this particular charge distribution.

$$\vec{E} = -\nabla\phi \qquad (2.46)$$

The general form of Gaussian theorem is explained below. See also Figure 2.8. Gaussian law generally states that the electric flux passing through any closed surface is equal to the total charge enclosed by that surface.

$$\oint \vec{D} \cdot d\vec{S} = q$$

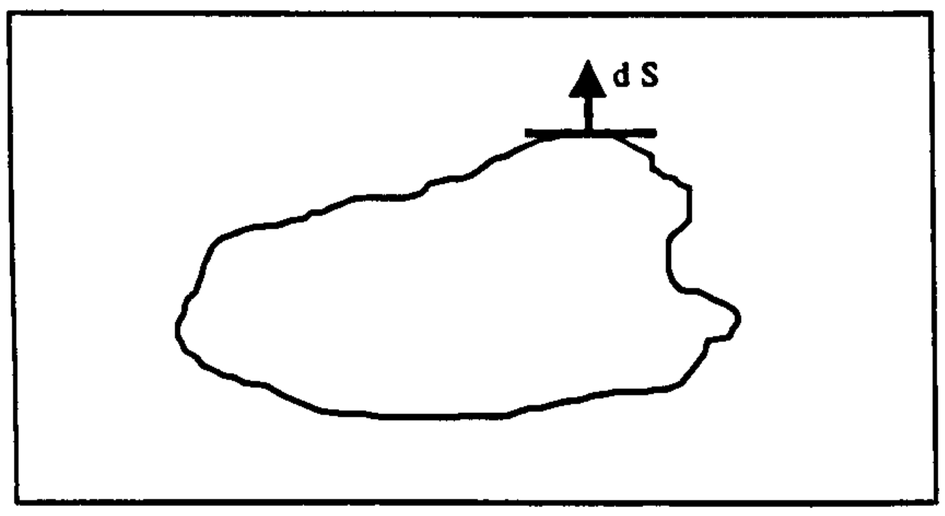

Figure 2.8 (Schematic of Gauss's law)

In this specific case the way to apply Gaussian law is as follows. Having put a unit charge on the x-axis at $z=0$, two closed surfaces (on the left and right sides of the z-axis) have to be considered. See Figure 2.9 and 2.10. Reducing the problem by considering only one side of the closed surface the equation for Gauss's law (in polar co-ordinates)

becomes

$$\int_a^{2\pi} \int_0^a D_z r dr d\Theta = \frac{1}{2} q \qquad (2.47)$$

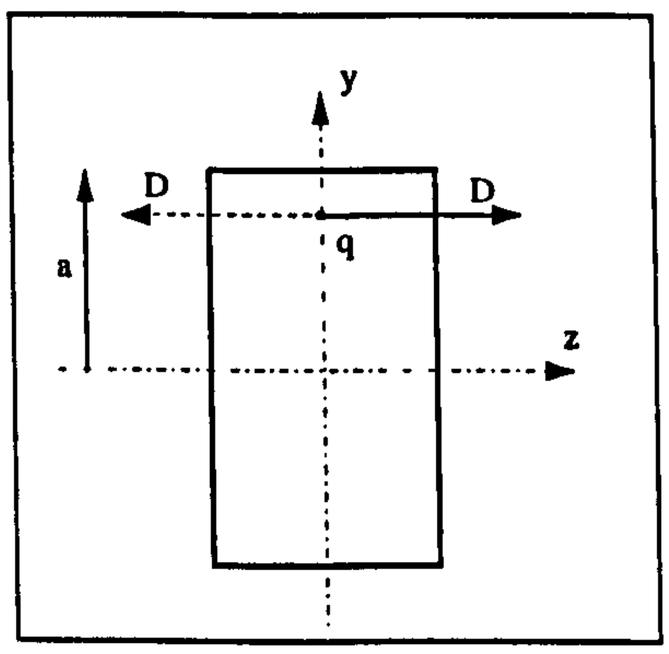

Figure 2.9

(Position of charge and electric flux density)

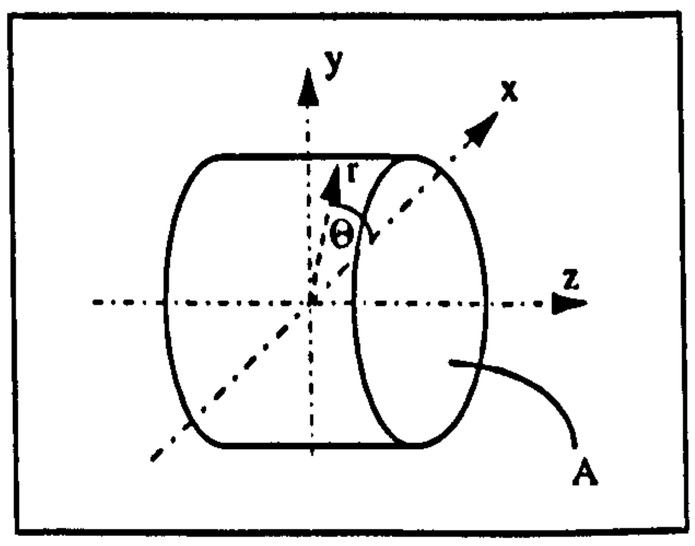

Figure 2.10

(Definition of radius and angle on charge)

Putting equation (2.46) and (2.47) together lends to

$$\int_A D \cdot dA = \iint \varepsilon \cdot 2 \left. \frac{\partial \phi}{\partial z} \right|_{z=0} r \cdot dr d\Theta = q \tag{2.48}$$

From equation (2.46) an expression for the electric flux density in z-direction can be extracted, so that D_z became

$$D_z = -\varepsilon \left. \frac{\partial \phi}{\partial z} \right|_{z=0} \qquad \varepsilon = \varepsilon_0 \varepsilon_r \tag{2.49}$$

At the point where the charge is a discontinuity the potential gradient occurs in the z-direction. This discontinuity can be represented by a Dirac Delta function. Hence the flux condition can now be expressed in terms of the two dimensional *Dirac* δ -function, for which

$$\iint \delta(r - s)\delta(\Theta) r dr d\Theta = 1 \tag{2.50}$$

Putting equation (2.48), (2.49) and (2.50) together, an expression for the flux condition due to a unit charge comes up and is stated in equation (2.51).

$$\frac{1}{\varepsilon_1} \frac{1}{r} q \delta(r - s)\delta(\Theta) = -2 \left. \frac{\partial \phi}{\partial z} \right|_{z=0} \tag{2.51}$$

A substitution of equation (2.45) into the above equation (2.51) leads to the expression (2.52) below.

$$\frac{1}{\varepsilon_1} \frac{1}{r} q \delta(r - s)\delta(\Theta) = -2 \sum_n \sum_l F_{nl} \bar{\phi}_{nl}(-m_{nl}) \tag{2.52}$$

The term $e^{-m_{nl}z}$ is omitted because for $z=0$ the exponential term becomes *1*.

2.6.3 Evaluation of the coefficients in equation (2.52)

The next step is to find the constants $F_{n.}$ For this task both sides of equation 2.52 are multiplied by $\overline{\phi}_{n'l'} \cdot \varepsilon$ and then integrated with respect to $rdrd\Theta$ by using the orthogonality properties of the eigenfunctions.

$$\iint \frac{1}{\varepsilon}\frac{1}{r} q\delta(r-s)\delta(\Theta)\varepsilon\overline{\phi}_{n'l'} rdrd\Theta = -2\sum_{n}\sum_{l}(-m_{nl})F_{n'l'} \qquad \underbrace{\iint \varepsilon\overline{\phi}_{nl}\overline{\phi}_{n'l'} rdrd\Theta}_{\substack{orthogonality-properties \\ =0 \rightarrow if\ldots n\neq n',or\ldots\ldots\ldots l\neq l' \\ \neq 0 \rightarrow if\ldots n=n',and\ldots\ldots l=l}}$$

(2.53)

To evaluate the left hand side of equation (2.53) it is known that when integrating a *Dirac* δ -function times a second function it becomes of the magnitude of the second function at that point where the *Dirac* δ -function is infinite.

Hence

$$q \cdot \overline{\phi}_{n'l'}\begin{pmatrix} r=s \\ \Theta=0 \end{pmatrix} = 2m_{n'l'}F_{n'l'}\int_{0}^{2\pi}\int_{0}^{c}\varepsilon\left(\overline{\phi}_{n'l'}\right)^2 rdrd\Theta \tag{2.54}$$

and an equation for the constants $F_{n'l'}$ is

$$F_{n'l'} = \frac{q\overline{\phi}_{n'l'}\begin{pmatrix} r=s \\ \Theta=0 \end{pmatrix}}{2\cdot m_{n'l'}\int_{0}^{2\pi}\int_{0}^{c}\varepsilon\left(\overline{\phi}_{n'l'}\right)^2 rdrd\Theta} \tag{2.55}$$

The remaining problem is to solve the integral in the denominator of equation (2.55). An integral of a product of two Bessel functions is given in Abramowitz & Stegun (Page 484, nr. 11.3.31) as

$$\int r^{\mu+\nu+1}\Re_{\mu}(r)\Im_{\nu}(r)dr=\frac{r^{\mu+\nu+2}}{2\cdot(\mu+\nu+1)}\left\{\Re_{\mu}(r)\Im_{\nu}(r)+\Re_{\mu+1}(r)\Im_{\nu+1}(r)\right\} \qquad (2.56)$$

To bring equation (2.56) in a shape corresponding to the integral in the denominator in equation (2.55), which includes the equations (2.30, 2.31, 2.32), the sum of the exponents μ,ν in equation (2.56) must vanish. To do that, the exponents are set equal and opposite, $\mu=-\nu$. Then a relation between Bessel functions of positive and negative orders is found in Abramowitz & Stegun (page 358 nr 9.1.5)

$$J_{-n}(r)=(-1)^n J_n(r) \qquad\qquad Y_{-n}(r)=(-1)^n Y_n(r)$$

in this case: $-\mu=\nu=n$

The final resolution for the integral of the Bessel function is as follows,

$$\int r^{-n+n+1}\Re_{-n}(r)\Im_{n}(r)dr=\frac{r^{-n+n+2}}{2\cdot(-n+n+1)}\left\{\begin{array}{cc}\underbrace{\Re_{-n}(r)}_{(-1)^n\Re_n(r)}\Im_n(r)+ & \underbrace{\Re_{-n+1}(r)}_{(-1)^{(n-1)}\Re_{n-1}(r)}\Im_{n+1}(r)\end{array}\right\}$$

$$=\frac{r^2}{2}\left\{\Re_n(r)\Im_n(r)-\Re_{n-1}(r)\Im_{n+1}(r)\right\}$$

(2.57)

The general resolution for the trigonometric integral is obtained from

$$\int(\cos n\Theta)^c d\Theta=\frac{(\cos n\Theta)^{c-1}\cdot\sin n\Theta}{2n}+\frac{c-1}{2}\int(\cos n\Theta)^{c-2}d\Theta \qquad (2.58)$$

valid for $n>0$.

The specific case $(c=2)$ becomes

$$\int (\cos n\Theta)^2 d\Theta = \frac{\cos n\Theta - \sin n\Theta}{2n} + \frac{1}{2}\Theta \tag{2.59}$$

2.6.3.1 Evaluation of the integrals

Having found the expressions for the integrals, these expressions are evaluated in the different regions.

A) Region 1

$$\int_0^a \int_0^{2\pi} \varepsilon_1 \left(\overline{\phi}_{nl}\right)_1^2 r dr d\Theta = \int_0^a \int_0^{2\pi} \varepsilon_1 \left(A_{nl} J_n(m_{nl}) \cdot \cos n\Theta\right)^2 r dr d\Theta$$

$$= \int_0^a \int_0^{2\pi} \varepsilon_1 A_{nl}{}^2 \left(J_n(m_{nl} r)\right)^2 (\cos n\Theta)^2 r dr d\Theta$$

$$= \varepsilon_1 A_{nl}^2 \left\{ \frac{r^2}{2} \left[\left(\left(J_n(m_{nl} r)\right)^2 - \left(J_{n-1}(m_{nl} r)\right) J_{n+1}(m_{nl} r) \right) \right] \right\} \Bigg|_{r=0}^{r=a} \left\{ \frac{\cos n\Theta \sin n\Theta}{2n} + \frac{1}{2}\Theta \right\} \Bigg|_{\Theta=0}^{\Theta=2\pi}$$

$$= \varepsilon_1 A_{nl}^2 \frac{a^2}{2} \left[\left(\left(J_n(m_{nl} a)\right)^2 - \left(J_{n-1}(m_{nl} a)\right) J_{n+1}(m_{nl} a) \right) \right] \cdot \pi$$

(2.60)

B) Region 2

$$\int_a^b \int_0^{2\pi} \varepsilon_2 \left(\overline{\phi}_{nl}\right)_2^2 r dr d\Theta \quad = \int_a^b \int_0^{2\pi} \varepsilon_2 \left\{\left[B_{nl} J_n\left(m_{nl} r\right) + C_{nl} Y_n\left(m_{nl} r\right)\right] \cdot \cos n\Theta\right\}^2 r dr d\Theta$$

$$\int_a^b \int_0^{2\pi} \varepsilon_2 \left\{B_{nl} J_n\left(m_{nl} r\right) \cdot \cos n\Theta\right\}^2 r dr d\Theta \; +$$

$$\int_a^b \int_0^{2\pi} \varepsilon_2 \left\{C_{nl} Y_n\left(m_{nl} r\right) \cdot \cos n\Theta\right\}^2 r dr d\Theta \; +$$

$$\int_a^b \int_0^{2\pi} \varepsilon_2 2 B_{nl} J_n\left(m_{nl} r\right) \cdot \cos n\Theta \cdot C_{nl} Y_n\left(m_{nl} r\right) \cdot \cos n\Theta r dr d\Theta$$

$$= \left[\varepsilon_2 \pi\right] \cdot$$

$$\left\{B_{nl}^2 \left[\left\{\frac{b^2}{2}\left[\left(J_n\left(m_{nl} b\right)\right)^2 - \left(J_{n-1}\left(m_{nl} b\right) J_{n+1}\left(m_{nl} b\right)\right)\right]\right\} - \left\{\frac{a^2}{2}\left[\left(J_n\left(m_{nl} a\right)\right)^2 - \left(J_{n-1}\left(m_{nl} a\right) J_{n+1}\left(m_{nl} a\right)\right)\right]\right\}\right] +$$

$$\left\{C_{nl}^2 \left[\left\{\frac{b^2}{2}\left[\left(Y_n\left(m_{nl} b\right)\right)^2 - \left(Y_{n-1}\left(m_{nl} b\right) Y_{n+1}\left(m_{nl} b\right)\right)\right]\right\} - \left\{\frac{a^2}{2}\left[\left(Y_n\left(m_{nl} a\right)\right)^2 - \left(Y_{n-1}\left(m_{nl} a\right) Y_{n+1}\left(m_{nl} a\right)\right)\right]\right\}\right] +$$

$$2 B_{nl} C_{nl} \left[\left[\frac{b^2}{2}\left\{J_n\left(m_{nl} b\right) Y_n\left(m_{nl} b\right) - J_{n-1}\left(m_{nl} b\right) Y_{n+1}\left(m_{nl} b\right)\right\}\right] - \left[\frac{a^2}{2}\left\{J_n\left(m_{nl} a\right) Y_n\left(m_{nl} a\right) - J_{n-1}\left(m_{nl} a\right) Y_{n+1}\left(m_{nl} a\right)\right\}\right]\right]\right\}$$

(2.61)

C. Region 3

$$\int_b^c \int_0^{2\pi} \varepsilon_3 \left(\overline{\phi}_{nl}\right)_3^2 r dr d\Theta \quad = \int_b^c \int_0^{2\pi} \varepsilon_3 \left\{\left[D_{nl} J_n\left(m_{nl} r\right) + E_{nl} Y_n\left(m_{nl} r\right)\right] \cdot \cos n\Theta\right\}^2 r dr d\Theta$$

The same procedure as used for region 2, is applied to evaluate the integral in region 3. However the appropriate constants and integral limits have to be used. The result is

$$\left[\varepsilon_3 \pi\right] \cdot$$

$$\left\{D_{nl}^2\left[\left\{\frac{c^2}{2}\left[\left(J_n\left(m_{nl}c\right)\right)^2 - \left(J_{n-1}\left(m_{nl}c\right)J_{n+1}\left(m_{nl}c\right)\right)\right]\right\} - \left\{\frac{b^2}{2}\left[\left(J_n\left(m_{nl}b\right)\right)^2 - \left(J_{n-1}\left(m_{nl}b\right)J_{n+1}\left(m_{nl}b\right)\right)\right]\right\}\right] +$$

$$\left\{E_{nl}^2\left[\left\{\frac{c^2}{2}\left[\left(Y_n\left(m_{nl}c\right)\right)^2 - \left(Y_{n-1}\left(m_{nl}c\right)Y_{n+1}\left(m_{nl}c\right)\right)\right]\right\} - \left\{\frac{b^2}{2}\left[\left(Y_n\left(m_{nl}b\right)\right)^2 - \left(Y_{n-1}\left(m_{nl}b\right)Y_{n+1}\left(m_{nl}b\right)\right)\right]\right\}\right] +$$

$$2D_{nl}E_{nl}\left[\left[\frac{c^2}{2}\left\{J_n\left(m_{nl}c\right)Y_n\left(m_{nl}c\right) - J_{n-1}\left(m_{nl}c\right)Y_{n+1}\left(m_{nl}c\right)\right\}\right] - \left[\frac{b^2}{2}\left\{J_n\left(m_{nl}b\right)Y_n\left(m_{nl}b\right) - J_{n-1}\left(m_{nl}b\right)Y_{n+1}\left(m_{nl}b\right)\right\}\right]\right]\right\}$$

(2.62)

A new expression for the constant F_{nl} is now

$$F_{nl} = \frac{q\overline{\phi}_{nl}\begin{pmatrix} r = s \\ \Theta = 0 \end{pmatrix}}{2m_{nl}\left(equ.2.60 + equ.2.61 + equ.2.62\right)} \tag{2.63}$$

Now that all unknown factors are solved, the equations for the potential distribution in each of the three regions due to a unit charge placed in the first region, can be written as

$$\phi_1 = \sum_n \sum_l F_{nl} A_{nl} J_n\left(m_{nl} r\right) \cos n\Theta \cdot e^{-m_{nl} z} \tag{2.64}$$

$$\phi_2 = \sum_n \sum_l F_{nl}\left(B_{nl} J_n(m_{nl} r) + C_{nl} Y_n(m_{nl} r)\right) \cos n\Theta \cdot e^{-m_{nl} z} \tag{2.65}$$

$$\phi_3 = \sum_n \sum_l F_{nl}\left(D_{nl} J_n(m_{nl} r) + E_{nl} Y_n(m_{nl} r)\right) \cos n\Theta \cdot e^{-m_{nl} z} \tag{2.66}$$

2.6.4 Field of the bubble dipole source in the duct

To work out the potential distribution $(\tilde{\phi})$ due to a dipole placed in a flow section that carries a dielectric medium, the above equations have to be differentiated with respect to z. The value for the dipole moment, established in equation (2.25) and repeated below, has to be included as well.

$$\vec{p} = -i\omega B y \left[\frac{\left(1 - \frac{\varepsilon_1}{\varepsilon_b}\right)}{\left(1 + \frac{2\varepsilon_1}{\varepsilon_b}\right)}\right] 4\pi\varepsilon_0 d^3 \tag{2.67}$$

The result is

$$\tilde{\phi}_1 = \sum_n \sum_l F_{nl} J_n(m_{nl} r) \cos n\Theta (-m_{nl}) \cdot e^{-m_{nl} z} \vec{p}_z \tag{2.68}$$

$$\tilde{\phi}_2 = \sum_n \sum_l F_{nl}\left[B_{nl} J_n(m_{nl} r) + C_{nl} Y_n(m_{nl} r)\right] \cos n\Theta (-m_{nl}) \cdot e^{-m_{nl} z} \vec{p}_z \tag{2.69}$$

$$\tilde{\phi}_3 = \sum_n \sum_l F_{nl}\left[D_{nl} J_n(m_{nl} r) + E_{nl} Y_n(m_{nl} r)\right] \cos n\Theta (-m_{nl}) \cdot e^{-m_{nl} z} \vec{p}_z \tag{2.70}$$

and in the duct (0 < r < a)

$$\tilde{\phi}_1 = \sum_n \sum_l -i\omega B y \left[\frac{\left(1 - \frac{\varepsilon_1}{\varepsilon_b}\right)}{\left(1 + \frac{2\varepsilon_1}{\varepsilon_b}\right)} \right] 4\pi\varepsilon_0 d^3 \frac{J_n(m_{nl} s)}{2m_{nl}(equ.2.60 + equ.2.61 + equ.2.62)} (-m_{nl}) J_n(m_{nl} r) \cos n\Theta \cdot e^{-m_{nl} z} \tag{2.71}$$

2.7 Results for point electrodes

In this section computed results of the transformer signal due to a bubble in a flowmeter with point electrodes are examined. The following calculations are achieved with FORTRAN coded programmes. Principle flowcharts of the programmes are given in Appendix A. Figure 2.11 shows calculated transformer signals for dipoles placed at various positions along the y-axis and moved along a line parallel to the pipe axis. The transformer signal is calculated for a frequency of 1500 *Hz*, a magnetic field strength of 0.01 *Tesla* and a pipe radius of 50 *mm*. Similar to Krafft's transformer signal for a bubble in a conducting medium the transformer signal in a dielectric fluid is anti-symmetric in z direction. The signal is significant over a pipe length of about 5 cm. It is observed that the magnitude of the signal increases by a factor of 2.08 for every 3 *mm* the dipole is positioned further away from the pipe centre. The magnitude of the signal for a bubble radius of a bubble of the pipe radius is in the range of 1E-5 to 8E-5 *Volts*.

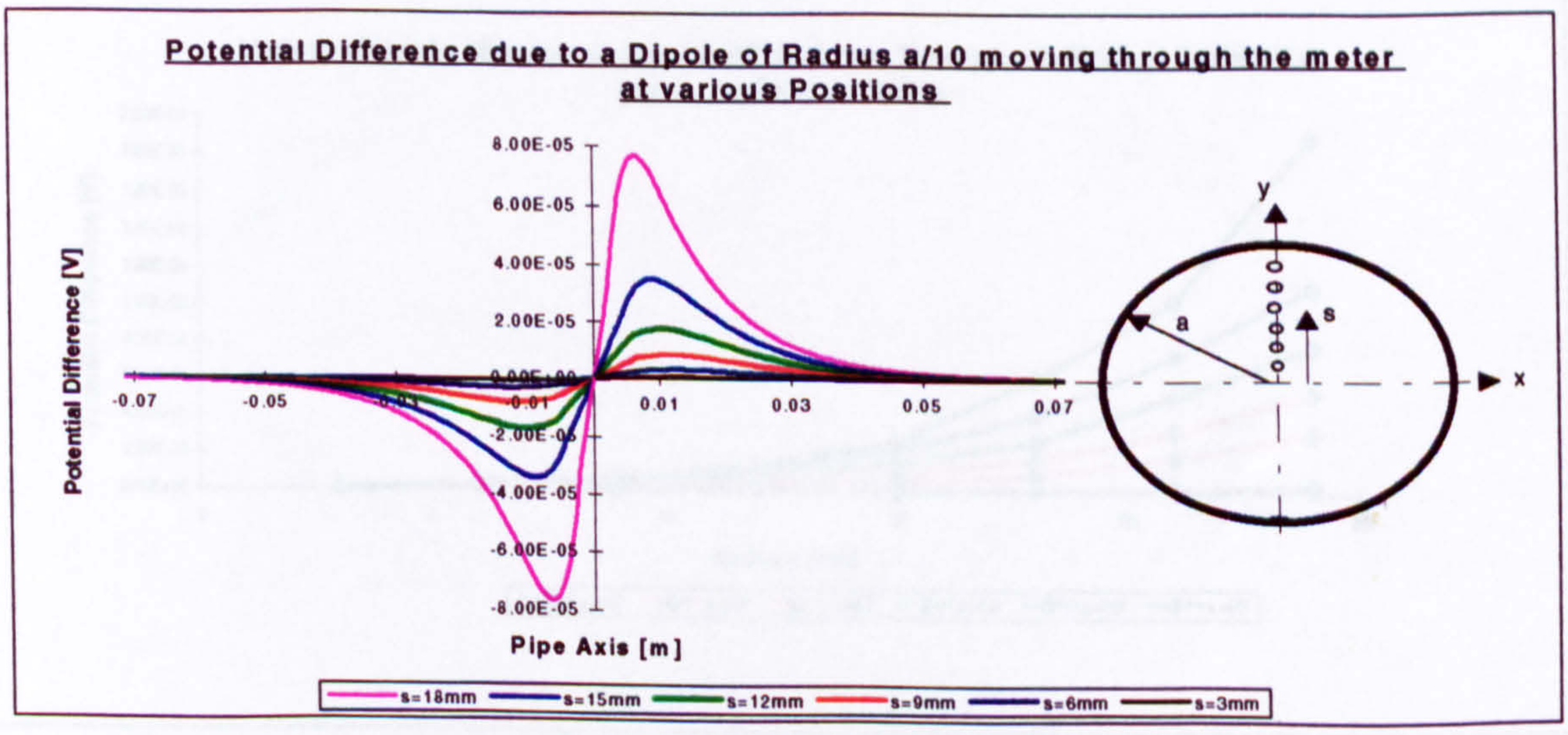

Figure 2.11

The graphs in Figure 2.12 show various transformer signals for bubbles crossing a line at an angle of 45°. The difference in transformer signal magnitude between a dipole positioned at an angle of 90° and 45° increases with increasing radius *s*. In order to investigate the behaviour of transformer signal magnitudes versus dipole positions at angles ranging from 15° to 90° and various radii *s*, plots in Figure 2.13 and Figure 2.14 are produced. It is clearly seen that dipole closer to the electrode produce a bigger transformer signal.

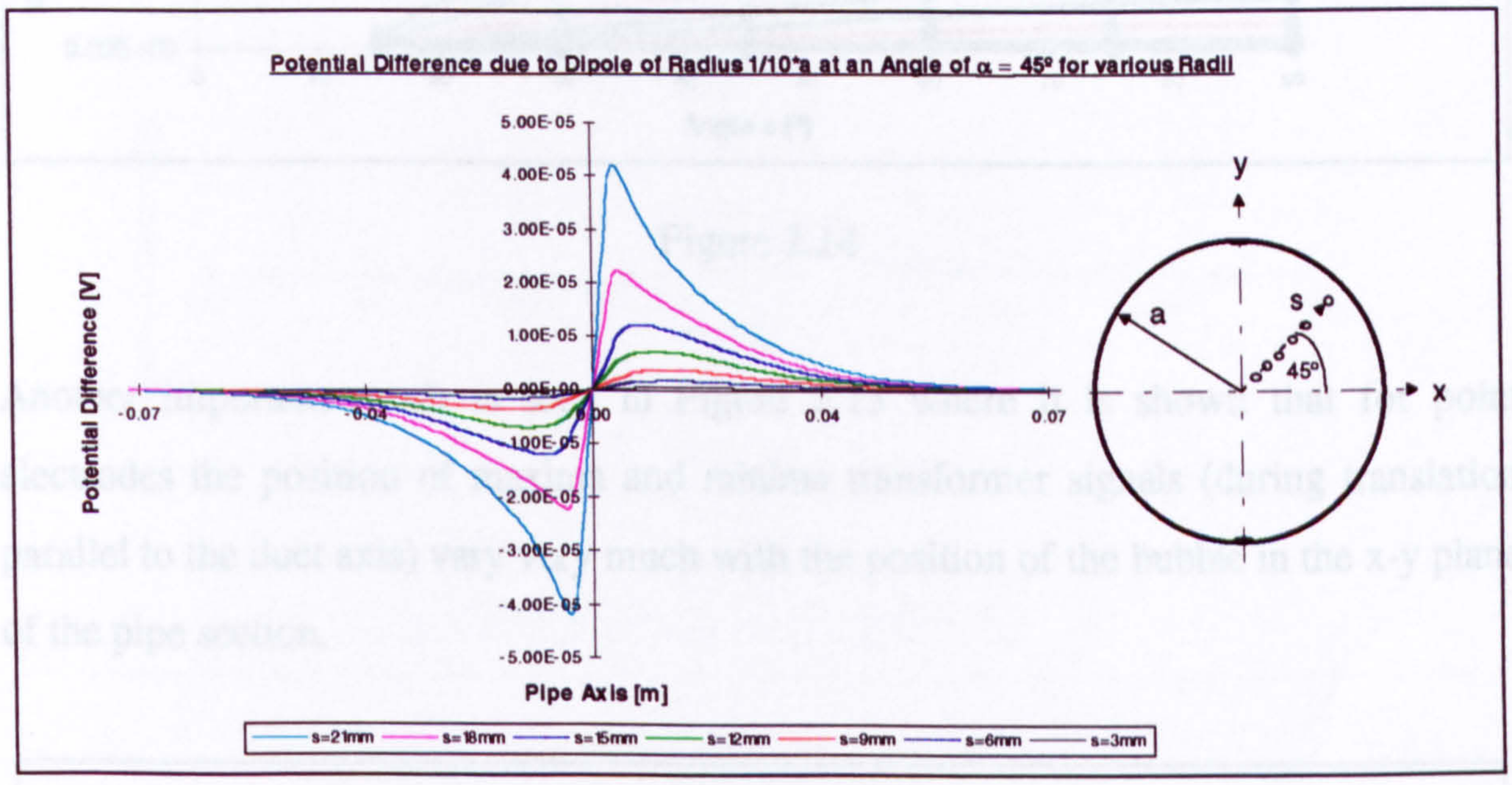

Figure 2.12

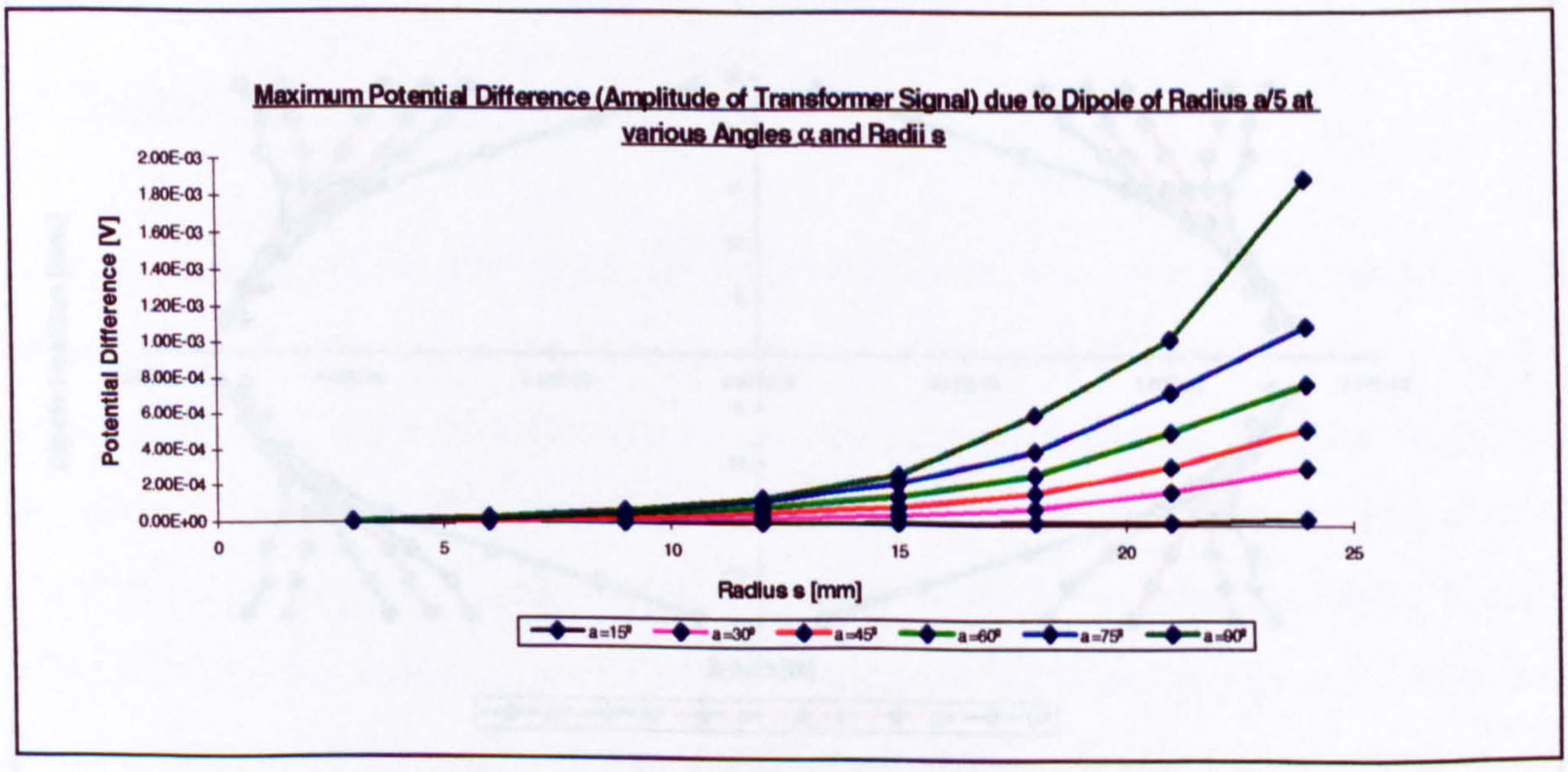

Figure 2.13

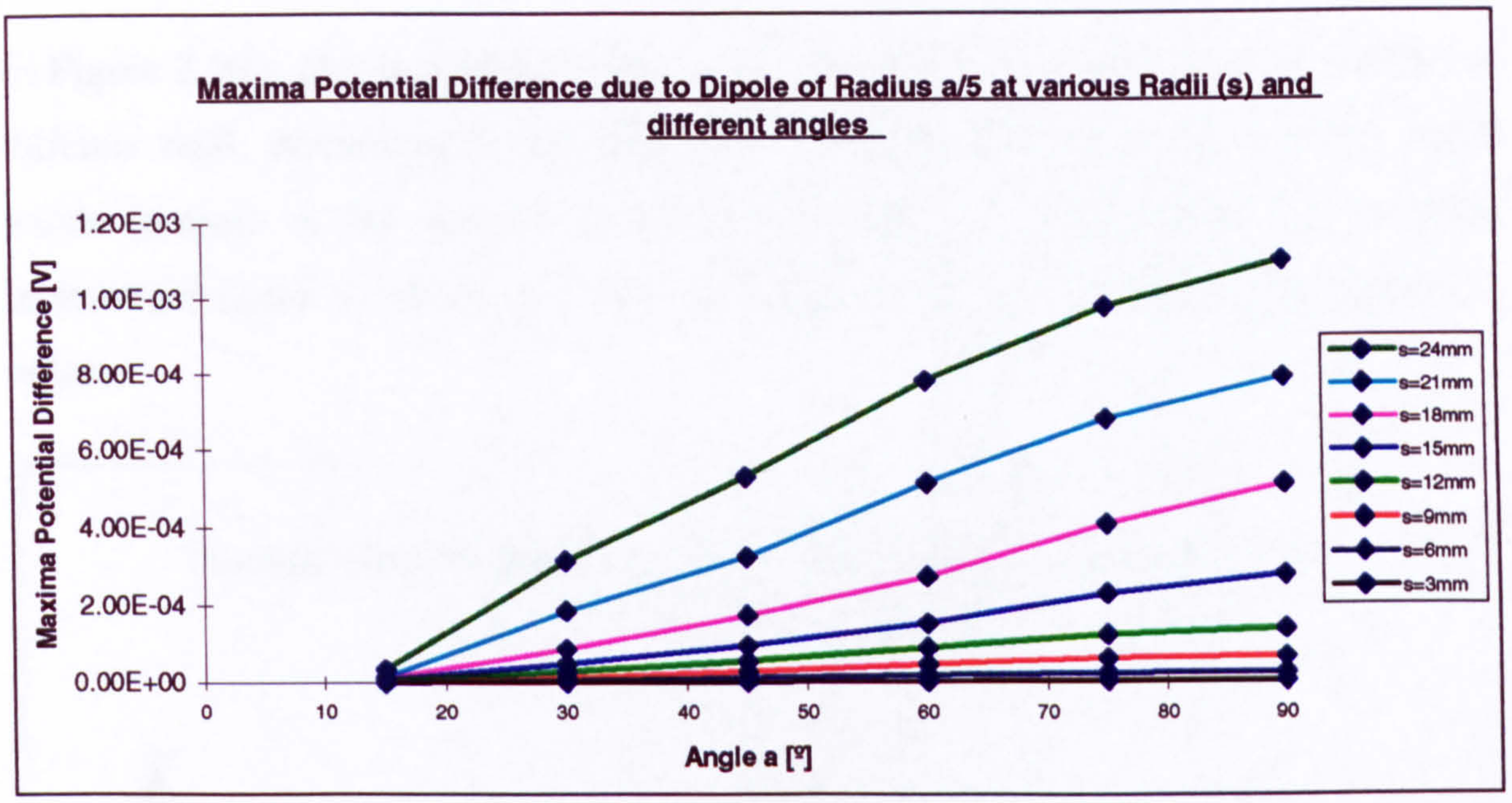

Figure 2.14

Another important result is seen in Figure 2.15 where it is shown that for point electrodes the position of maxima and minima transformer signals (during translation parallel to the duct axis) vary very much with the position of the bubble in the x-y plane of the pipe section.

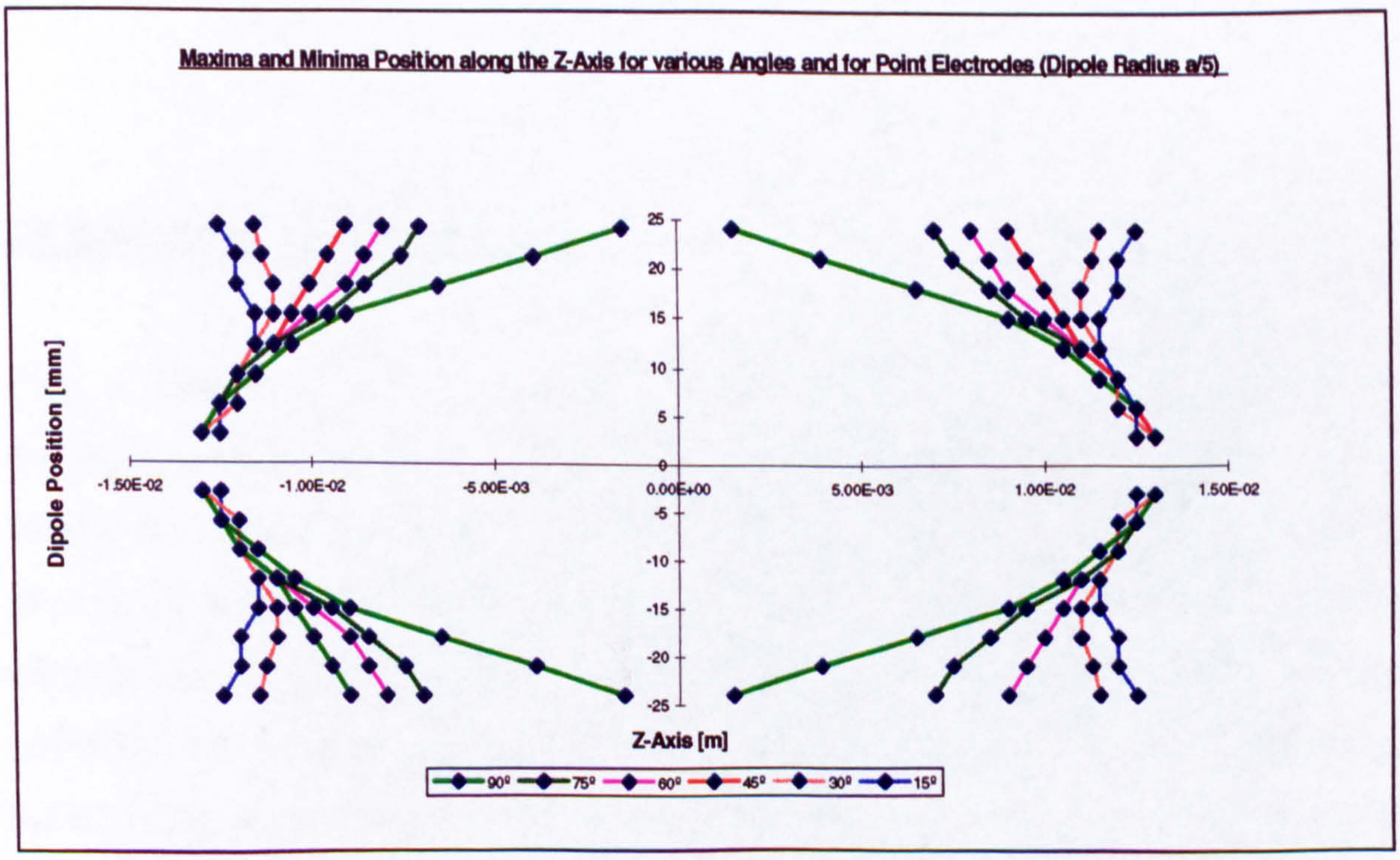

Figure 2.15

In Figure 2.16 a plot is produced that shows the transformer signal due to bubbles of different radii. According to equation 2.71 it is expected that the transformer signal would increase as the cube of the radius. The positions of maximum and minimum transformer signal on the pipe axis are also anticipated to be at equal and opposite z values.

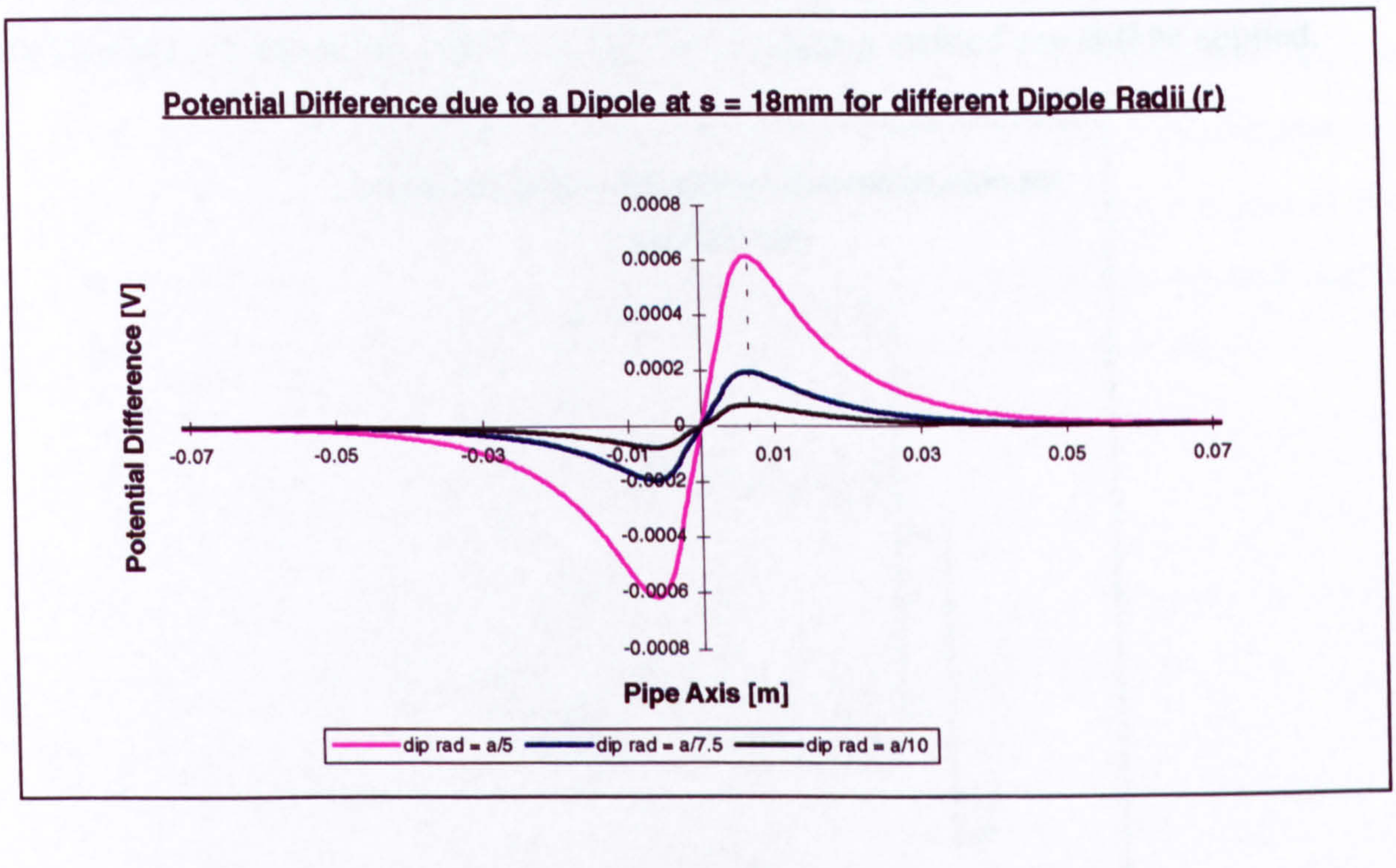

Figure 2.16

2.8 Results for strip electrodes

After a calculation of the potential difference between two point electrodes an investigation of strip electrodes is made. From earlier work (Cox and Wyatt [14]) it is known that large and non-contacting electrodes have an averaging effect of changes in the velocity profile and therefore reduce noise pick up due to turbulence. This average effect definitely applies for electromagnetic flowmeters for conducting fluids, because of the fact that conducting currents will not penetrate the isolating pipe wall. Therefore for a theoretical calculation of the potential on evenly distributed locations on the electrode can be added up and then averaged over the number of points taken. This

effect is illustrated in figure 2.17. For dielectric electromagnetic flowmeters it is a different matter, since in this case instead of conduction currents displacement currents have to be considered and therefore the above argument does not apply in this case. But since the relative permativity for the dielectric fluid is different from the relative permitivity of the pipe wall and consequently a discontinuity on the interface between the liquid face and the pipe wall is apparent. Therefore a first approach to investigate the transformer signal for area electrodes the averaging method can still be applied.

Averaging Method of Potential calculated for Strip and Area Electrodes

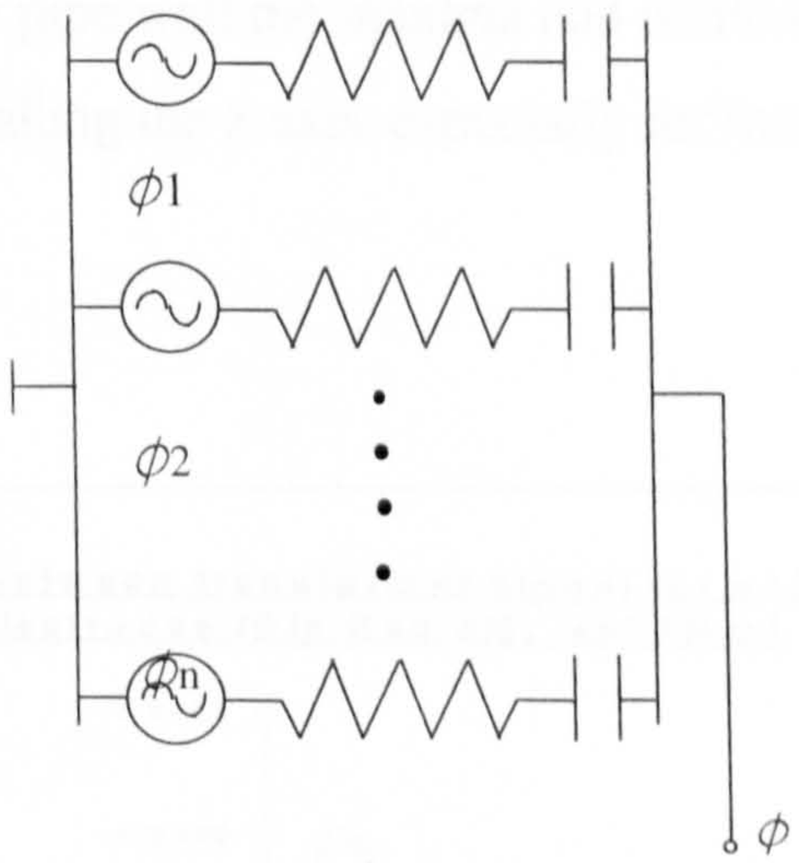

$$\phi = \frac{1}{n}\sum_{i=1}^{n}\phi_i$$

Figure 2.17

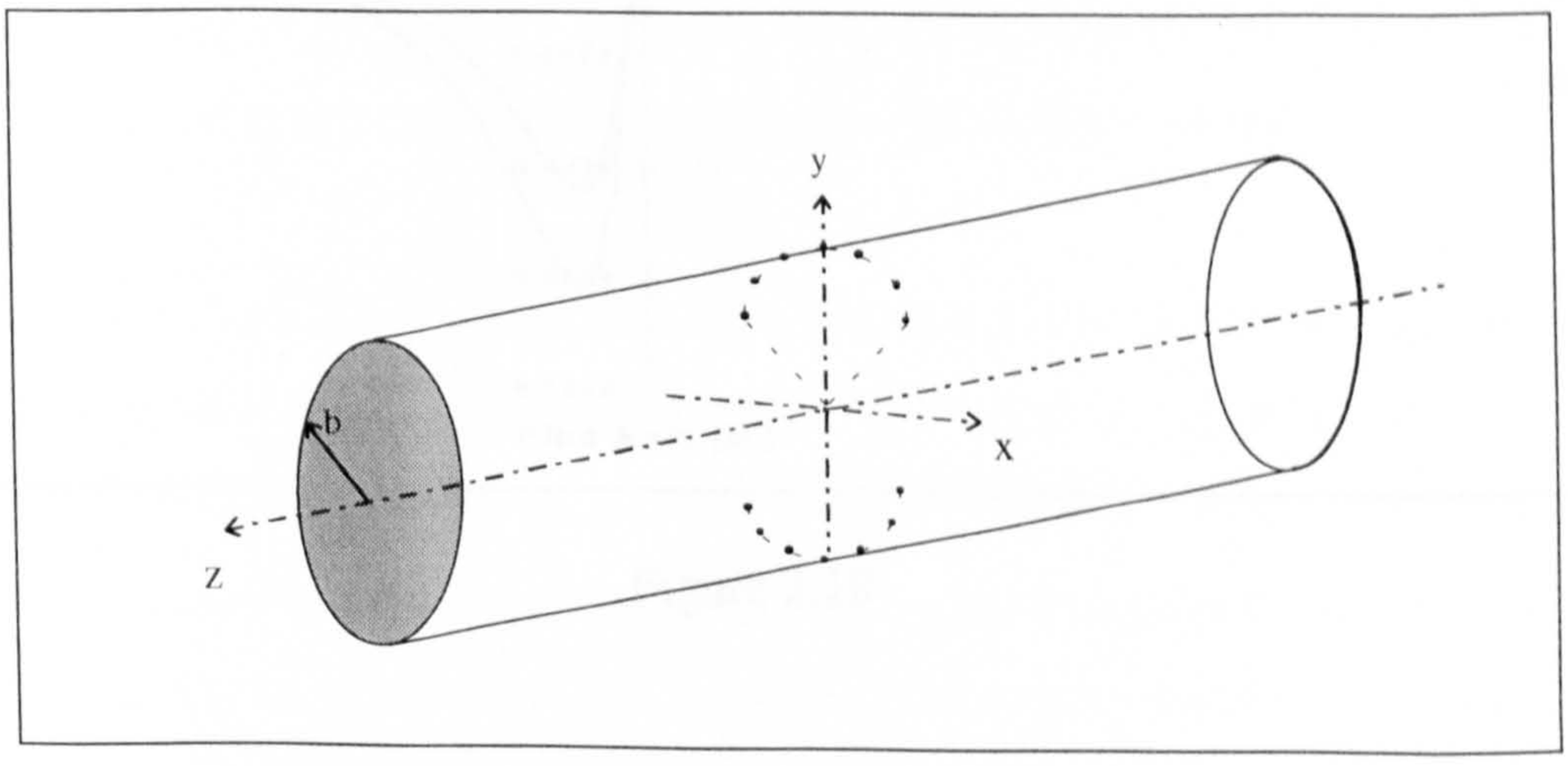

Figure 2.18 (Illustration of Strip Electrodes)

The large electrodes can be modelled as a number of point electrodes over which the signal is averaged (see Figure 2.18), because it is assumed that these types of electrodes are non contacting and capacitive coupled. Various calculations for different bubble positions and diameters are implemented. In Figure 2.19 the transformer signal for point electrodes and strip electrodes are shown. The only apparent difference between the two signals is the magnitude. The signal amplitude for strip electrodes is slightly less then the one for point electrodes. Figure 2.20 shows that the distribution for maxima and minima of the transformer signal with strip electrodes is similar to the transformer signal calculated for point electrodes. The apparent difference is that for locations of the bubble (dipole) closer to the pipe wall the maxima and minima of the transformer signal occurs on a narrower width along the z-axis, especially for increasing angles.

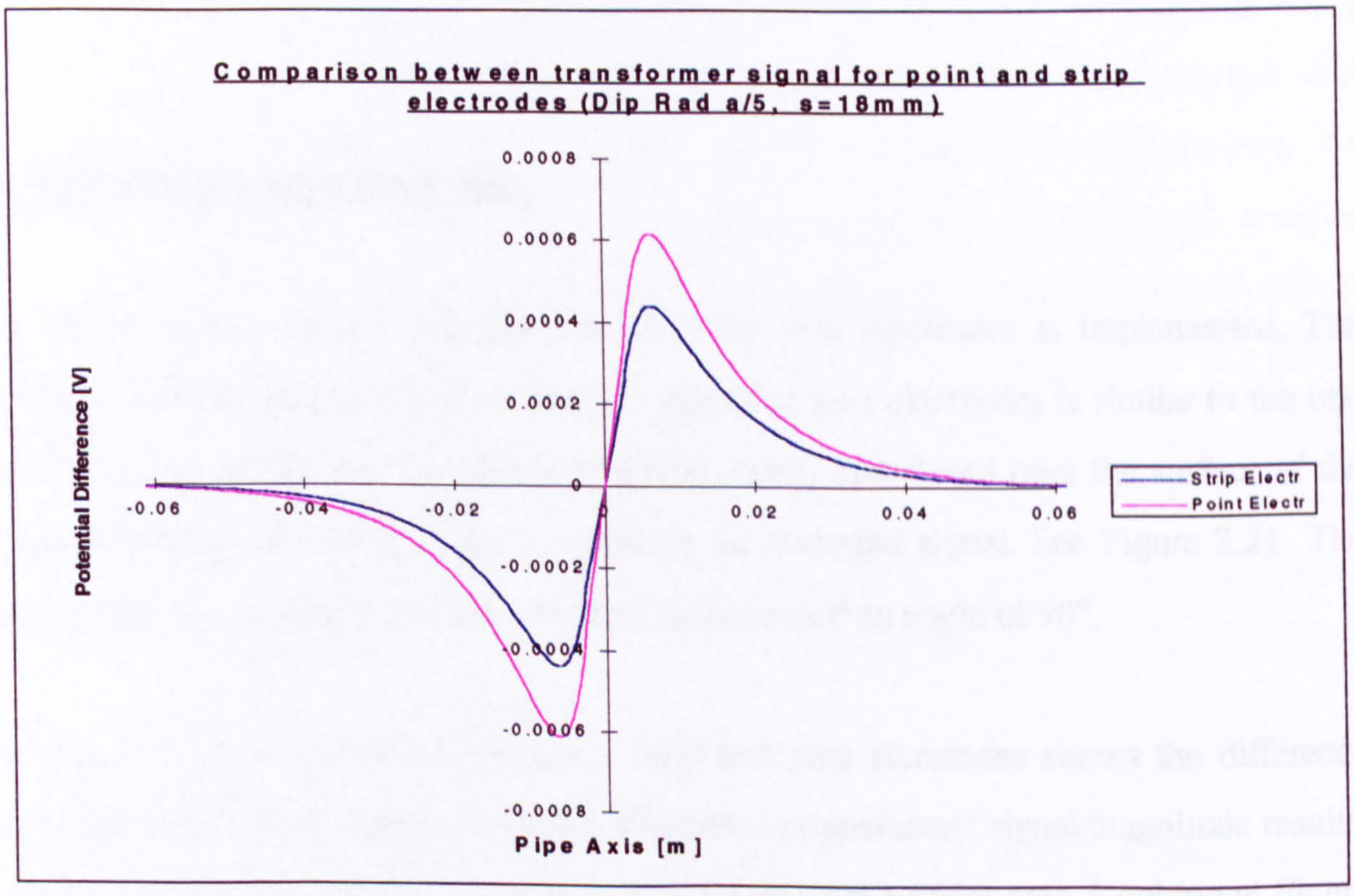

Figure 2.19

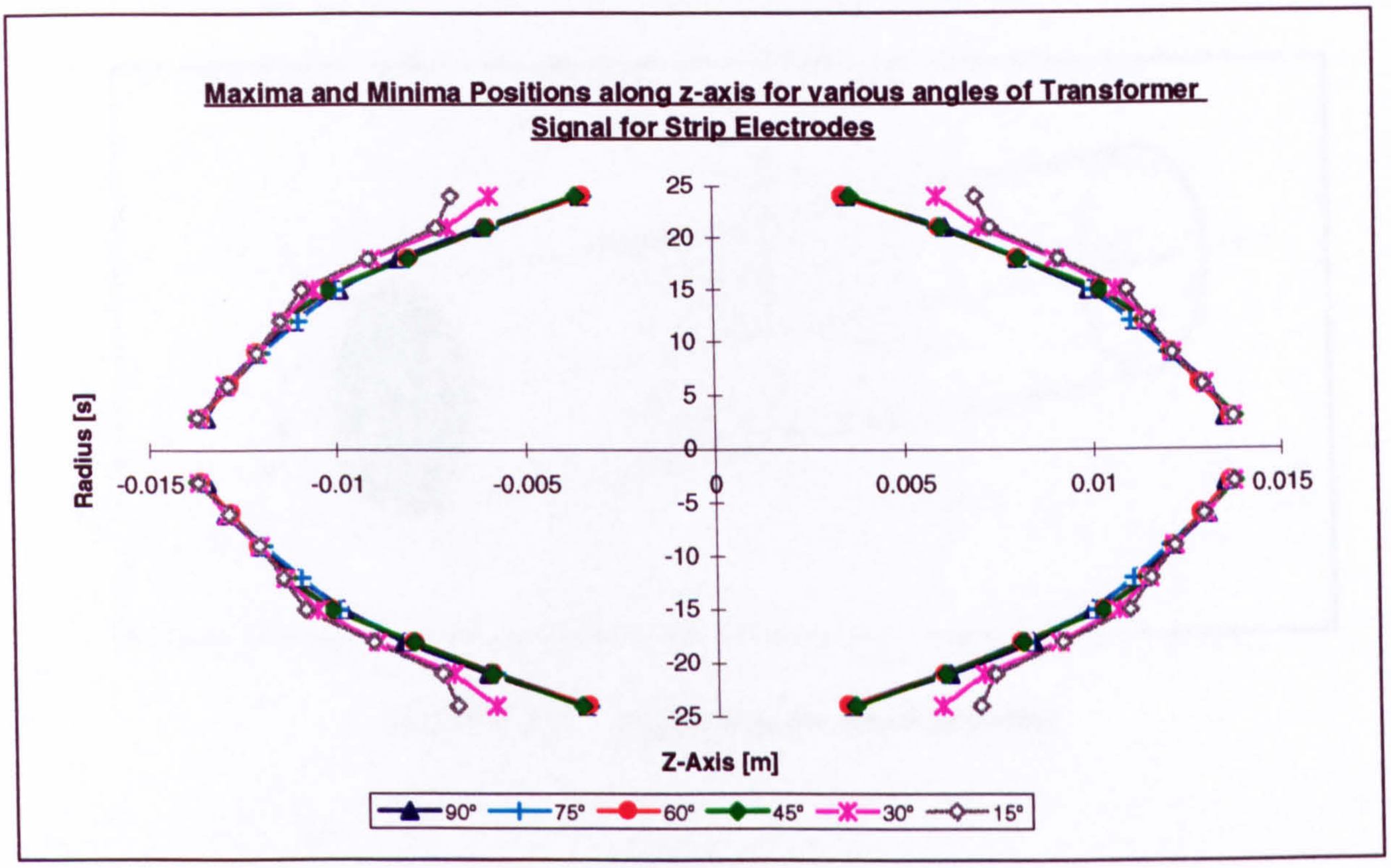

Figure 2.20

2.9 Results for area electrodes

In this section a further investigation for wide area electrodes is implemented. The method used to calculate the transformer signal for area electrodes is similar to the one used for strip electrodes. A number of points evenly distributed over the surface of the area electrodes is used in order to calculate an averaged signal. See Figure 2.21. The electrodes have a length of twice the tube radius *a* and an angle of 90°.

In Figure 2.22 a comparison of point, strip and area electrodes shows the difference between transformer signals. A further decrease in transformer signal magnitude results, because of the fact that the averaging takes places over a wider area. Looking at Figure 2.23, a plot of maximum and minimum positions of the transformer signal shows that, compared with the same plot for point and strip electrodes in Figure 2.15 and 2.20 respectively, the variation between maximum and minimum positions has remarkably decreased.

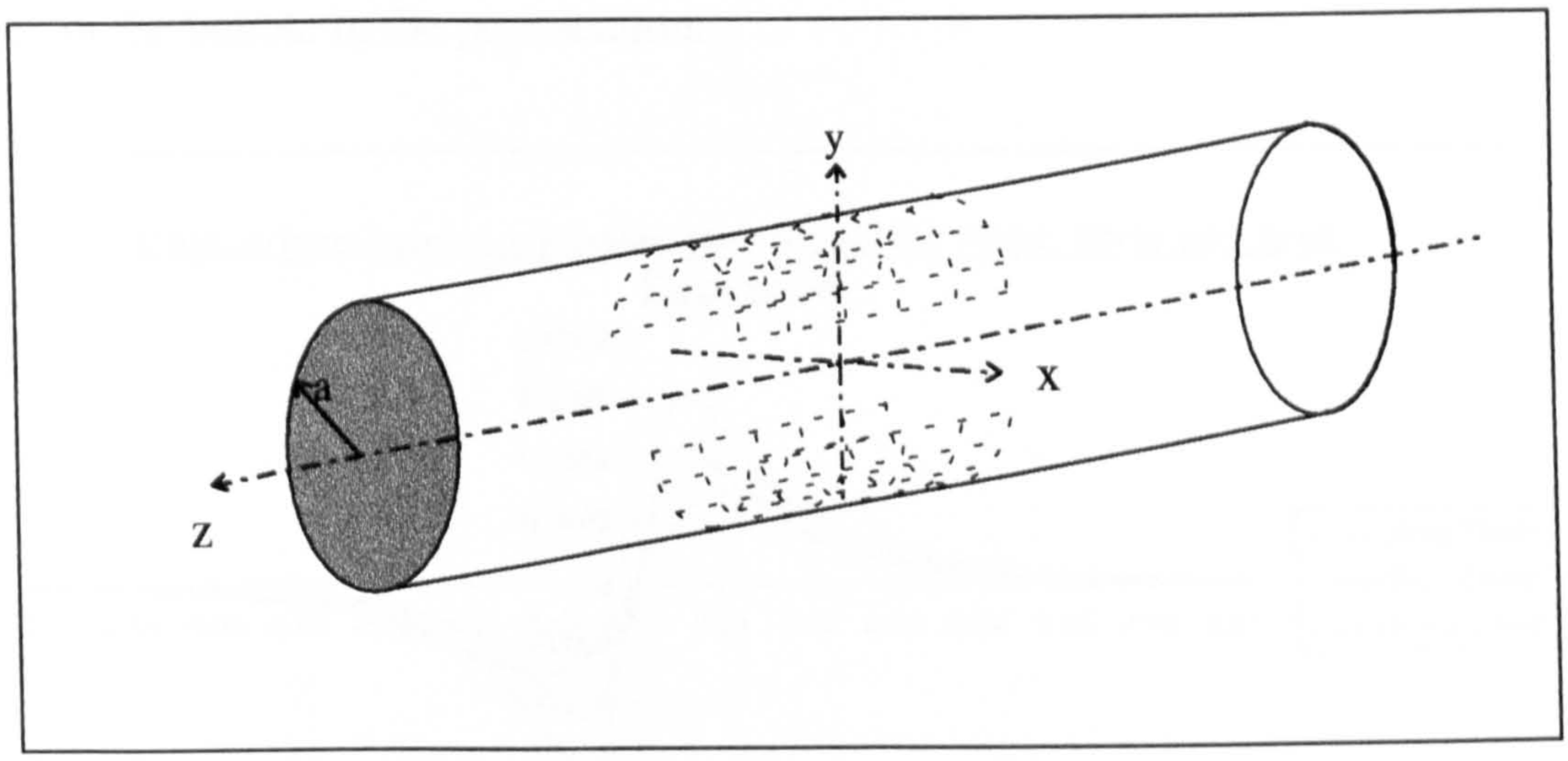

Figure 2.21 (Illustration for Area Electrodes)

The power spectrum of the transformer signal has a characteristic frequency and will change for different bubble velocities and distances between the maximum and minimum positions. With respect to the fact that for wide area electrodes the variation between these maxima and minima decreases considerably, the frequency analysis would depend less on the position of the bubble in the pipe cross section and depend more on the velocity of the bubble. A higher bubble velocity would result in a higher frequency and slower bubble velocities would achieve lower frequencies. Consequently a desirable feature of the electrodes would be a constant difference between maxima and minima for all bubble positions in the pipe cross section. For this reason transformer signals are calculated for even larger electrodes. The length of the electrodes is extended to twice the tube diameter.

As it can be seen in Figure 2.24 the extension of the occurrence of maximum and minimum signals has further decreased and is almost a straight line. This leads to the conclusion that with large area electrodes (about two times the tube diameter long and

with a subtended angle of 140° a frequency analysis would no longer depend on the position of the bubble in the pipe section.

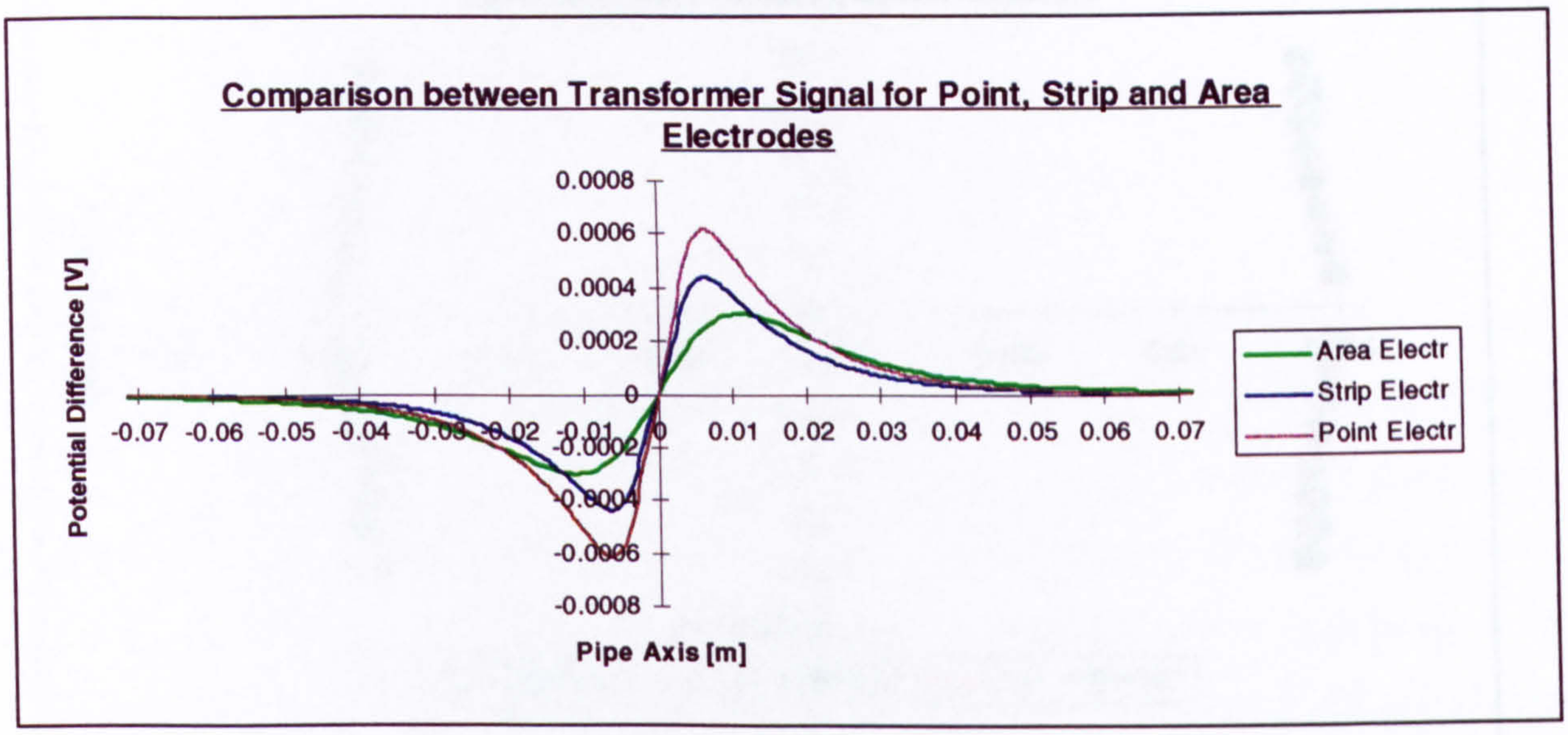

Figure 2.22

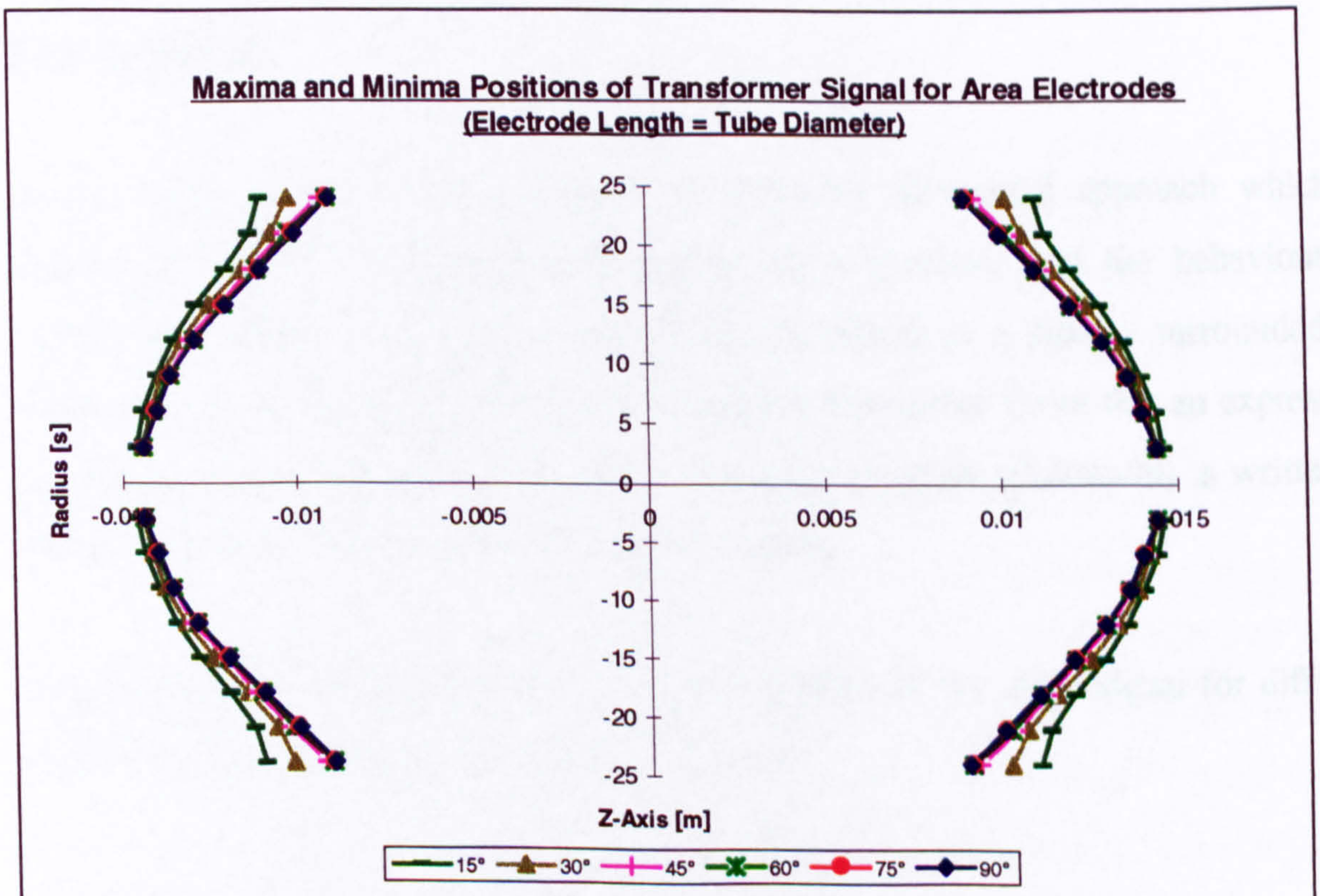

Figure 2.23

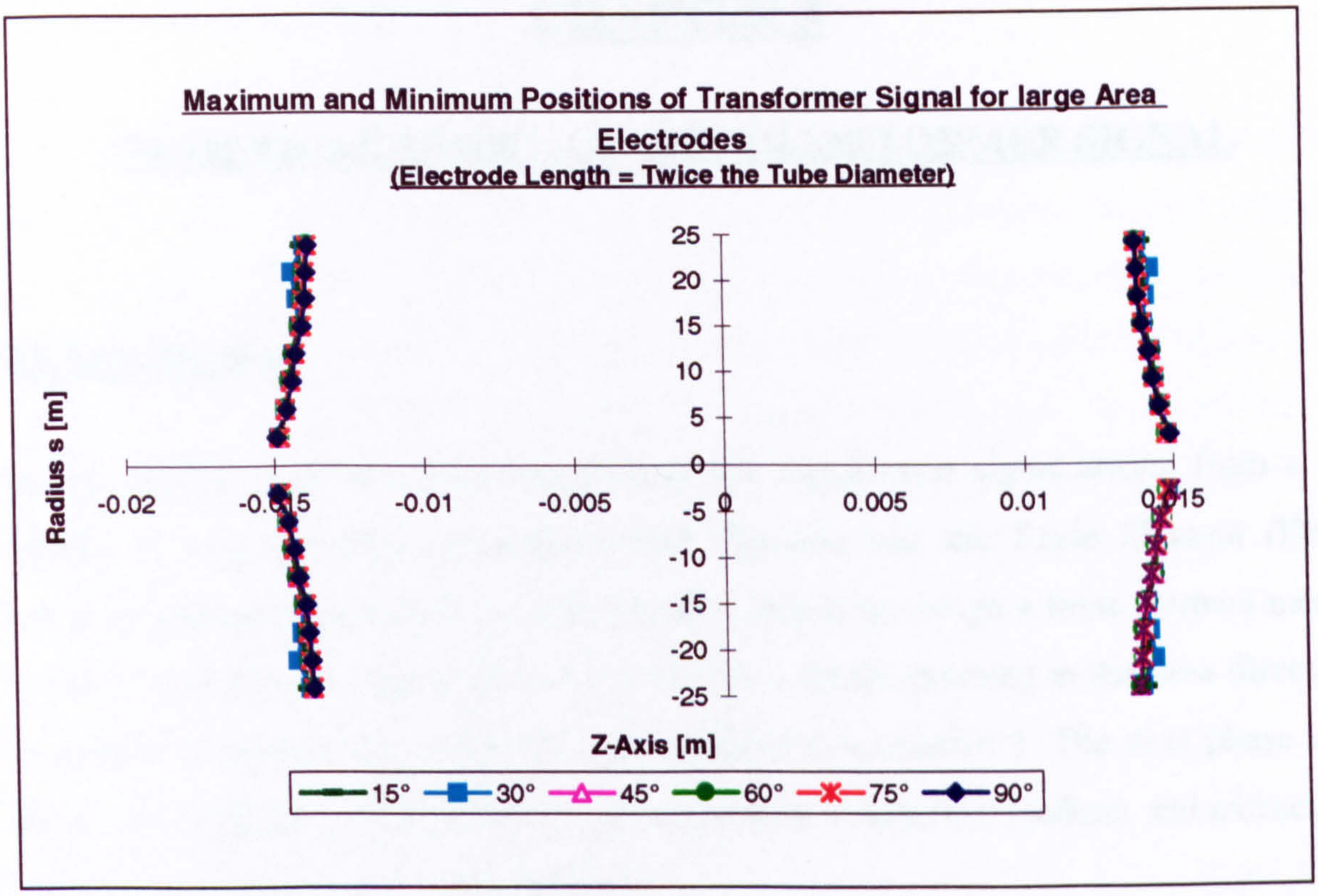

Figure 2.24

2.10 Summary

In summary the above chapter covers an extensive theoretical approach which is required in order to investigate and analyse the occurrence and the behaviour of transformer signal arising when a gas bubble (modelled as a dipole) surrounded by dielectric liquid passes through an electromagnetic flowmeter. From this an expression for the transformer signal is obtained. A computer program (Fortran99) is written in which this expression is used to calculate the signals.

It is also possible to achieve results for the behaviour of the same signal for different electrodes (point, strip and wide area electrodes).

CHAPTER 3

NUMERICAL MODEL OF THE TRANSFORMER SIGNAL

3.1 Introduction

In this chapter a numerical investigation of the transformer signal arising from a gas bubble as a second phase is implemented. For this task the Finite Element (FEM) software application ANSYS is used. The first step is to design a finite element model, which represented the transformer signal due to a dipole, pointing in the flow direction, in order to compare and verify the results achieved in chapter 2. The next phase is to model a gas bubble in the form of a sphere within a dielectric medium and extract the transformer signal on the point electrodes.

3.2 ANSYS for electric field analysis

ANSYS is a multi-purpose design Analysis Software Package, which is able to cope with 2 Dimensional and 3 Dimensional Problems. Electrostatic Field Analysis is used to determine the electric field and electric scalar potential (Voltage) distribution due to charge distributions or potential drop. Two types of loads, applied voltage and charge densities, can be utilised in this analysis. There are three main steps to produce a complete analysis. The starting point is to build the model, which included the specification of the element types, material properties, model geometry, and the mesh on the solid model. The next stage is to apply the so called loads (voltages or charge densities) on the model (Nodes or Elements). Finally, after running the program, results from the analysis are reviewed. They consist of Primary Data (Voltages on Nodes) and Derived Data (Electric Field, Electric Flux Density, and Electrostatic Forces on Nodes and Elements). These results are reviewed by obtaining graphics displays and tabular listings.

3.3 Modelling a dipole within a dielectric medium

As it is found out in the previous chapter that a bubble can be modelled as a dipole pointing in the flow direction. In a first step, using a Finite Element Method program, such a dipole is modelled. It is well known that as less nodes are used when meshing the solid model it takes less time to run the program. Therefore the method of images for a dipole is used which reduced the number of nodes down to 50%. We know that an infinite plane, midway between the two charges of the dipole has zero potential and the electric field intensity is therefore normal to this surface. Thus the dipole is replaced with a single charge and conducting plane shown in Figure 3.1.

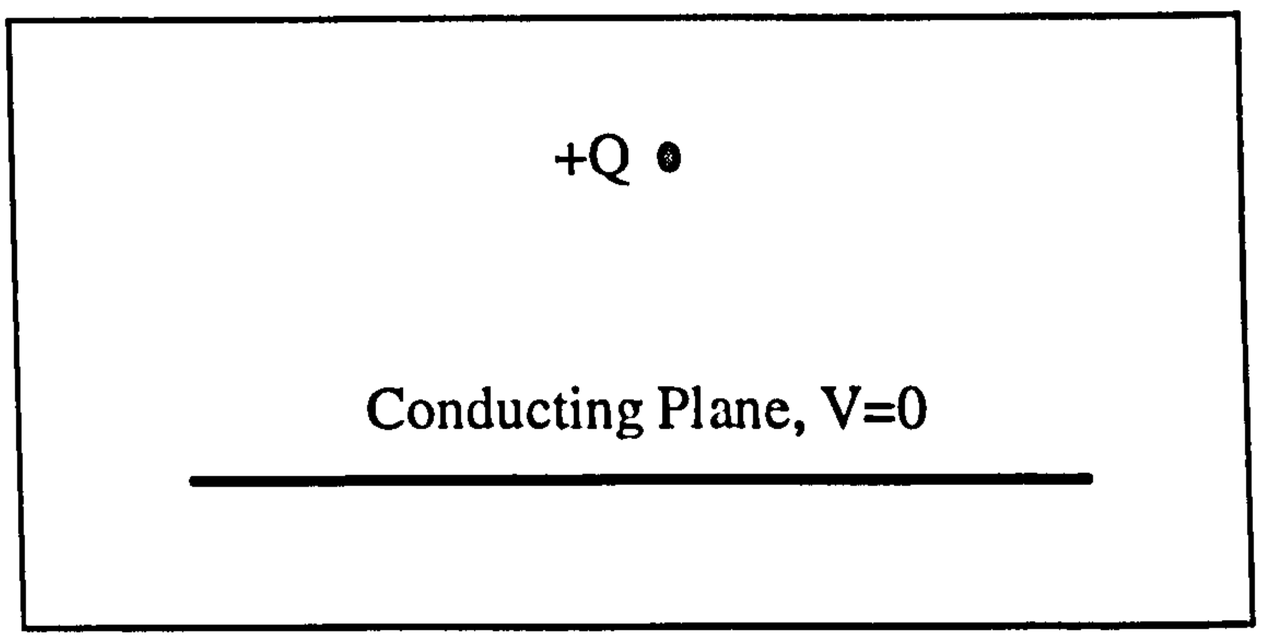

Figure 3.1 (Method of Images)

The amount of charge can simply be extracted from the general equation for a dipole

$$\delta \cdot Q = \vec{p} \qquad 3.1$$

3.3.1 Operation conditions

The operating conditions and dimensions for the problem under consideration are:

Pipe Length:	40cm
Pipe Diameter:	50mm
Pipe Material:	Perspex

Liquid:	Dielectric Oil
Dielectric Constant of Pipe Material:	3.4
Dielectric Constant of Liquid:	2.2
Element Type for Pipe Section:	SOLID 122, (Element with 3-D category and Brick Shape)
Element Type for Liquid Section:	SOLID 122, (Element with 3-D category and Brick Shape)
Element Type for Air Gap (Shield):	SOLID 122, (Element with 3-D category and Brick Shape)

In this case loads are applied on nodes. As a boundary condition the entire outer pipe contour as well as the front and end plane of the pipe is set to zero potential. See Figure 3.2a. The node placed at a distance half of the dipole diameter from the zero potential plane, and at a certain distance (y-axis) from the pipe centre is given a beforehand calculated amount of charge (from equation 3.1). Having finished the procedure for applying the loads the package is run and solutions for the potential could be achieved.

Figure 3.2b and 3.2c show a graphics of the potential distribution in of the pipe in the y-z projection and x-y projection respectively.

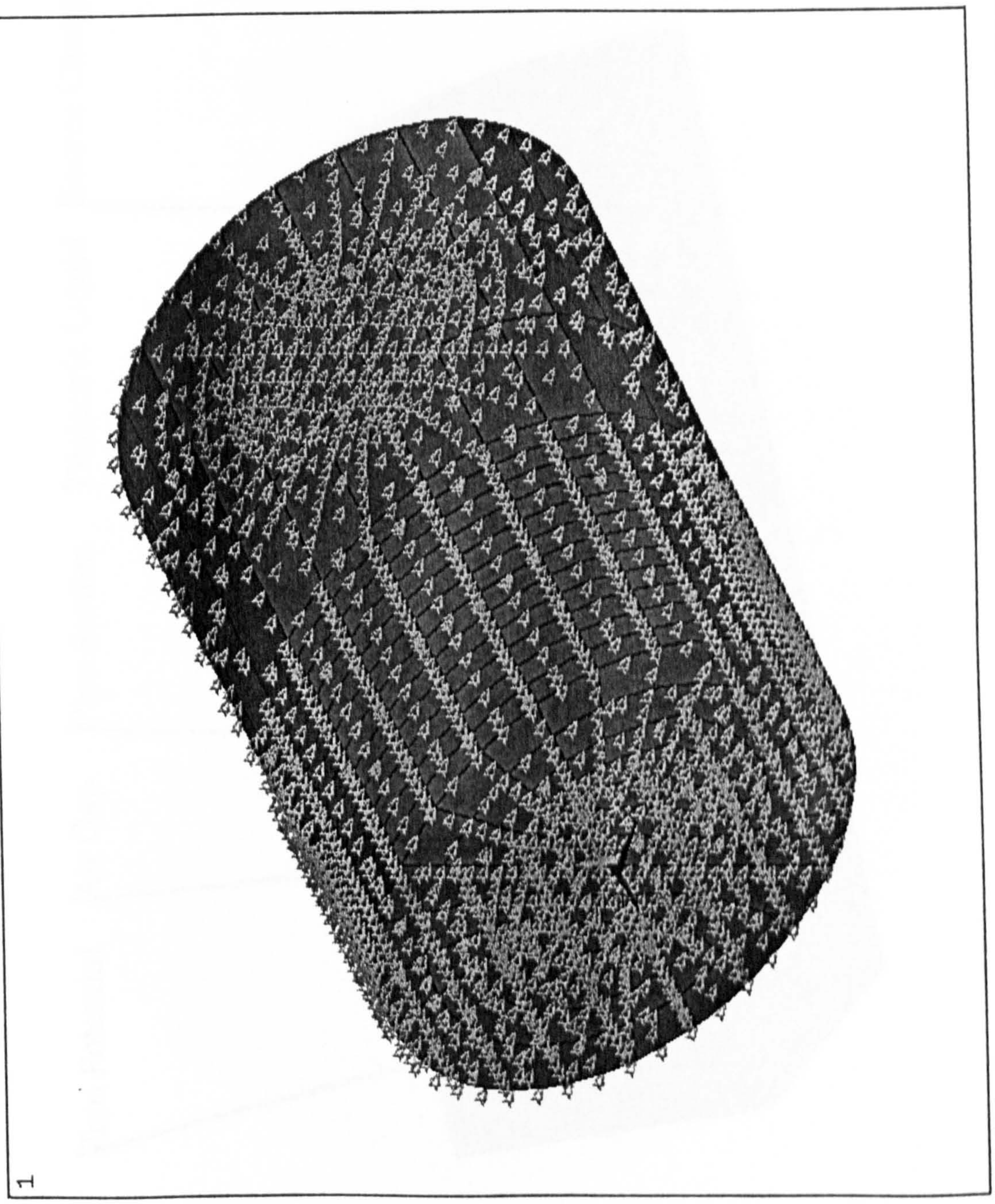

Figure 3.2a (Boundary Conditions on FEM-Model)

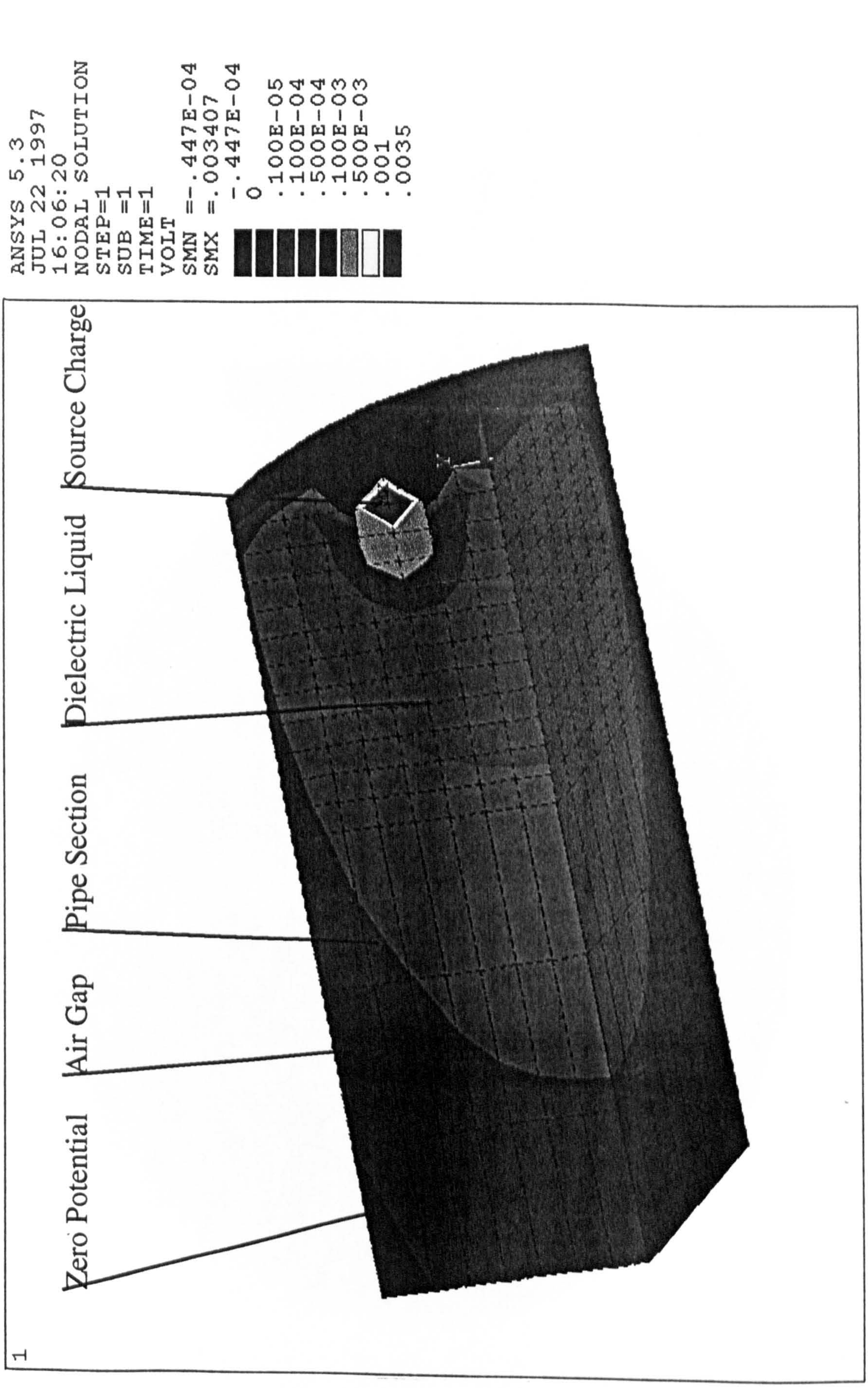

Figure 3.2b (Potential distribution in y-z plane)

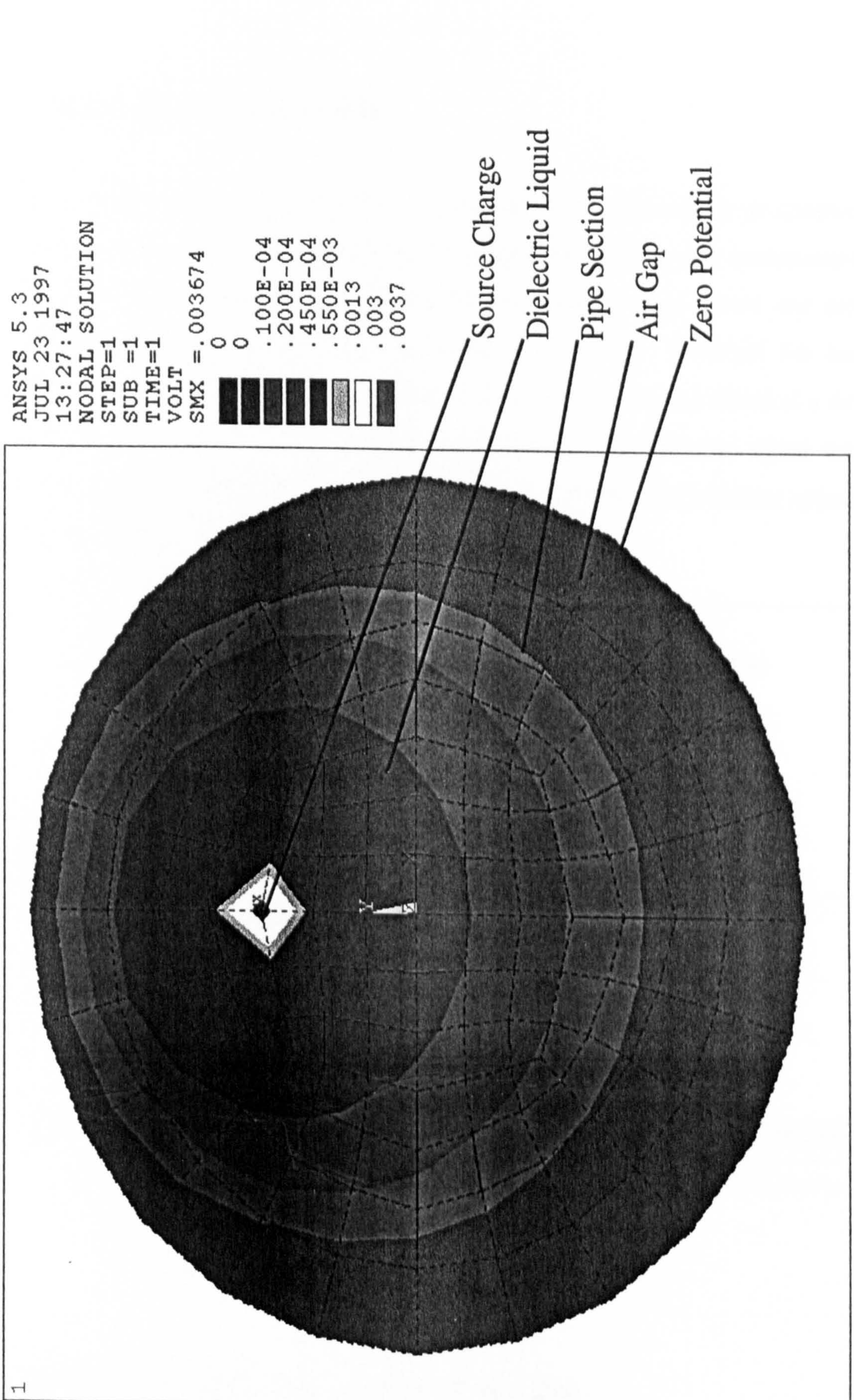

Figure 3.2.c (Potential distribution in y-x plane)

3.3.2 Results for dipole modelling

Results are depicted in order to compare and verify analytical results (in chapter 2). In Figure 3.3 a comparison of the transformer signal (numerically and analytically) due a dipole (of 5 mm in diameter) of placed halfway between pipe centre and pipe wall shows that the shape of the two signals are very similar. Although the boundary conditions, geomtries and parameters for the signal calculation are identical a deviation of 33% between the analytically achieved signal maximum and the signal maximum calculated with the FEM-Model occurred. The same percentage deviation appeared for bubbles at different locations.

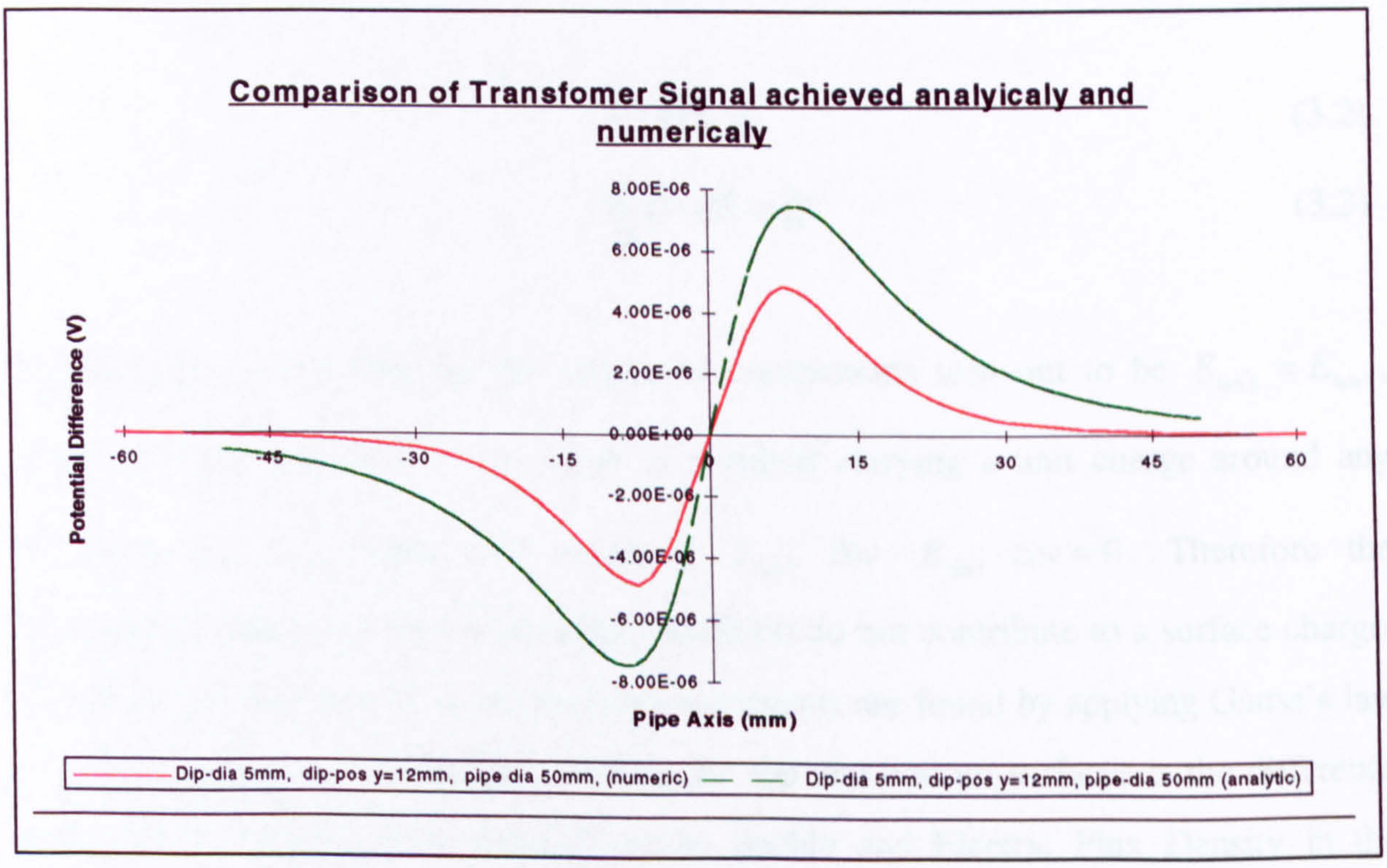

Figure 3.3

3.4 Model of a sphere within a dielectric medium

In this section a further investigation of the transformer signal is made. Instead of the previous method of using a dipole representing a gas bubble passing through the meter

this time a sphere in a plastic pipe which is filled with insulating liquid is modelled and the resulting effect is analysed. We have evaluated equation 2.23 in chapter 2 (the resulting electric field due to a gas bubble placed in a uniform field) a calculation for the surface charge on the bubble surface is conducted.

3.4.1 Physical model

We start from one of Maxwell's equations, also known as Gauss's law, which states that the electric flux passing through any closed surface is equal to the total charge enclosed by that surface.

$$\nabla \cdot \vec{D} = \rho \tag{3.2}$$

$$\oint_S \vec{D} \cdot d\vec{S} = Q \tag{3.3}$$

The boundary conditions for the tangential components turn out to be $E_{\tan b} = E_{\tan 1}$, because from $\oint \vec{E} \cdot d\vec{L} = 0$ (no work is required carrying a unit charge around any closed path), see Figure 3.4, obtaining $E_{\tan b} \cdot \Delta w - E_{\tan 1} \cdot \Delta w = 0$. Therefore the tangential components on the boundary condition do not contribute to a surface charge. The boundary conditions on the normal components are found by applying Gauss's law as shown in Figure 3.4. The flux leaving the top and bottom surfaces is the difference between the Electric Flux Density in the bubble and Electric Flux Density in the dielectric liquid and is written down in equation

$$D_{nb}\Delta S - D_{n1}\Delta S = \Delta Q = \rho_S \Delta S \tag{3.4}$$

from which $D_{nb} - D_{n1} = \rho_S$

or $\varepsilon_b E_{nb} - \varepsilon_1 E_{n1} = \rho_S$

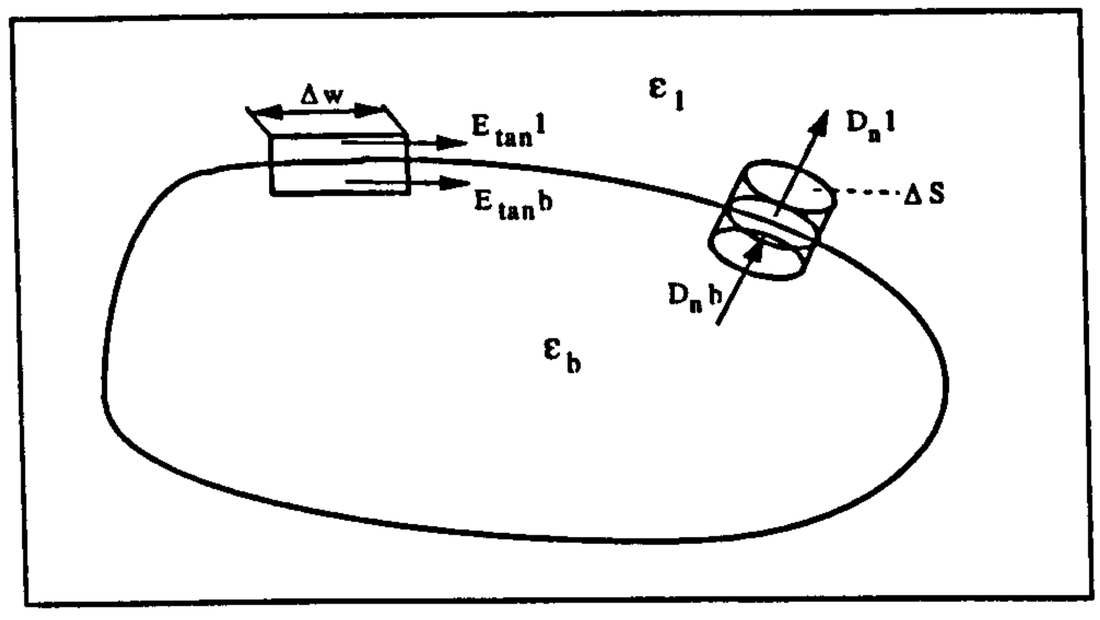

Figure 3.4 (Boundary Conditions)

The final equation for the surface charge, that can be used as a "load" in the FEM-investigation is going to be

$$(\varepsilon_b - \varepsilon_1)\vec{E} \cdot \hat{n} = \rho_s \tag{3.5}$$

where $\vec{E}$ is the electric field in the fluid when the bubble is absent.

A sphere placed in the eddy current electric field is shown in Figure 3.5.

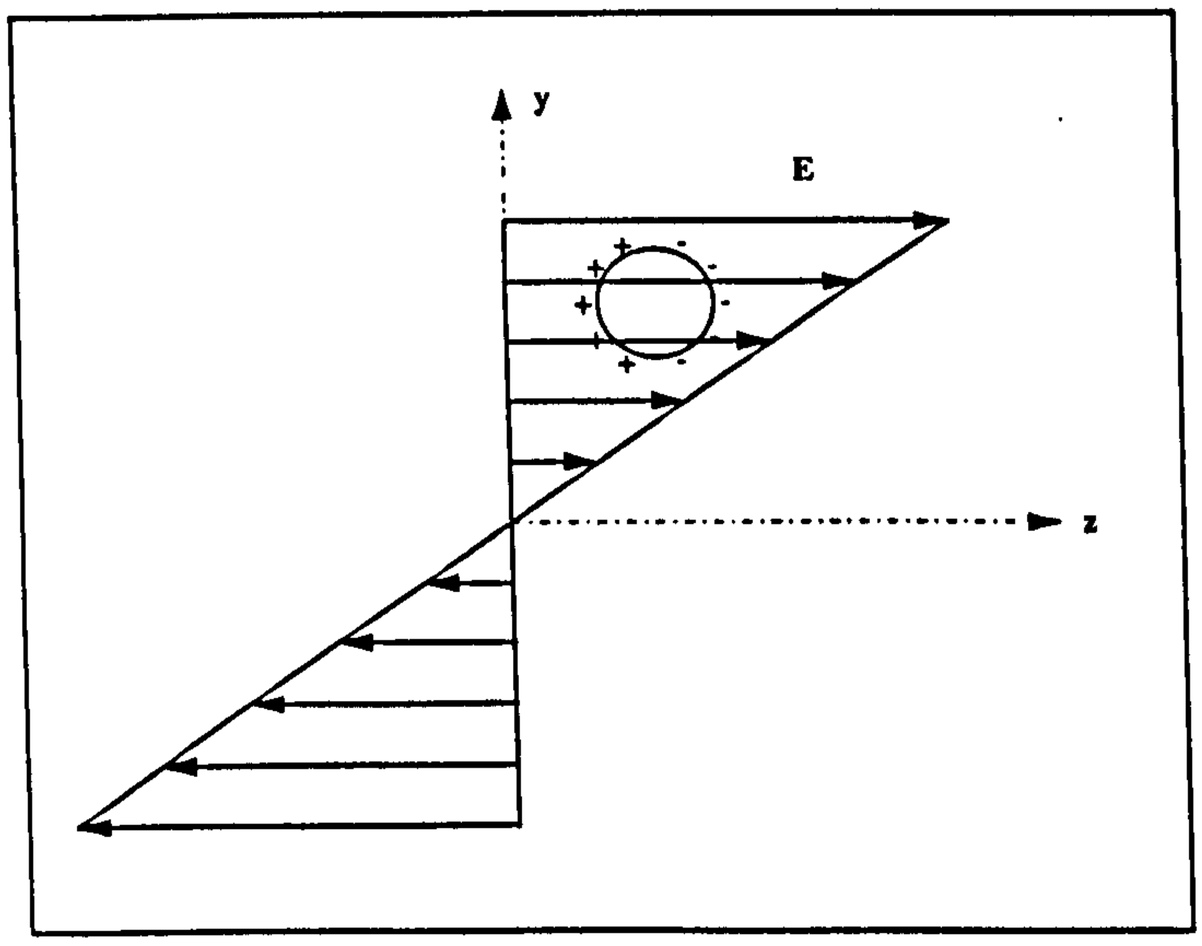

Figure 3.5 (Eddy Current Field)

The surface charge in equation 3.5 is the source of the secondary electric field due to the bubble.

3.4.2 Operating conditions

Operating conditions such as the geometry of the model, the appropriate material properties as well as the applied element types are given in the following table.

Pipe Length:	40 cm
Pipe inner Diameter:	50 mm
Pipe outer Diameter:	55 mm
Pipe Material:	Perspex
Liquid:	Dielectric Oil
Bubble:	Nitrogen
Dielectric Constant of Pipe Material:	3.4
Dielectric Constant of Liquid:	2.2
Dielectric Constant for Nitrogen:	1.01
Element Type for Pipe Section:	SOLID 122, (Element with 3-D category and Brick Shape)
Element Type for Liquid section:	SOLID 122, (Element with 3-D category and Brick Shape)
Element Type for Bubble:	SOLID 122, (Element with 3-D category and Brick Shape)
Element Type for Air Gap (Shield):	SOLID 122, (Element with 3-D category and Brick Shape)

3.4.3 Results for bubble modelling

Results are achieved for sphere diameters of 2.5 *mm*, 5 *mm*, 10 *mm*, and 15 *mm*. Sphere positions are varied from 10 *mm* to 28 *mm* along the y-axis. Transformer signals across the electrodes are shown in Figure 3.6 and 3.7. It can clearly be seen that the behaviour is the same as it is for the analytically calculated signals. The closer to a electrode a bubble passes through the meter the larger the signal.

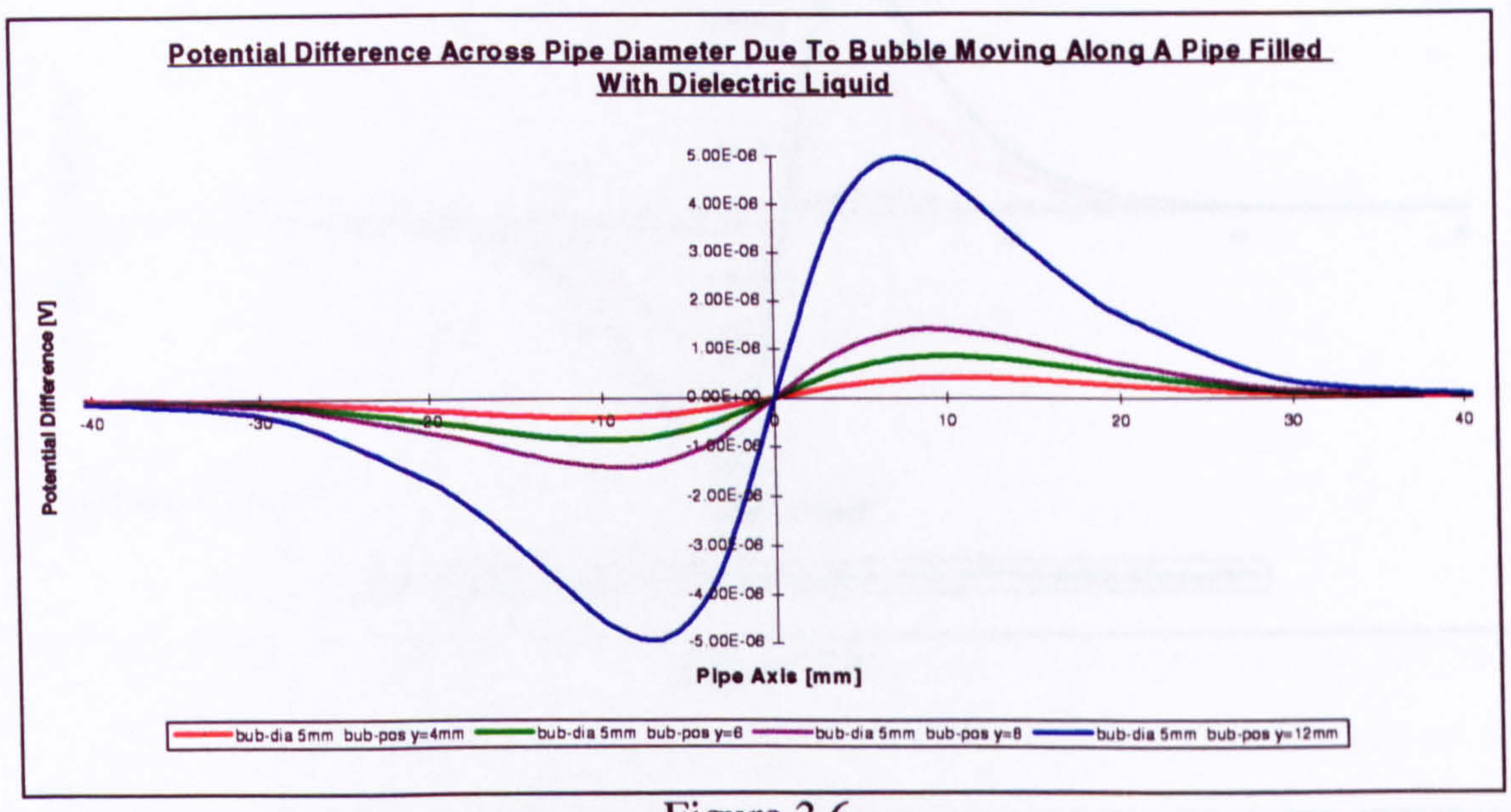

Figure 3.6

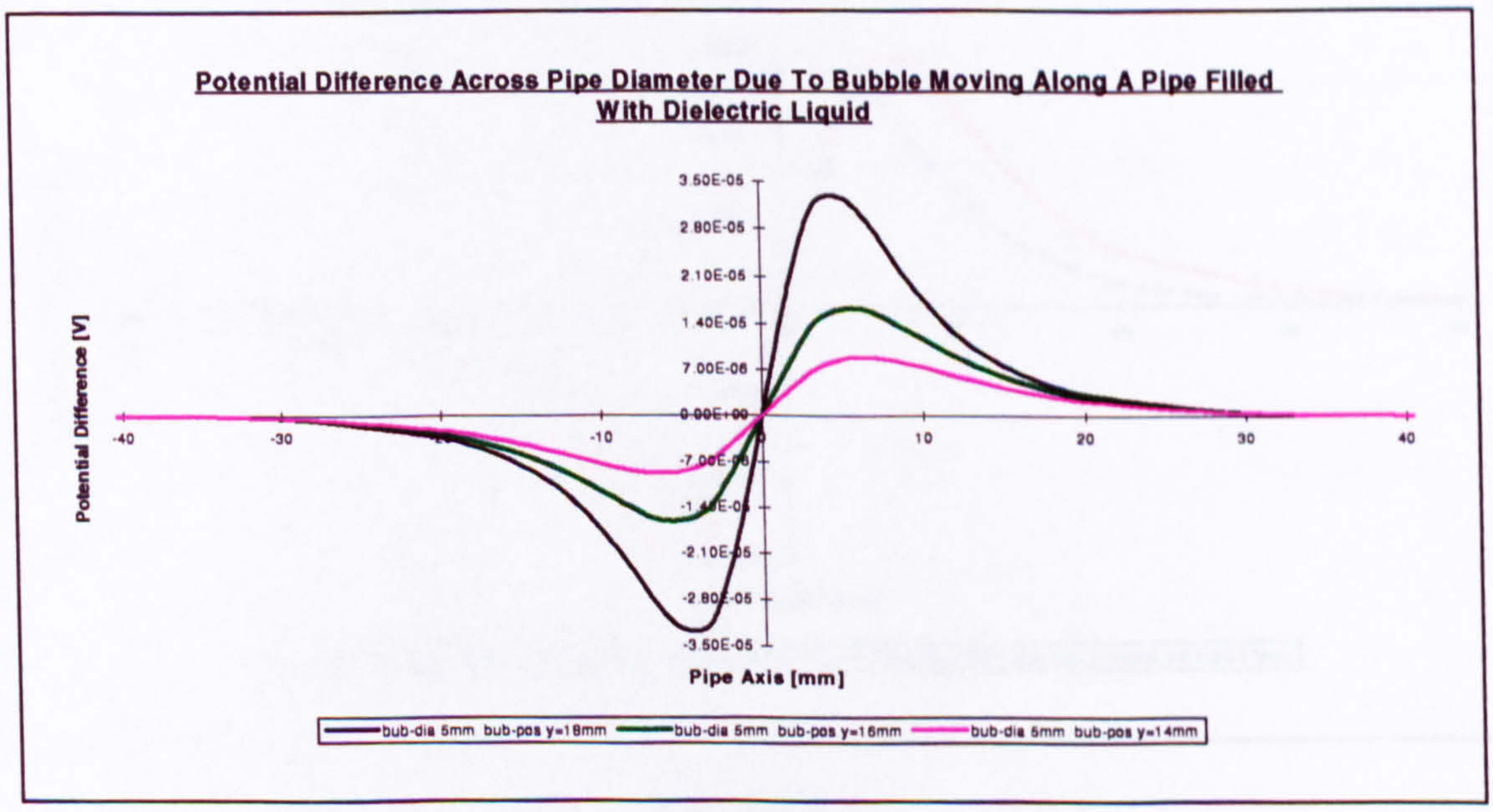

Figure 3.7

Figure 3.8 and 3.9 compare transformer signals of different bubble diameters. As expected, the larger the bubble diameter the larger the transformer signal. An investigation of the correlation of bubble diameter (relatively small bubble diameter, bubble radii ≤ a/10) and magnitude of the transformer signal shows that the magnitude of the signal is proportional to the cube of the bubble diameter.

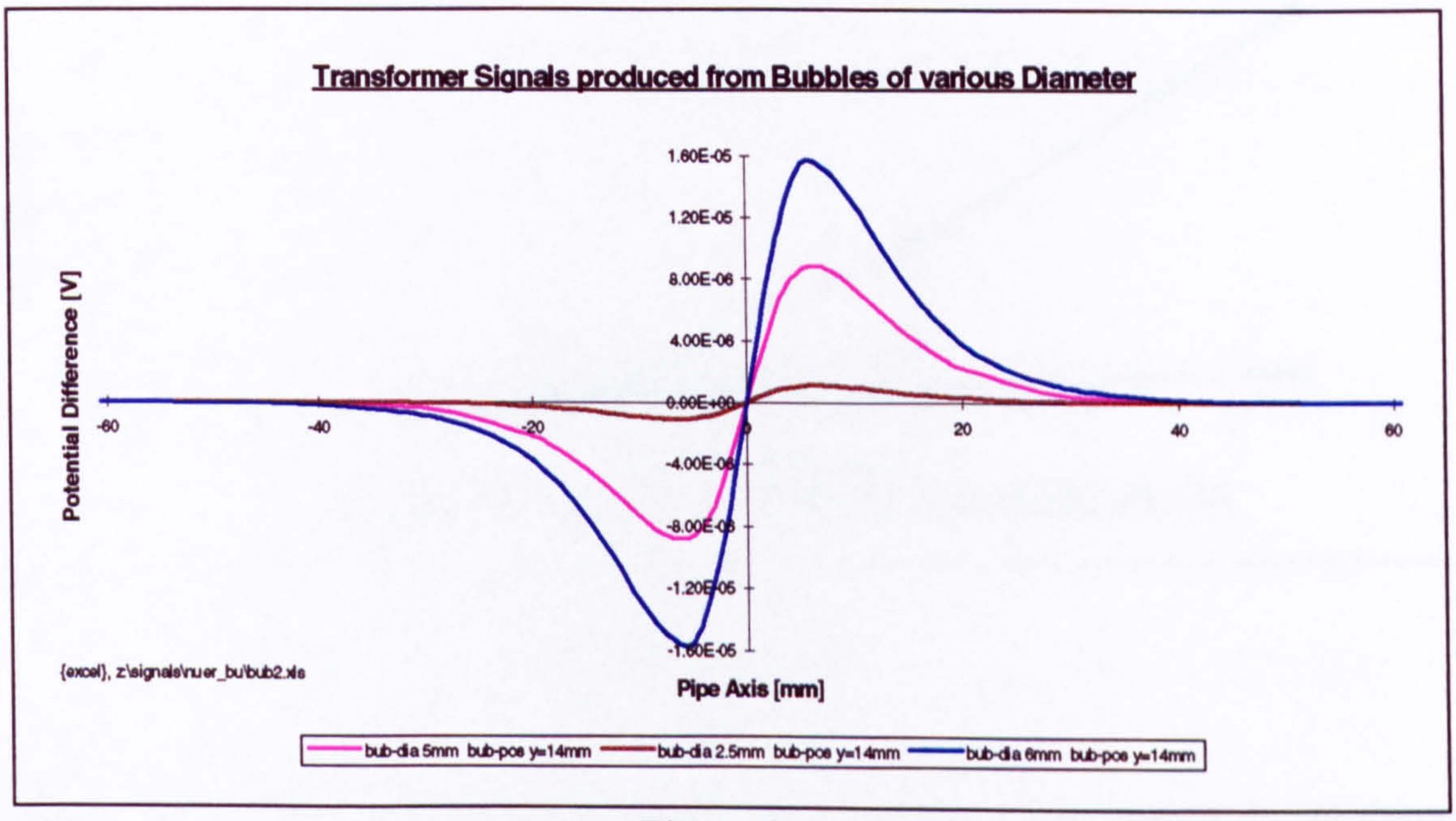

Figure 3.8

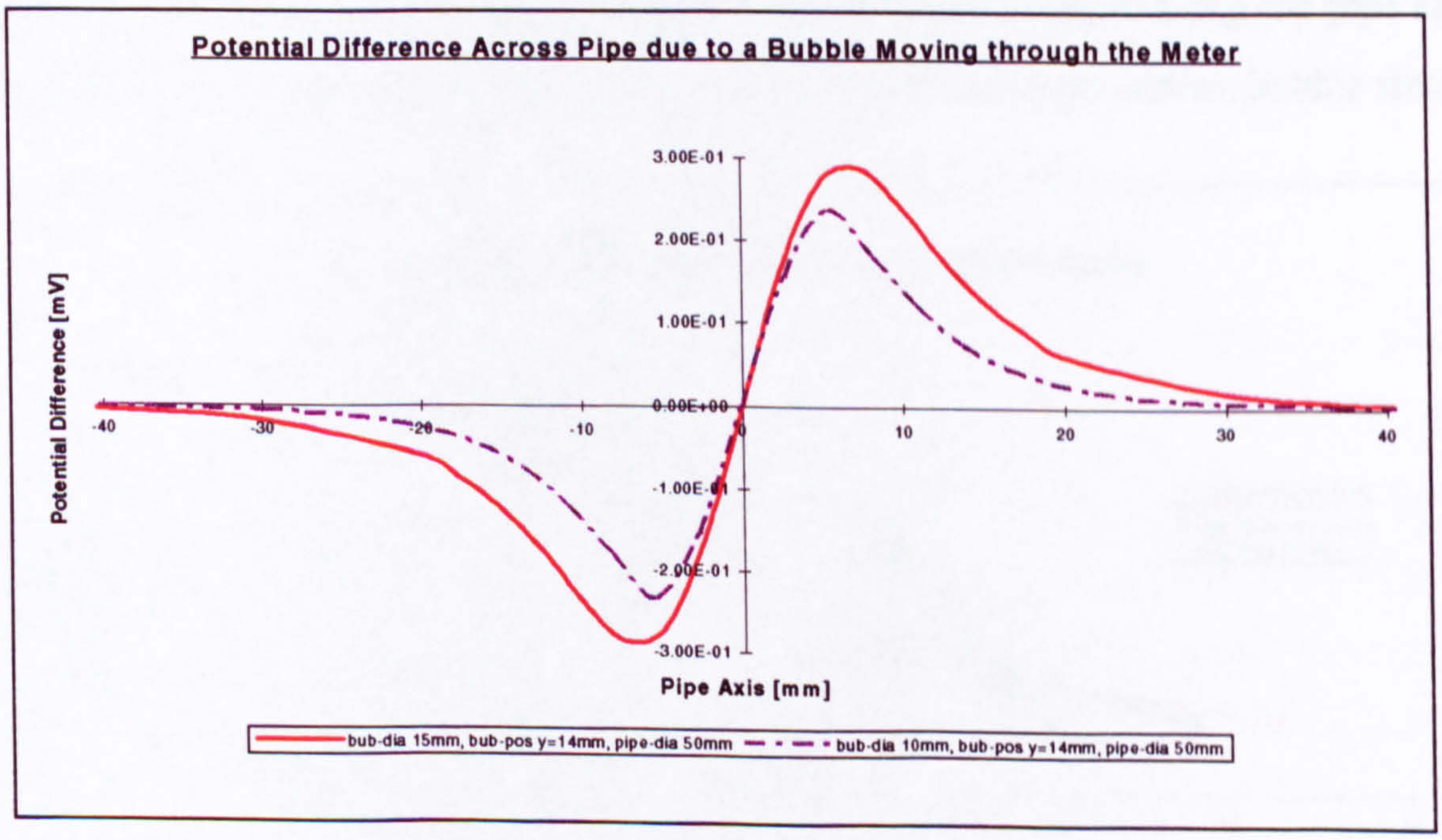

Figure 3.9

In Figure 3.10 graphs are plotted, which show the maximum potential difference against different bubble diameter for various bubble positions. It can be seen that the magnitude of the transformer signal increases very rapidly for bigger size bubbles (bubble radii >> a/10).

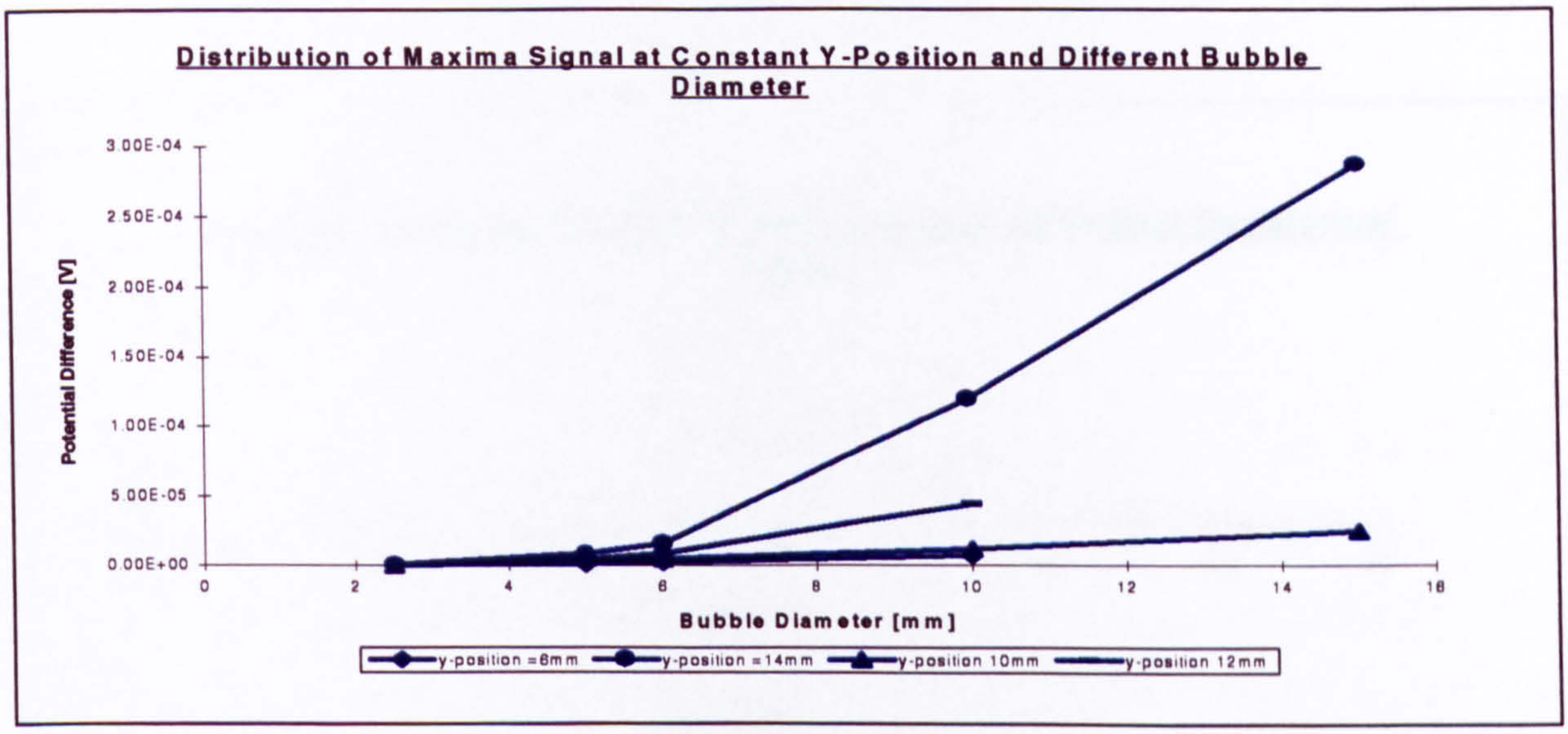

Figure 3.10

Figure 3.11 shows a plot of bubble positions along the y-axis versus the positions of peak signals along the pipe axis and for different bubble diameters. The curves show that the distribution of peak signals extends over the same distance along the pipe axis, and therefore the location of peak signals do not depend much on various bubble sizes.

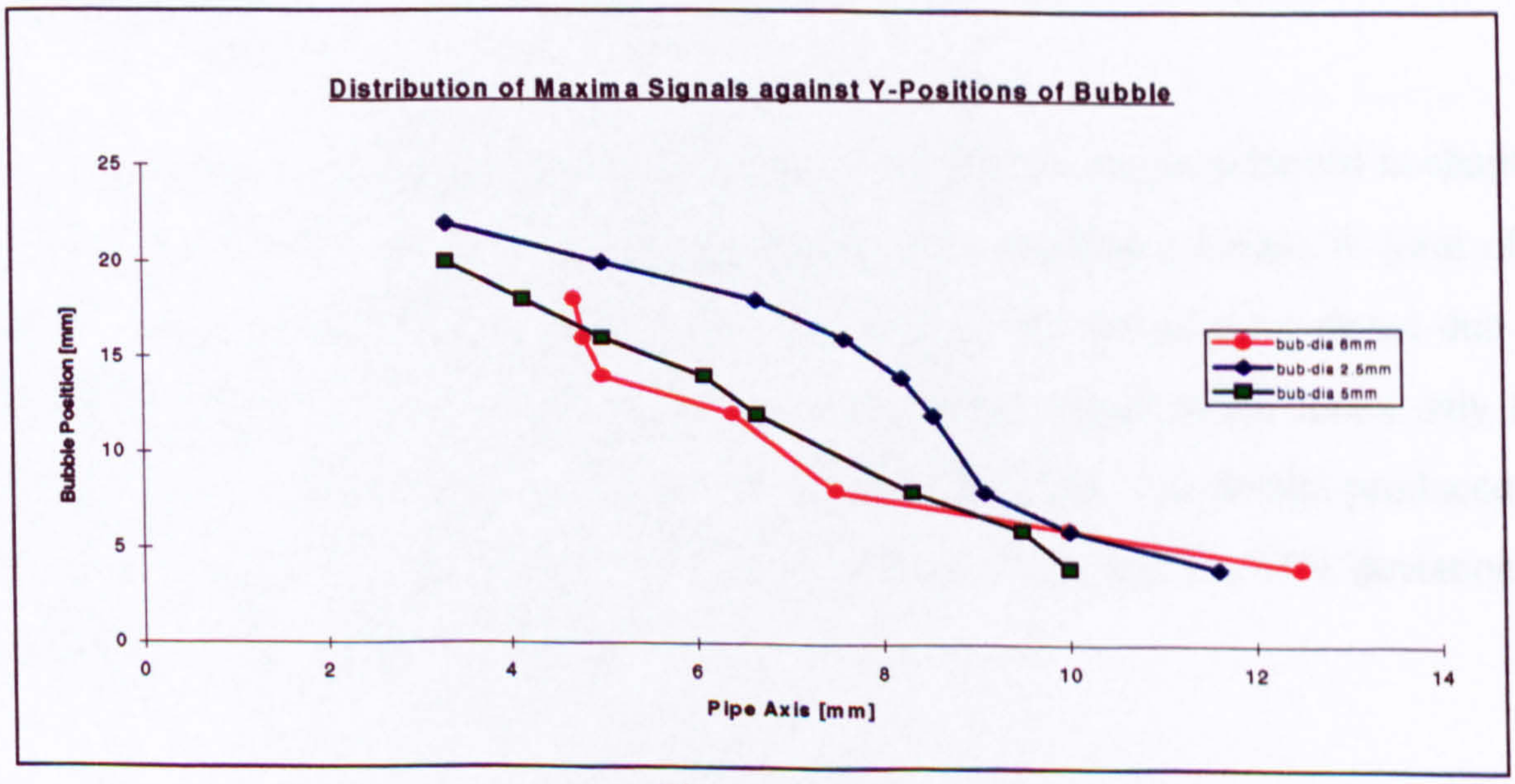

Figure 3.11

A final comparison of the transformer signal calculated analytically and numerically is provided in Figure 3.12 and shows that the two (dipole model and sphere model) numerically achieved transformer signals are virtually identical. The analytically produced transformer signal shows again a deviation of 30%.

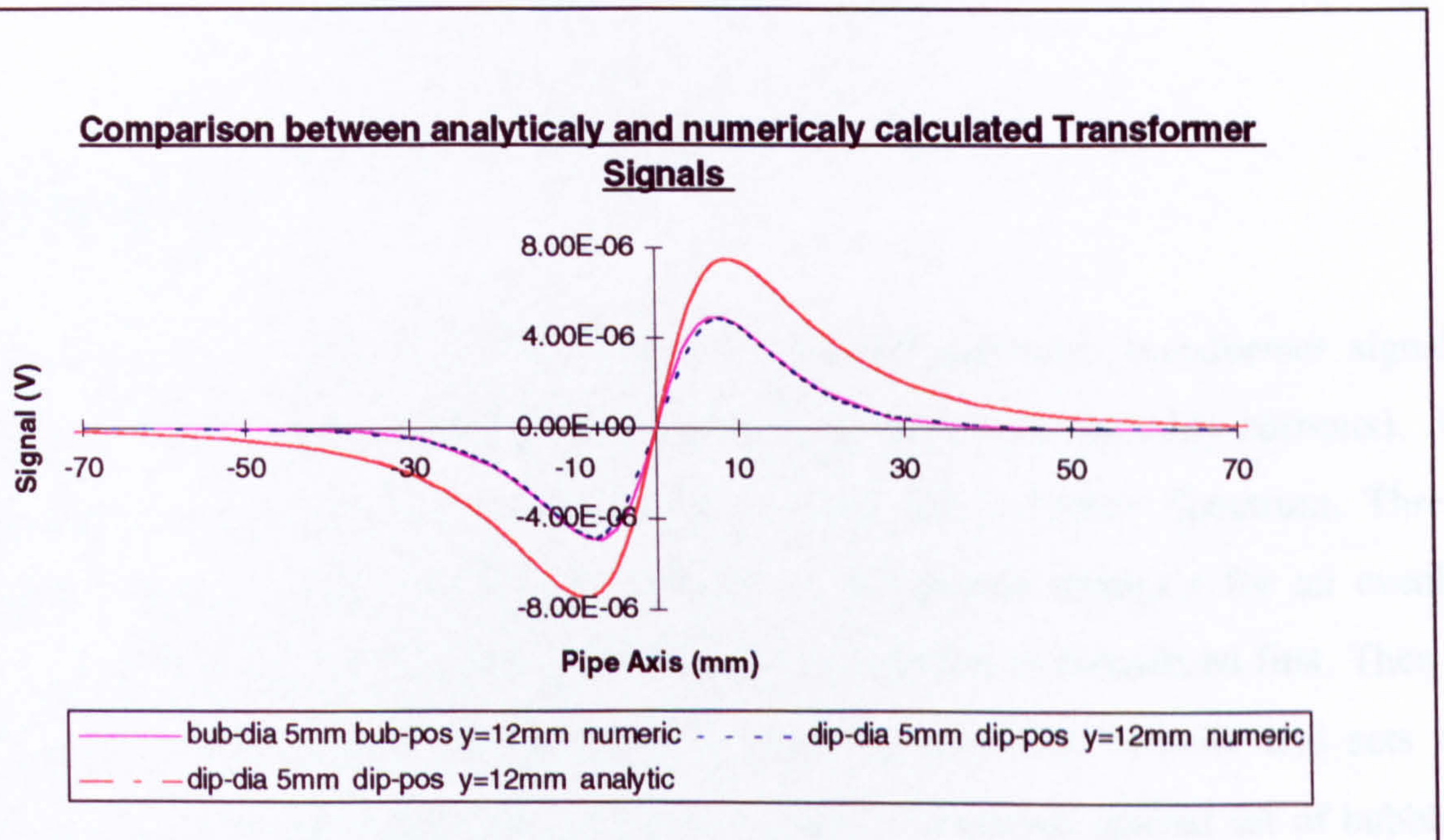

Figure 3.12

3.5 Summary

In this chapter the principal emphasis is to prove theoretical results achieved in chapter 2 and to further develop the numerical approach by modelling a bubble in form of a sphere, which allowed to investigate the behaviour of the transformer signal due to bubble sizes larger than the constriction for the dipole model which holds only for bubble diameter of maximum one tenth of the pipe diameter. The results produced in this chapter agree well in shape with those in chapter 2 but show a 30% deviation in magnitude of the signal amplitude.

CHAPTER 4

THEORETICAL FREQUENCY ANALYSIS OF THE TRANSFORMER SIGNAL

4.1 Introduction

In this section the data of the theoretical (analytical/numerical) transformer signal, obtained in earlier work (produced by bubble interference with the eddy currents), is transformed with a Fast Fourier Transform Method into a Power Spectrum. Three different conditions are examined. The shapes of the power spectra's for an evenly spaced set of bubbles and a changing velocity of the bubbles, is considered first. Then a set of power spectra for just the opposite condition (constant velocity and sets of different evenly spaced bubbles) is considered. Lastly a randomly spaced set of bubbles is examined to see the effect on the power spectrum. The Fast Fourier Transform is implicated with 4096 Data Points. The data for the signals are extracted from a maximum magnetic field of 0.01 *Tesla*, a field excitation of 1.5 *kHz*, a pipe radius of 50 *mm* and a bubble radius of 5 *mm*.

Because of the fact that the eddy currents are varying with time (sinusoidal drive excitation) a distorted Transformer Signal can be expected. Such a distorted Transformer Signal would obviously change the power spectrum. It is investigated how the Transformer Signal would change for different drive frequencies and bubble velocities. The drive frequencies used are 10 *Hz*, 100 *Hz*, 1000 *Hz* and 1500 *Hz*. The considered bubble velocities are 0.5 *m/s*, 1 *m/s*, 1.5 *m/s* and 2 *m/s*. At the same time the power spectra are computed and analysed.

4.2 Frequency analysis

To further investigate the transformer signal use is made of the mathematical tool of the Fourier Transform. The Fourier Transform is a signal representation that basically involves the decomposition of the signal in terms of sinusoidal (or complex exponential) components. With such a decomposition, a signal is said to be represented in the frequency domain. The frequency content of a signal is called its spectrum and a spectrum provides an identity for the signal in the sense that no other signal has the same spectrum.

Although frequency analysis is a well established mathematical device and is enormously used in the field of signal processing a brief introduction to the theory is given next. A continuous and periodic signal can be represented as a linear combination of harmonically related complex exponentials (or a combination of sine's and cosines) of the form

$$x(t) = \sum_{k=-\infty}^{\infty} c_k e^{j2\pi kF_0 t} \qquad (4.1)$$

with the fundamental period $T_p = 1/F_0$. Therefore the exponential signals $\left\{e^{j2\pi kF_0 t} \ldots\ldots k = 0,\pm1,\pm2,\ldots\right\}$ are the basic "building blocks" from which we can construct periodic signals of various types by proper choice of the fundamental frequency and the coefficients $\{c_k\}$. F_0 determines the fundamental period of x(t) and the coefficients $\{c_k\}$ specify the shape of the waveform. For a given periodic signal x(t) with period T_p, we can represent the periodic signal by the series (4.1) which is called a Fourier series, where the fundamental frequency F_0 is the reciprocal of the given period T_p. To derive the coefficients we use the following result

$$c_l = \frac{1}{T_p}\int_{T_p} x(t)e^{-j2\pi lF_0 t}\,dt \tag{4.1a}$$

A periodic signal has infinite energy and a finite average power, which is given as

$$P_x = \frac{1}{T_p}\int_{T_p} |x(t)|^2\,dt \tag{4.2}$$

Since the signal is periodic, the transform signals exists only at discrete values of frequencies $(i.e., F = 0, \pm F_0, \pm 2F_0, \ldots)$, the signal is said to have a line spectrum. The spacing between two consecutive spectral lines is equal to the reciprocal of the fundamental period T_p, whereas the shape of the power spectrum depends on the time domain characteristics. In order to represent an aperiodic signal the period is allowed to increase without limit, therefore the line spacing tends toward zero. In the limit, when the period becomes infinite, the signal becomes aperiodic and its spectrum becomes continuous. This argument suggests that the spectrum of an aperiodic signal will be the envelope of the line spectrum in the corresponding periodic signal obtained by repeating the aperiodic signal with a period T_p. Considering an aperiodic signal *x(t)* with finite duration, a periodic signal $x_p(t)$ with period T_p can be created. Clearly, $x_p(t) = x(t)$ in the limit as $T_p \to \infty$ that is,

$$x(t) = \lim_{T_p \to \infty} x_p(t) \tag{4.3}$$

This interpretation implies that by taking the limit $T_p \to \infty$ the spectrum of *x(t)* from the spectrum of $x_p(t)$ can be obtained. Coming back to the Fourier series representation of $x_p(t)$,

$$x(t) = \sum_{k=-\infty}^{\infty} c_k e^{j2\pi kF_0 t} \tag{4.4}$$

where

$$c_k = \frac{1}{T_p}\int_{-T_p/2}^{T_p/2} x_p(t)e^{-j2\pi lF_0 t}\,dt \qquad F_0 = \frac{1}{T_p} \tag{4.5}$$

Because $x_p(t) = x(t)$ for $-T_p/2 \le t \le T_p/2$ (17) may be expressed as

$$c_k = \frac{1}{T_p}\int_{-T_p/2}^{T_p/2} x(t)e^{-j2\pi lF_0 t}\,dt \tag{4.6}$$

Because it is also true that $x(t) = 0$ for $|t| > T_p/2$ the limits on the integral in (18) may be replaced by $-\infty$ and ∞. Therefore

$$c_k = \frac{1}{T_p}\int_{-\infty}^{\infty} x(t)e^{-j2\pi lF_0 t}\,dt \tag{4.7}$$

Now a function *X(F)* is defined, and is called the Fourier transform of *x(t)*.

$$X(F) = \int_{-\infty}^{\infty} x(t)e^{-j2\pi Ft}\,dt \tag{4.8}$$

X(F) is a function of the continuous variable F, and does not depend on T_p or F_0. Comparing (4.7) and (4.8) the Fourier coefficient c_k can be expressed in terms of *X(F)* as

$$c_k = \frac{1}{T_p}X(kF_0)$$

or equivalently,

$$T_p c_k = X(kF_0) = X\left(\frac{k}{T_p}\right) \tag{4.9}$$

Thus the Fourier coefficients are samples of *X(F)* taken at multiples of F_0 and scaled by F_0. If we substitute c_k from equation 4.9 into equation 4.4 the following result will be obtained

$$x_p(t) = \frac{1}{T_p} \sum_{k=-\infty}^{\infty} X\left(\frac{k}{T_p}\right) e^{j2\pi k F_0 t} \tag{4.10}$$

Taking the limit of (4.10) as T_p approaches infinity. Defining $\Delta F = \frac{1}{T_p}$ and substituting this in (4.10) it becomes

$$x_p(t) = \sum_{k=-\infty}^{\infty} X(k\Delta F) e^{j2\pi k \Delta F t} \Delta F \tag{4.11}$$

Remembering that in the limit as T_p approaches infinity, $x_p(t)$ reduces to *x(t)*. Now, ΔF becomes the differential dF and $k\Delta F$ becomes the continuous frequency variable *F*. In turn, the summation in (24) becomes an integral over the frequency variable *F*. Thus

$$\lim_{T_p \to \infty} x_p(t) = x(t) = \lim_{\Delta F \to 0} \sum_{k=-\infty}^{\infty} X(k\Delta F) e^{-j2\pi \Delta F t} \Delta F \tag{4.12}$$

$$x(t) = \int_{-\infty}^{\infty} X(F) e^{j2\pi F t} dF \tag{4.13}$$

This integral relationship yields to *x(t)* when *X(F)* is known, and is called the inverse Fourier transform. Finally the Fourier transform pair (4.8) and (4.13) can be expressed in terms of the radian frequency variable $\Omega = 2\pi F$. Since $dF = \frac{d\Omega}{2\pi}$ (4.13) and (4.8) become

$$x(t) = \frac{1}{2\pi} \int_{-\infty}^{\infty} X(\Omega) e^{j\Omega t} d\Omega \tag{4.14}$$

$$X(\Omega) = \int_{-\infty}^{\infty} x(t) e^{-j\Omega t} d\Omega \tag{4.15}$$

The Fourier transform exists if the signal *x(t)* has finite energy, that is, if

$$\int_{-\infty}^{\infty} |x(t)|^2 dt < \infty \tag{4.16}$$

If a signal *x(t)* is absolutely integrable, it will also have finite energy. That is,

$$E_x = \int_{-\infty}^{\infty} |x(t)|^2 dt \leq \left[\int_{-\infty}^{\infty} |x(t)| dt \right]^2 \tag{4.17}$$

This energy equation, in turn, can be expressed in terms of X(F) as follows:

$$E_x = \int_{-\infty}^{\infty} x(t) x^*(t) dt$$

$$= \int_{-\infty}^{\infty} x(t) dt \left[\int_{-\infty}^{\infty} X^*(F) e^{-j2\pi Ft} dF \right]$$

$$= \int_{-\infty}^{\infty} X^*(F) dF \left[\int_{-\infty}^{\infty} x(t) e^{-j2\pi Ft} dt \right]$$

$$= \int_{-\infty}^{\infty} |X(F)|^2 dF$$

Therefore, it can be concluded that

$$E_x = \int_{-\infty}^{\infty} |x(t)|^2 dt = \int_{-\infty}^{\infty} |X(F)|^2 dF \tag{4.18}$$

This is Parseval's relation for aperiodic, finite energy signals and expresses the principle of conservation of energy in the time and frequency domains.

In the above paragraphs a Fourier series for continuous-time periodic (power) signals and the Fourier transform for finite energy aperiodic signals is briefly explained. Now the Fourier series and Fourier transform for discrete-time signals are considered.

Suppose we are given a periodic sequence *x(n)* with period *N*. By substituting the Sample Period *N* for the Time-Period T_p in the Synthesis Equation (4.1) and Analysis Equation (4.1a) from the continuous Fourier Series Analysis a form which represents the Synthesis Equation (4.19) and Analysis Equation (4.20) can be achieved.

$$x(n) = \sum_{k=0}^{N-1} c_k e^{j2\pi kn/N} \tag{4.19}$$

$$c_k = \frac{1}{N} \sum_{n=0}^{N-1} x(n) e^{-j2\pi kn/N} \tag{4.20}$$

The average power of a discrete-time periodic signal with period *N* is defined as

$$P_x = \frac{1}{N} \sum_{n=0}^{N-1} |x(n)|^2 \tag{4.21}$$

The expression for P_x in terms of the Fourier coefficient $\{c_k\}$ is

$$P_x = \sum_{k=0}^{N-1} |c_k|^2 \tag{4.22}$$

To achieve a Fourier transform for discrete aperiodic signals the same procedure as that for periodic signals can be used. We substitute sample's n for time t and define the (Analysis Equation) Fourier Transform of a finite-energy discrete-time signal $x(n)$ as

$$X(\omega) = \sum_{n=-\infty}^{\infty} x(n) e^{-j\omega n} \tag{4.23}$$

The Synthesis Equation as

$$x(n) = \frac{1}{2\pi} \int_{2\pi} X(\omega) e^{j\omega n} dn \tag{4.24}$$

The Energy relation between $x(n)$ and $X(\omega)$ of an Aperiodic Signal is

$$E_x = \sum_{n=-\infty}^{\infty} |x(n)|^2 = \frac{1}{2\pi} \int_{-\pi}^{\pi} |X(\omega)|^2 d\omega \tag{4.25}$$

A major reason for the importance of the discrete Fourier transform (DFT) is the existence of efficient algorithms for computing the DFT. The computational problem of the DFT is to compute the sequence {X(k)} of N complex-valued numbers given another sequence of data{x(n)} of length N, according to the formula

$$X(k) = \sum_{n=0}^{N-1} x(n) e^{-j2\pi nk/N} \qquad 0 \le k \le N-1 \tag{4.26}$$

The computationally efficient algorithms, known collectively as fast Fourier transform (FFT) algorithms, are used here.

4.3 Power spectra of evenly spaced bubbles compared with varying velocities

Considered are 8 cycles with a bubble spacing of 300 *mm* for velocities of 0.25 *m/s*, 0.5 *m/s* and 1.5 *m/s*. In Figure 4.1 a set of calculated transformer signals for bubbles with a velocity of 0.5 *m/s* are illustrated. According to equation. (4.21) the magnitude of the power is not expected to change. The results shown in Figure 4.2 to Figure 4.4 indicate clearly that the power remains exactly the same for all different velocities. It is, therefore, independent of velocities. But it also can be seen that the frequency band increases with increasing velocity. This effect is very much as expected, because the transformer signal for a higher velocity has a narrower width in time and therefore has to be made up with higher frequencies in the Fast Fourier Transform.

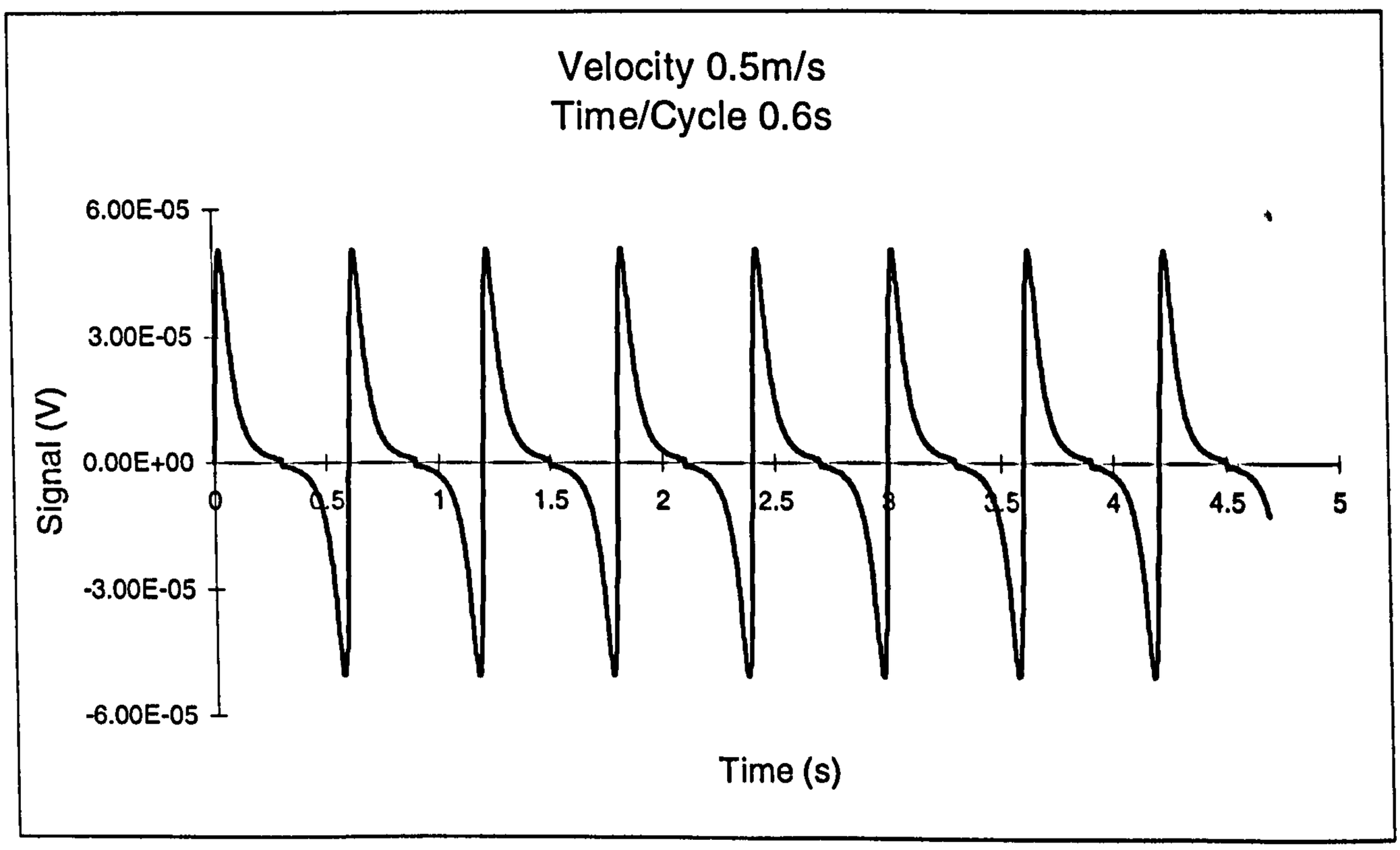

Figure 4.1 (Transformer signal produced from evenly spaced bubbles)

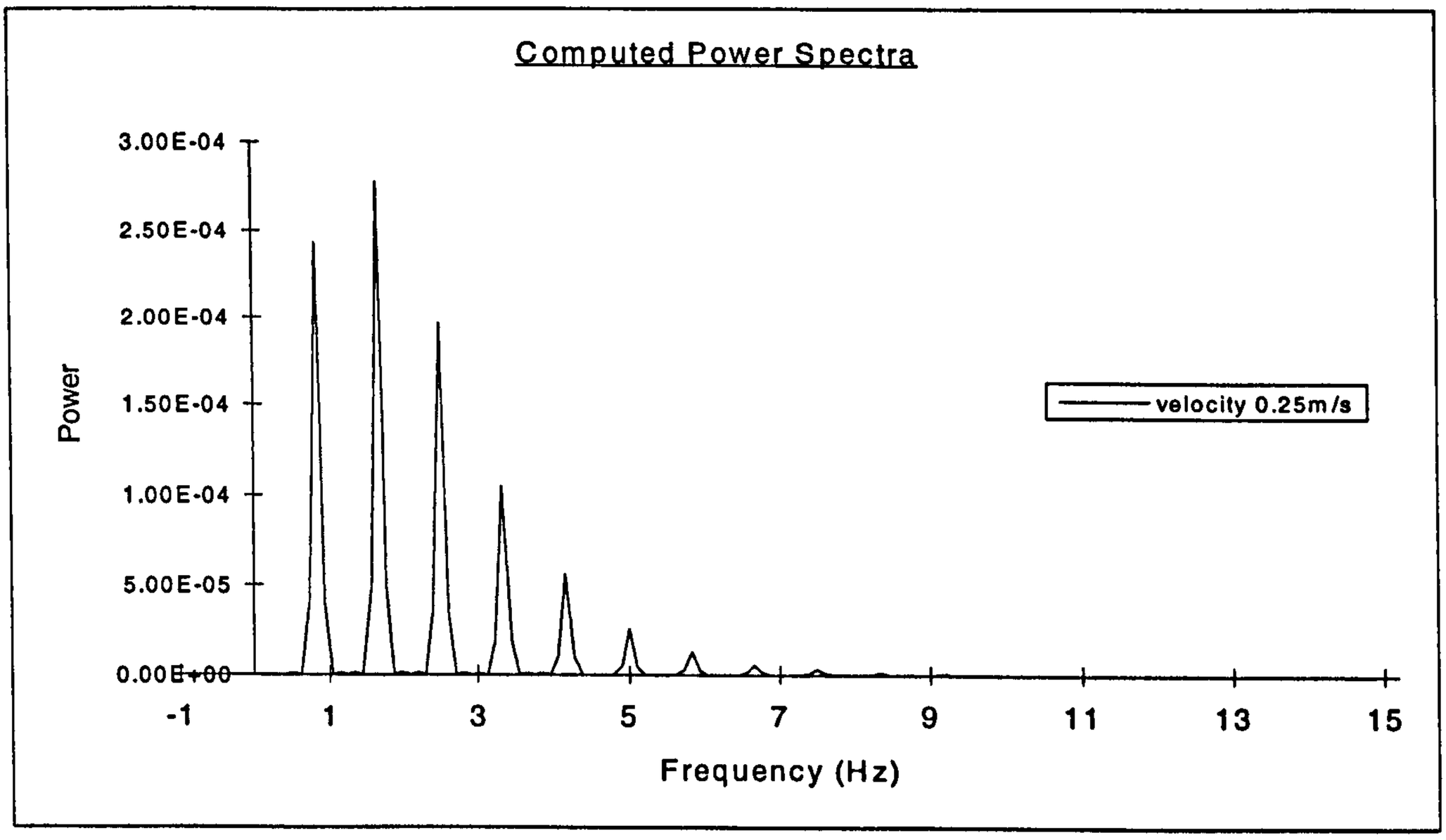

Figure 4.2

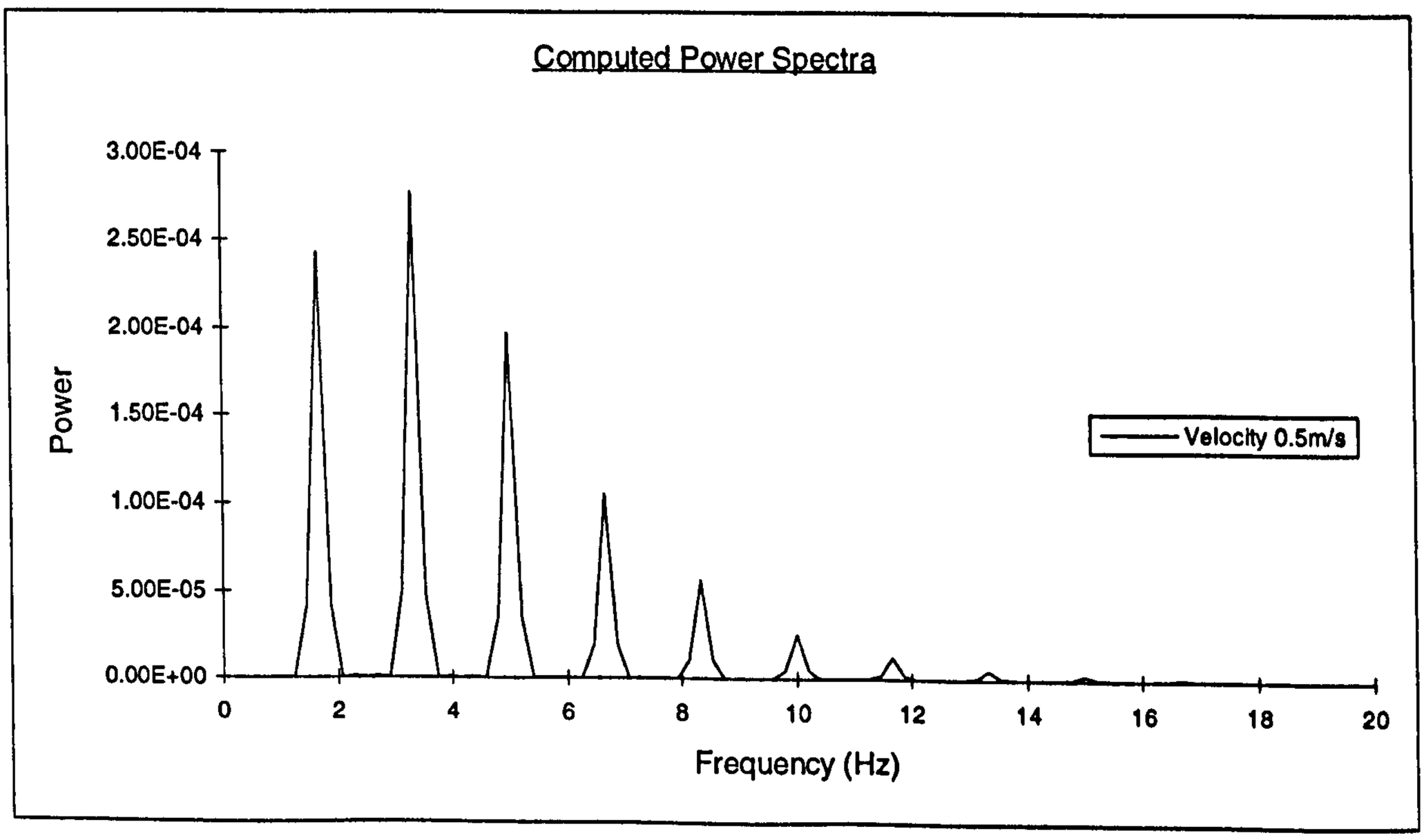

Figure 4.3

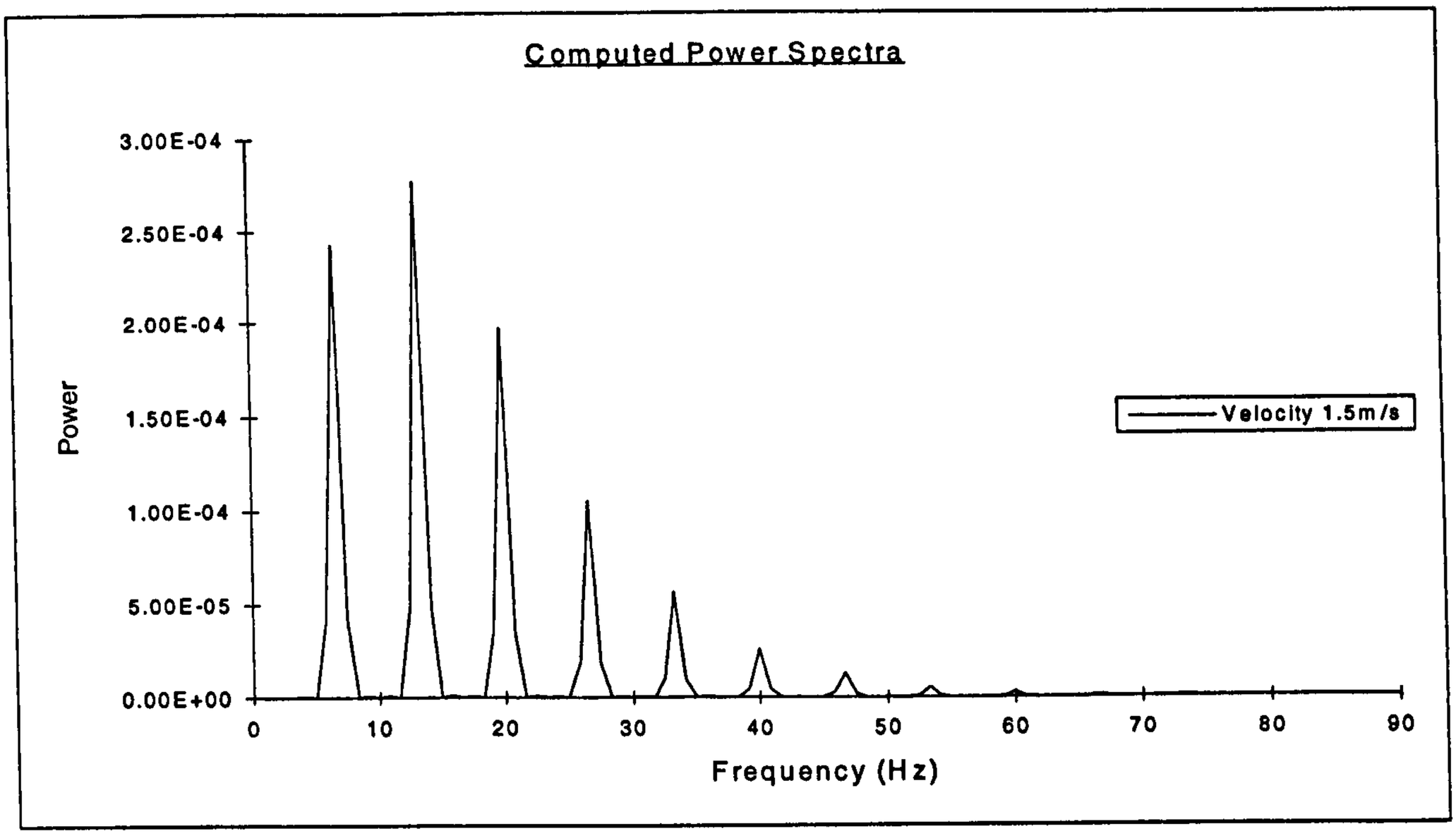

Figure 4.4

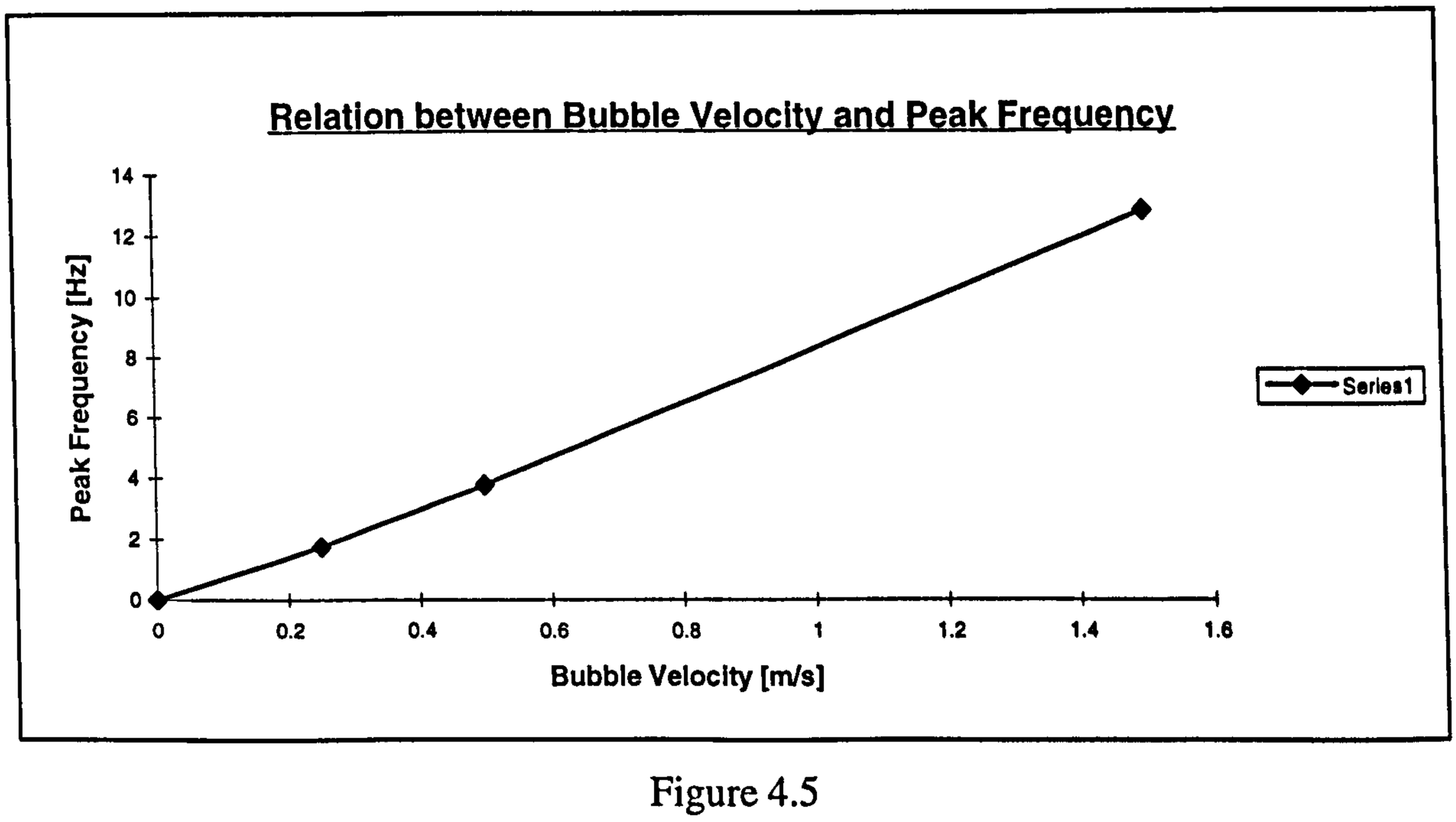

Figure 4.5

Figure 4.5 shows a linear relationship between Peak Frequency and Bubble Velocity.

4.4 Power spectra of varying bubble spacing

In this section resulting power spectra for transformer signals, obtained with a constant bubble velocity and different bubble spacing where performed and compared. The results are shown in Figure 4.6 and Figure 4.7 and depict clearly that for decreasing spacing the power increases. This is also expected with respect to equation (4.21). The position of maximum frequency is nearly the same for all signals with different spacing.

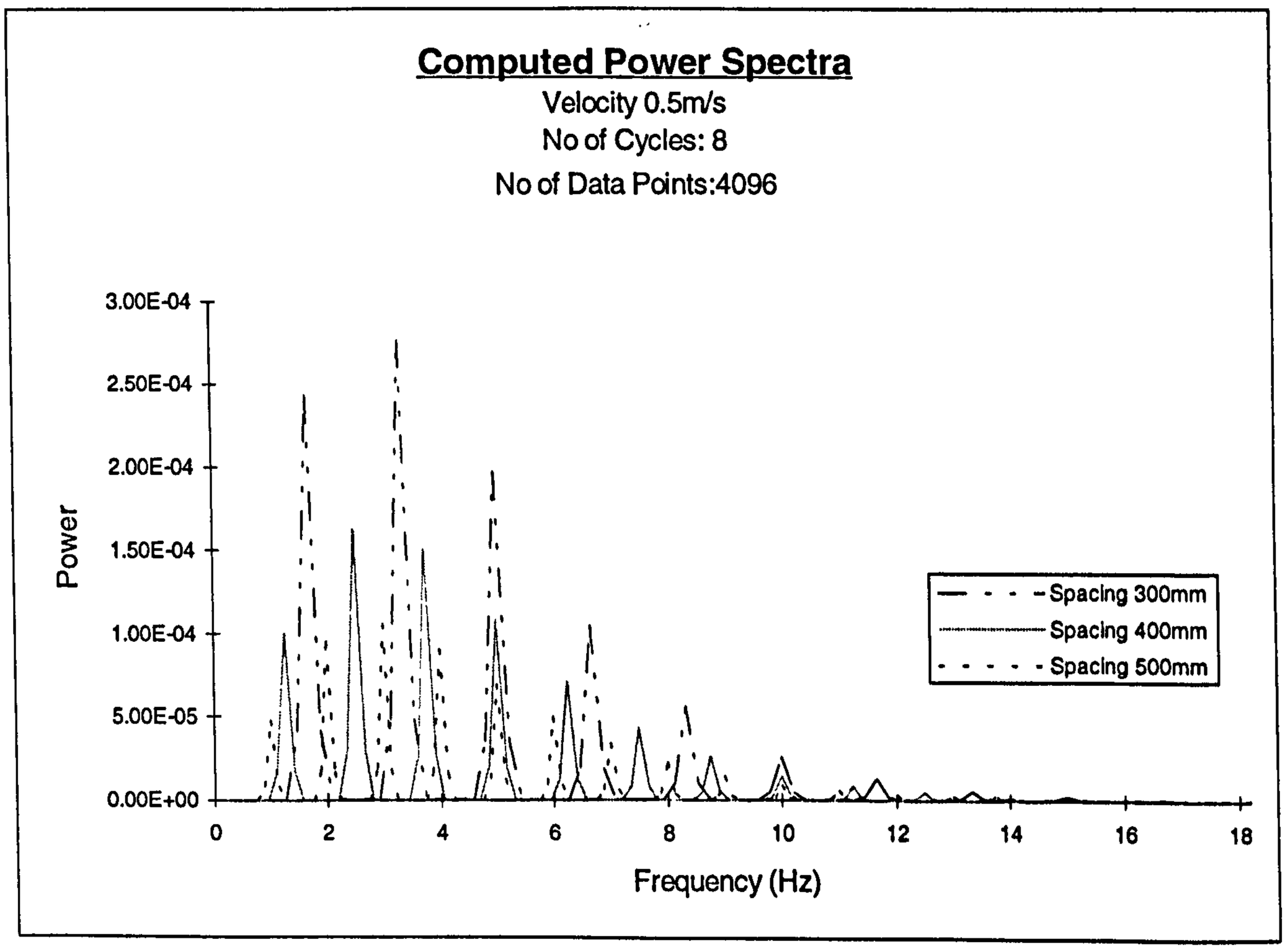

Figure 4.6

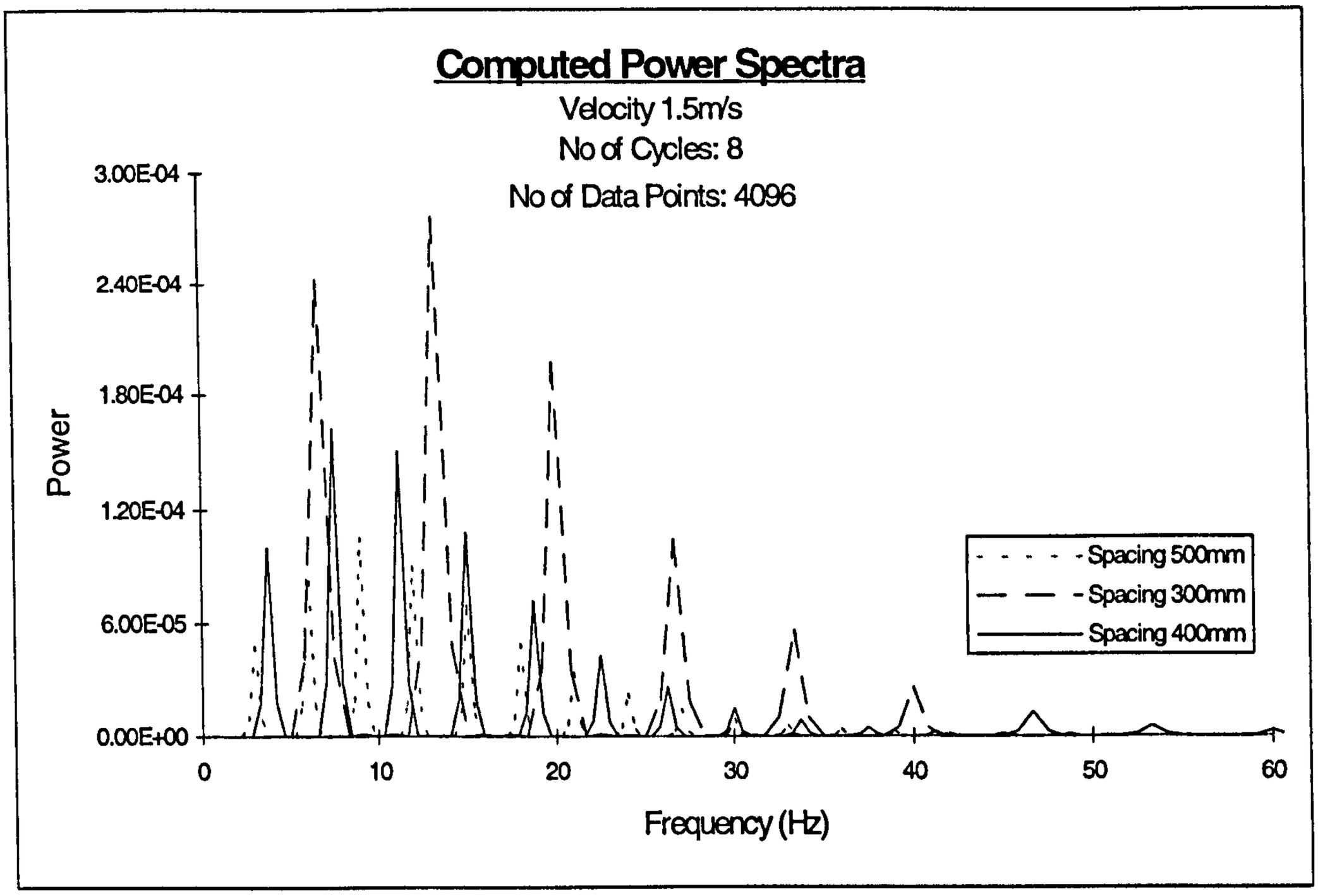

Figure 4.7

4.5 Power spectra of randomly spaced bubbles

Figure 4.8 shows the power spectrum of a set of randomly spaced bubbles. This is compared with the power spectrum (Figure 4.9) for a set of bubbles that has a constant spacing that is equal to the average of the one with random spacing. The two compared spectra are very similar. On account of the theoretical analysis this is anticipated.

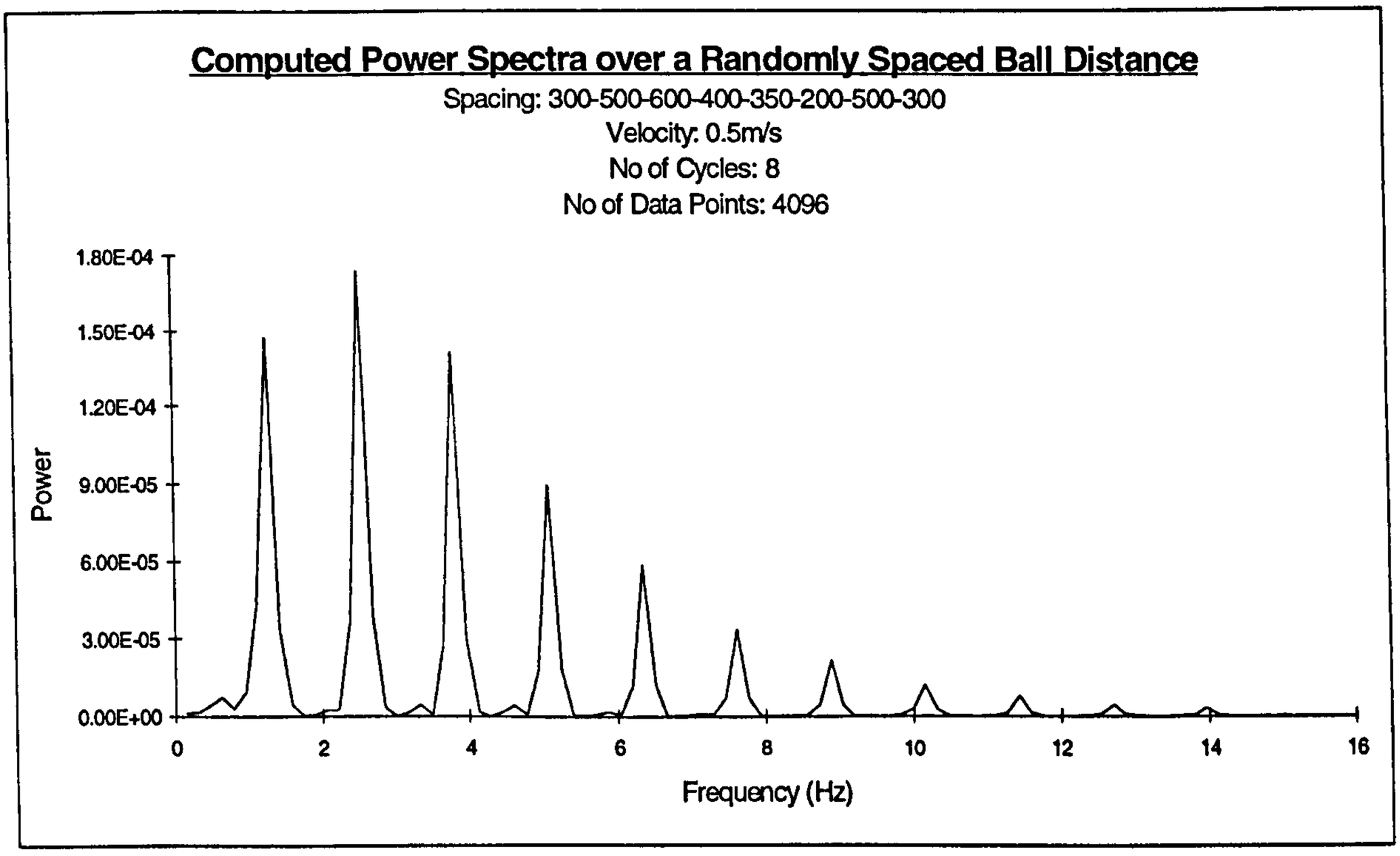

Figure 4.8

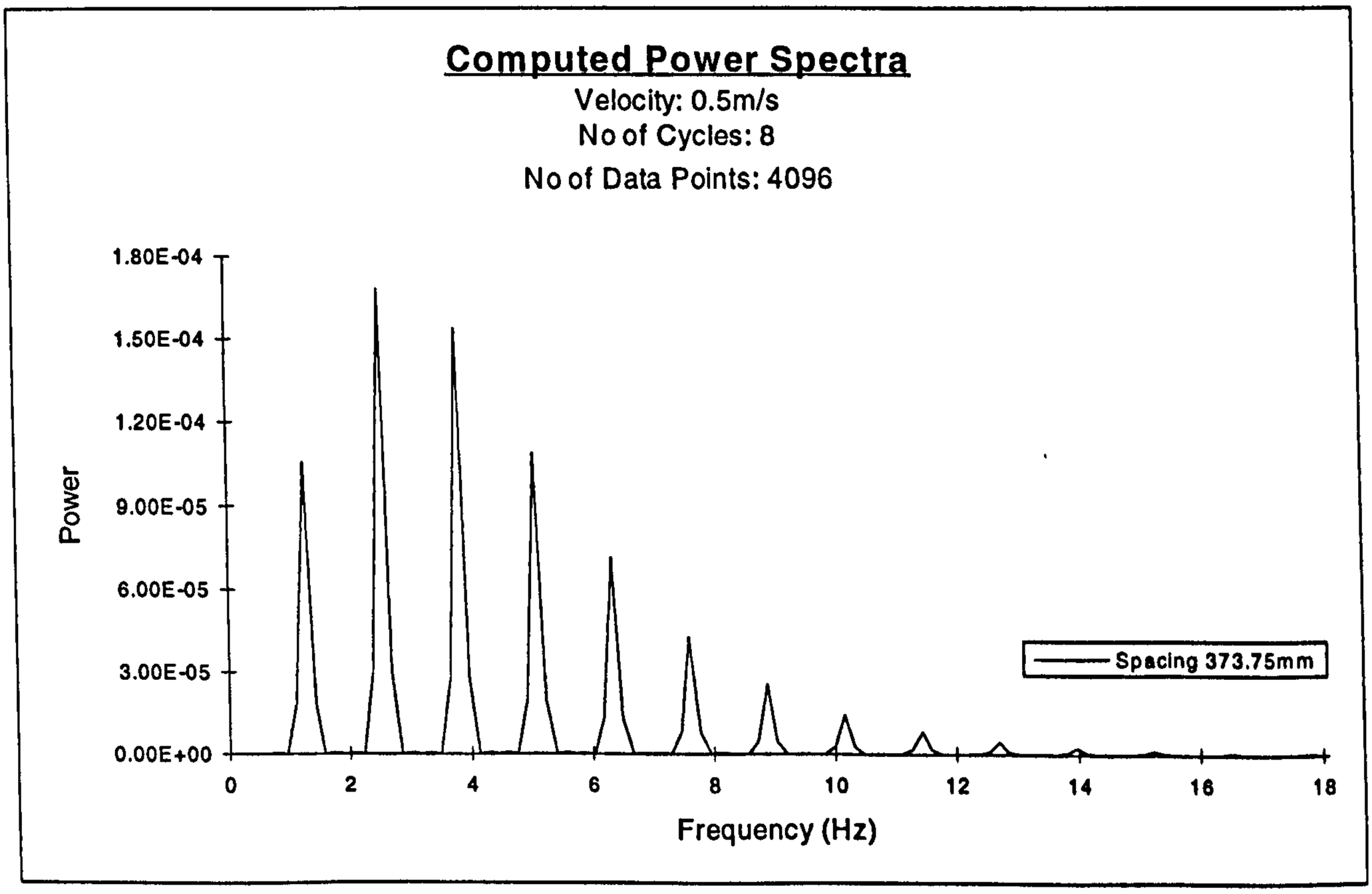

Figure 4.9

4.6 Frequency analysis for transformer signal due to time varying eddy currents

In the previous section time varying eddy currents, which occur in the fluid, is not considered. On the experimental side, the meter is driven with a sinusoidal frequency. The drive frequency should be at least about 1000 *Hz* for an electromagnetic flowmeter in use with a dielectric liquid. This is because of the known fact that for isolating liquids the method of inductive flowmeasurement becomes extremely difficult due to electrostatic charges that arises in moving liquid. The reasons for this electrostatic charge, which shows up as an electrostatic disturbance potential on the electrodes, is contact between the liquid and the pipe wall and charge separation in the turbulent dielectric liquid. The magnitude of this disturbance potential depends on flow velocity, liquid properties, liquid contamination and on boundary conditions like pipe wall roughness. From intensive investigations (Hentschel [21]) an appropriate operating frequency for an inductive flowmeter has to be chosen in such a way that in connection with the bandwidth on the system output an allowable signal to noise ratio appears. A spectral distribution of electrostatic charge is achieved by Hentschel. Although the operating frequency for electromagnetic flowmeters for insulating liquids is rather high, a general investigation of transformer signals and associated power spectra beginning at 10 *Hz* and up to 1500 *Hz* is computed and analysed. Also looked at is the behaviour of the transformer signal for different bubble velocities. Figure 4.9 to 4.16 show the transformer signal for non time varying eddy currents, a rectified (rectified because the power is taken after signal processing) sine function at the operating frequency and the distorted transformer signal which is the product of the two. An obvious difference is that the lower the bubble velocity and the higher the drive frequency the less deformed became the rectified transformer signal. In Figure 4.17 to 4.35 the effect on the power spectra is compared. As previously examined, transformer signals became more distorted for low drive frequencies and high bubble velocities it appears that these distortions hardly influence the power spectra. The only difference is noticed that the magnitude of the power varies slightly. There is no verification on the frequency

distribution to be seen. A reason for this behaviour of the power spectra is the averaging effect that takes place over the time period.

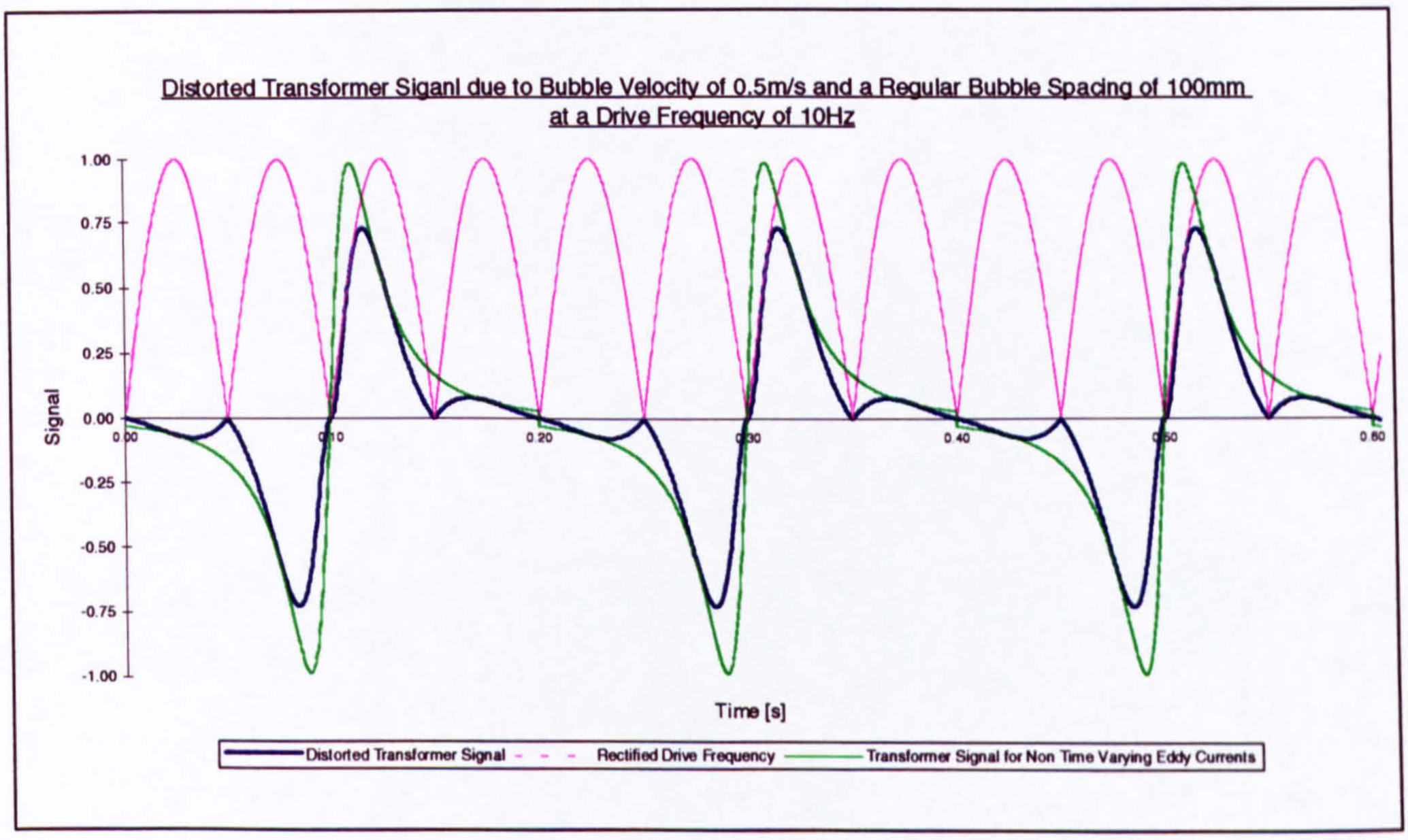

Figure 4.10

Figure 4.11

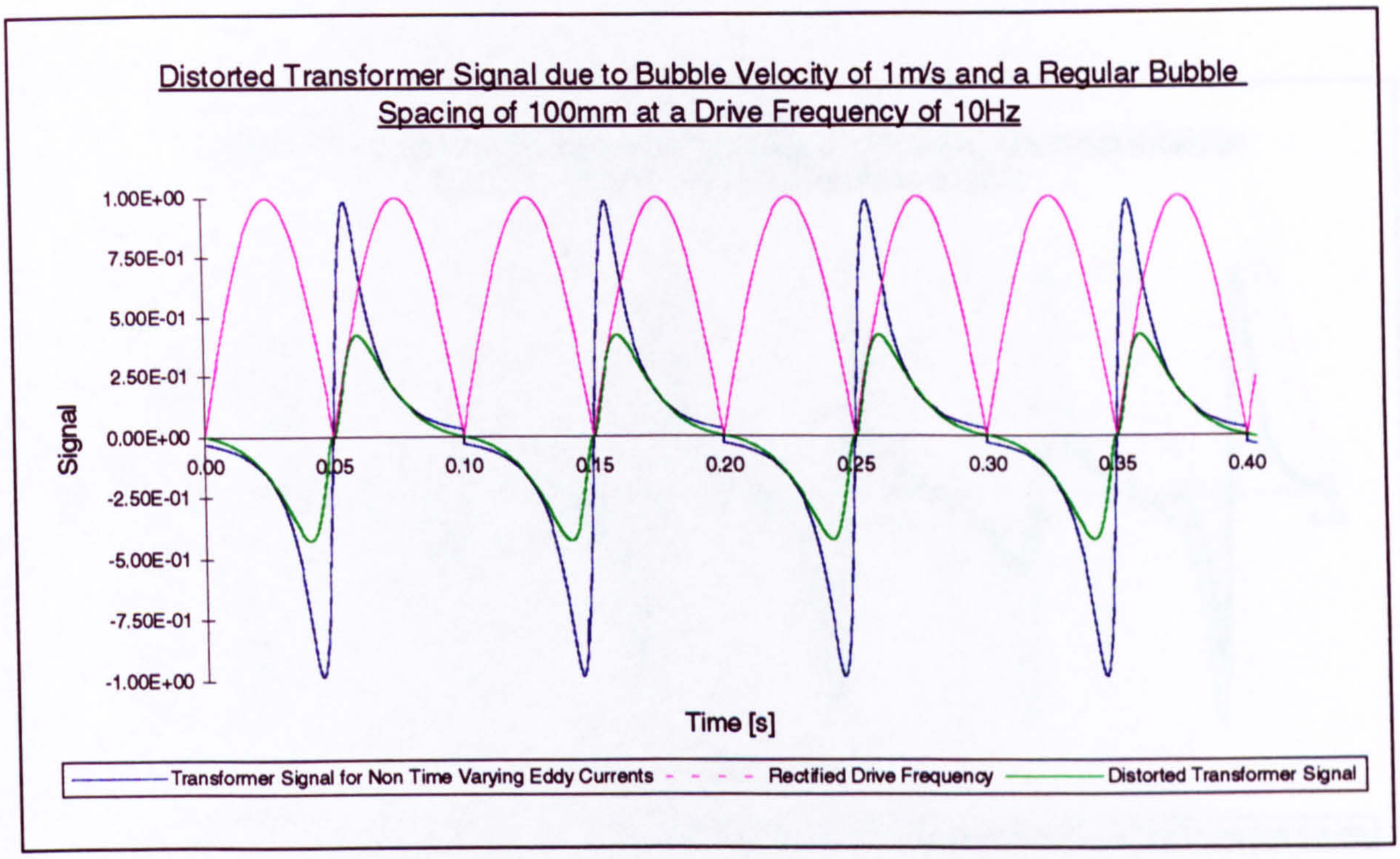

Figure 4.12

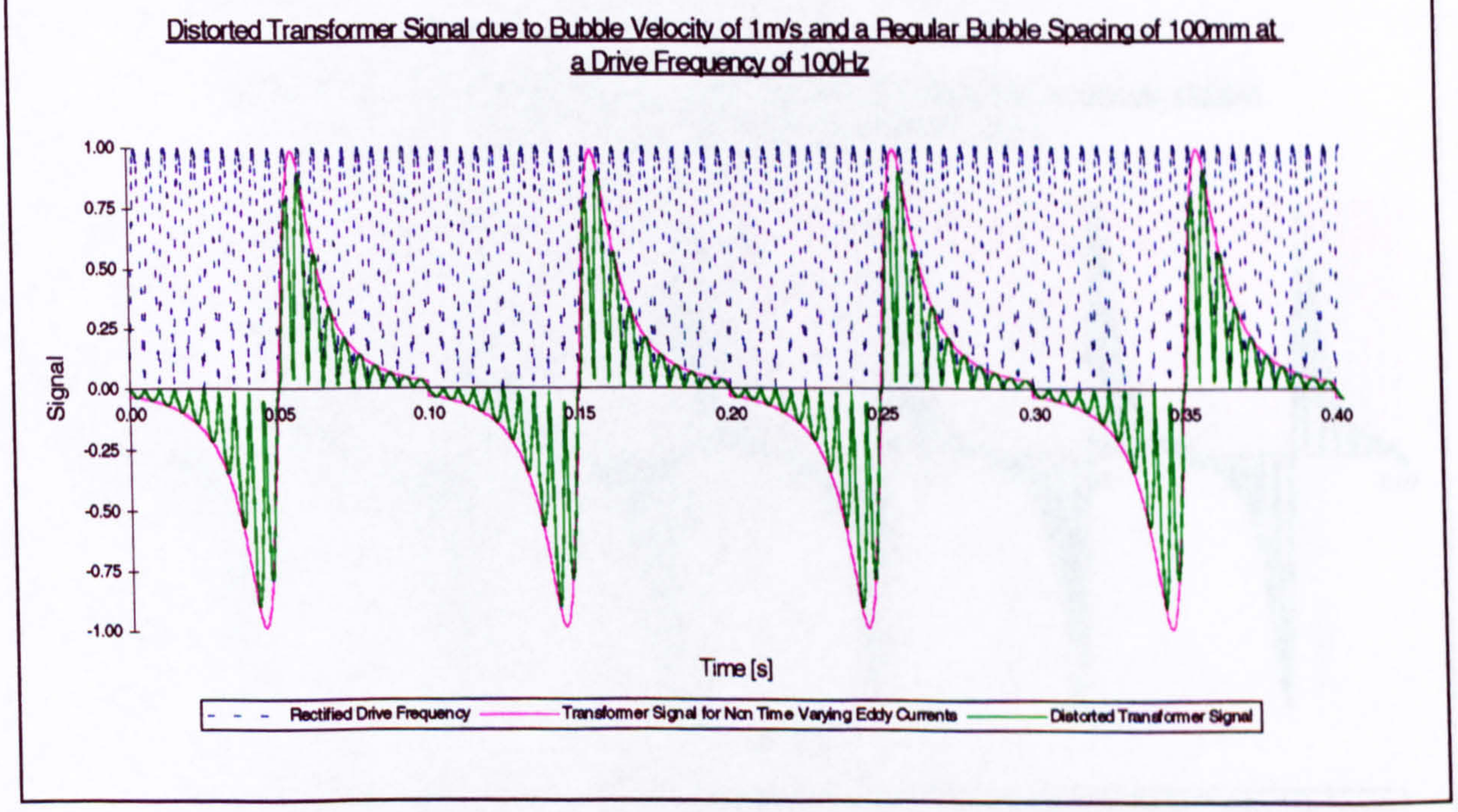

Figure 4.13

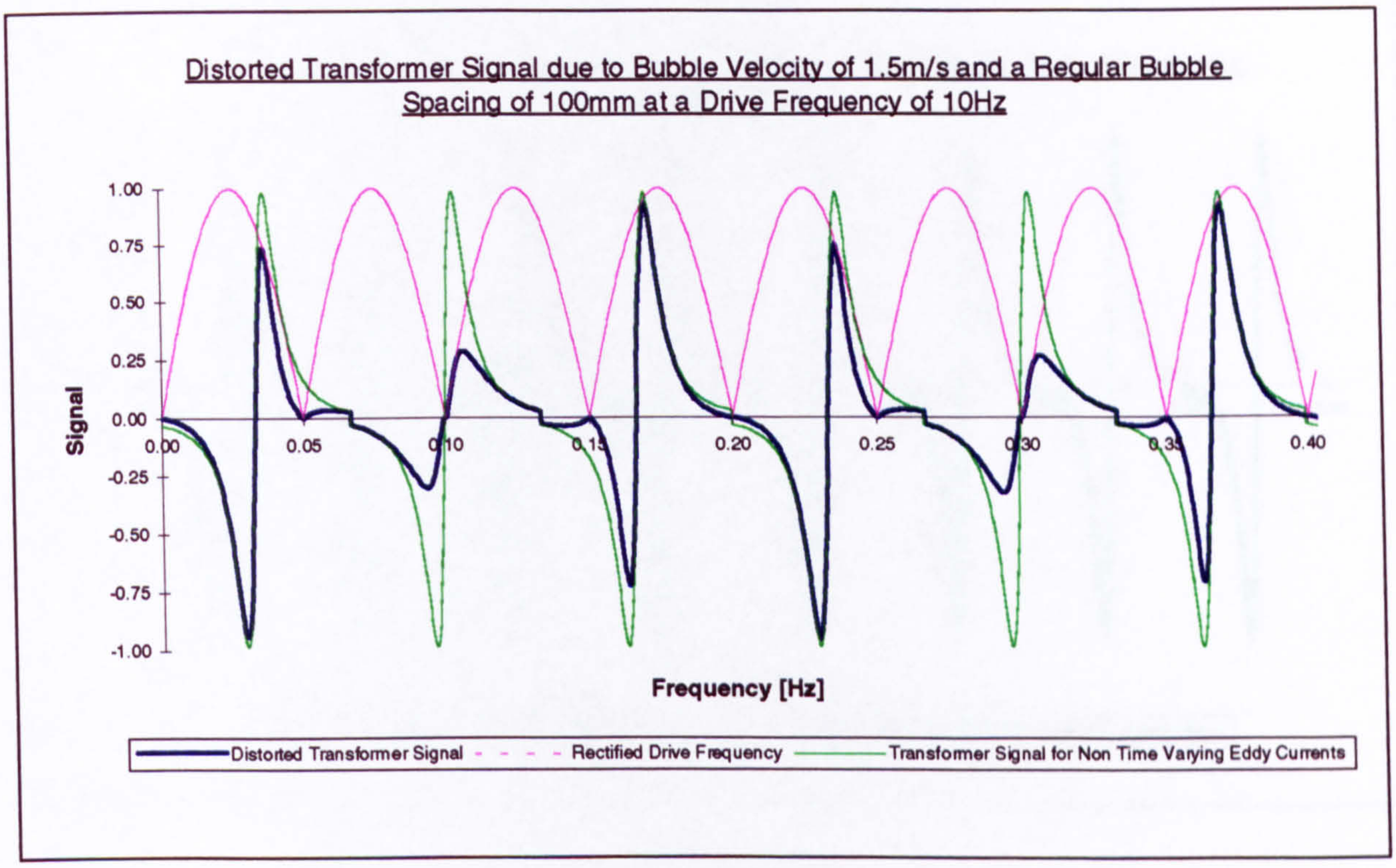

Figure 4.14

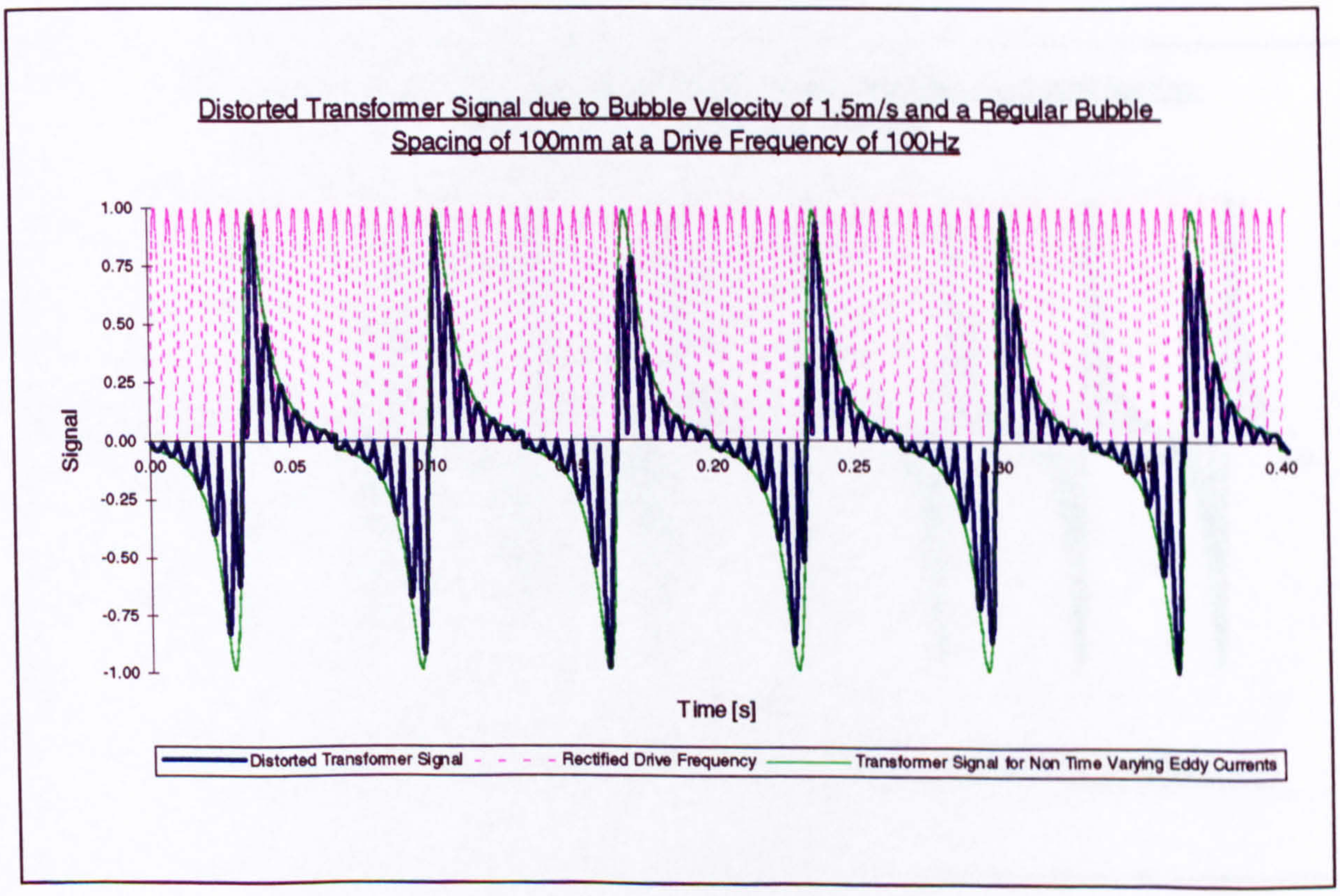

Figure 4.15

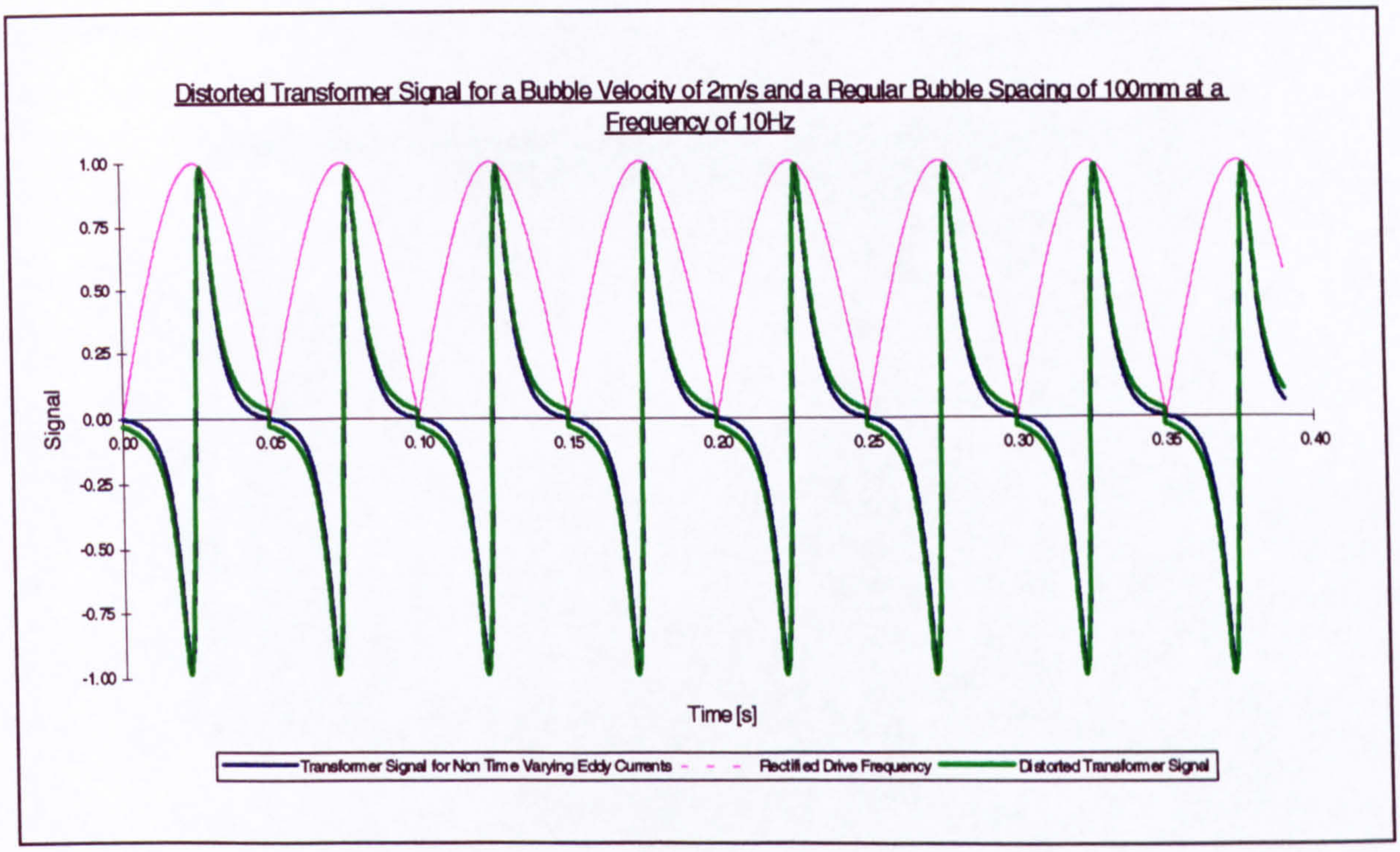

Figure 4.16

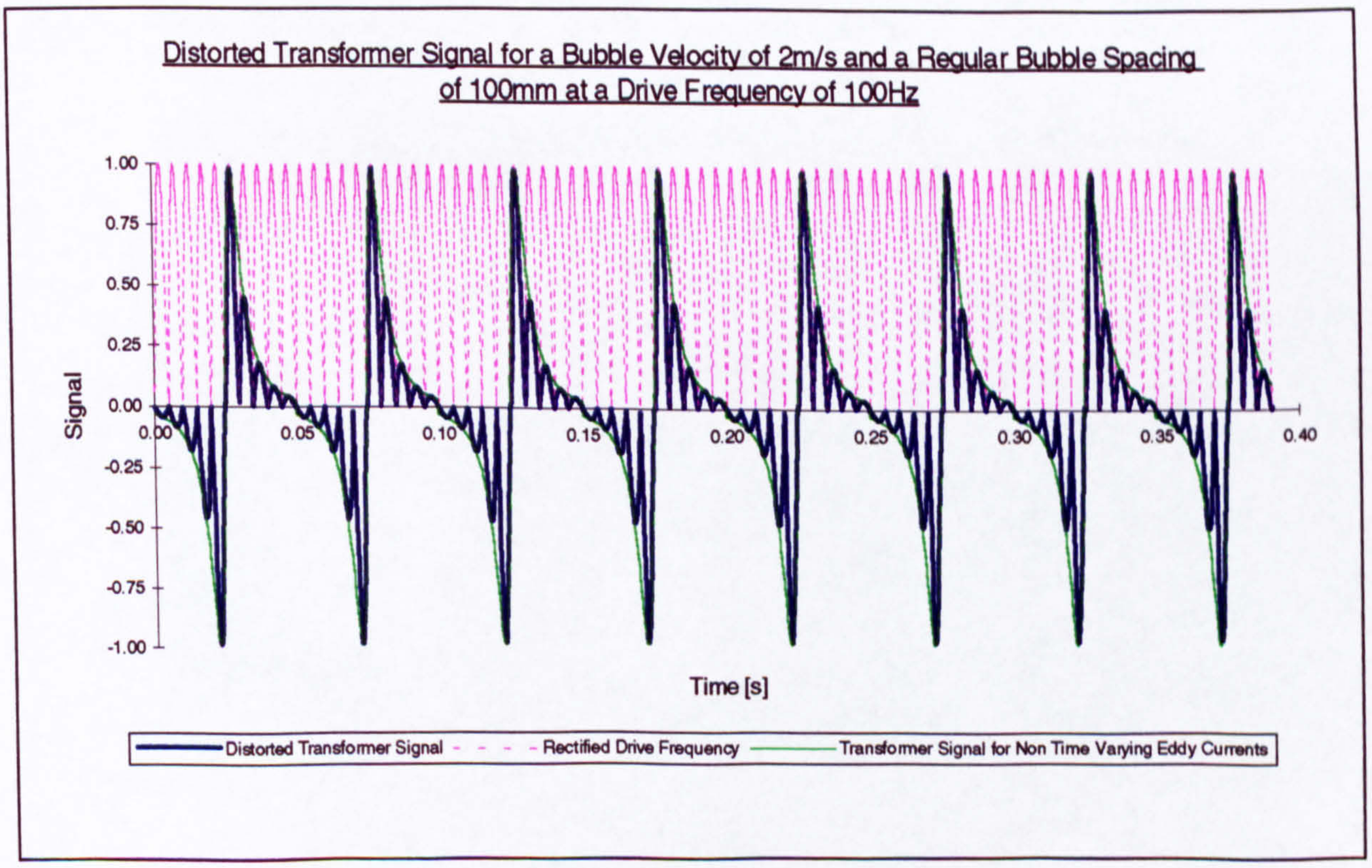

Figure 4.17

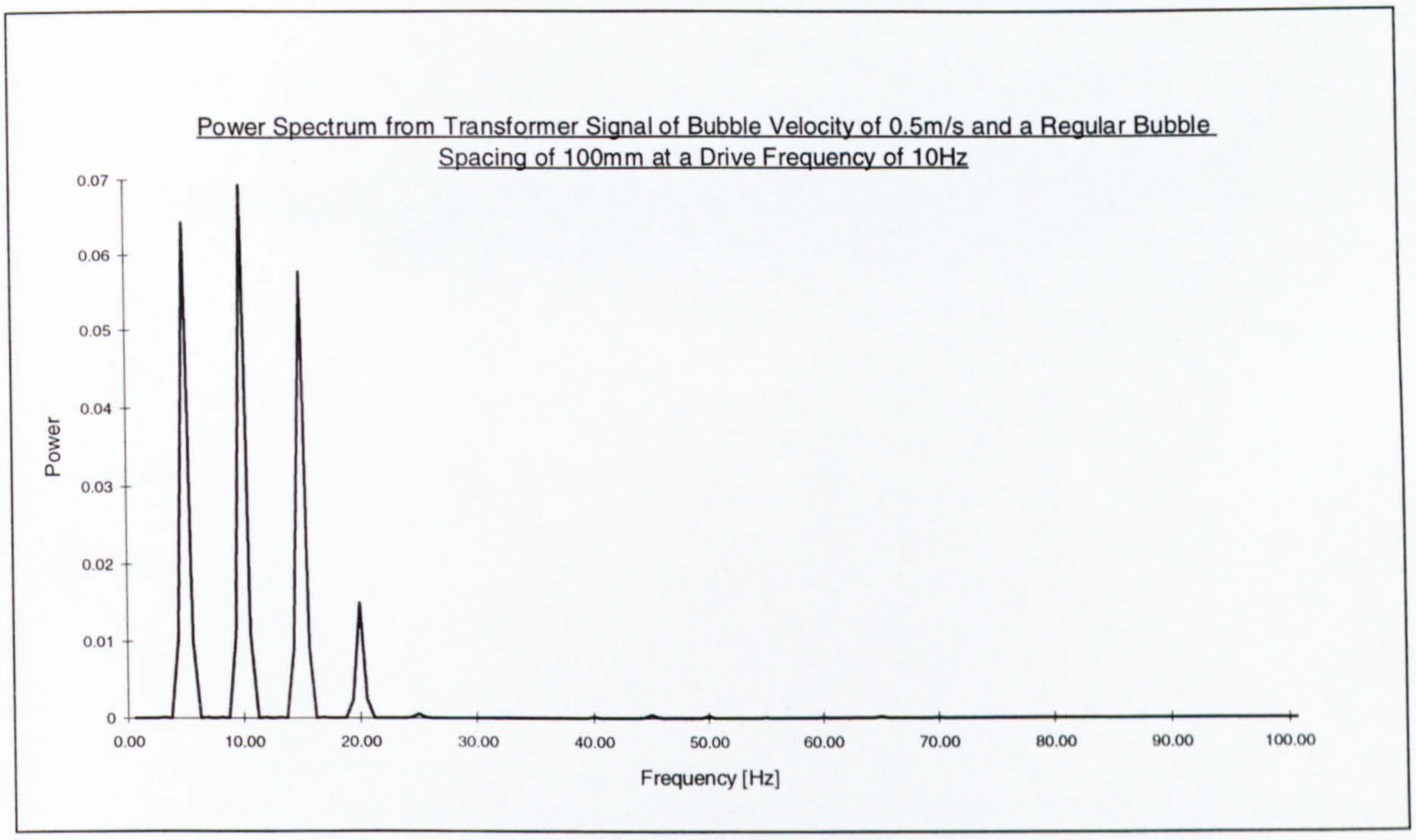

Figure 4.18

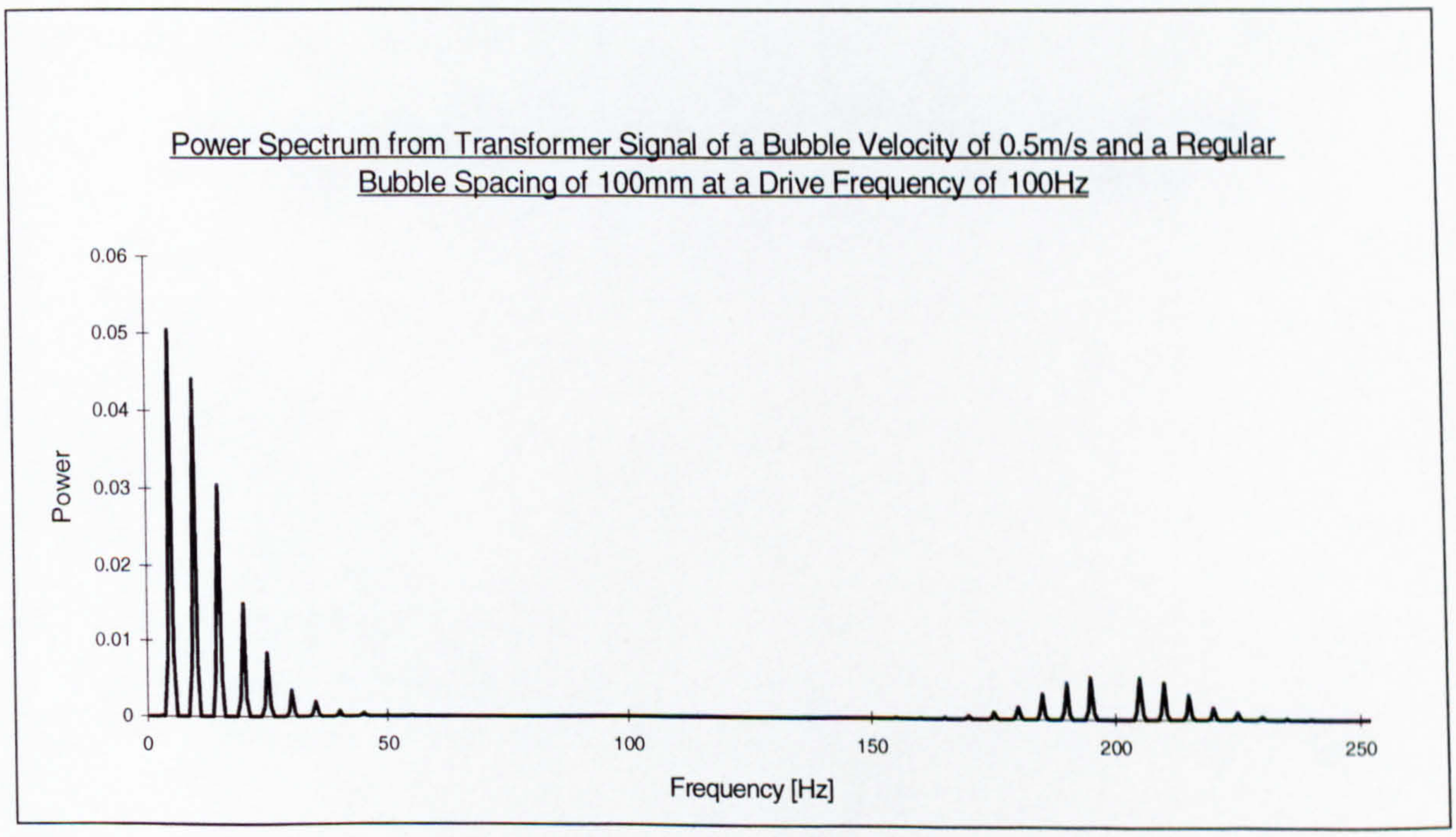

Figure 4.19

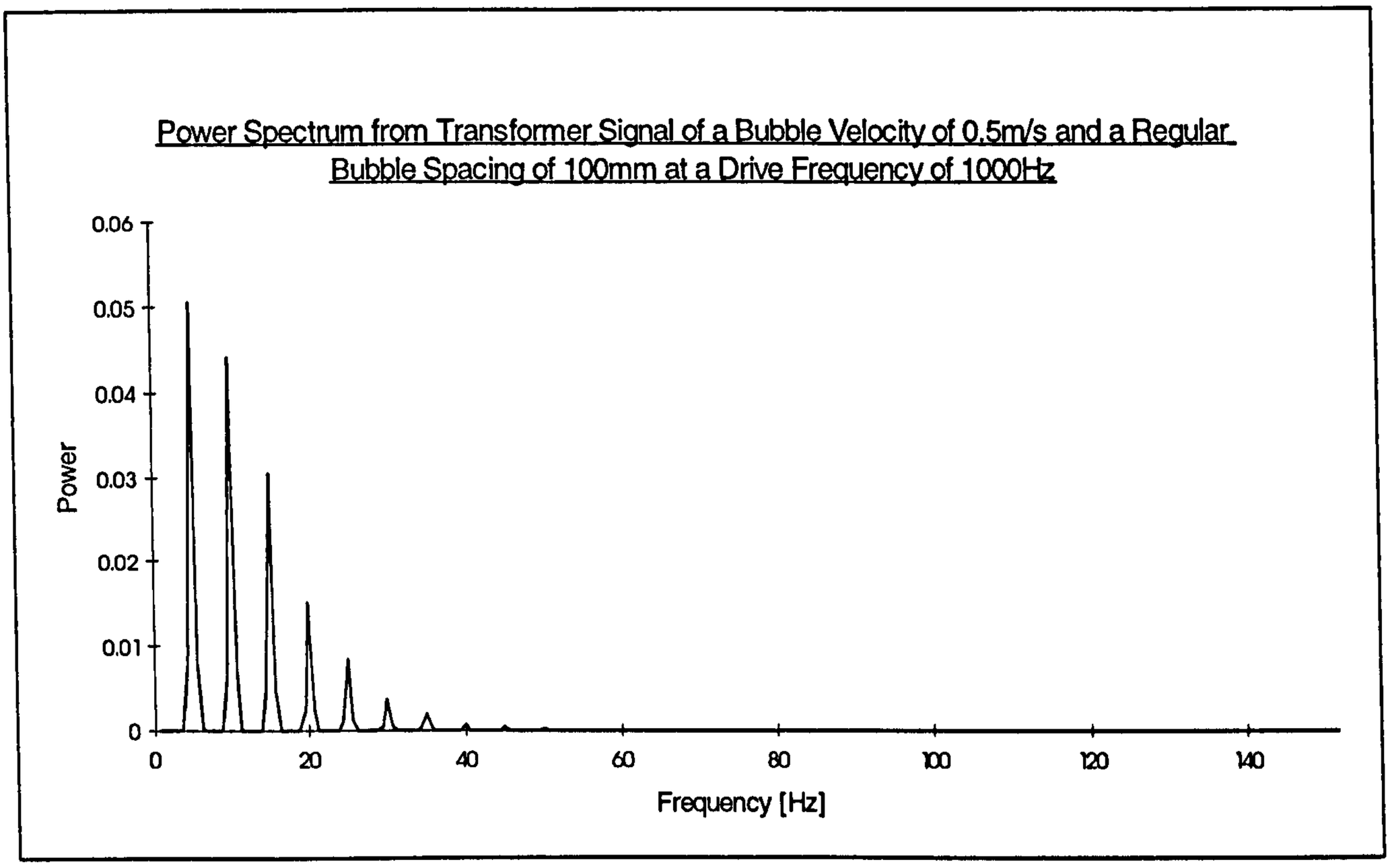

Figure 4.20

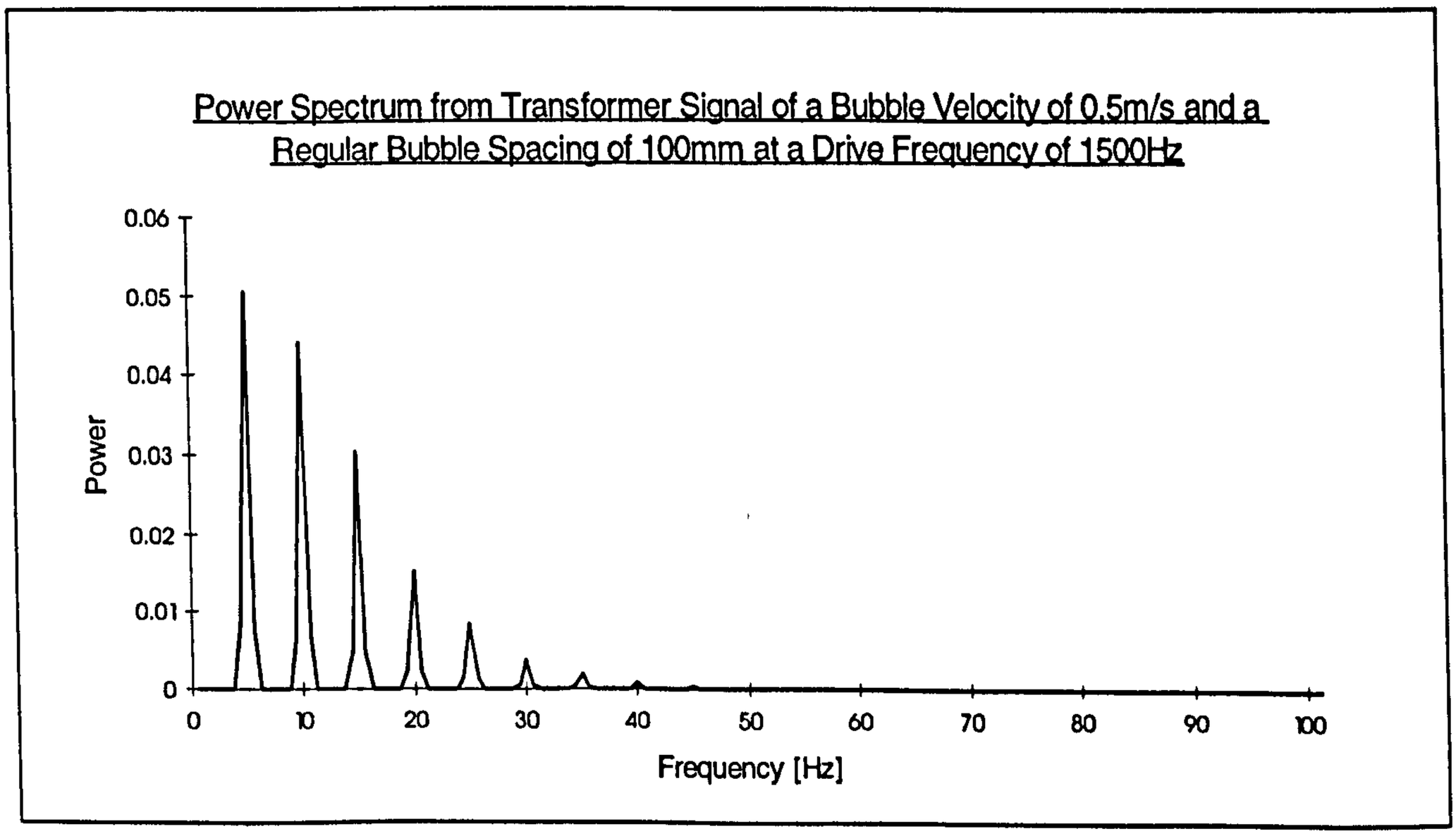

Figure 4.21

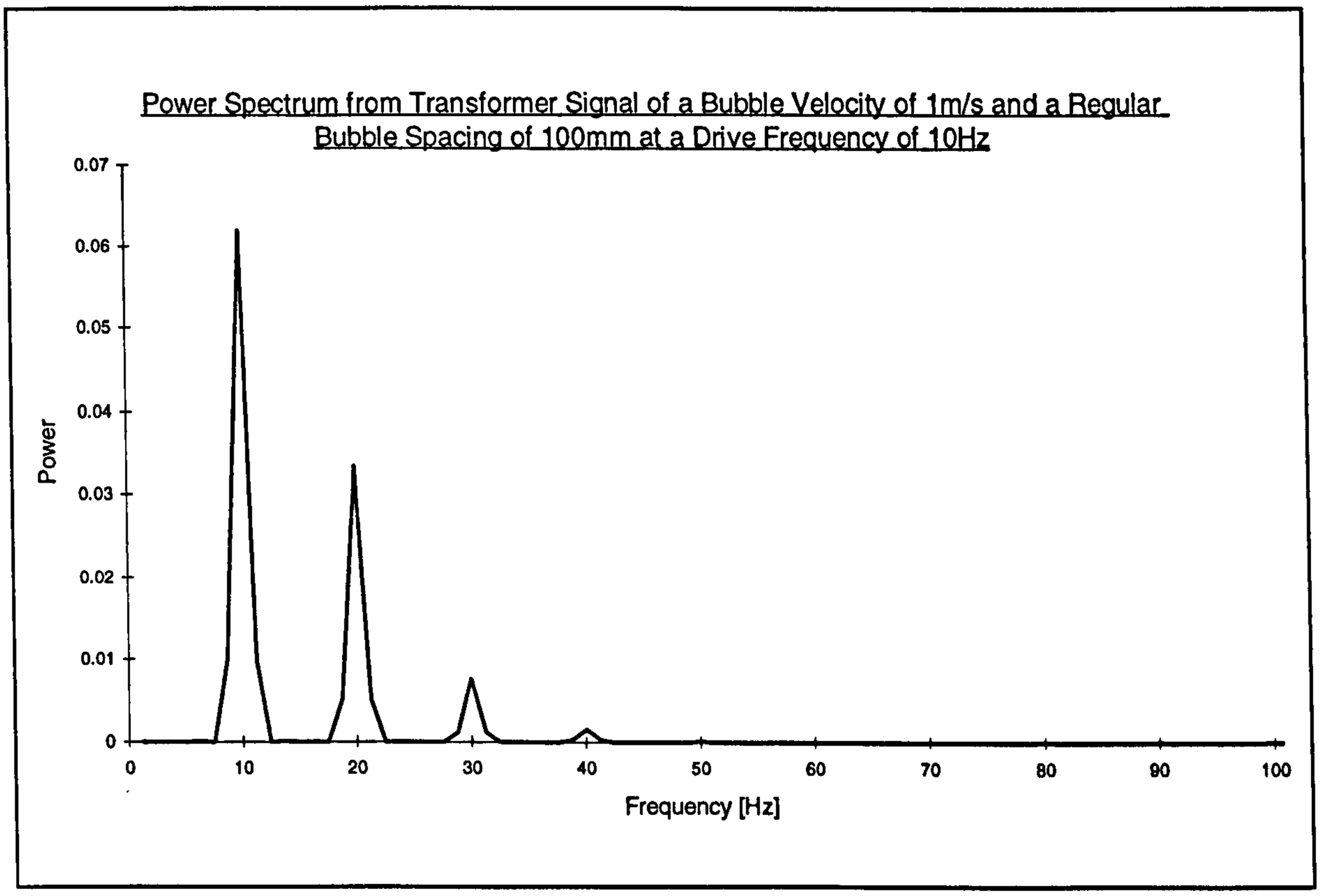

Figure 4.22

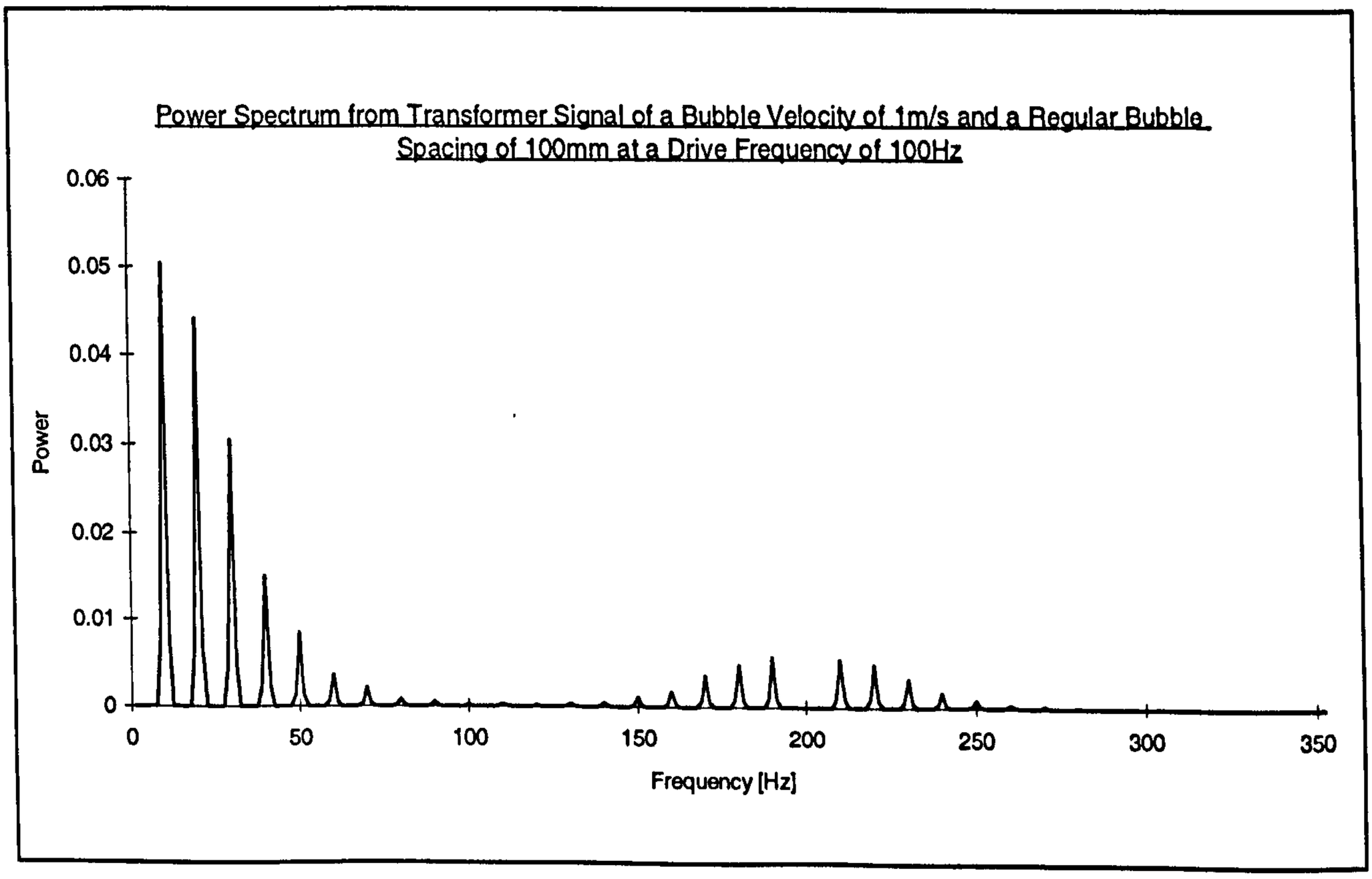

Figure 4.23

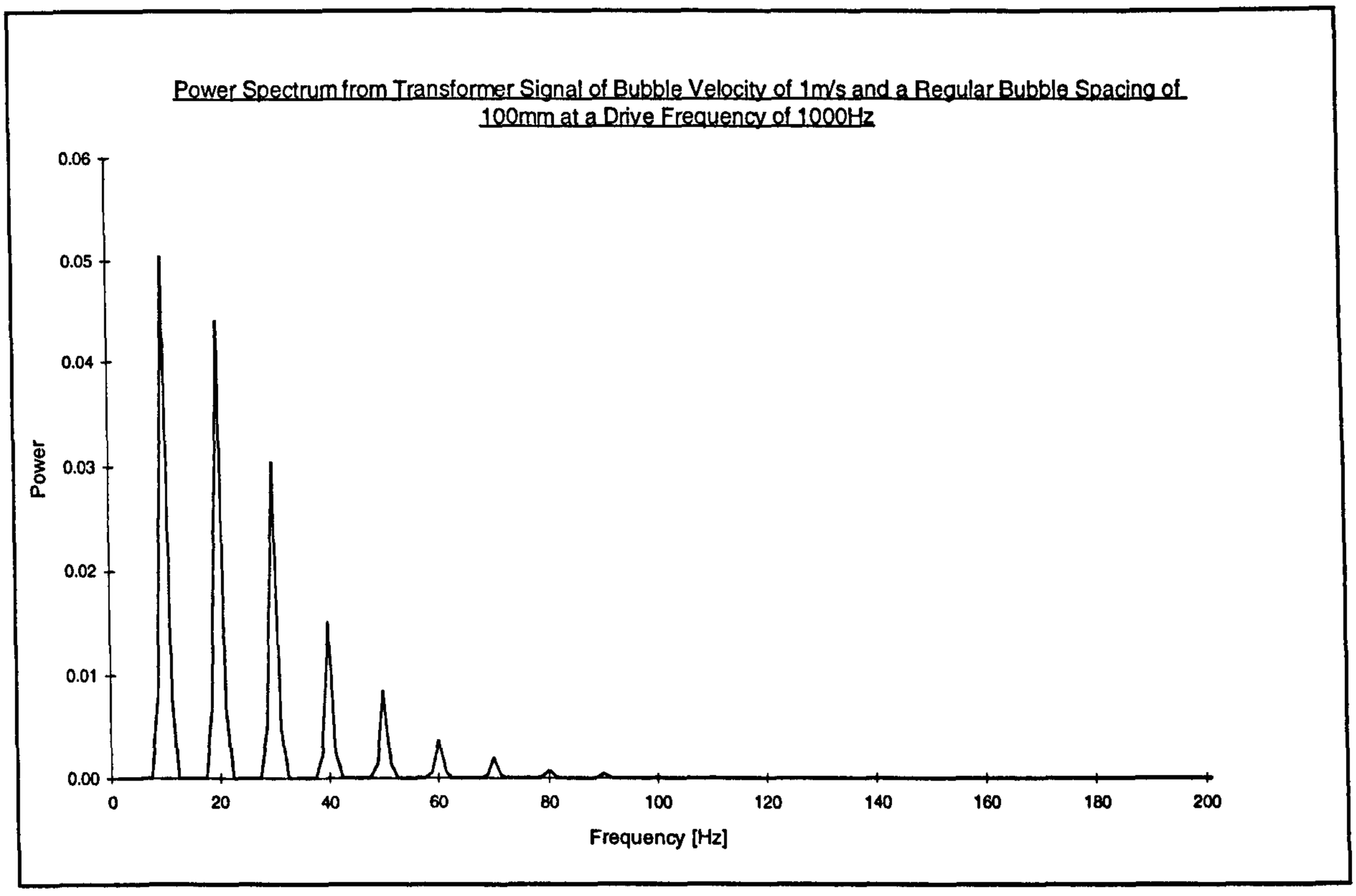

Figure 4.24

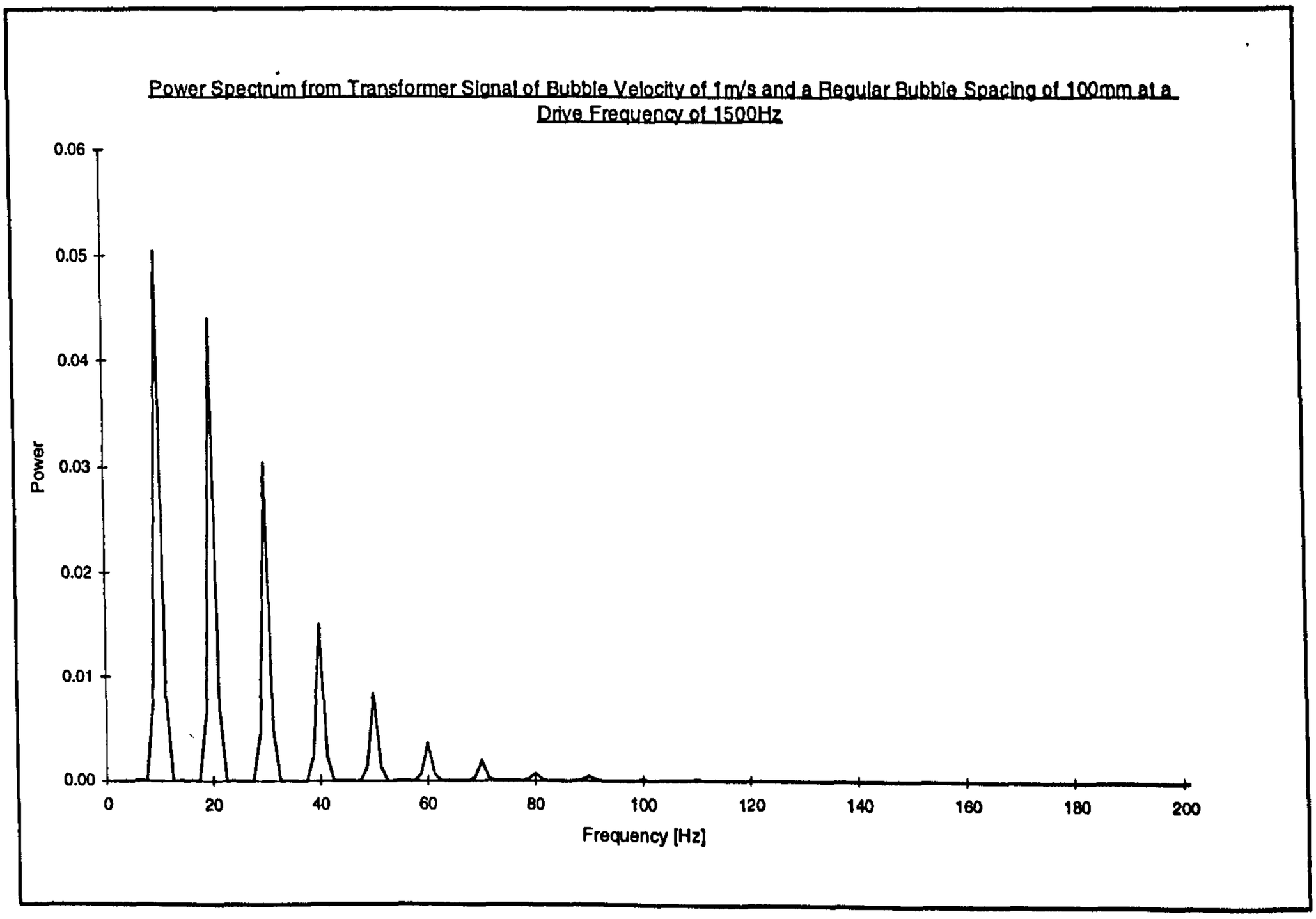

Figure 4.25

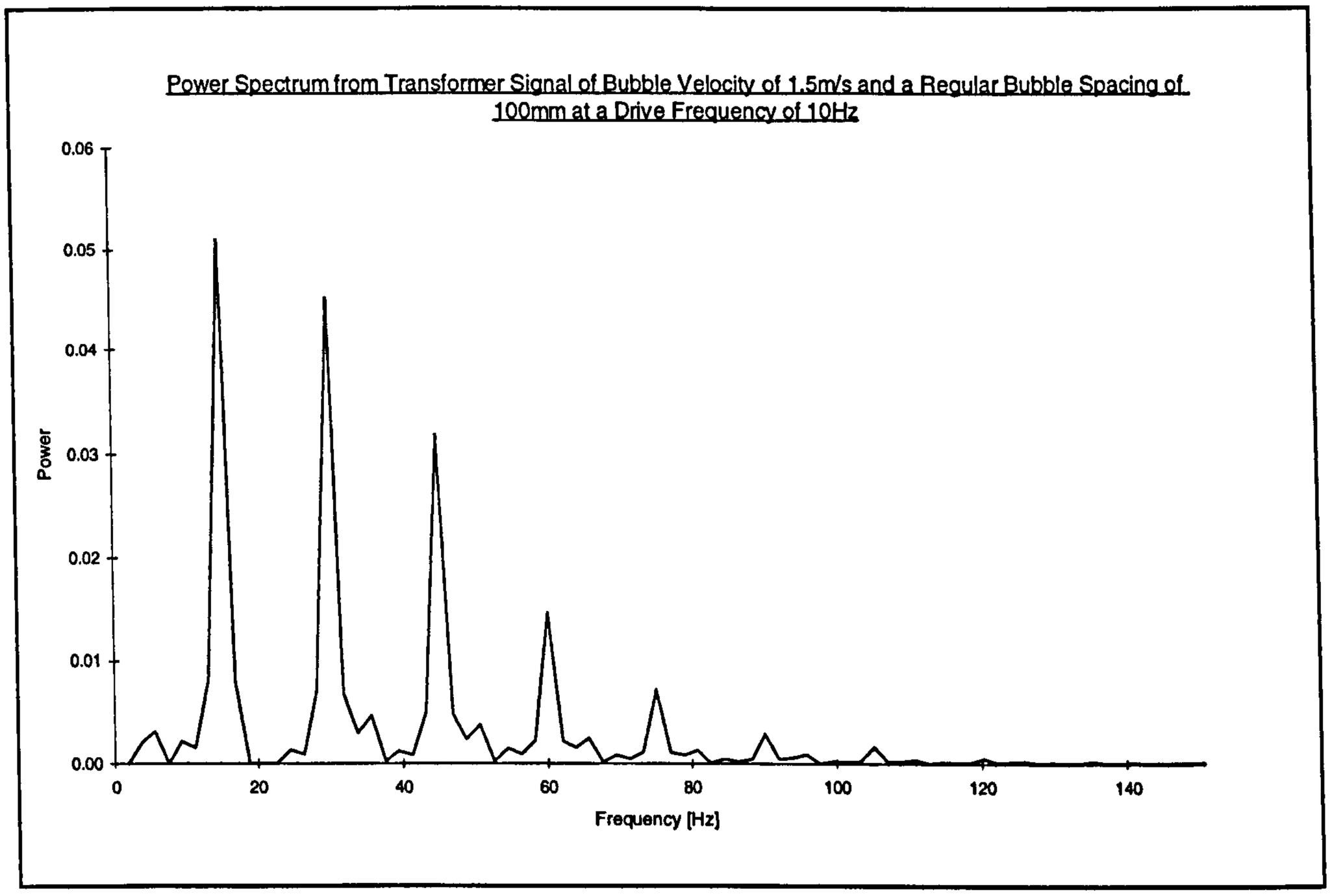

Figure 4.26

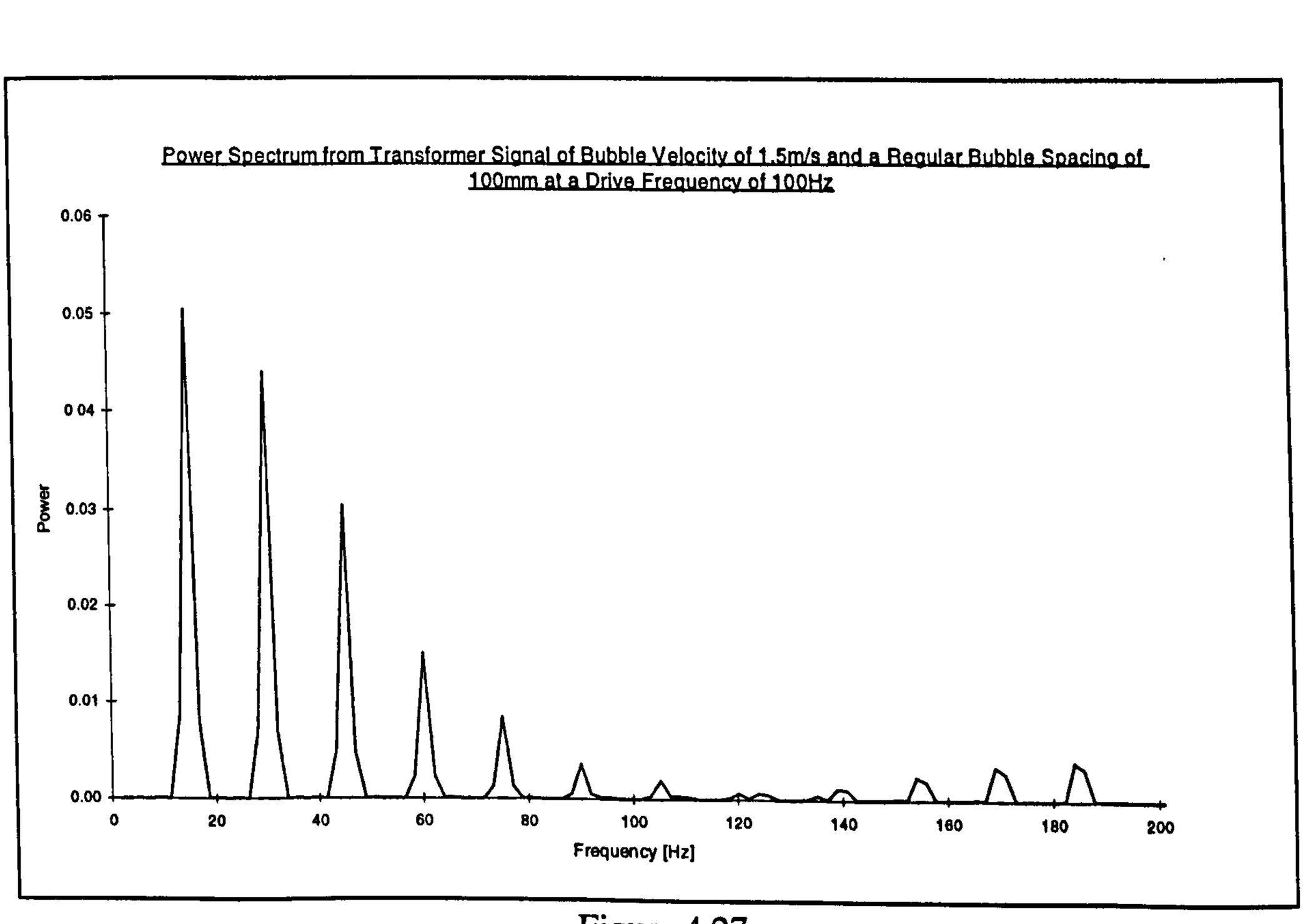

Figure 4.27

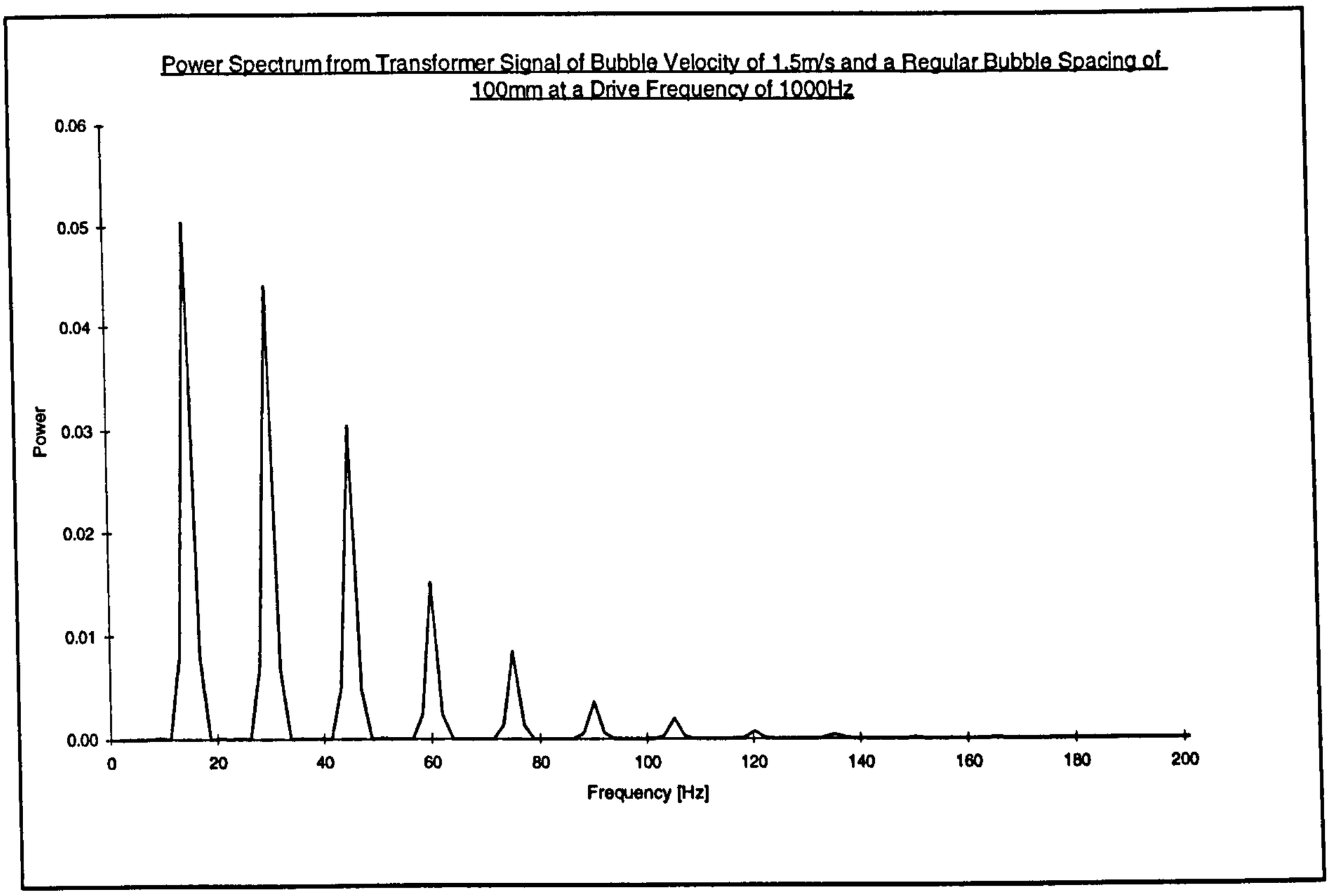

Figure 4.28

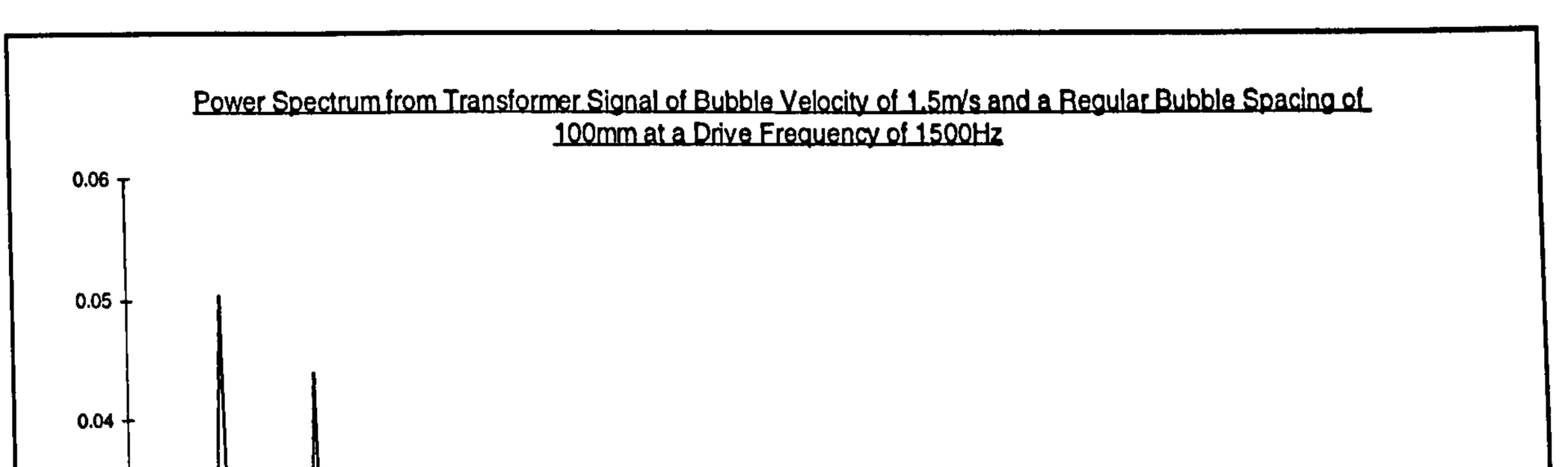

Figure 4.29

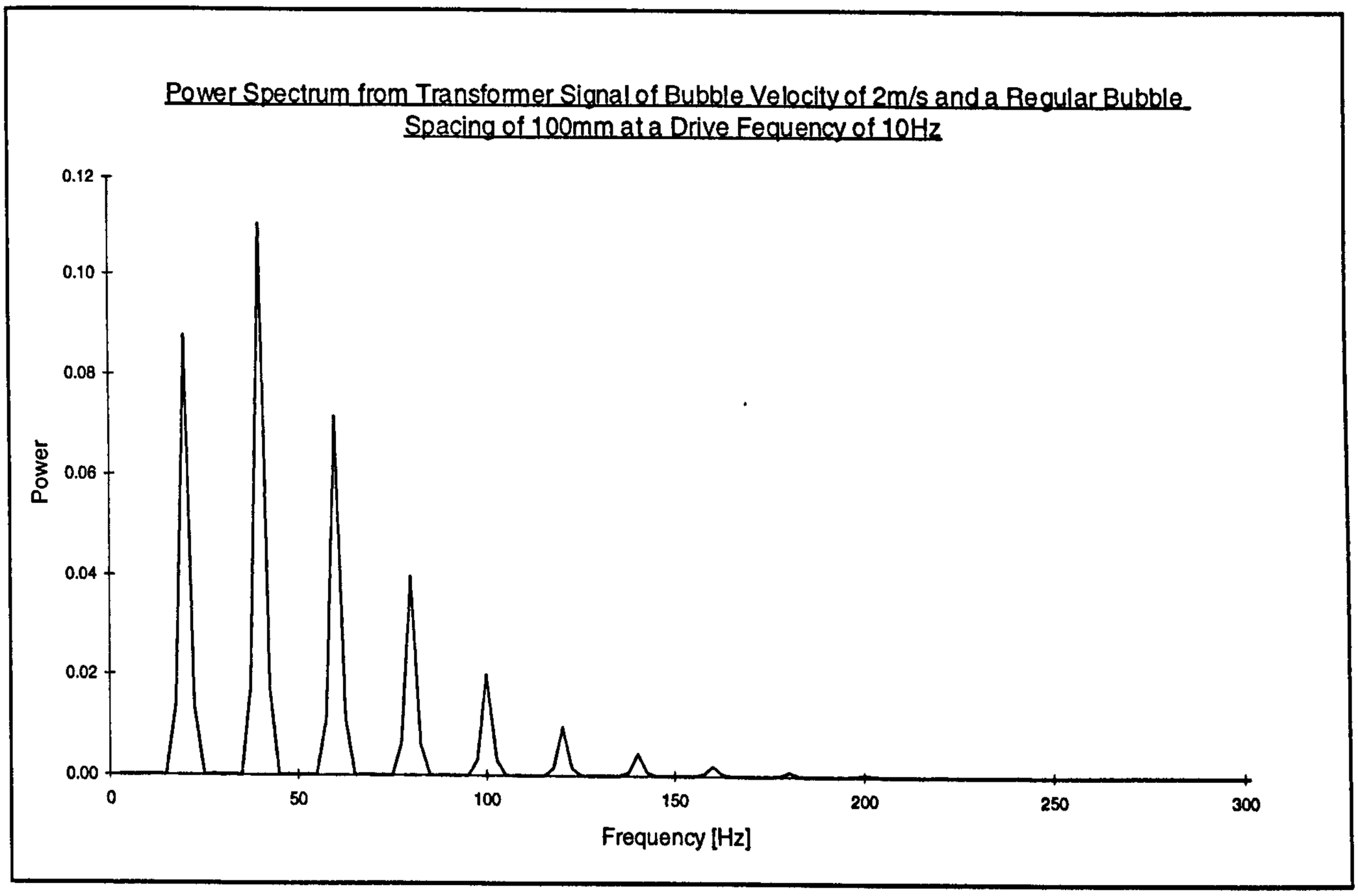

Figure 4.30

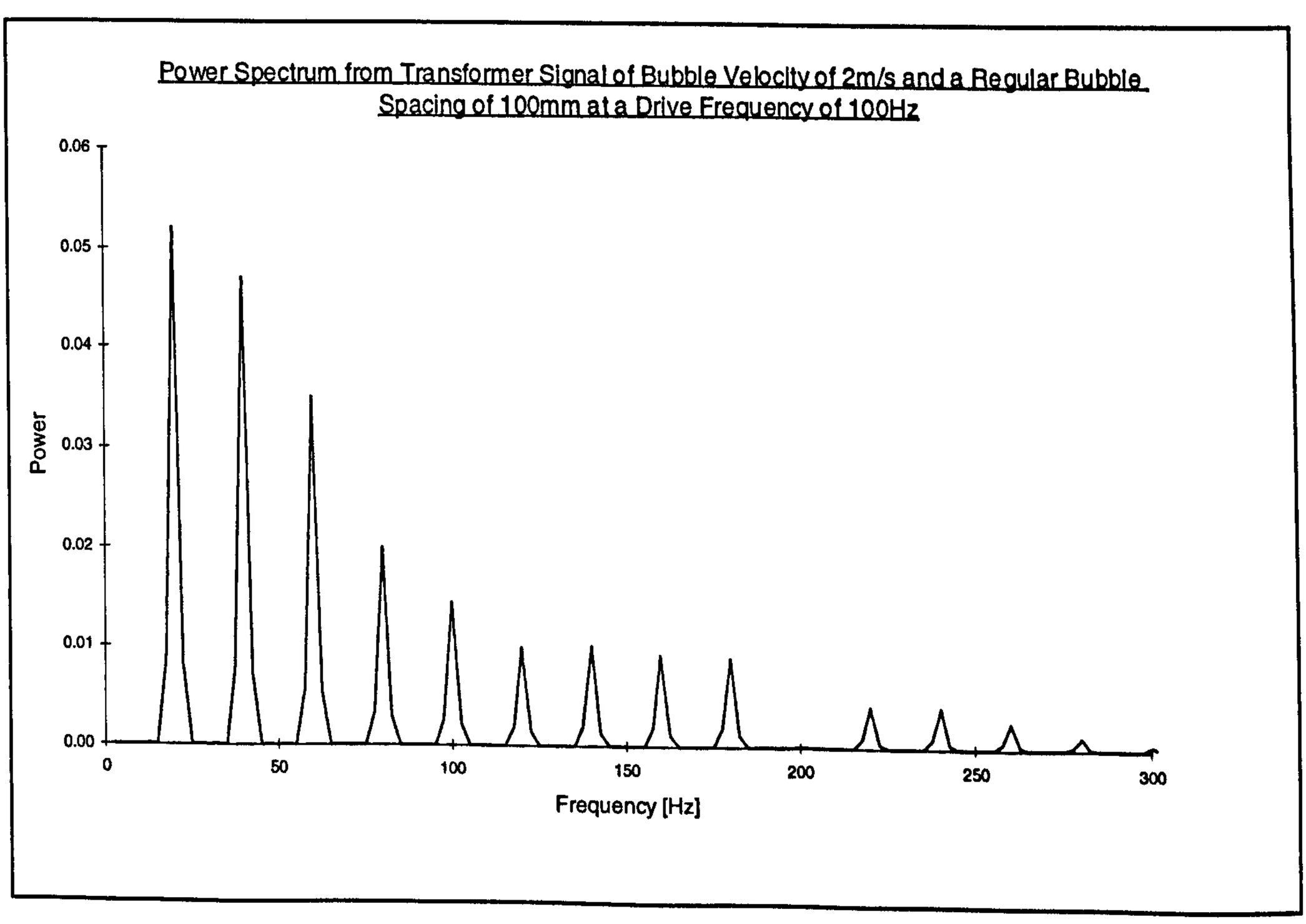

Figure 4.31

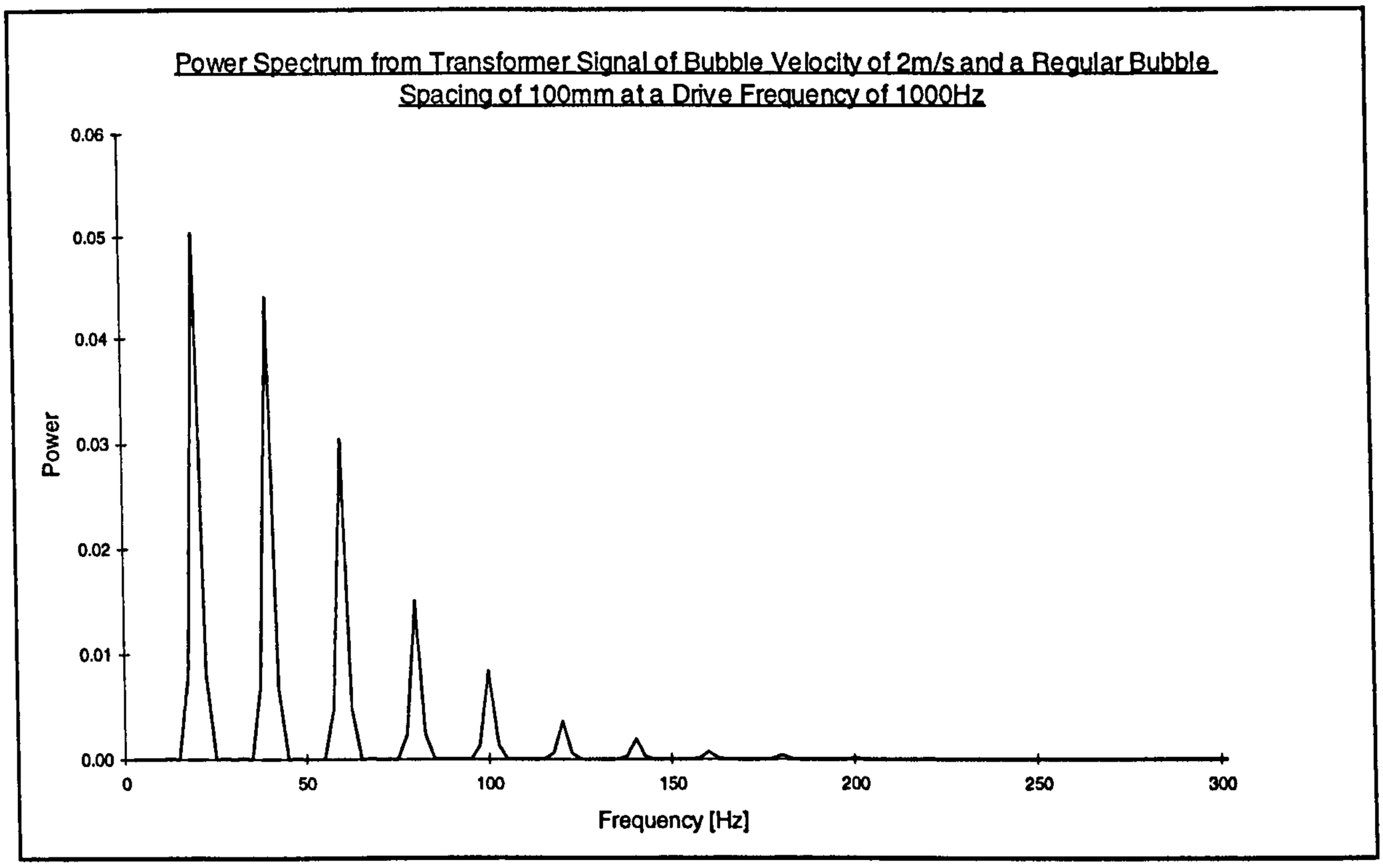

Figure 4.32

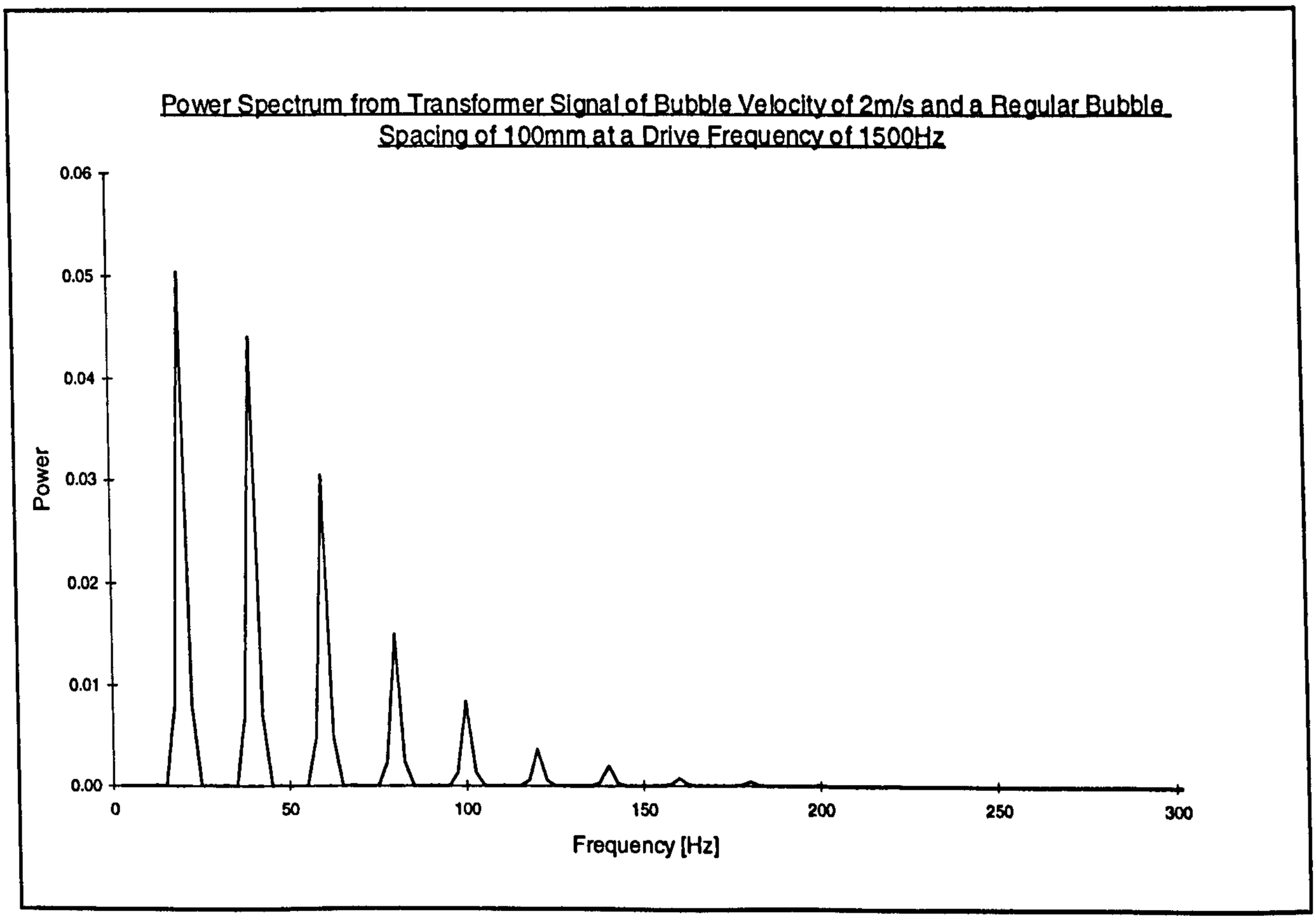

Figure 4.32

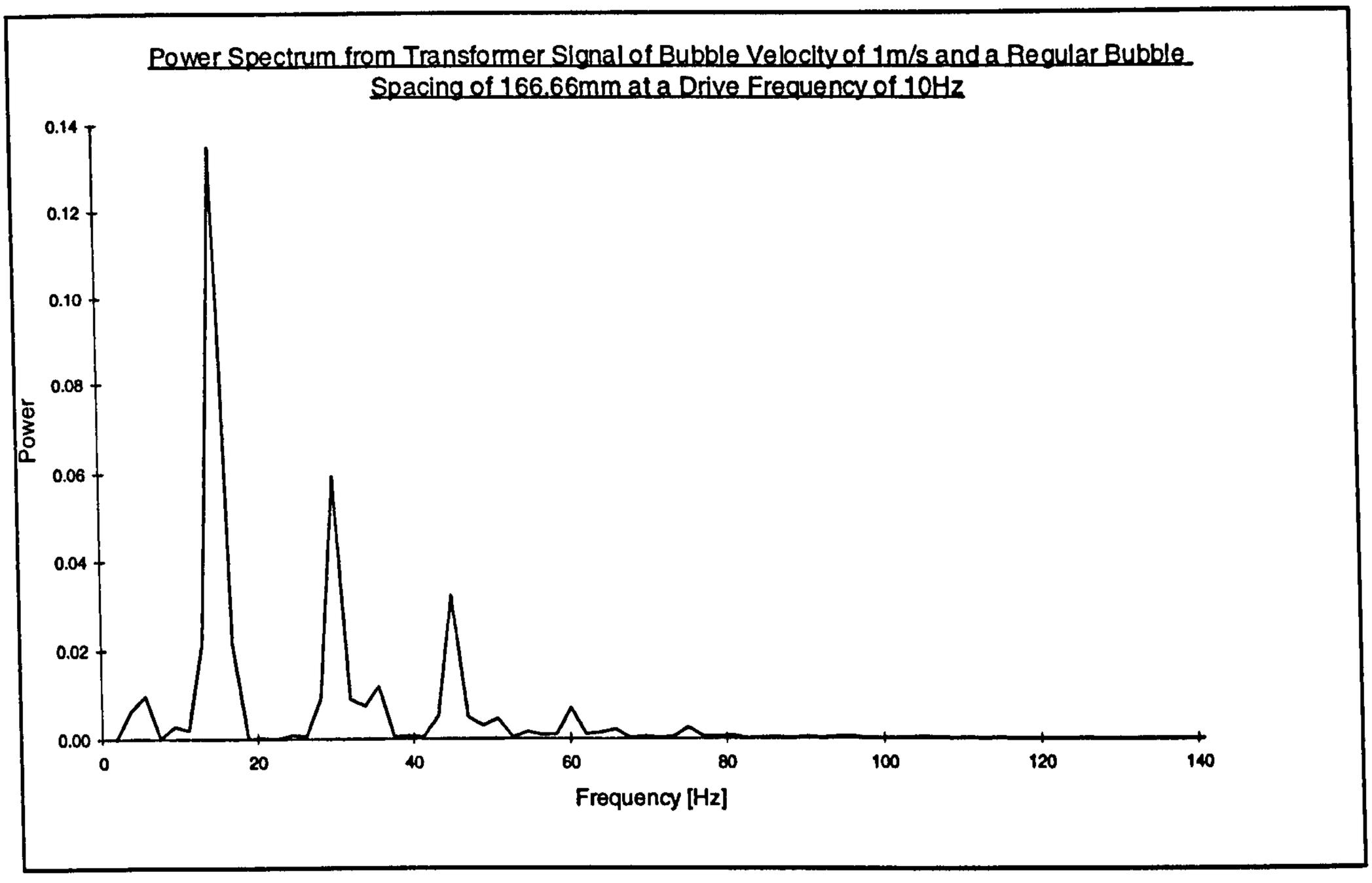

Figure 4.33

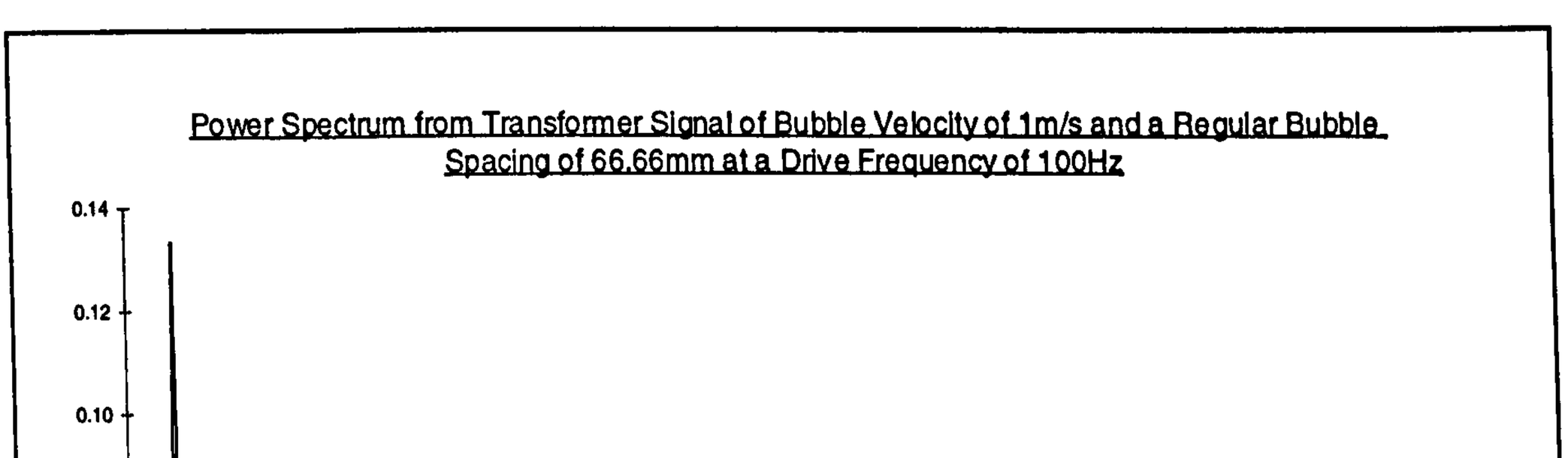

Figure 4.34

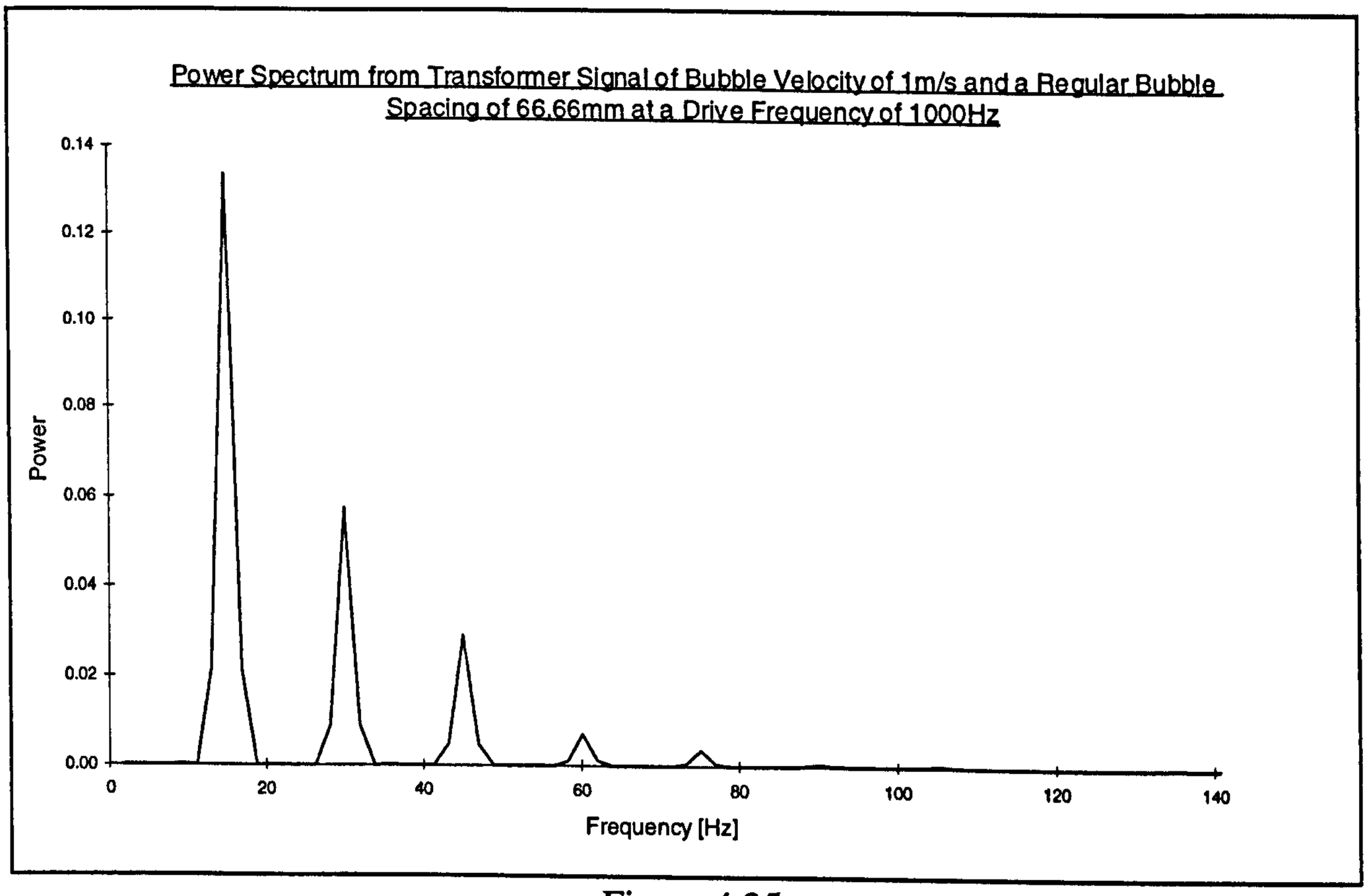

Figure 4.35

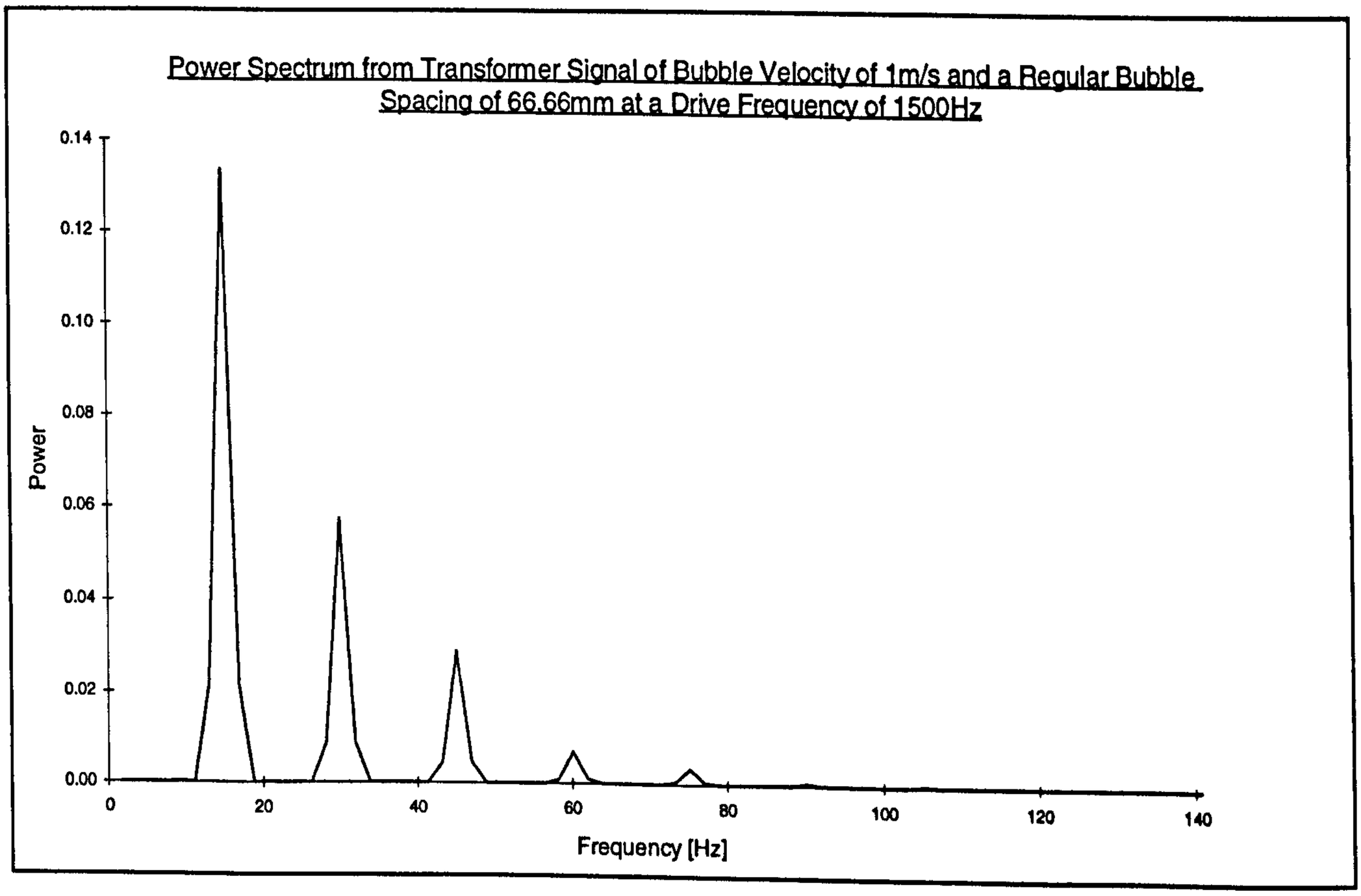

Figure 4.36

4.6 Summary

In summary this chapter dealt with the frequency analysis of the transformer signal. It showed that from the frequency information of the transformer signal a correlation with the bubble velocity could be obtained. A linear relation between peak frequency of the signal and bubble velocity is found.

A further examination showed that the power spectra does not change significantly for distorted transformer signals due to time varying eddy currents.

CHAPTER 5

PREDICTION OF FLOW SIGNAL DUE TO A BUBBLE PASSING THROUGH THE METER

5.1 Introduction

This chapter shows the effect on the flow signal due to a bubble that is moving through the dielectric liquid electromagnetic flowmeter. When a bubble travels through a liquid (whether the liquid is stationary or moves with a different velocity than the bubble) it creates liquid flow around the bubble. This effect is shown in Figure 5.1. This flow of the liquid could affect the flow signal. The following model predicts the order of magnitude of the flow signal in the meter.

Liquid flow around a bubble

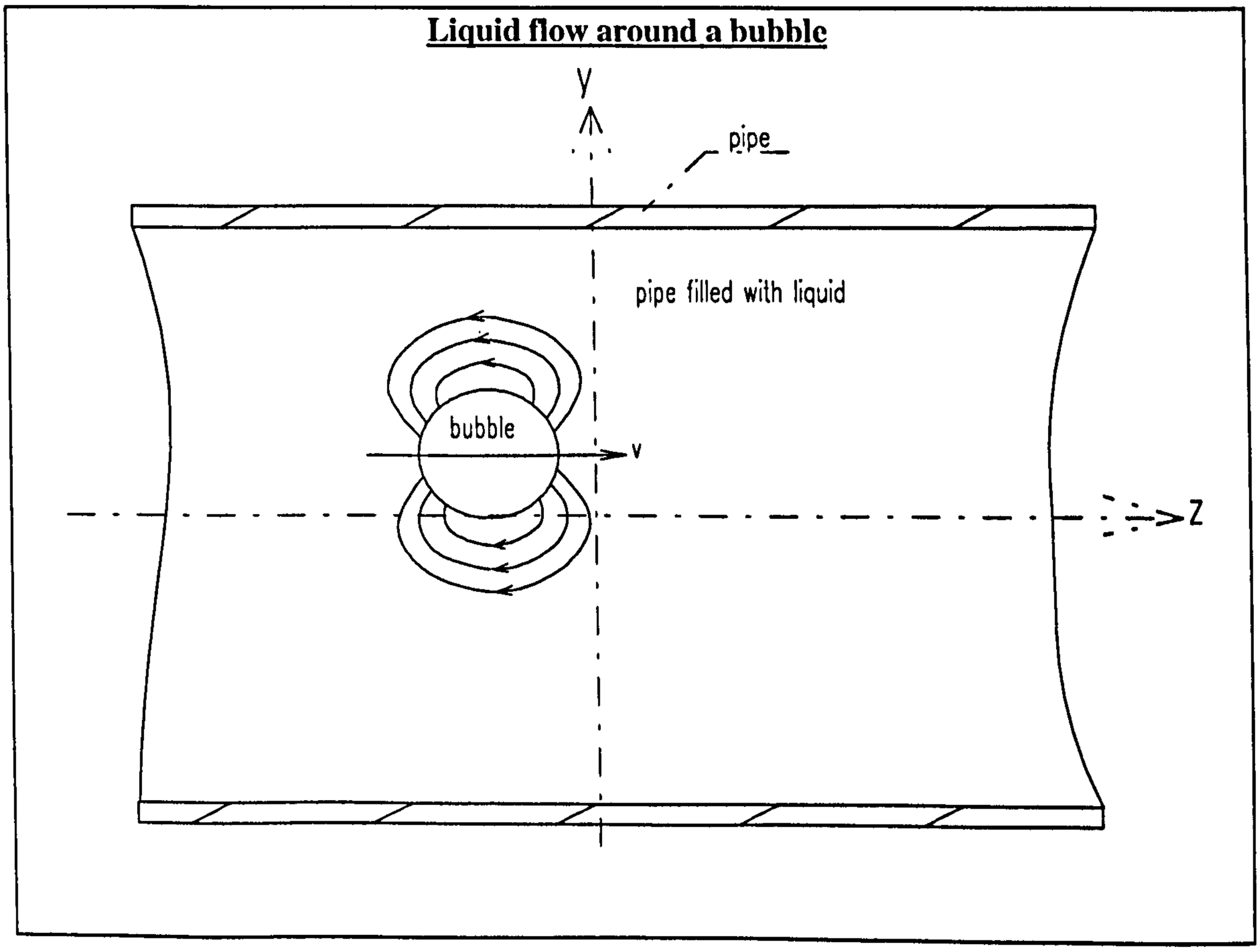

Figure 5.1

5.2 Development of model

The following sections derive a model which predicts an order of magnitude of the flow signal due to a bubble passing through the dielectric fluid electromagnetic meter.

5.2.1 Governing equations

The condition for a dielectric fluid is that conduction currents are much smaller than displacement currents. The mathematical expression for this is given in equation 5.1.

$$\sigma E \ll i\omega\varepsilon E \tag{5.1}$$

Maxwell's equations for $\vec{E}$ and $\vec{D}$ in a single fluid due to the external magnetic field $\vec{B}$ and the velocity $\vec{v}$ are

$$\nabla \cdot \vec{D} = 0 \tag{5.2}$$

$$\nabla \times \vec{E} = -\dot{\vec{B}} \tag{5.3}$$

$$\vec{D} = \varepsilon\vec{E} + K\left(\vec{v} \times \vec{B}\right) \qquad \left(K = \varepsilon - \varepsilon_0\right) \tag{5.4}$$

These equations contain two source terms $-\dot{\vec{B}}$ and $K\left(\vec{v} \times \vec{B}\right)$. Without those terms $\vec{D}$ and $\vec{E}$ would be equal to zero. The source term $-\dot{\vec{B}}$ leads to the $\vec{E}$ and $\vec{D}$ fields associated with the transformer signal. The source term $K\left(\vec{v} \times \vec{B}\right)$ leads to the flow signal. The boundary conditions for Maxwell's equations at the bubble surface are

$\vec{E}_t$ is continuous (5.5)

$\vec{D}_n$ is continuous (5.6)

Because the flow signal was considered in this section the source term $-\dot{\vec{B}}$ in equation (5.3) was left out.

$$\therefore \qquad \nabla \times \vec{E} = 0 \qquad \text{and} \qquad \vec{E} = -\nabla\phi \tag{5.7}$$

From equation (5.2) and (5.4) it was found that

$$\nabla \cdot \vec{D} = \varepsilon \, \nabla \cdot \vec{E} + K\nabla \cdot \left(\vec{v} \times \vec{B}\right) = 0 \tag{5.8}$$

$$\therefore \qquad \nabla^2\phi = -\frac{K}{\varepsilon}\nabla \cdot \left(\vec{v} \times \vec{B}\right)$$

Applying vector identity the following expression was produced

$$\nabla \cdot \left(\vec{v} \times \vec{B}\right) = \vec{B} \cdot \nabla \times \vec{v} - \vec{v} \cdot \nabla \times \vec{B}$$

Since $\nabla \times \vec{B} = 0$ (for any field $\vec{B}$), a form for equation (5.8) is

$$\nabla^2\phi = -\frac{K}{\varepsilon}\vec{B} \cdot \nabla \times \vec{v} \tag{5.9}$$

For the fact that inside the bubble (gas) the relative permitivity is 1 ($\varepsilon = \varepsilon_0$), therefore K=0. Hence inside the bubble equation (5.9) became

$$\nabla^2\phi = 0 \tag{5.10}$$

Considering the area in moving liquid and assuming potential flow the second term in equation (5.9) becomes zero ($\nabla \times \vec{v} = 0$). Therefore in the fluid equation (5.9) became

$$\nabla^2\phi = 0 \tag{5.11}$$

The boundary conditions on the bubble surface are as follows

$$\phi \text{ is continuous} \tag{5.12}$$

$$-\varepsilon_b \left.\frac{\partial\phi}{\partial r}\right|_{r=d_-} = -\varepsilon_1 \left.\frac{\partial\phi}{\partial r}\right|_{r=d_+} + K\left(\vec{v}\times\vec{B}\right)_r \quad \left(K = \varepsilon_b - \varepsilon_0\right) \tag{5.13}$$

where ε_b is assumed equal to ε_0.

5.3 Solution of governing equations

After deriving a way in order to evaluate the flow signal due to a bubble passing through the meter, the established equations in the above section where solved in the following part.

5.3.1 Evaluation of vector product

In order to find an expression for the potential, equations (5.10), (5.12) and (5.13) had to be solved. The first step was to evaluate the term $\left(\vec{v}\times\vec{B}\right)_r$ in equation (5.13). The expressions for the radial and angular components of fluid velocity around a stationary sphere and moving liquid are as follows

$$v_r = v_\infty\left[1-\left(\frac{d}{r}\right)^3\right]\cos\theta \tag{5.14}$$

$$v_\theta = -v_\infty \sin\theta\left[1+\frac{1}{2}\left(\frac{d}{r}\right)^3\right] \tag{5.15}$$

For the case of a moving bubble (see Fig. 5.2) in a stationary fluid the above equations would be invalid, because the liquid flow around the bubble would not become equal to zero far away from the bubble. In order to make equation (5.14) and (5.15) valid the terms $-\vec{v}_\infty \cos\theta$ and $\vec{v}_\infty \sin\theta$ had to be added respectively (i.e. $-\vec{v}_\infty$ is added to all particles of the system). Hence the final equations for the fluid velocity around the moving bubble became

$$v_r = v_\infty \cos\theta\left(\frac{d}{r}\right)^3 \tag{5.16}$$

$$v_\theta = -v_\infty \sin\theta\frac{1}{2}\left(\frac{d}{r}\right)^3 \tag{5.17}$$

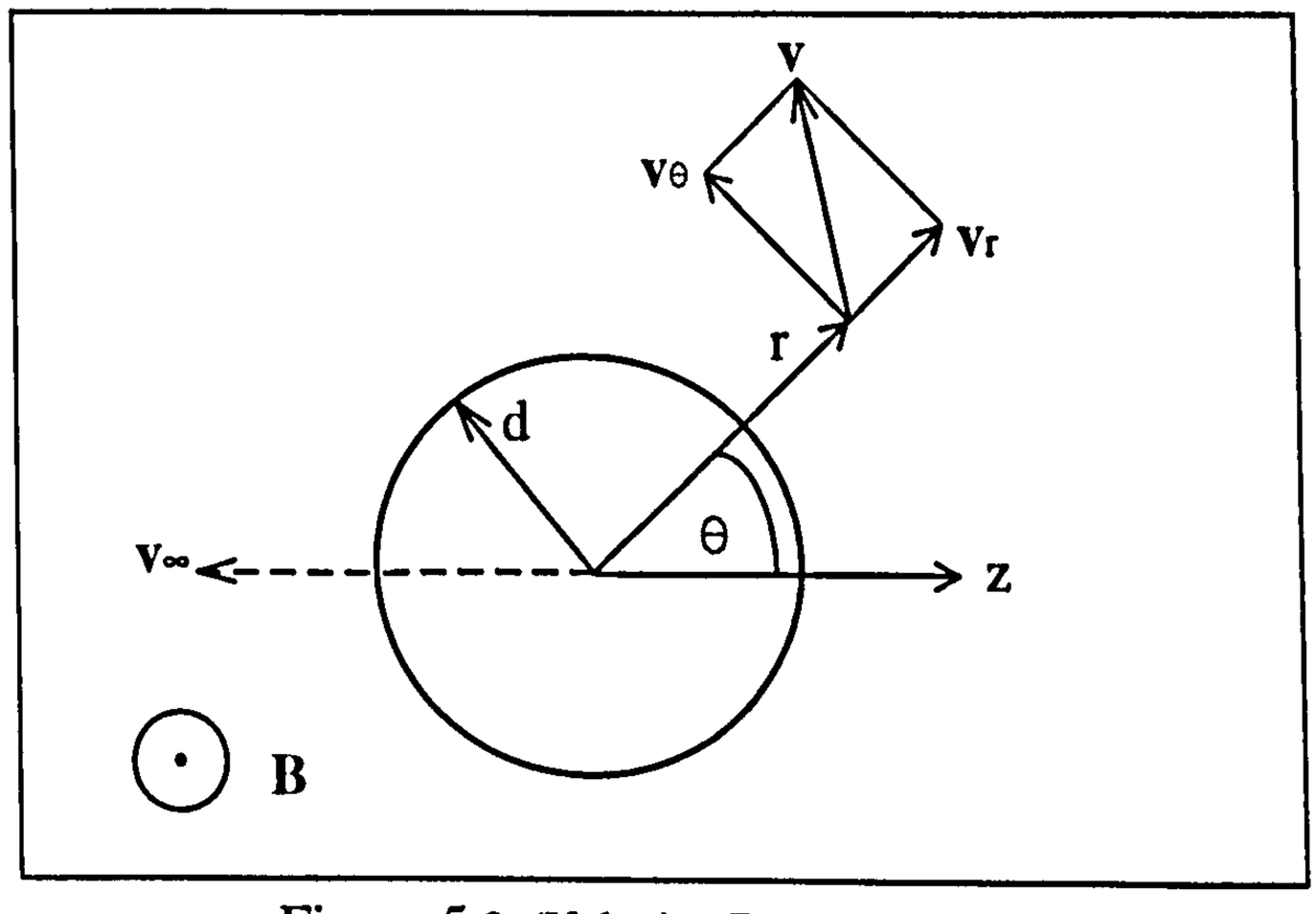

Figure 5.2 (Velocity Components)

Now the vector product was solved as follows

$$\left(\vec{v}\times\vec{B}\right)_x=\begin{vmatrix} i & j & k \\ v_x & v_y & v_z \\ B_x & B_y & B_z \end{vmatrix}=v_yB_z-v_zB_y \tag{5.18}$$

This result was transformed into spherical co-ordinates and became

$$\left(\vec{v}\times\vec{B}\right)_r=v_\theta B_\phi-v_\phi B_\theta \tag{5.19}$$

For the fact that $v_\phi=0$ and $B_\phi=-B\sin\phi$ the final expression was

$$(v\times B)_r\big|_{r=d}=v_\infty\sin\theta\cdot 0.5B\sin\phi \tag{5.20}$$

5.3.2 Solution of Laplace's equation

An expression for the potential was derived. Using the general solution of Laplace's equation which was previously provided in chapter 2, solutions for the potential distribution inside and outside the bubble were found similar to the solutions in chapter 2. The potential distribution inside the bubble with the correct symmetry and correct behaviour at $r\to 0$ and $r\to\infty$ became

$$\phi_1=\sum_{n,m}A_{n,m}r^nP_n^m(\mu)\sin m\phi \tag{5.21}$$

and outside the bubble

$$\phi_2=\sum_{n,m}B_{n,m}r^{-n-1}P_n^m(\mu)\sin m\phi \tag{5.22}$$

where n=0,1,2,... and m=1,2,3,....

5.3.2.1 Evaluation of constants

A simple observation of equation (5.13) shows that m has to be equal to 1, because for m=0 and m>0 the terms $\sin m\phi$ and $\sin\phi$ in equation (5.13) would not balance. For n it appeared that it also had to be equal to 1. A general expression for $P_n^m(\mu)$ is given in Abramowitz and Stegun (Page 334 Nr. 8.6.6) as

$$P_n^m(\mu)=(-1)^m\left(1-x^2\right)^{\frac{1}{2}m}\frac{d^m P_n(\mu)}{d\mu^m} \tag{5.23}$$

and $$P_1(\mu)=\mu=\cos\theta \tag{5.24}$$

$\therefore$ For n=1 $$P_1^1(\mu)=(-1)\left(1-(\cos\theta)^2\right)^{\frac{1}{2}} \quad \text{(because } \frac{d\ P_1(\mu)}{d\mu}=1\text{)} \tag{5.25}$$

$$=-\sin\theta$$

Therefore a balance between $P_1^1(\mu)=-\sin\theta$ and $\left(\vec{v}\times\vec{B}\right)_r \propto \sin\theta$ occurs. Using the boundary conditions in (5.12) and (5.13) gives a solution for the constants $A_{1,1}$ and $B_{1,1}$.

$$A_{1,1}=\frac{\frac{\varepsilon_1-\varepsilon_b}{\varepsilon_b}v_\infty\,\frac{1}{2}B}{\left(1+\frac{2\varepsilon_1}{\varepsilon_b}\right)} \tag{5.26}$$

$$B_{1,1}=\frac{\frac{\varepsilon_1-\varepsilon_b}{\varepsilon_b}v_\infty\,\frac{1}{2}B}{\left(\frac{1}{d^3}+\frac{2\varepsilon_1}{\varepsilon_b d^3}\right)} \tag{5.27}$$

and the potential is

$$\phi_1=-A_{1,1}r\sin\theta\sin\phi \qquad r<d \tag{5.27a}$$

$$\phi_2 = -B_{1,1}\frac{1}{r^2}\sin\theta\sin\phi \qquad r > d \tag{5.27b}$$

5.3.2.2 Resulting dipole strength

Because the potential outside the bubble is the same as it would be for a dipole source at the bubble centre the dipole moment was found by setting the general expression of the potential of a dipole moment (5.28) equal to the expression found for the potential outside a bubble (5.27b).

$$\phi_{dipole} = \frac{1}{4\pi\varepsilon_0}\frac{\vec{p}\cdot\vec{r}}{r^3} \tag{5.28}$$

Knowing from equation (5.18) that the dipole moment has to point in the negative y-direction (also illustrated in Figure 5.3) the dot product in equation (5.28) became

$$\vec{p}\cdot\vec{r} = (\vec{r})_y p = r\cdot\sin\theta\cdot\sin\phi\cdot p$$

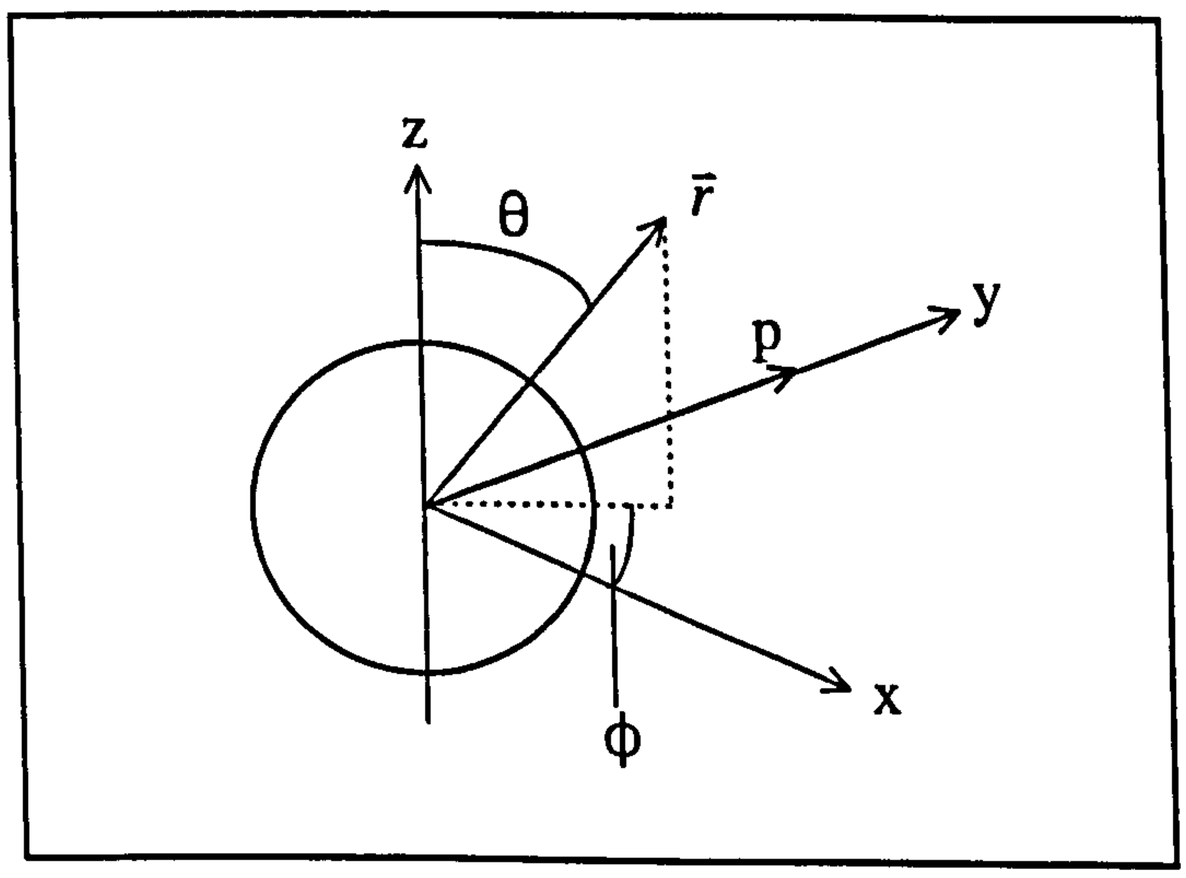

Figure 5.3 (Dipole Moment in Coordinate System)

$$\therefore \qquad \phi_{dipole} = \frac{1}{4\pi\varepsilon_0}\frac{\sin\theta\sin\phi}{r^2}p = \phi_2 = -B_{1,1}\frac{1}{r^2}\sin\theta\sin\phi$$

The dipole strength became

$$p = -\frac{\left\{\frac{\varepsilon_1 - \varepsilon_b}{\varepsilon_1} v_\infty \tfrac{1}{2} B\right\}}{\frac{1}{d^3} + \frac{2\varepsilon_1}{\varepsilon_b d^3}} 4\pi\varepsilon_0 \tag{5.29}$$

5.4 Summary

A simple calculation showed that the magnitude of the dipole strength for the flow signal is to the order $10^{-21} Cn$ whereas it was to the order $10^{-17} Cm$ for the transformer signal and therefore is about 10^4 times smaller. This means that a bubble passing through the meter should not have a significant effect on the flow signal and hence it was not taken into further consideration.

CHAPTER 6

SET-UP AND EXPERIMENTS WITH ARTIFICIAL BUBBLE FLOW

6.1 Introduction

The development of theoretical (analytical/numerical) background of the transformer signal in insulating liquid (main phase) and an interfering second phase in form of a gas bubble has been discussed. An experimental set-up is designed and built, which enabled a series of experiments to be conducted. This set of experiments showed the effect on the second phase only. In the following chapter a description of the experimental apparatus, the electromagnetic flowmeter, the electronics including data acquisition and signal processing instruments is given, as well as the results of the experiments.

6.2 System design of the experimental rig

In the following experiments the effect of the second phase only is considered. Investigations of the interference of the eddy currents in the liquid due to a sphere are made. Spheres are used to represent bubbles of different sizes, positions and velocities. An adequate experimental rig is designed and built. A drawing of the final arrangement is shown in Figure 6.1. The electromagnetic flowmeter is mounted between two tanks (containing dielectric liquid). The idea is to simulate the second phase with a hollow plastic sphere that is fixed on a thin piece of string. In order to move this artificial "bubble" through the meter, the string is bound around two wheels. To achieve different ball velocities one of the wheels is powered with an adjustable electromotor. The design for the wheel mounting also allowed adjustable ball

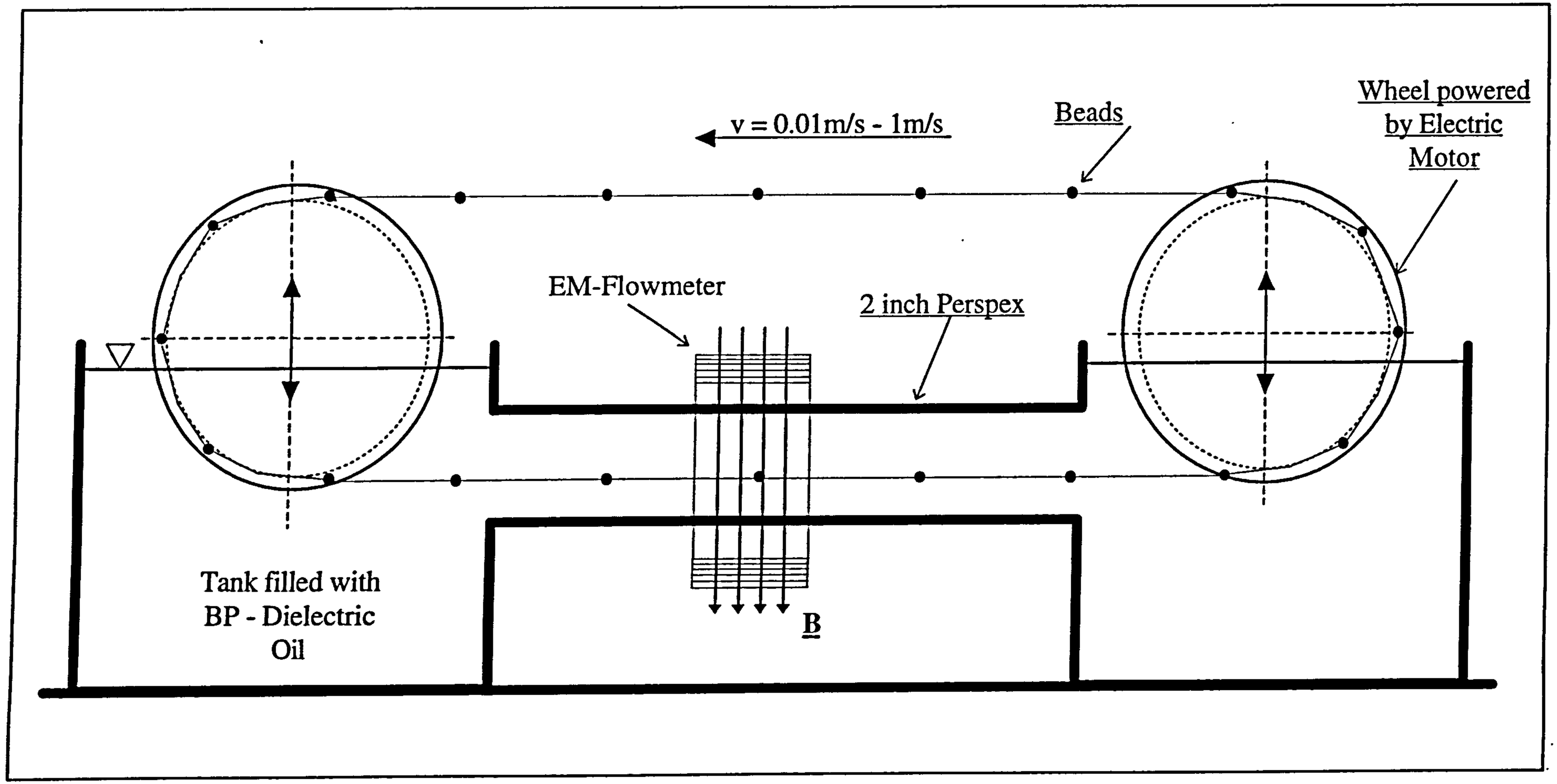

Figure 6.1 (Schematic of experimental rig)

positioning in the pipe section (x-y plane). This leads to an investigation of transformer signal and ball positioning.

Unfortunately, for bubble speeds of around 0.8 m/s and faster significant vibrations of the spheres in vertical direction took place. This unwanted occurrence is expected to alter the shape and magnitude of the transformer signal. It also could produce an increasing amount of noise on the electrodes, since the additional vibrating movement of the sphere creates more charge separation. Therefore, the use of this experimental apparatus, for investigations of an ideal bubble movement on the transformer signal, is confined to bubble velocities lower than 0.8 *m/s*.

6.3 The electromagnetic flowmeter

A schematic drawing of the electromagnetic flowmeter for the use in dielectric liquids and a second gas phase is shown in Figure 6.2. The flowmeter consists mainly of the flow conduit, the detection electrodes, the driven electrodes, the electrode clamps, the excitation coils for the magnetic field and the electrostatic shield. These parts are described next.

6.3.1 The flow conduit

A two inch perspex pipe of 370 *mm* length is used for the flow conduit of the meter. It is an advantage that a non conducting pipe wall does not give rise to eddy currents in the magnetic field. Because capacitive signal detection is used, perspex could be used as an adequate dielectric medium between the two capacitor sides. The magnitude of the capacitance, estimated with the geometry equation *C=Er*Eo*A/d (Plate Capacitors)*, can be determined with *2.0 E-10 C/V = F*.

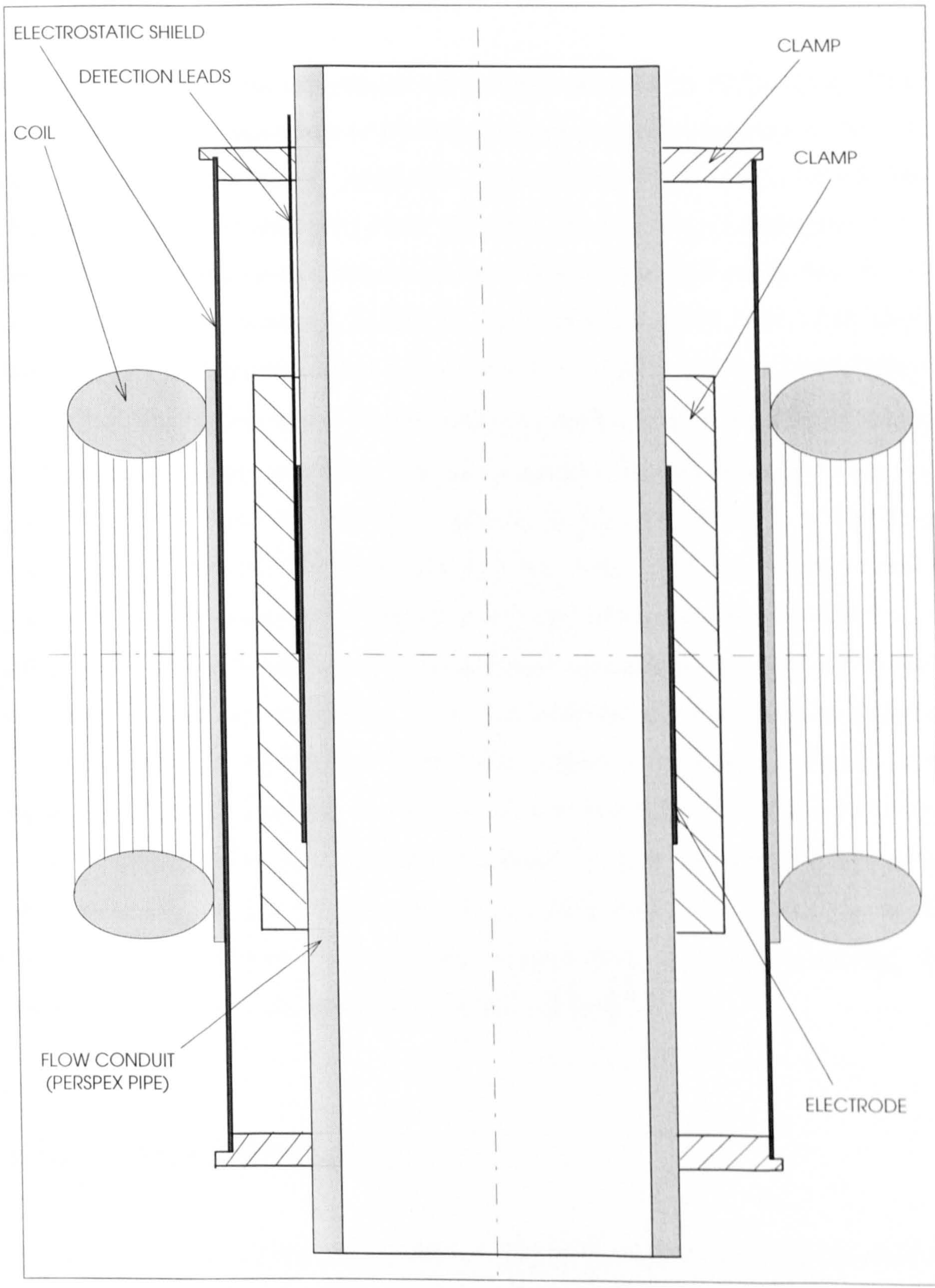

Figure 6.2 (Schematic of Electromagnetic Flowmeter)

6.3.2 The detection and guard electrode

The electrodes used in the experiments are designed and made by Schlumberger Dowell and provided to the Department of Fluid Engineering and Instrumentation in 1991. The electrode arrangement has a large area (detection electrode) with a driven shield electrode behind. Both electrodes, made of copper, are mounted and separated on three flexible, rectangular insulating boards, so they could be smoothly added onto the flow conduit. The flexible insulating boards are made from 125 micro meter thick Kapton film. Kapton is a Polyamide with a permittivity of 3.4 and an electrical conductivity of $10^{-16}\,S/m$. The flexible boards on which the two electrodes are mounted have a length of 100 *mm* and a height of 160 *mm*. The driven shield, or 'guard electrode' as it is often called, is used to keep the detection electrode at the same potential as the arising voltage on the detection electrodes and therefore avoid capacitive coupling between ground and the detection electrodes. This is a very effective method of shielding the detection electrodes. The guard electrode is placed extremely close behind the detection electrode and both are separated by a thin insulating layer. These guard electrodes are driven by the noninverting output of the buffer amplifiers. A schematic drawing of the signal detection and feed back system is given in Figure 6.3, and a further description on the buffer amplifier and associated electronics is given in section 6.4. The two electrodes have a so called fishbone like shape, which keeps them, in comparison with ordinary area electrodes, virtually eddy current free. A principle drawing with dimensions of this special arrangement is given in Figure 6.5.

6.3.3 Electrode and weir clamp

An important general feature for an electromagnetic flowmeter is to keep the electrodes and detection leads in a stable position. Durcan (1996 [33]) designed, for a related project, a clamping mechanism that keeps the electrodes and detection leads in a prearranged position and ensures that the detection leads will be placed in a straight line

in order not to create a loop that would increase the transformer signal. These clamps are rebuilt by courtesy of L. Durcan and used on the meter. Figure 6.4 shows the design of the clamps.

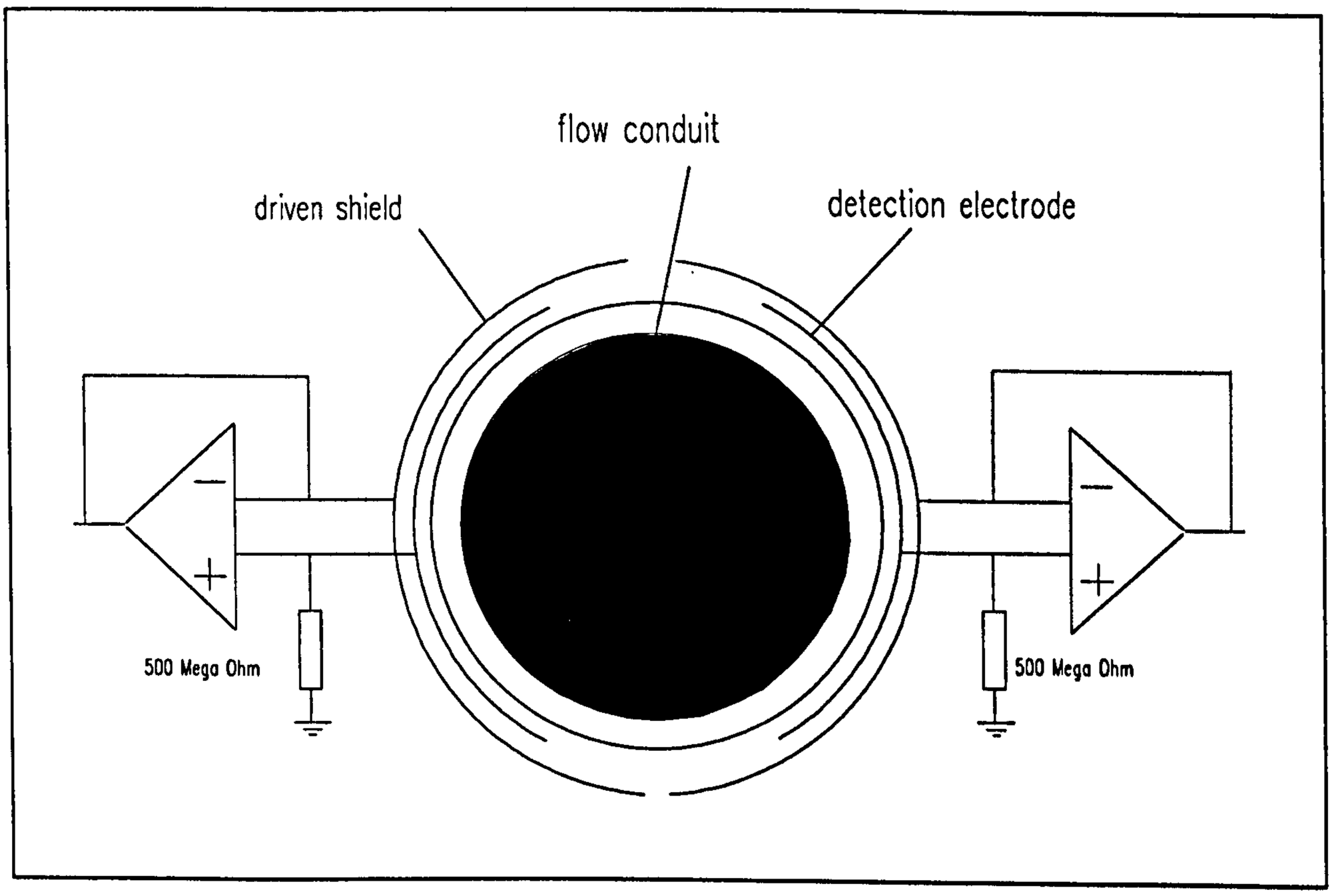

Figure 6.3 (Signal detection and feed back system)

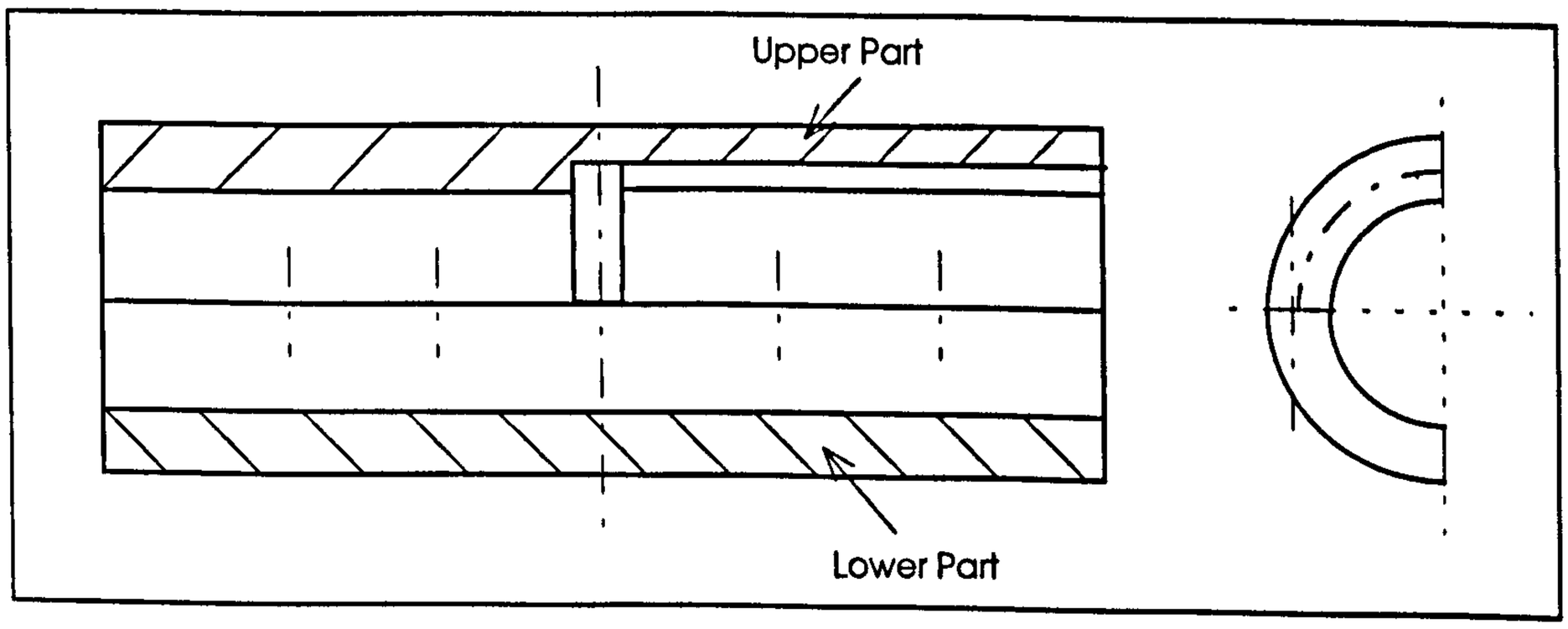

Figure 6.4 (Design for electrode clamps)

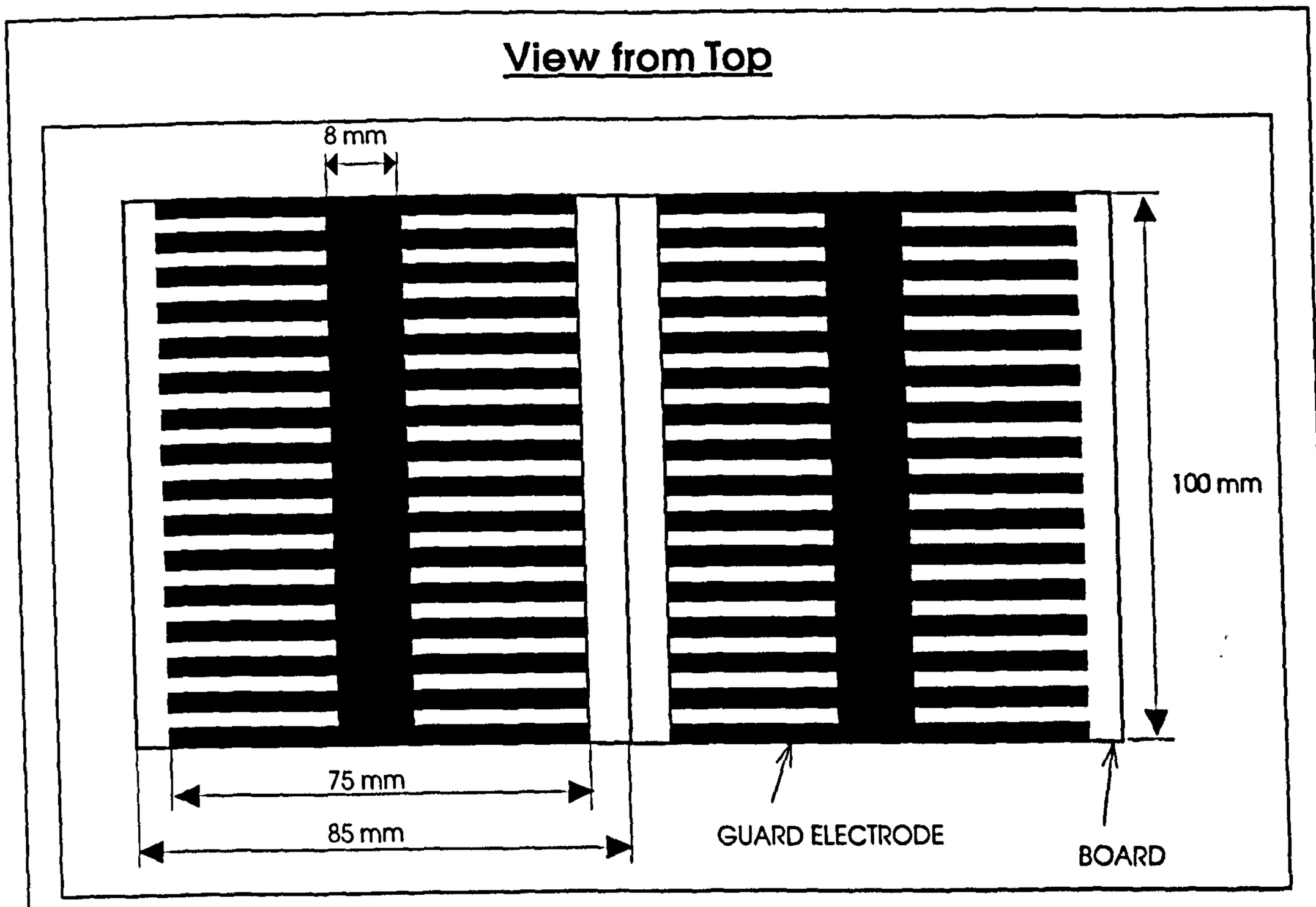

Figure 6.5 (Design of 'Fishbone' electrodes)

6.3.4 The electrostatic shield

A common device to avoid capacitive coupling in many electronic systems and applications is a grounded electrostatic shield. When dealing with signals in the range of milli Volts or even smaller then electrostatic shielding is necessary. For electromagnetic flowmeters the shield becomes penetrated by the magnetic field, and hence is exposed to eddy currents. In return these eddy currents would disturb the transverse magnetic field, both in magnitude (causing a power loss) and phase (causing difficulties in reduction of the quadrature signal). The range of the circulating eddy currents depends on the magnitude and area of the magnetic field lines. The absolute eddy current is the summation of all the circulating eddy currents in the area fluxed by the field lines. Therefore a special shield, that keeps the capacitve coupling and the magnetic field as low as possible, is necessary. Amare (1991 [26]) designed an eddy current free shield from a grid like arrangement that breaks the circulating loops of the eddy currents. In recent work Durcan (1995 [33]) improved the design of the shield when he wound two layers of insulated thin copper wire around a plastic cylinder. The electric field attenuation is found to be 60 *dB* (i.e. for a 1000 *volt* source voltage, the coupling voltage is 1 *volt*). Figure 6.6 depicts the electrostatic shield. By courtesy of L. Durcan an identical shield is rebuilt and used in these experiments.

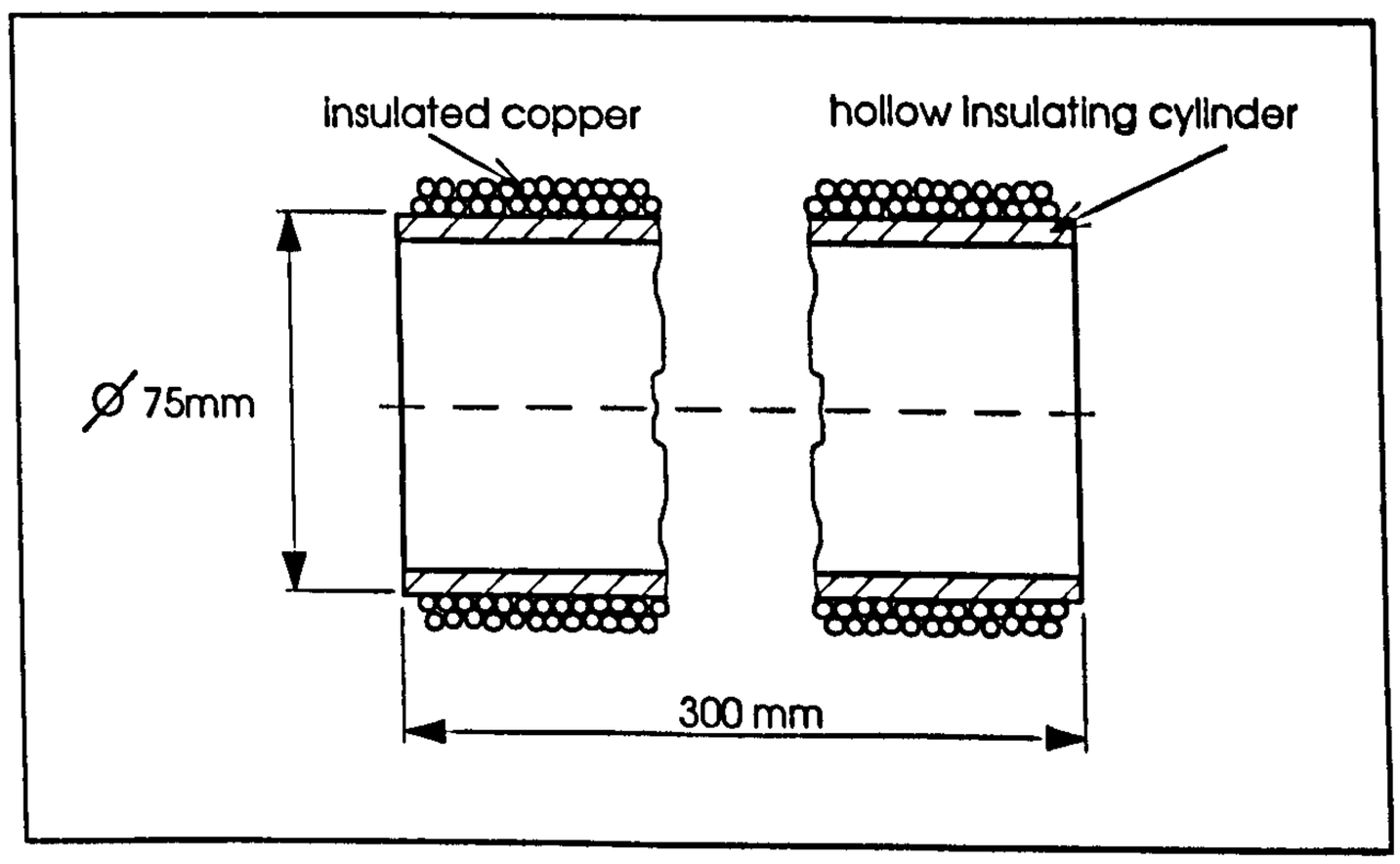

Figure 6.6 (Schematic of electrostatic shield)

6.3.5 Excitation coils

The design and geometry of the coils depended mainly on the required magnetic field strength and excitation frequency.

The magnetic field strength for electromagnetic flowmeters in insulating liquids that is necessary to generate a reasonable flow signal is 100 *Gauss* (0.01 *Tesla*). Although in this work the flow induced signal is considered less than the transformer signal generated by gas bubbles passing through the meter. With respect to measure both, main and second phase with one meter, a field strength of 100 *Gauss* is chosen.

The choice of excitation frequency depended upon the following factors: magnitude of quadrature signal; charge noise bandwidth; eddy currents in the electrostatic shield; and the voltage on the coils. From the fact that the quadrature signal is proportional to the operation frequency ($\phi_{quad} = \omega BA\cos\omega t$), the higher the frequency the larger the quadrature signal. From previous research work (Al-Rabeh [23], Hentschel [21], Amare [26]) the charge noise frequency increases with the flowrate. For a flowrate of 3 *m/s* a noise level of 0.4 *mV* at 1000 *Hz* occurred. Eddy currents in the electrostatic shield are also proportional to the operational frequency ($i_{eddy} \approx \frac{\sigma\omega BR^2 t}{2}$) as derived by Amare [26]. Knowing that these eddy currents cause a power loss and a disturbance to the magnetic field, they should therefore be kept as low as possible. It should be targeted to keep the voltage on the coils on a low level, because as higher the voltage on the coils as higher is the electrostatic pick up at the electrodes and associated electronics. The voltage on the coils results mainly from the inductance *(L)*. Capacitance *(C)* and resistance *(R)* have only a minor influence on the voltage. The magnitude of the reactance of the coils is described in equation 6.1. For an alternating current that flows through the coils the voltage on the coils can be calculated from equation 6.2.

$$X_L = |\omega L| \qquad 6.1$$

$$u_L = i \cdot X_L \qquad 6.2$$

From the above two equations it can be seen that the reactance is proportional to the operating frequency and therefore the voltage increases with increasing frequency. To find the optimal operating frequency a compromise between these four factors had to be found. It is decided to follow Amare's choice to use an operational frequency of 1500 *Hz*.

Therefore the same type of coils as used by Amare are used for this meter and subsequently for our experiments. A brief description and calculation of the coils are given next. Because of the relatively high operating frequency (1500 *Hz*) of the magnetic field, that would create strong eddy currents in the usually iron cored coils, only air cored coils could be used. The geometry of the coils (width *w* and thickness *t* of the coils, wire diameter, as well as the number of turns for each coil) is calculated by Amare as follows. The magnetic field strength is determined from the Biot-Savart law and is given by equation 6.3.

$$B_1 = \frac{\mu_0 I R^2}{2\left(R^2 + z^2\right)^{\frac{3}{2}}} \qquad 6.3$$

For a steady current (I) flowing in a circular loop of Radius R you can derive the magnetic field strength at a vertical distance z from the above equation. See geometry details in Figure 6.7. The maximum field strength is found to be at $R = z\sqrt{2}$. To avoid over heating in copper wire coils the thickness *(t)* and width *(w)* are chosen to be 25 *mm* by 25 *mm*, according to the rule of thumb *(2540 Ampere / cm²)*. An insulated copper wire of 0.8 *mm* diameter capable of carrying an r.m.s. current of 2 *Ampere* is used. The distance *(z)* is the radius of the electrostatic shield plus half of the thickness of the coil. To achieve maximum magnetic field strength the radius R is chosen to be $R = z\sqrt{2}$. To produce a field strength of 50 *Gauss* on each coil the number of turns per coil is determined to 475. To calculate the inductance of a coil, for low frequency given in Terman [36], equation 6.4 is used.

$$L = \frac{3.2R^2N^2}{12R + 9t + 10w} \qquad 6.4$$

The value for the inductance on one coil is 30 *mH*.

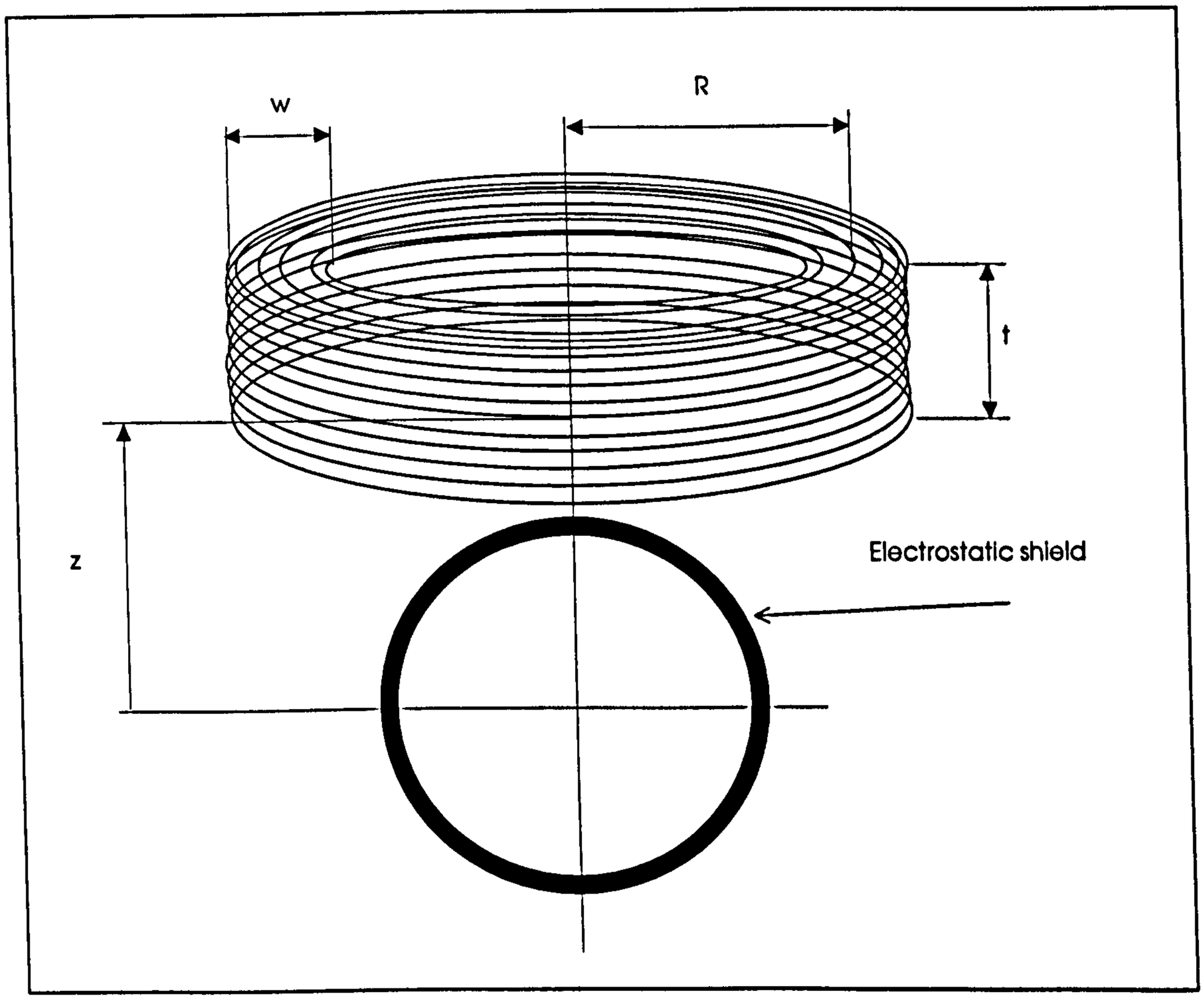

Figure 6.7 (Schematic of geometry of excitation coils)

Therefore the voltage on the coils could be estimated as 1225 *Volt*, using equations 6.1 and 6.2.

6.4 The electronics

Two sets of electronics are used to run the flowmeter. The first set considered are the excitation electronics and the second set is the detection electronics. Both systems are explained in the following sections.

6.4.1 The excitation electronics

The two series coils are connected to a capacitor to form a resonant circuit. In order to have the operating frequency (1.5 *kHz*) as the resonance frequency, equation 6.5 (Horowitz and Hill [34] page 33) had to be applied.

$$f_o = \frac{1}{2\pi\sqrt{LC}} \qquad 6.5$$

With the inductance of the series coils of 65 *mH* and the targeted resonance frequency of 1.5 *kHz* the required capacitance is calculated to be 0.0166 μF. To provide this capacitance six capacitors in series each of 0.1 μF are used.

As evaluated in the previous section the electronics are designed to deliver an alternating current of 2 *A* through the coils that subsequently could produce a magnetic field strength of 100 *Gauss*. The resistance R_L of the coils is measured to be 8.7 Ω and the resistance R_C from the capacitors in series is given as 5.6 Ω. Using Ohm's law, in order to deliver a sinusoidal current of 2 *A* through a resistor of 14.3 Ω ($R_L + R_C$) a voltage of 28.6 volts is required. The power amplifier (RS MOS 248 type which is available from previous work) could provide such a voltage. The characteristics of the power amplifier are that it operated on a +/- 55 volts d.c. supply and could deliver a power of 120 watts onto a 8 Ω load. The input of the power amplifier is then linked to a

signal generator (Hewlett Packart 3312A). The arrangement of the excitation electronics is shown in figure 6.8.

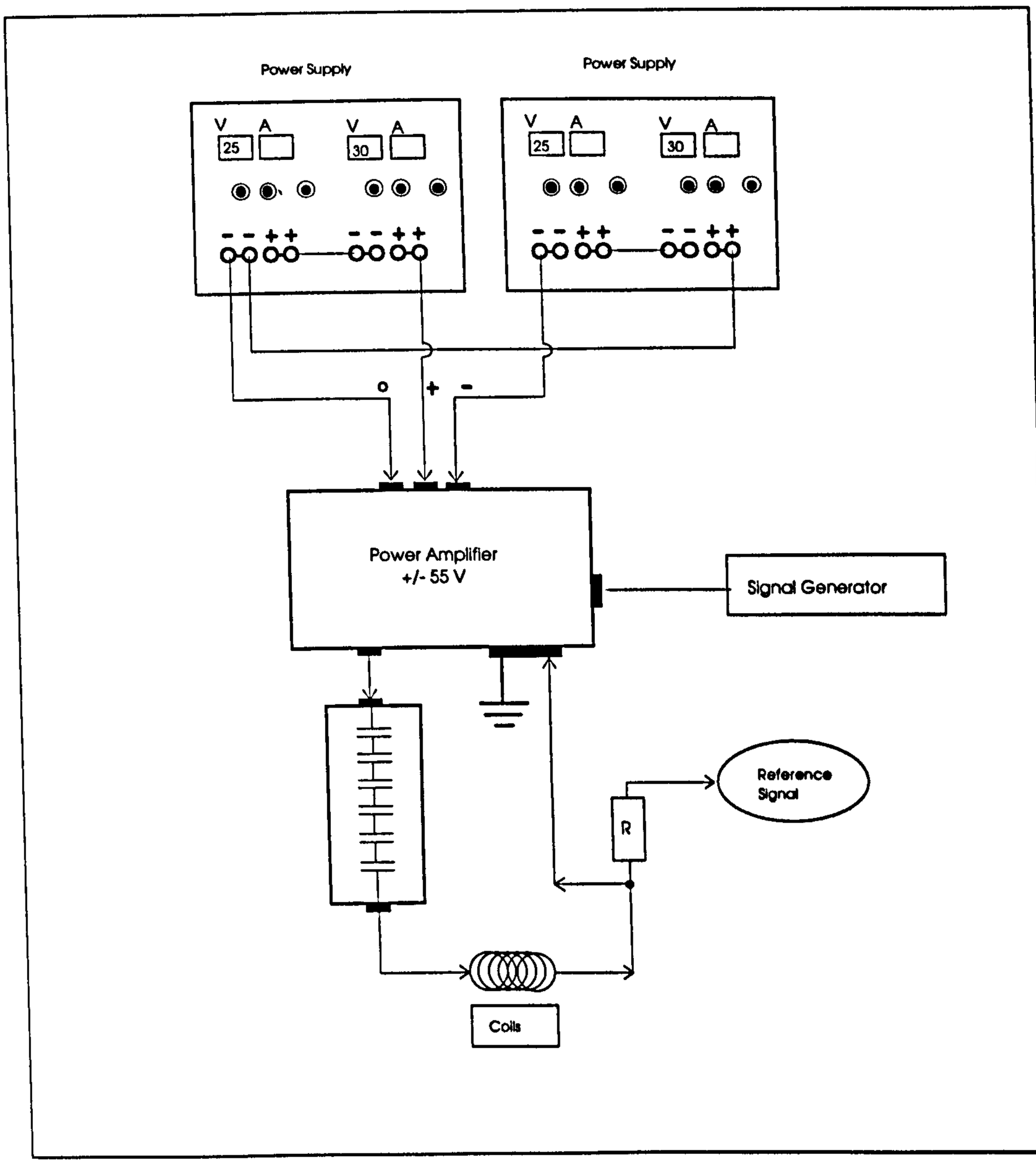

Figure 6.8 (Excitation electronics)

This set of excitation electronics is built and tested. The actual resonance frequency is found to be 1365 *Hz*. This deviation from the theoretically calculated resonance frequency comes from the tolerance of the dimensions of the coils and the estimated inductance (equation 6.4) which of course is only an approximation. By altering the capacitance it would have been possible to increase the frequency, but since charge noise is only severe at 1000 *Hz* the resonance frequency is kept at 1365 *Hz*. In the

following three graphs (Figure 6.9-6.11) the measured correlation between adjusted voltage from the signal generator, current and voltage output from the power amplifier as well as the relation between maximum magnetic field strength in the pipe centre and current output from the power amplifier are depicted. As expected from Ohm's law $\left(I = \frac{U}{R}\right)$ and the equation for the magnetic field strength (equation 6.3) all these relationships are linear. In the experiments carried out the final setting for the voltage on the signal generator is put to 850 *mV* peak to peak, that meant that the value of the magnetic field strength in the pipe centre is 0.0078 *Tesla*. This setting provided a stable baseline, after nulling the quadrature signal down and also generated a reasonable signal created by the bead.

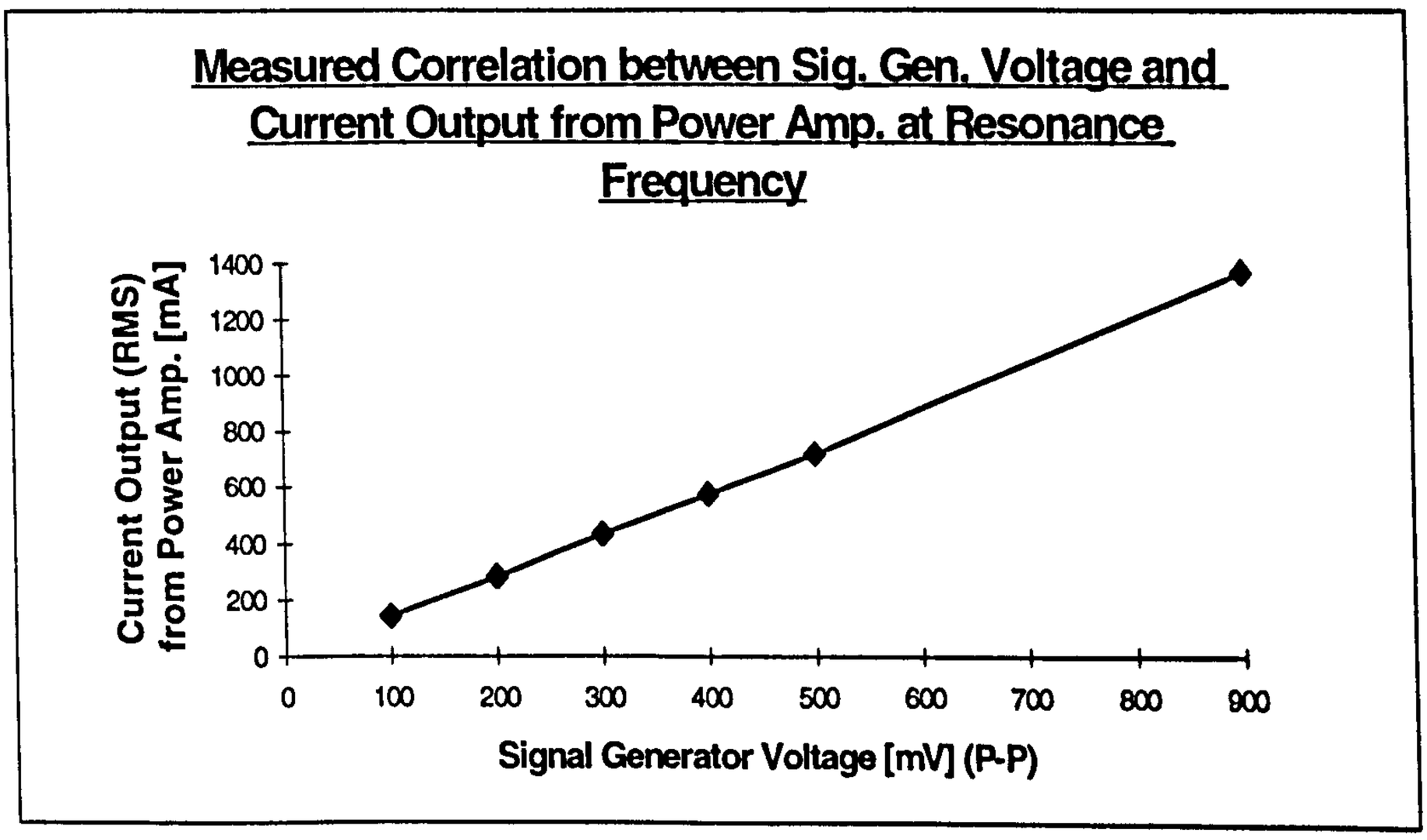

Figure 6.9

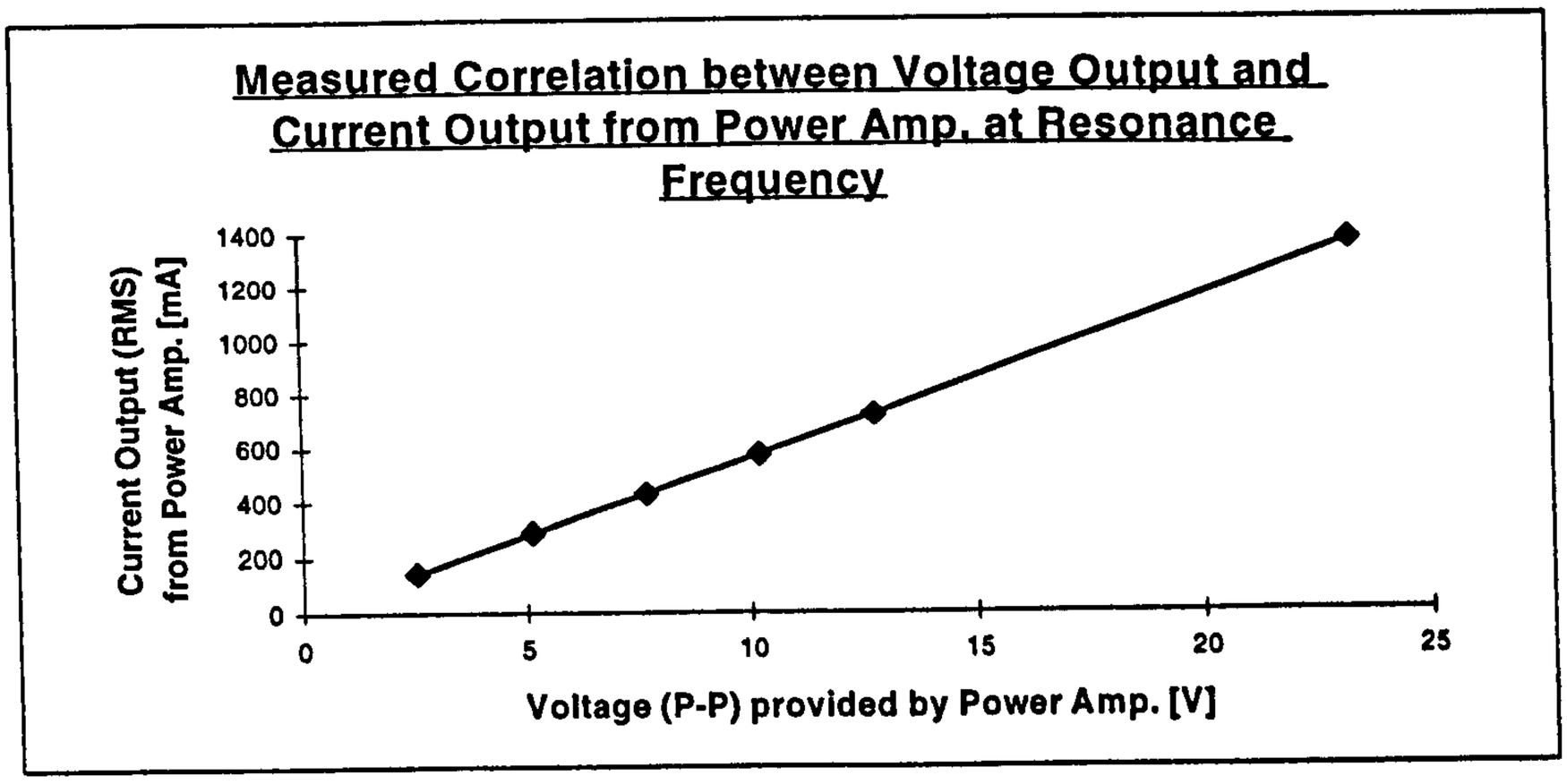

Figure 6.10

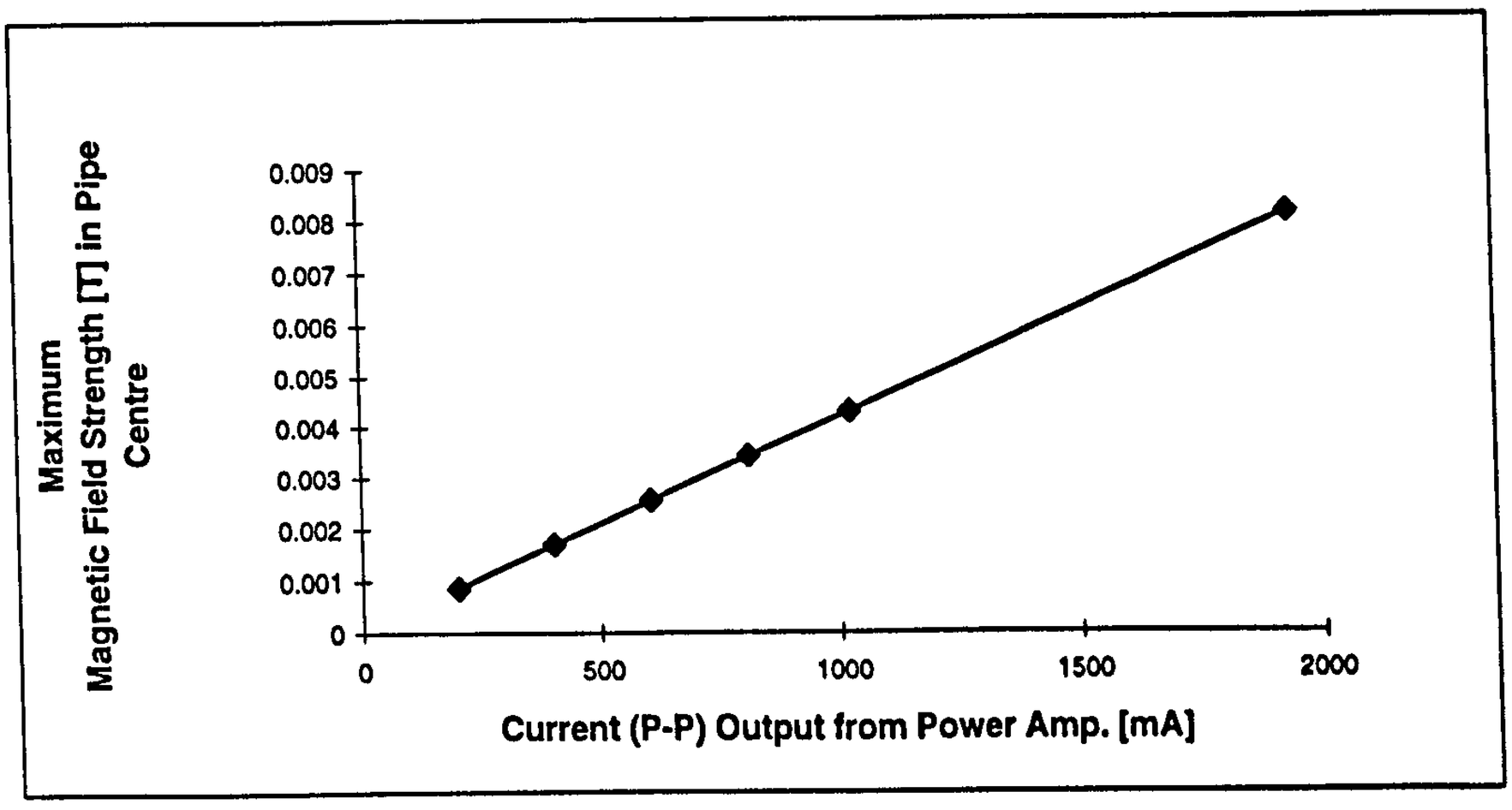

Figure 6.11

6.4.2 Detection and quadrature suppression electronics

The principle system used for the detection and quadrature suppression electronics builds on work previously done by Hentschel and Amare. The design used for the electronics is described in the following sections. The detection and quadrature suppression electronics are grouped in to three units (I, II, III), see Figure 6.12. The first part (I) shows how the signal is retrieved. The second part (II) is the amplitude and phase shifting of the reference signal, and the third unit (III) shows the final quadrature deduction stage.

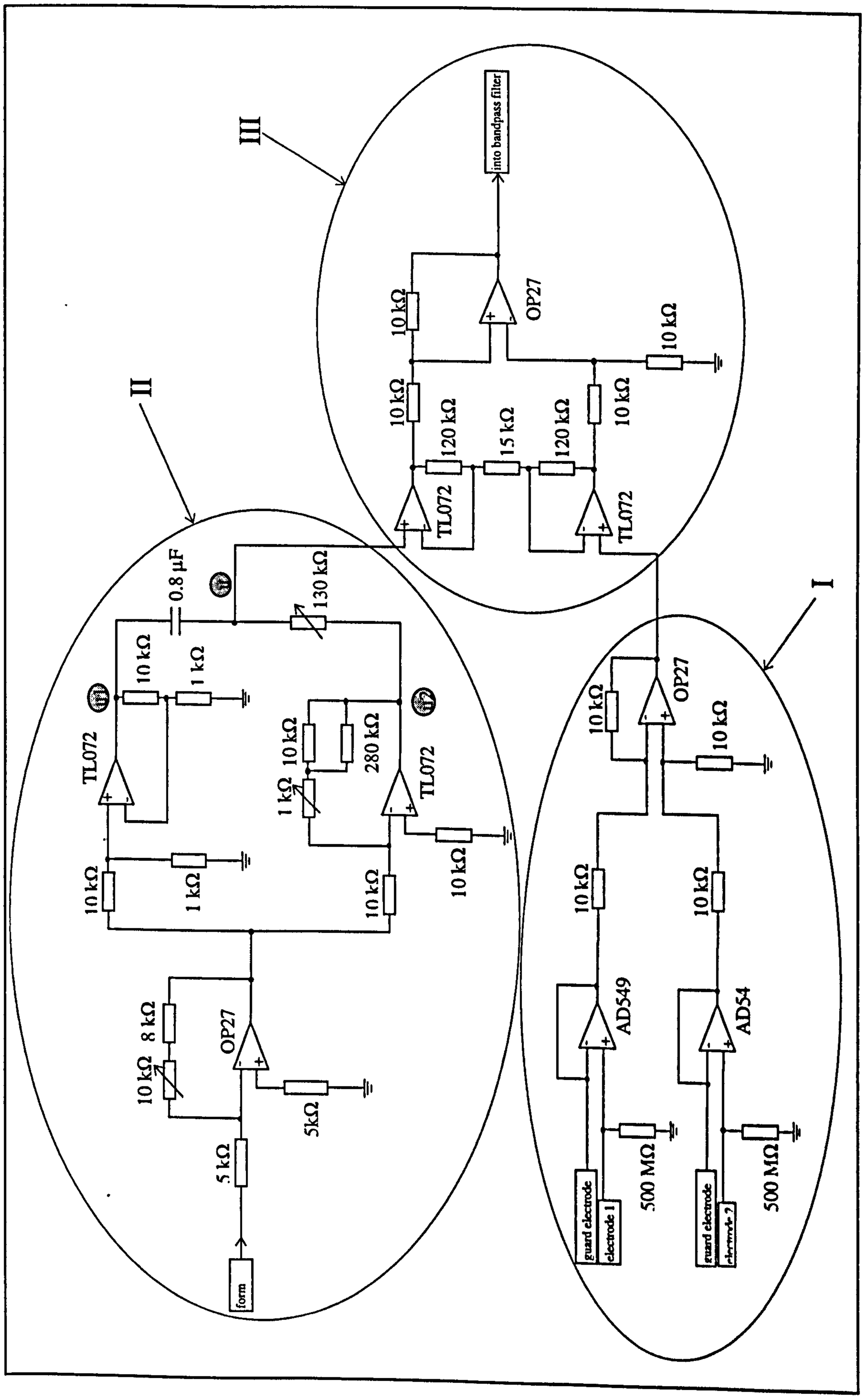

Figure 6.12 (Detection and quadrature suppression electronics)

6.4.2.1 Signal detection unit (I)

The arising signals on the two detection electrodes are put in to the noninverting input of the follower amplifiers (AD549). The guard electrodes are connected to the inverting input of the AD549 amplifiers. Since the gain of the follower amplifier is assumed to be one (in practice very close to one), the potential on the detection electrodes are virtually the same as on the guard electrodes and therefore the detection electrodes are practically not interfered by capacitive coupling. This method is also called 'bootstrapping'.

A 500 MΩ resistor linked between the detection electrode and ground is used to let the high input bias current of the follower amplifier flow to ground. Another reason why a follower amplifier is used, is because of its high input impedance that matches the high impedance of the flowmeter. With an input impedance of 10^{13} Ω and 1 *pf*, an ultra low input bias current of 50 *fA*, and a very low offset drift (0.2 $\mu v/°C$) for stability reasons, the AD549 has the appropriate characteristics for the required purposes.

The difference voltage of the two output signals from the two follower amplifiers, which are of opposite sign, is identified by using a differential amplifier. The gain of the differential amplifier is 1. The specifications of the operational amplifier OP-27 are suitable for our needs. OP-27 had a ultra low noise of 2 *nv* at 1500 *Hz*, a very low offset voltage drift of 0.2 $\mu v/°C$, and a high common mode rejection ratio (CMRR) of 126 *dB*.

6.4.2.2 Amplitude and phase shifting unit (II)

The voltage detected by the electrodes contained the flow signal and a certain amount of quadrature voltage. This quadrature occurrence is generated from various deviations

axisymetric placing of the electrodes, non identical contact impedance on electrodes, non-identical gain on buffer amplifier, non-uniform transverse field, or non-perfect wiring geometries. Even an extremely carefully built and designed flowmeter can only reduce such quadrature build up to a minimum, but it is obviously never possible to avoid it completely. The remaining quadrature signal is of the order of 400 *mV*. Therefore an electronic method is necessary to remove of the remaining quadrature voltage. Following the now described technique, known as Phase-Sensitive Detection, that generates a signal of the same magnitude and phase as the quadrature signal but of opposite sign, the quadrature signal cancels out. First the current flowing through the coils is branched off as a reference signal and connected to a variable resistor on the feedback of an inverting amplifier (OP27). With the variable resistor the amplitude of the voltage can be controlled and adjusted equal to the quadrature voltage, and the inverting amplifier (voltage gain = $V_{out} / V_{in} = -R_2 / R_1$) produces a voltage of opposite sign on its output. The reference voltage is then connected to a phase shifting circuit that gives an output sine wave of adjustable phase from 0° to 180° and keeps the amplitude constant. For this purpose the voltage is split in to u_1 and u_2, and both are equal in magnitude but 180° apart in phase.

6.4.2.3 Quadrature deduction stage (III)

Both signals, the quadrature contaminated baseline signal and the generated signal that is adjusted to the right amplitude and in anti-phase to the quadrature signal, are fed in to an instrumentation amplifier. This instrumentation amplifier contained a TL072 dual operational amplifier and a OP27 operational amplifier, that is used as a differential amplifier. The instrumentation amplifier arrangement is designed for a gain of 120, and then finally a suppression of the original existing quadrature voltage to a minimum of about 20 *mV* could be achieved. See Figure 6.13. The output signal is then connected to a Band-pass Filter.

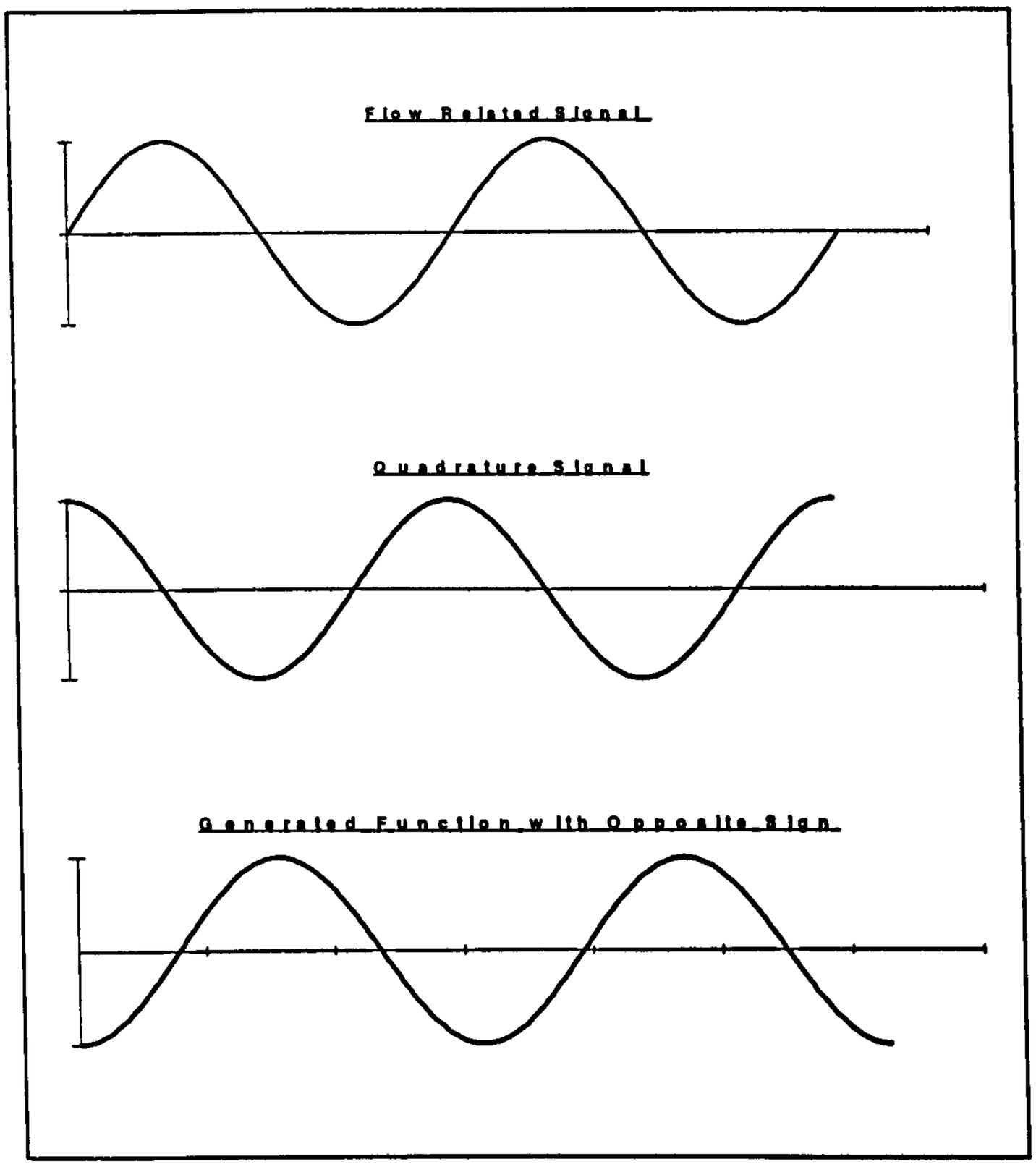

Figure 6.13 (Schematic of quadrature supression)

6.4.3 Bandpass filter design

In order to refine the output signal from disturbing noise sources and harmonics, a band-pass filter is designed and built.

It is decided to use a pass-band width (BW) of 400 *Hz* with lower (f_l) and upper (f_u) pass-band frequency limits of 1.3 *kHz* and 1.7 *kHz* respectively. These two limits are normally chosen at 3 *dB*. This meant the arithmetic centre frequency (f_0) is 1.5 *kHz*. The ratio of upper band-pass frequency (f_u) to lower band-pass frequency is a criteria whether the to be built filter is a WIDE-BAND PASS Filter (for a ratio of 2 or bigger)

or a NARROW-BAND PASS Filter (for ratios smaller than 2). Since this ratio in our case is 1.3076 a Narrow Band Pass Filter is designed. See Figure 6.14.

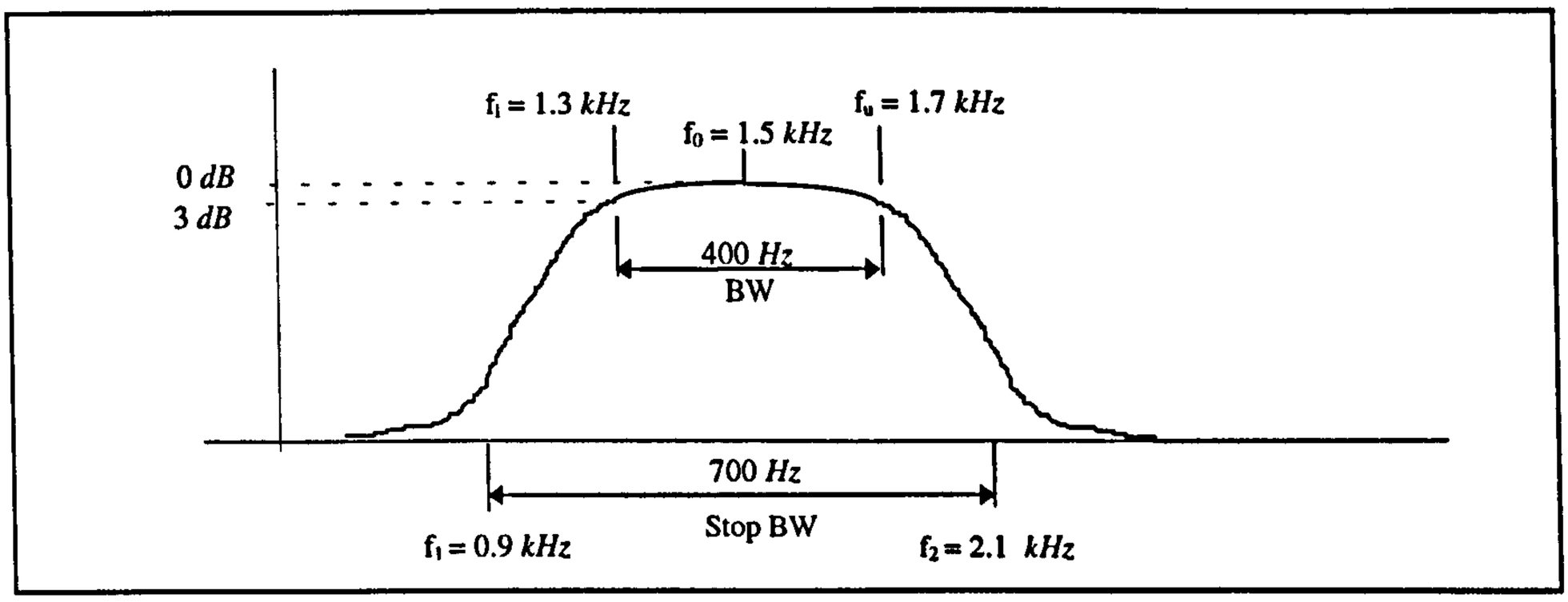

Figure 6.14 (Design of narrow band pass filter)

The selectivity factor (Q) that is defined as $Q = \frac{f_0}{BW}$, and serves as a criteria that states that f_0 can be kept as the arithmetic mean for $Q \geq 10$, and for $Q < 10$ a normalised centre frequency of $f_0^{'} = \sqrt{f_l + f_u}$ should be used. Inasmuch as Q is calculated as 3.75 the band-pass filter had to be normalised. The new normalised centre frequency is fond to be 1.4866 *kHz*. The normalised and geometrically related stopp-band frequency points are calculated with $f_1^{'} = \frac{f_0^{'2}}{f_2}$ and $f_2^{'} = \frac{f_0^{'2}}{f_1}$ and became 1.052 *kHz* and 2.455 *kHz* respectively. The two pairs

are $f_1 = 0.9kHz$ and $f_2^{'} = 2.45kHz$ $\left(f_2^{'} - f_1 = 1.55kHz\right)$

and $f_1^{'} = 1.05kHz$ and $f_2 = 2.1kHz$ $\left(f_2 - f_1^{'} = 1.05kHz\right)$

The second pair is retained, since it had lesser separation. The steepness factor (A_s) could be calculated as $A_s = \frac{StoppBW}{BW} = \frac{1.05kHz}{0.4kHz} = 2.62$.

A Butterworth low-pass filter could now be selected from the normalised curves, which are given in Appendix [B]. The constant Ω in this table simply is the ratio $\frac{BW_s}{BW_{3dB}}$,

where BW_x is the band width of interest. In our case BW_x is the stopp band width. Therefore Ω is calculated as 2.62. The stopp band attenuation of 25 dB needed a three section filter. The chosen circuit is a Active Dual-Amplifier Bandpass (DABP) structure, because of its remarkable performance. This type of structure is first introduced by Sedra and Espinoza. The final circuit is given in Appendix [C].

6.4.4 Phase sensitive detection (Lock-in Amplifier)

The final signal processing stage is the application of a Lock-in-Amplifier. It is used to separate the remaining quadrature part and the flow related signal from each other and to monitor the flow related and transformer signal.

This method, used in the Lock-in-Amplifier, is called phase sensitive detection (PSD) and works in principal as follows. In order to detect the quadrature phase, the signal, coming from the band pass filter, is multiplied by a square wave function, that is in phase with the quadrature signal and then integrated (which gives a d.c. output) over time. As it can be seen in Figure 6.15b, the flow related signal becomes equals to zero and the transformer signal remains and can be monitored. To get the transformer signal equals to zero, the original signal, coming from the band pass filter, has to be multiplied by a square wave function, that is in phase with the flow related signal, and then integrated over time. See figure 6.15a. The final signal amplification after the signal processing electronics and filtering method is measured to be 120.

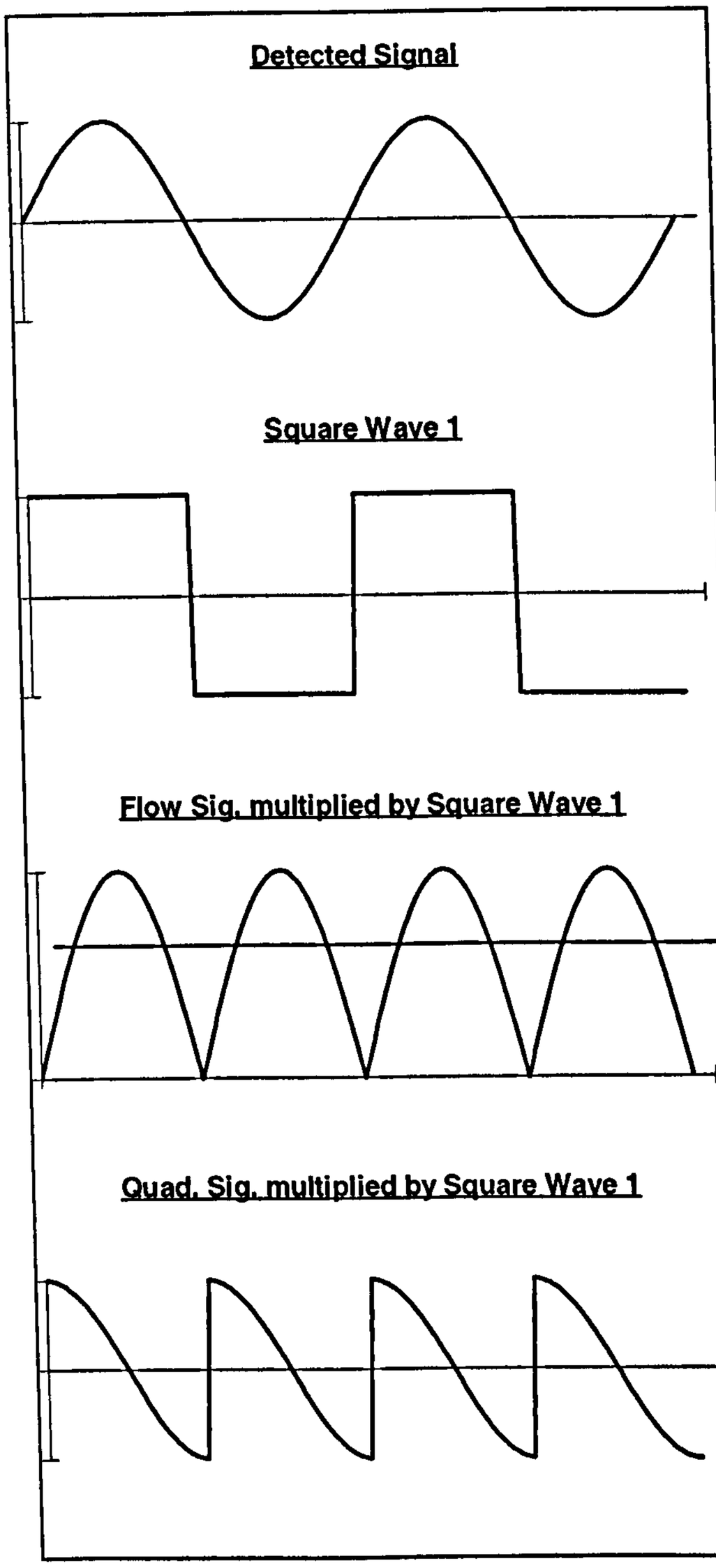

Figure 6.15a (PSD regarding flow signal)

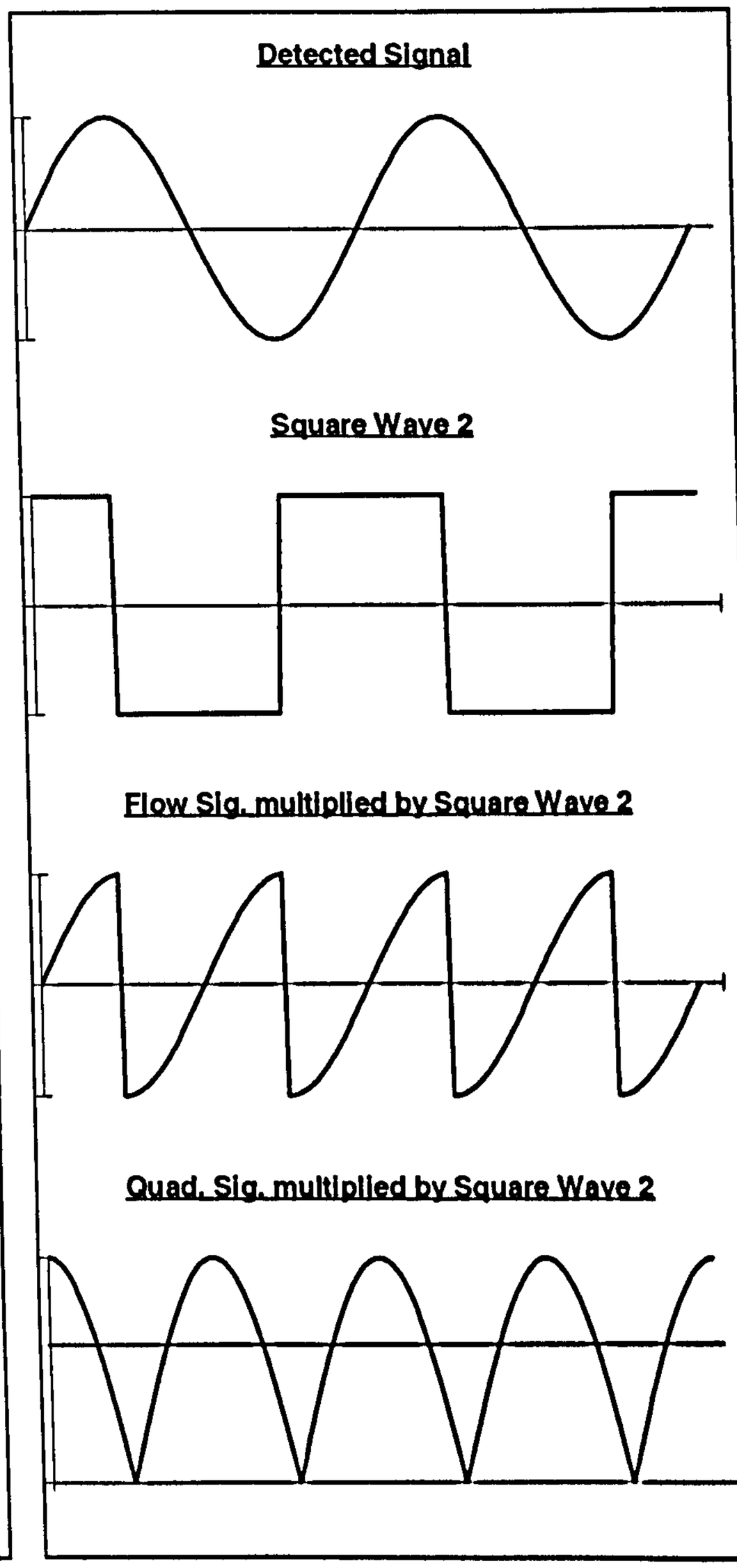

Figure 6.15b (PSD regarding quad. signal)

The term LOCK-IN comes from the fact that the instrument (ORTHOLOG-SC 9505E) locks into the frequency of the reference signal (taken from the coils). The quadrature signal, that theoretically lags 90° behind the flow induced signal, experienced phase shifts from previous signal processing. To acquire the condition of the desired phase (phase of the flow signal or quadrature signal) the PSD can be adjusted to the appropriate phase using a phase shifter. The output of the PSD is connected to a low-

pass filter. The purpose of the low-pass filter is to remove all components of the mixer output with frequencies far from reference frequency.

6.4.5 Signal recording method

For the signal recording the software package PICO-LOGIN-Systems is used. The output from the Lock-in-Amplifier is connected to the Analog to Digital Converter of the PICO-LOGIN-software package, which collects sets of measurements and stores them on disk. It is provided with tools to scale the measurements and to produce text and graphical reports.

6.4.6 The ONO-SOKKI analyser

For frequency analysis the ONO-SOKKI instrument is used. Signals are fed in to the ONO SOKKI and Fast Fourier Transformations, which led to power spectra, are executed.

6.5 The used fluid

The dielectric liquid used in the experiments is BP180. The relevant properties of this very pure and highly insulating oil are conductivity (σ) of 5.7 E-11 Ω^{-1}, relative permittivity of 2.2, viscosity of 0.001492 N/m^2, and density of 748 kg/m^3.

6.6 Experiments carried out

Two different types of experiments are carried out. The first group of experiments looked at the behaviour of the transformer signal for plastic beads, of different

diameters, surrounded by a dielectric liquid (BP 180, Dielectric Oil) passing through the electromagnetic flowmeter. The second set of experiments investigated the response of the frequency analysis carried out for various bubble velocities.

6.6.1 Transformer signal behaviour

In Figure 6.16 the transformer signal generated by a bubble passing through the meter is recorded. The bead, representing the bubble, moved passed the meter very near (at a vertical distance of about 15 *mm* measured from the pipe centre) one of the electrodes. The diameter of the bead is 20 *mm*. The emerging shape of the signal is as expected. It rose in an exponential manner as the bead entered the magnetic field. At very close to half of the length of the magnetic field the signal reaches its peak and then decreases and falls down to a maximum negative value from where it increases to a zero value. As it can be seen the two maximum points are not of the same magnitude. This was not expected. The positive peak reaches a value of 1.2 *mV* whereas the negative peak only approaches about -0.9 *mV*. It could also be observed that as the final signal approached zero there is slight overshoot of the signal before it settled at zero voltage. This incidence is, with regards to theoretical investigations, not anticipated. Reasons for this occurrence where most likely to come from a slightly asymmetrical arrangement of one of the electrodes. But even after a careful readjustment of the electrodes this occurrence could not be avoided.

A set of experiments examining the response of the transformer signal for different vertical positions at which the bubbles moved passed the electrodes (vertical positions at 5 *mm*, 10 *mm*, and 15 *mm*) as well as for different bubble diameters (10 *mm*, 15 *mm*, and 20 *mm*) are conducted. The graphs in Figure 6.17a to 6.17c show the maximum signal for various bubble locations and diameters. As predicted it is perceived that with increasing bubble diameter the peak signal increased. The relation between bubble diameter and transformer signal is theoretically established as $\phi \propto d^3$ (see equations

2.67 and 2.71). This proportionality holds for the recorded results, within a close tolerance. E.g. bubble diameter of 10 *mm* and 20 *mm* cause the maximum transformer signals of 0.00018 *V* and 0.0015 *V* respectively see Figure 6.16c. The theoretically calculated signal (using the above mentioned relationship $\phi \propto d^3$) would be 0.0014 *V* for the bubble of 20 *mm* diameter.

A close agreement between the magnitudes of experimentally recorded transformer signals and the computed signals is described in chapter 3. Comparing the peak signals for bubble diameters of 10 *mm* and 15 *mm* in Figure 6.17c and the equivalent computational results shown in Figure 3.9, a deviation of 20% and 35% respectively exists.

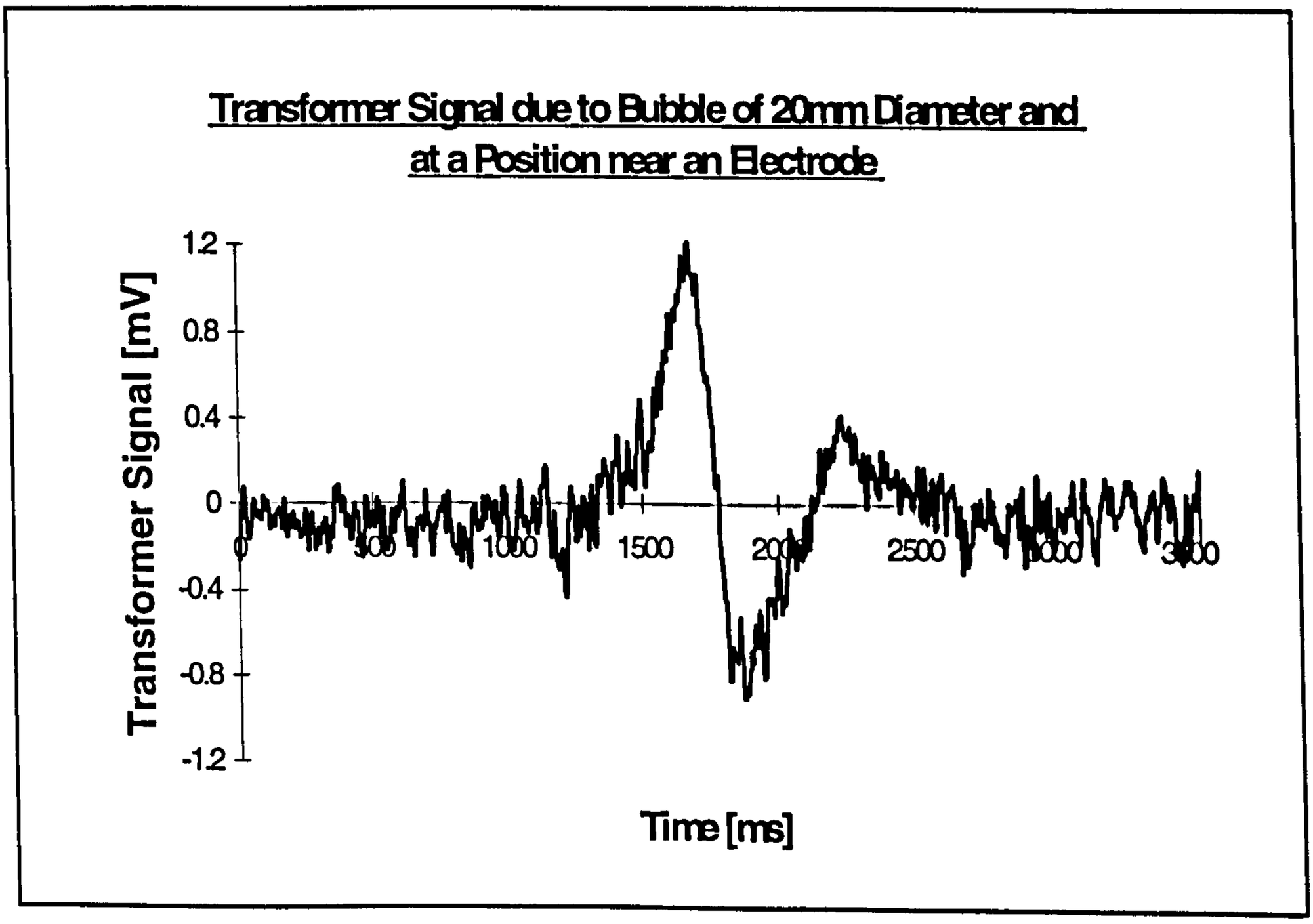

Figure 6.16

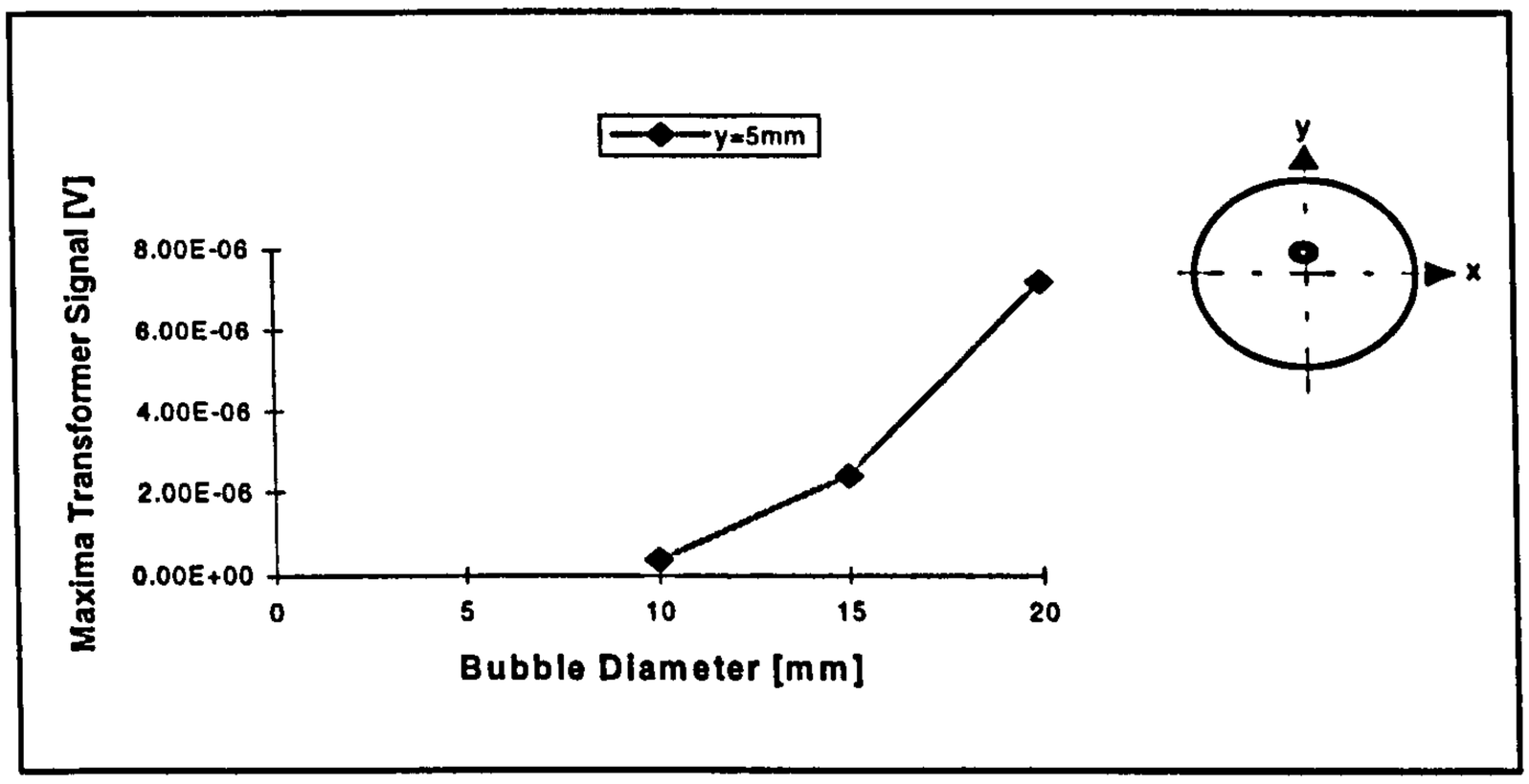

Figure 6.17a (Maxima transformer signal)

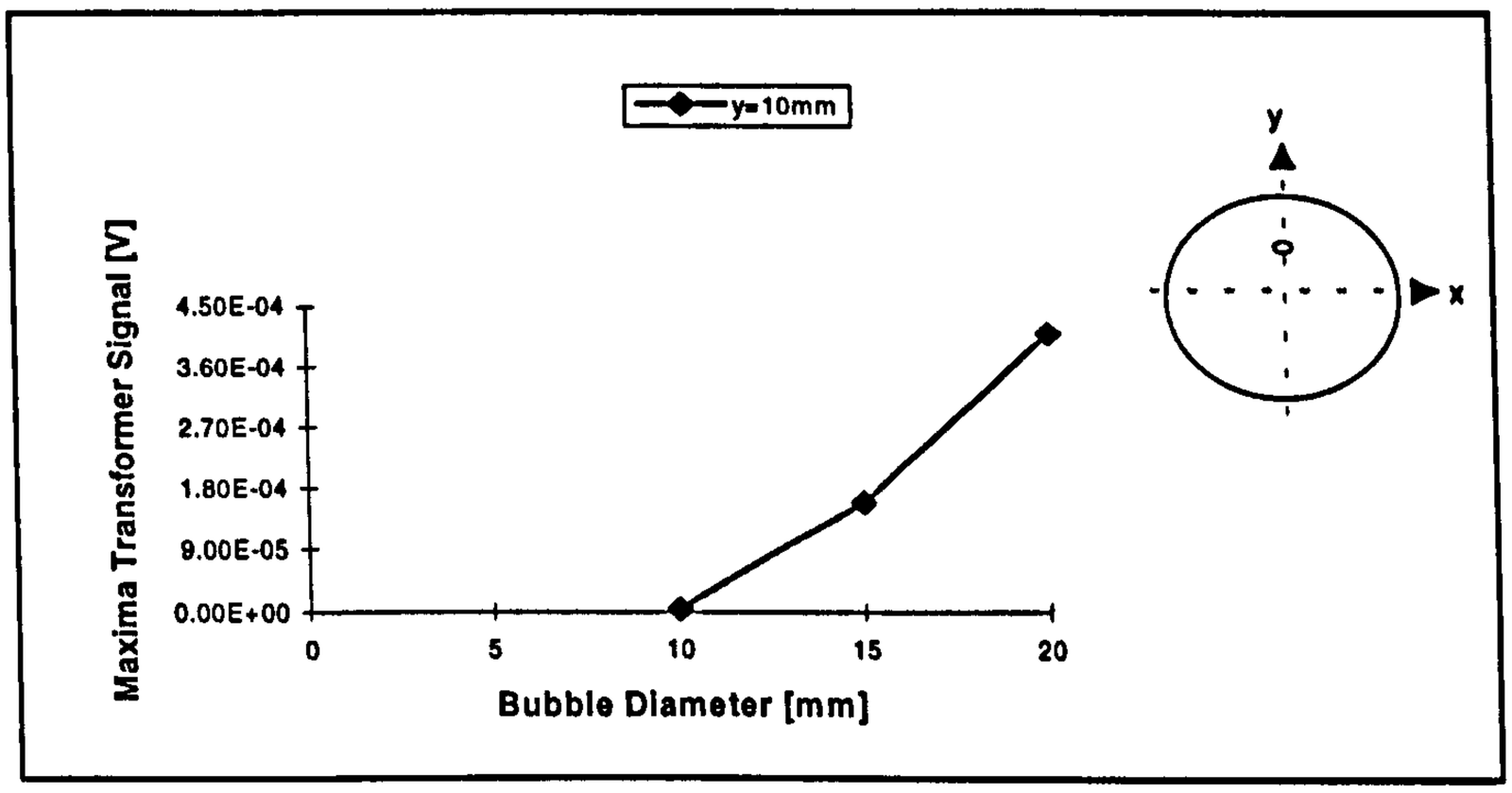

Figure 6.17b (Maxima transformer signal)

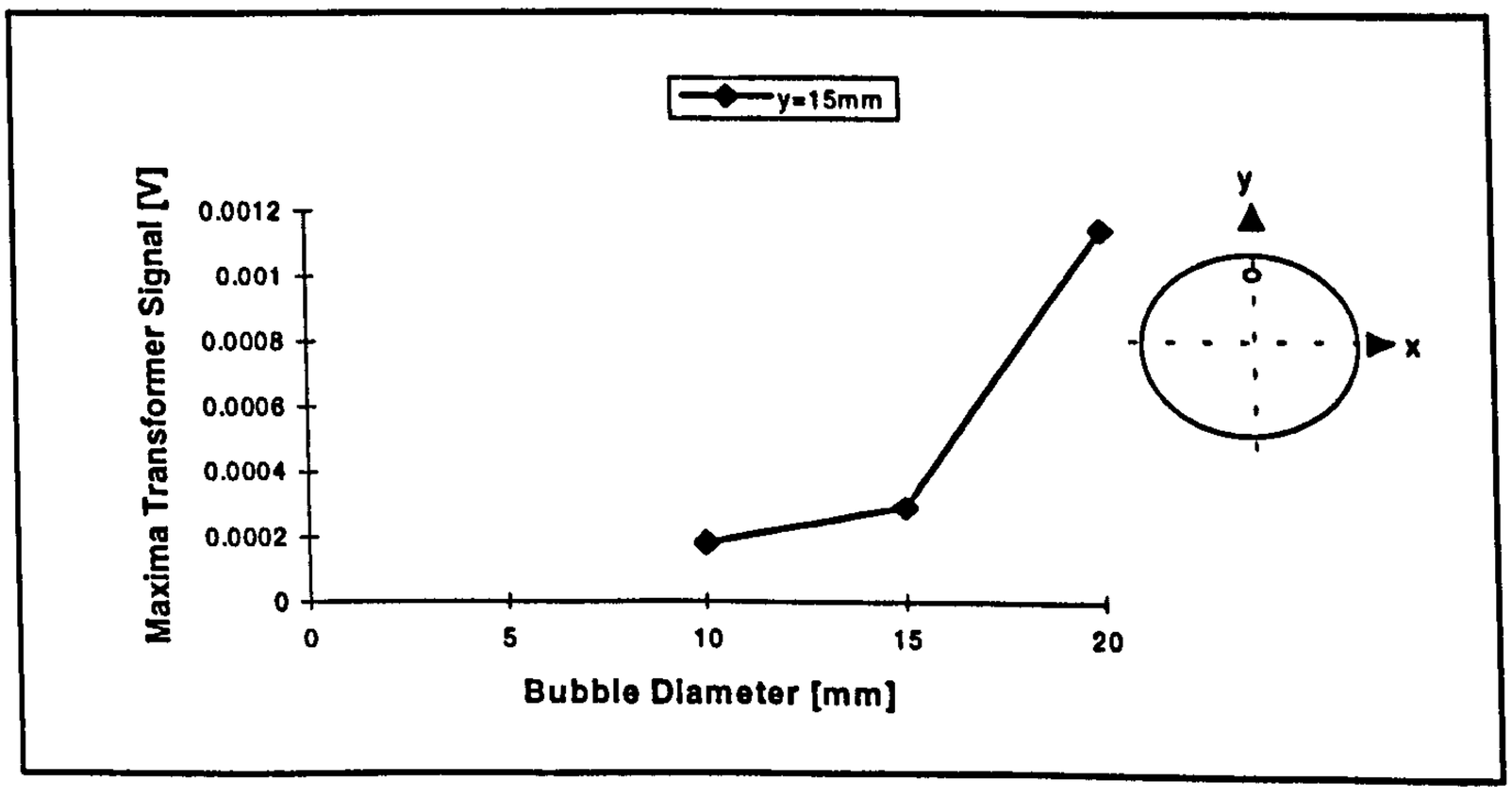

Figure 6.17c (Maxima transformer signal)

6.6.2 Experimental frequency analysis of the transformer signal

The following experiments are conducted in order to see the effect of bubbles moving through the meter with different velocities. The investigated bubble velocities varied from 0.1 *m/s* up to 0.5 *m/s*. This range secured a horizontal bubble movement only. A higher bubble velocity would introduce significant bubble vibration in the vertical direction, which is not desirable feature at this stage. The output signal of the Phase-Sensitive-Detector is fed in to the ONO-SOKKI analyser, where a Fast Fourier Transform is carried out. The corresponding power spectra are printed out and are shown in Figures 6.18 to 6.23. The particular power spectra show that the frequency of the occurring peak increases with higher bubble velocities. A correlation of peak frequencies versus bubble velocities is given in the plotted graph in Figure 6.24.

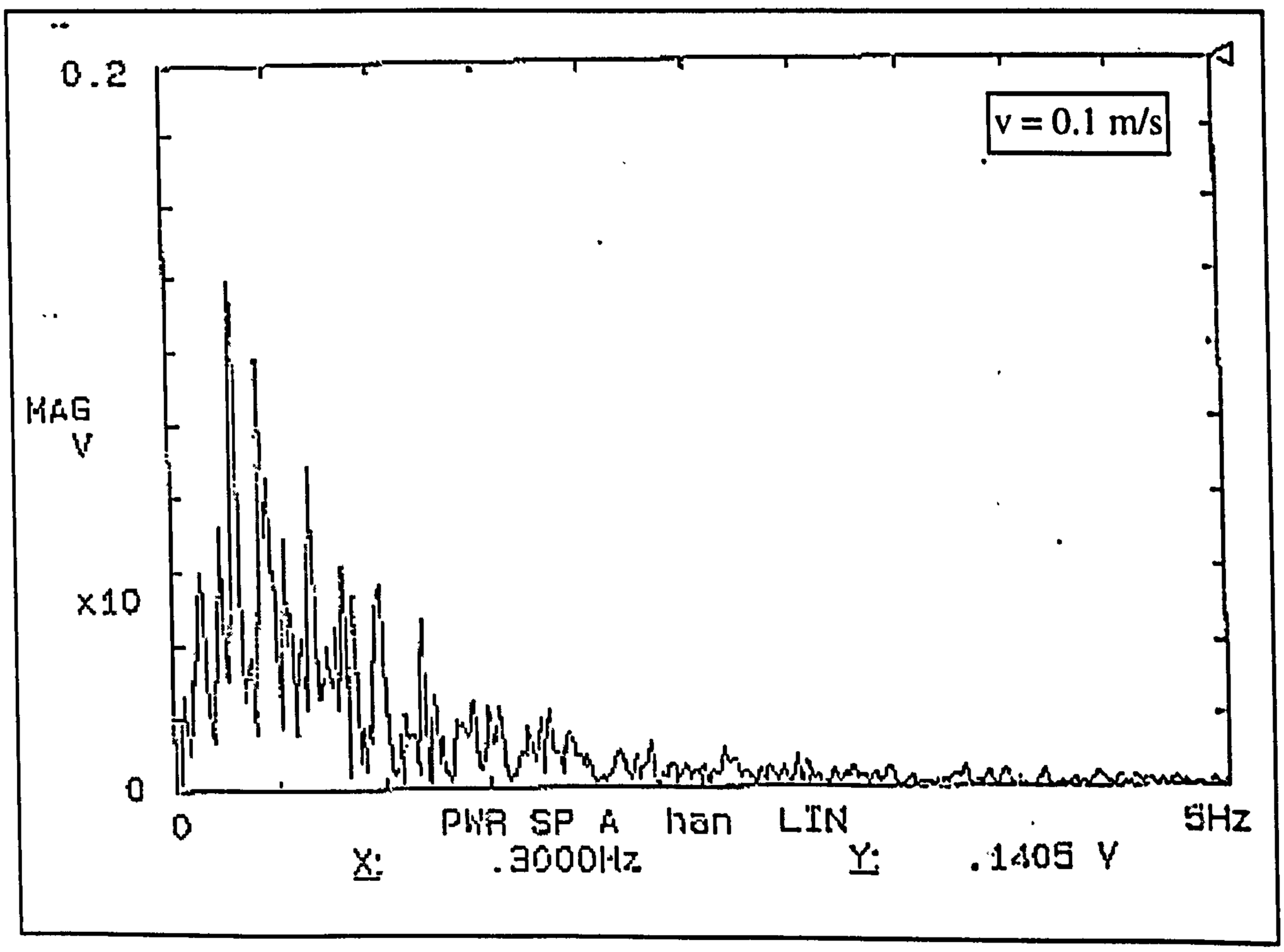

Figure 6.18 (Power spectra for bubble velocity of 0.1 *m/s*)

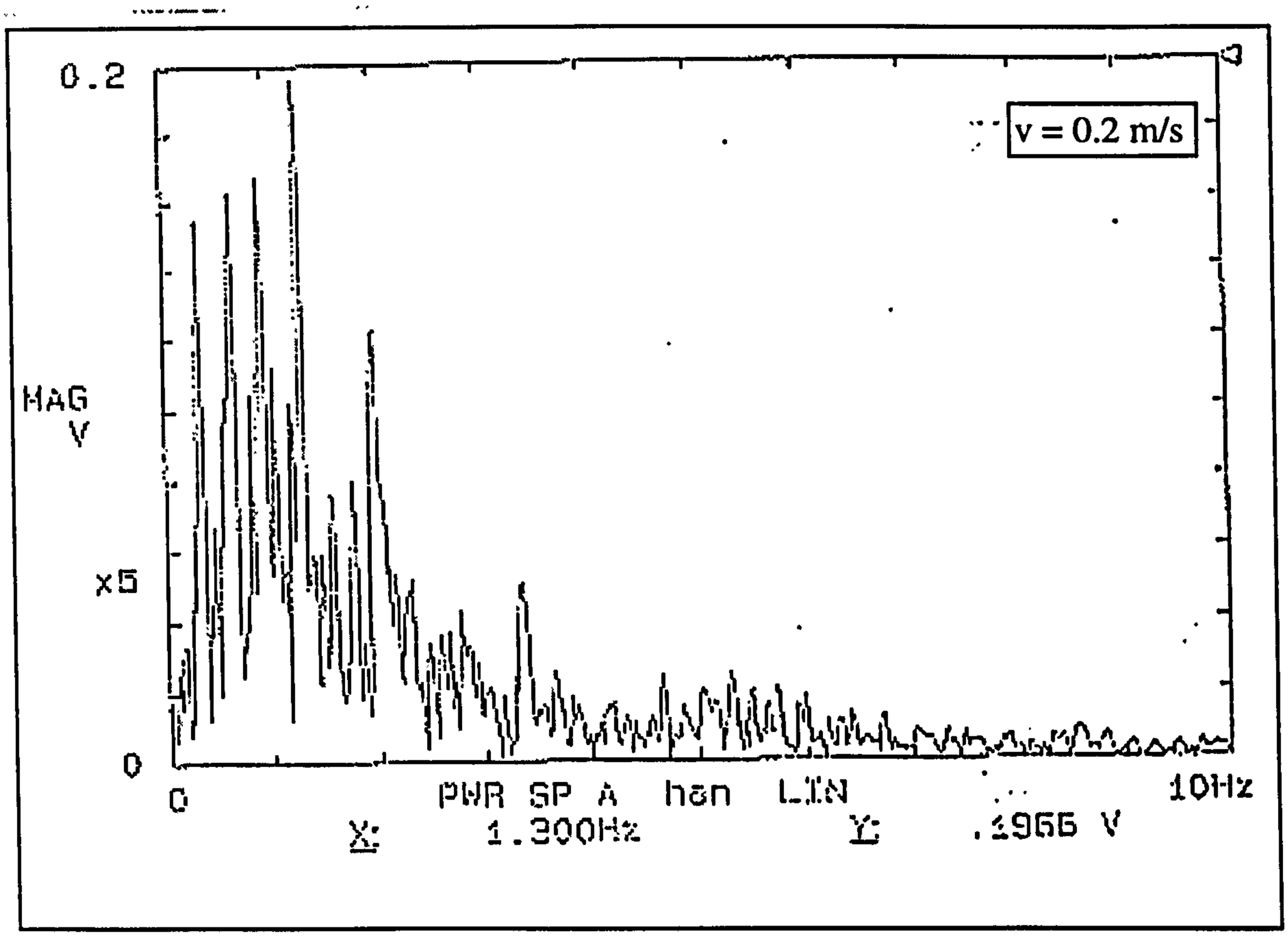

Figure 6.19 (Power spectra for bubble velocity of 0.2 m/s)

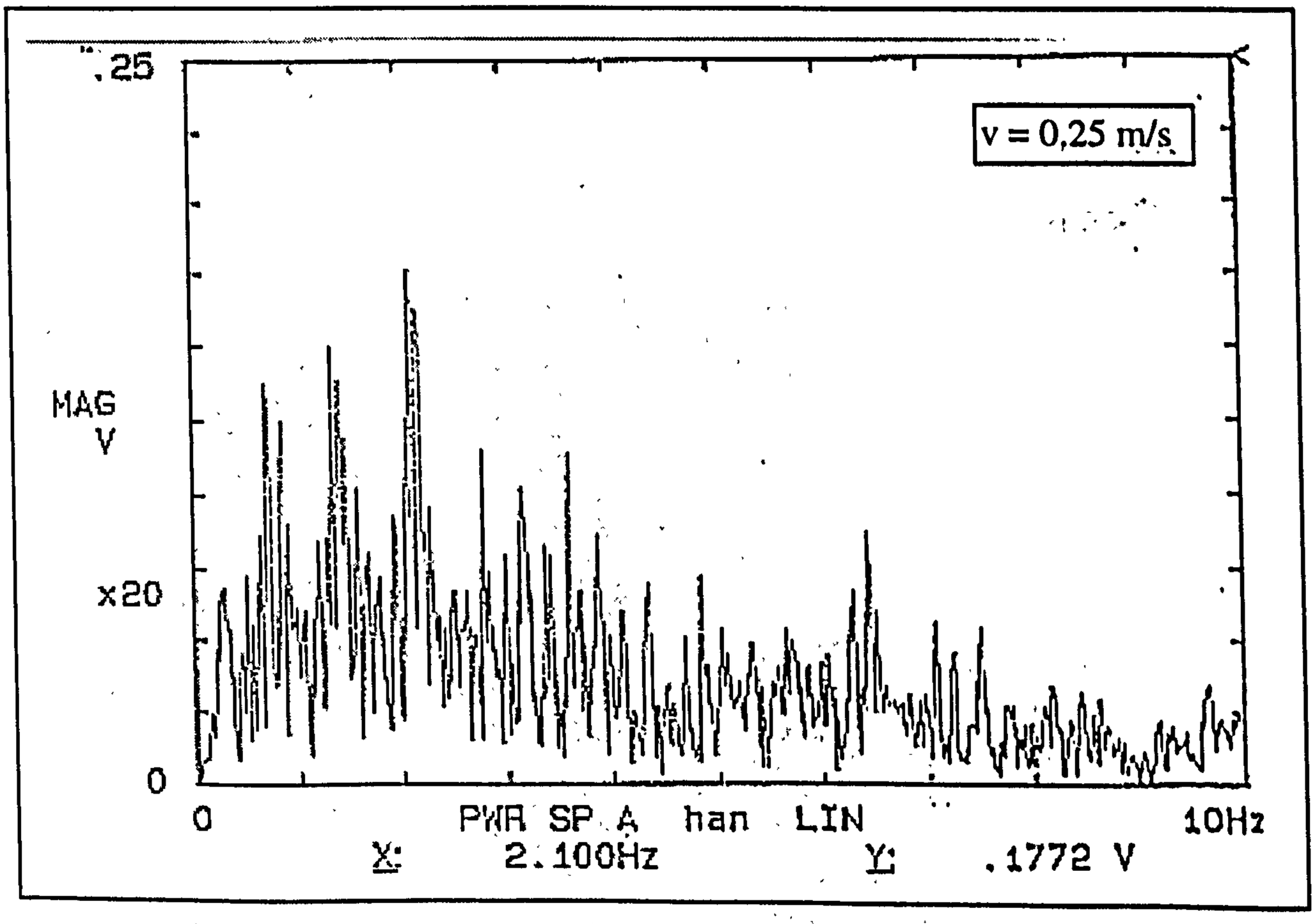

Figure 6.20 (Power spectra for bubble velocity of 0.25 m/s)

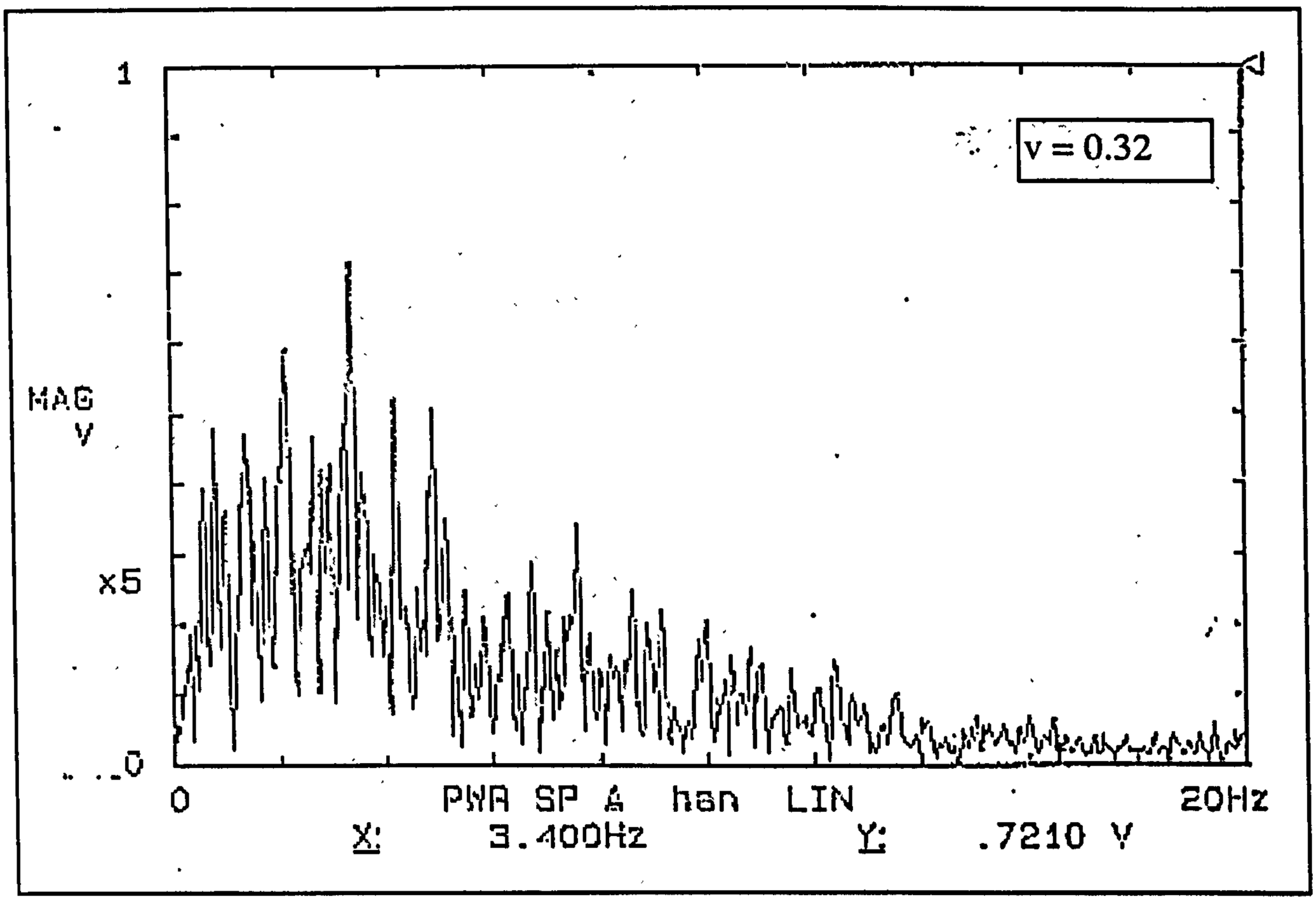

Figure6.21 (Power spectra for bubble velocity of 0.32 m/s)

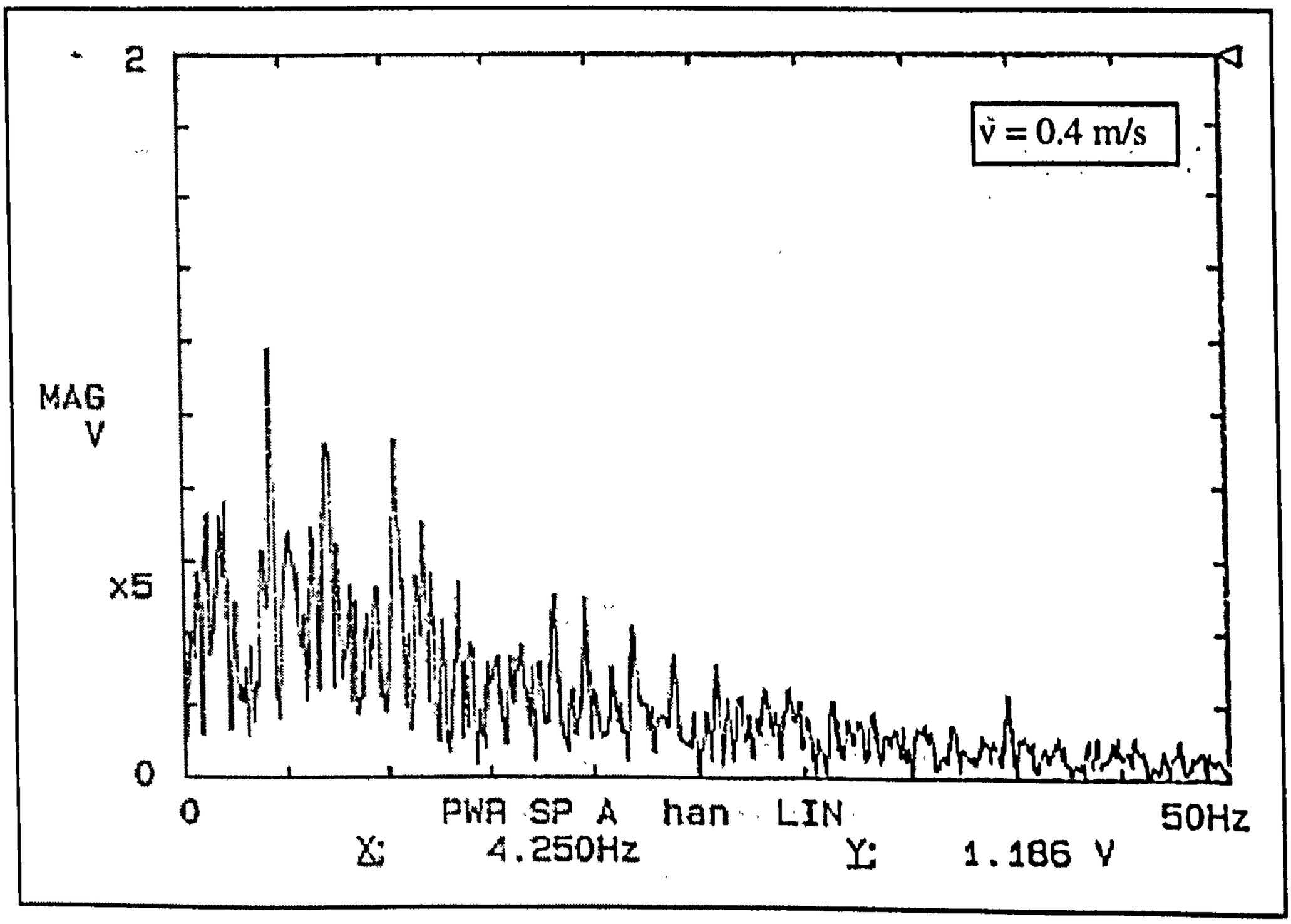

Figure 6.22 (Power spectra for bubble velocity of 0.4 m/s)

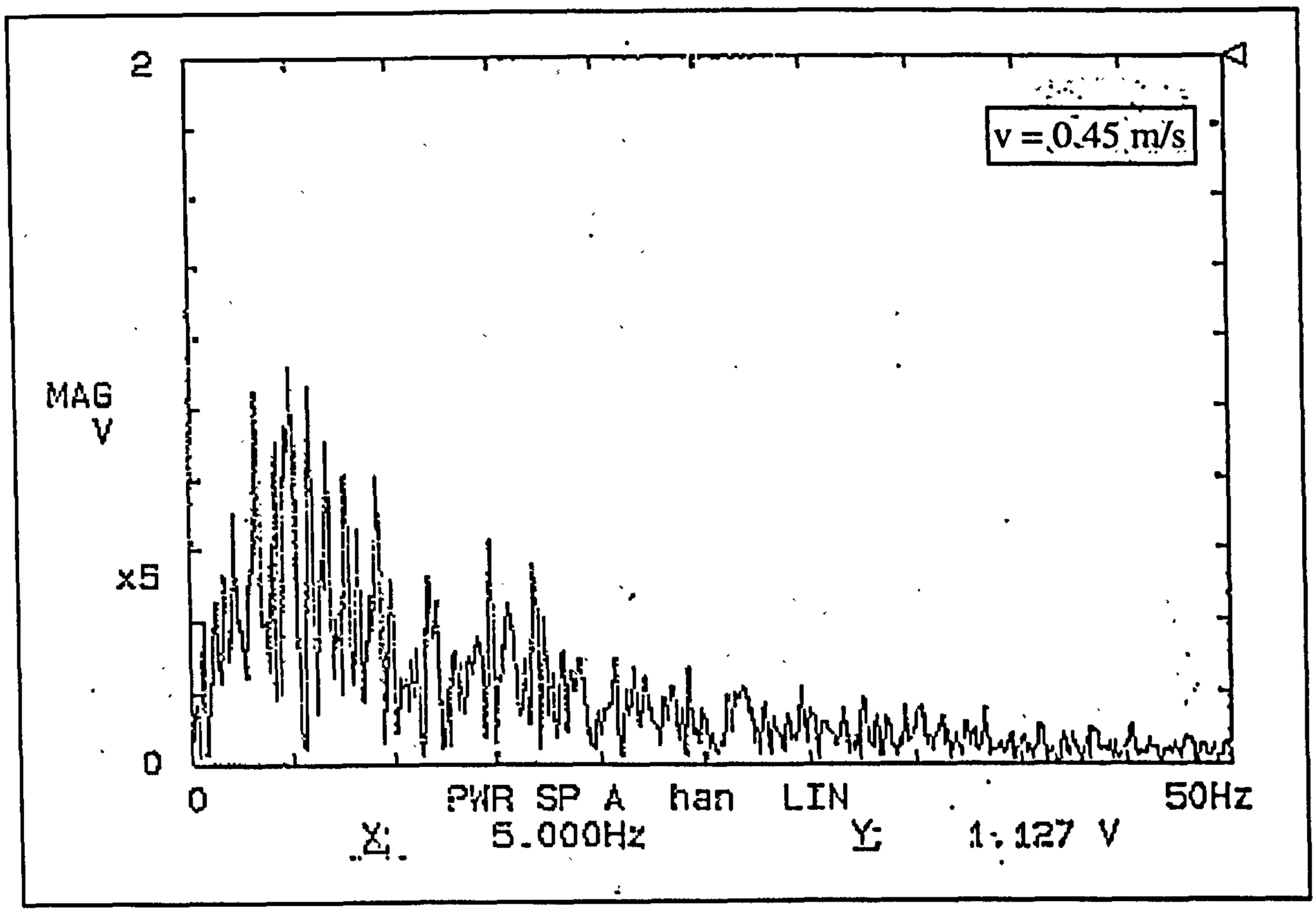

Figure 6.23 (Power spectra for bubble velocity of 0.45 m/s)

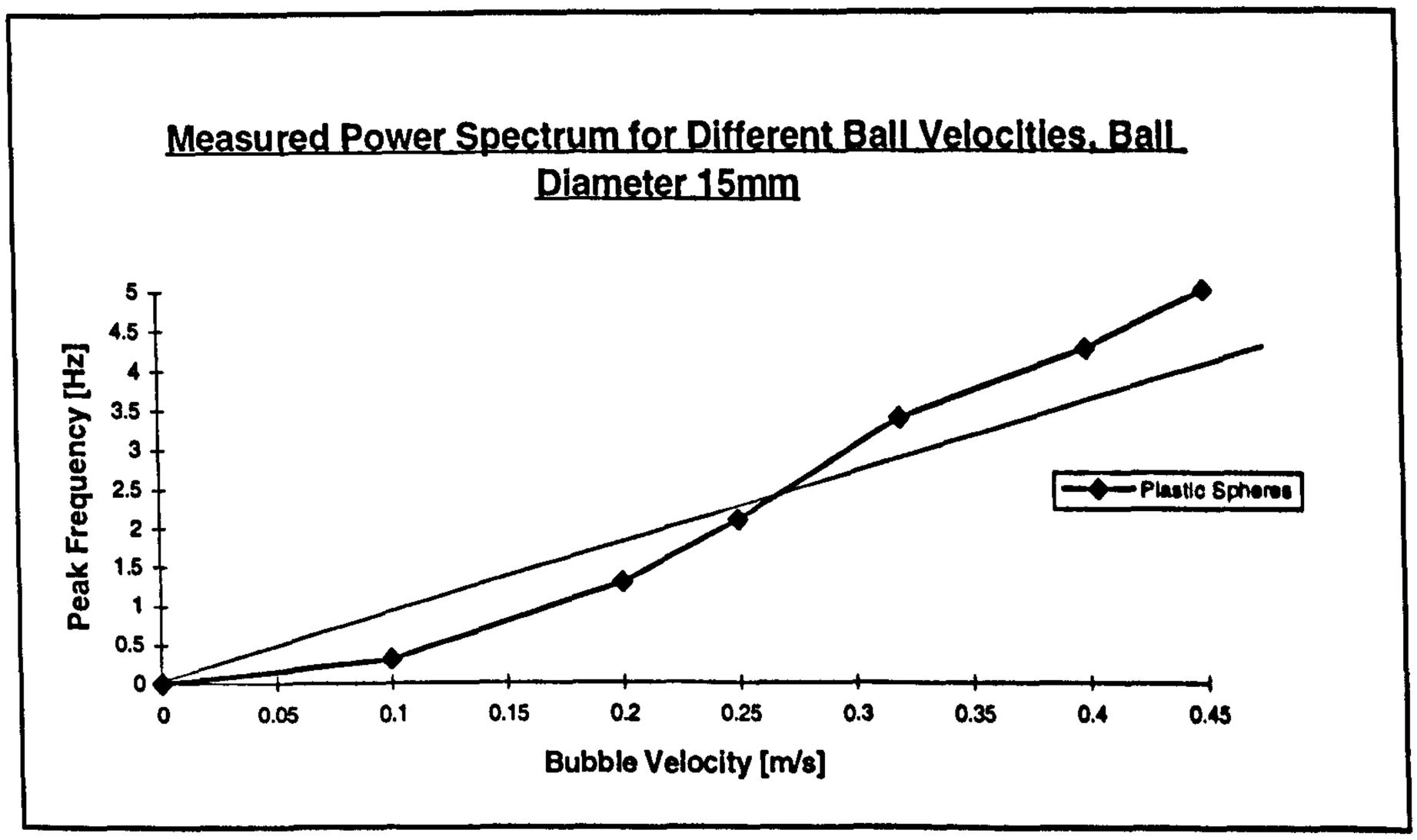

Figure 6.24

6.6 Summary

In this chapter the experimental apparatus, including rig, flowmeter, and electronics is described and explained.

Also, two different sets of experiments are carried out. In this first group of experiments the shape of the transformer signal is investigated. Although the general form of the transformer signals that are recorded agreed with the theoretically determined signals, a slight deviation, in form of overshooting, on the shape of the signal is noticed. Despite a careful rearrangement of the electrodes (because an asymmetry in the electrode arrangement is suspected) no significant improvement could be achieved. However the results in terms of magnitude of the transformer signals proved to be very close to the theoretically predicted signals and showed similar characteristics.

The second set of experiments concentrated on the behaviour of the produced power spectra for different ball speeds. It is discovered that the peak frequency of the transformer signal is related to the velocity of the bubbles passing through the meter. This provides a possibility to measure the velocity of the second phase in form of a bubble.

CHAPTER 7

EXPERIMENTS FOR INSERTED NITROGEN BUBBLES

7.1 Introduction

The results in chapter 6 showed the potential to measure the velocity of the second phase. In this chapter a set-up for a more realistic approach is implemented by having nitrogen bubbles passing through the meter.

7.2 Experimental set-up

The flowmeter used in chapter 6 is put in a vertical perspex pipe section, filled with dielectric fluid. The lower end of the pipe is connected via a hose to a pressurised nitrogen supply tank. The bubble velocity in the column is controlled by a valve connected on to the plastic hose. The used arrangement is shown in Figure 7.1. The velocity of the bubbles is measured with a video camera. The video camera is equipped to review the recorded experiments in pictures for every 0.02 seconds. The electronic set-up (excitation as well as detection electronics) is identical to the one used in chapter 6.

7.3 Experiments carried out

In Figure 7.2 the noise spectra for zero flow is printed. It can be seen that the noise has a continuous magnitude over the bandwidth. The next step is to insert gas bubbles with different velocities and to examine the corresponding frequency analysis. The bubble velocity range is between 0 and 0.38 *m/s*. In Figures 7.3 to 7.8 the power spectra and

corresponding pictures of bubble flow are plotted. These clearly reflected the same coherence as seen in chapter 6. The peak frequency of the analysed fourier transform depends on the velocity of the bubbles. In Figure 7.9 a comparison of the relation between peak frequency versus bubble velocity gained from the experiments achieved in chapter 6 and the above results show good outcomes.

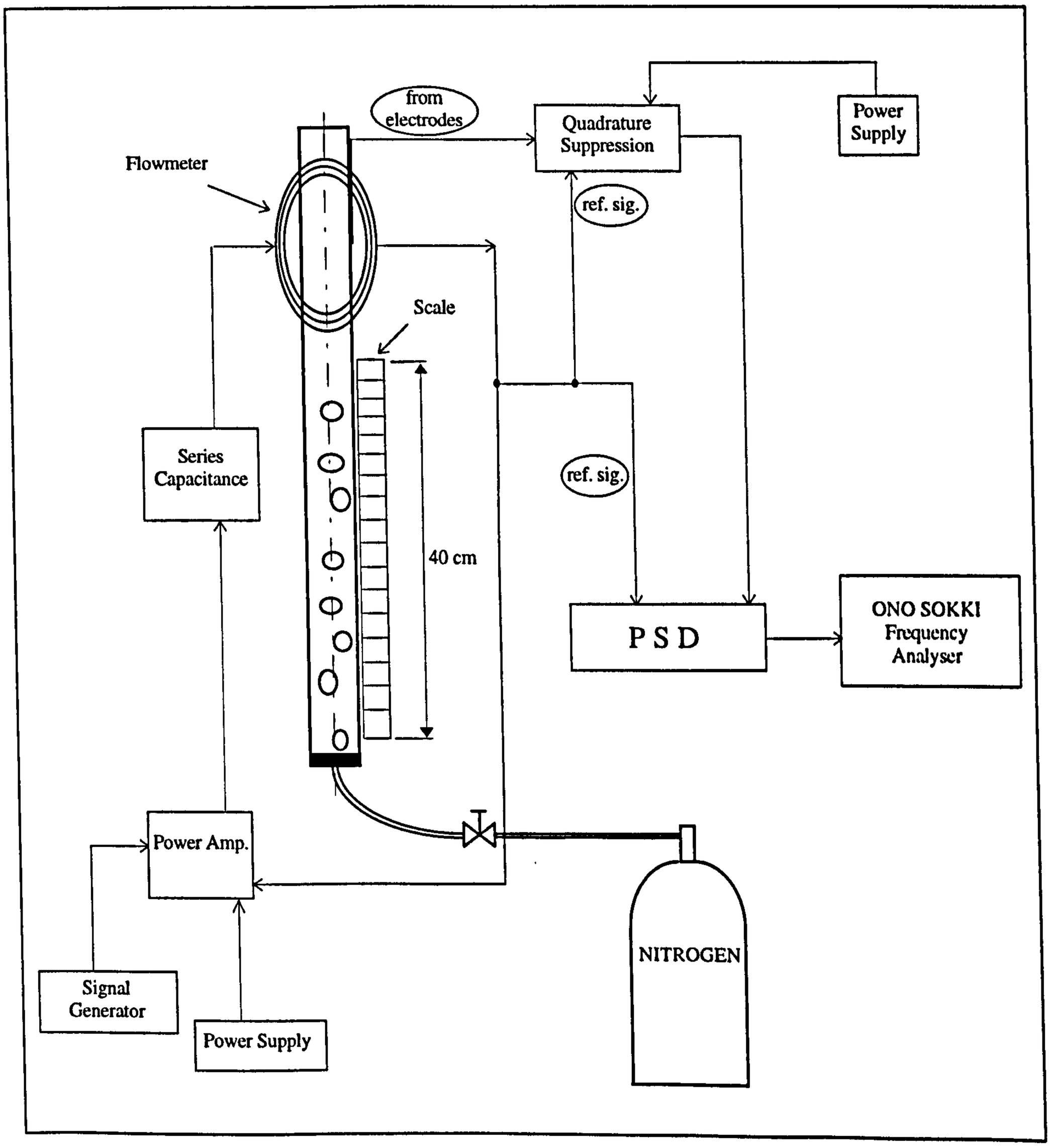

Figure 7.1

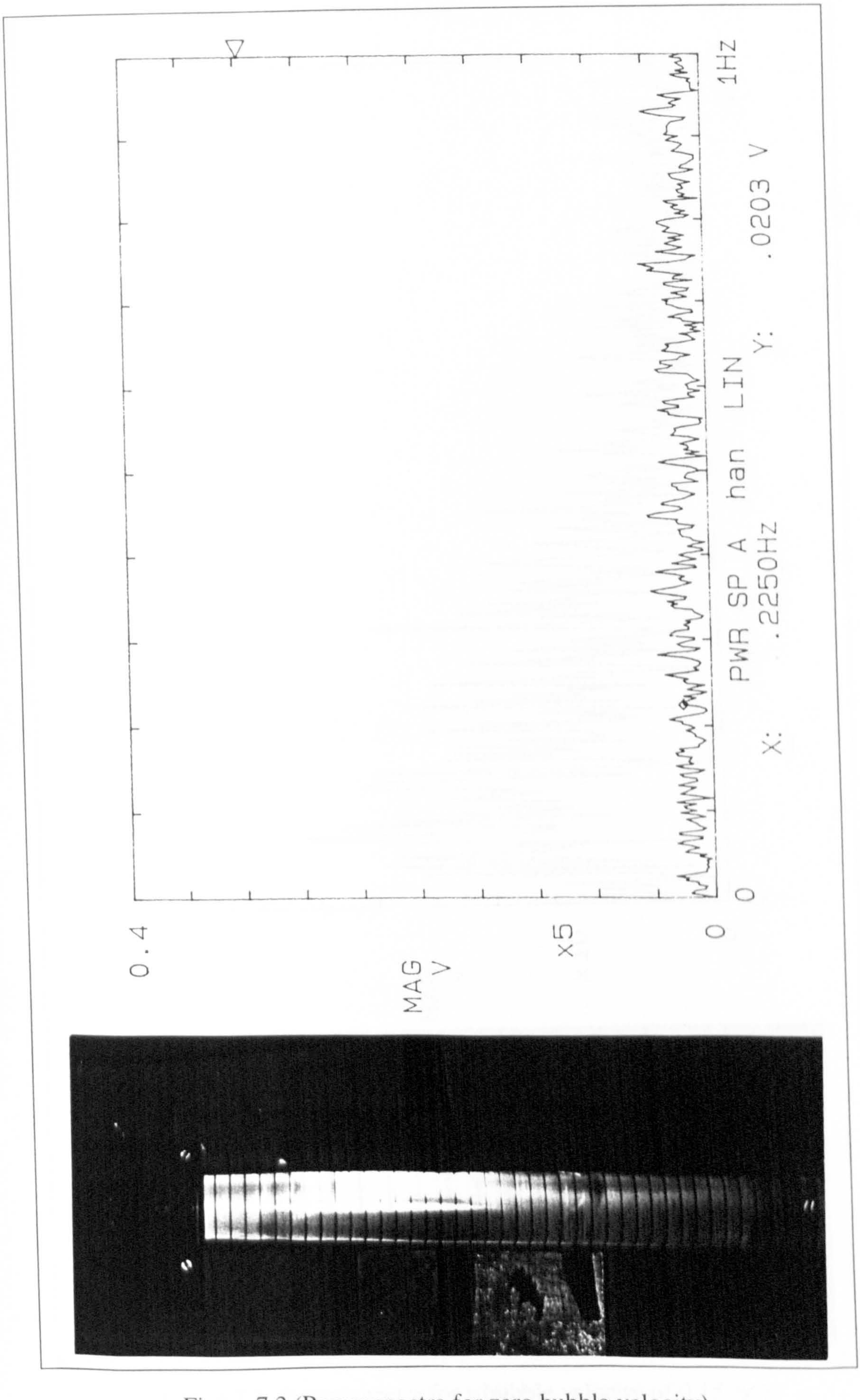

Figure 7.2 (Power spectra for zero bubble velocity)

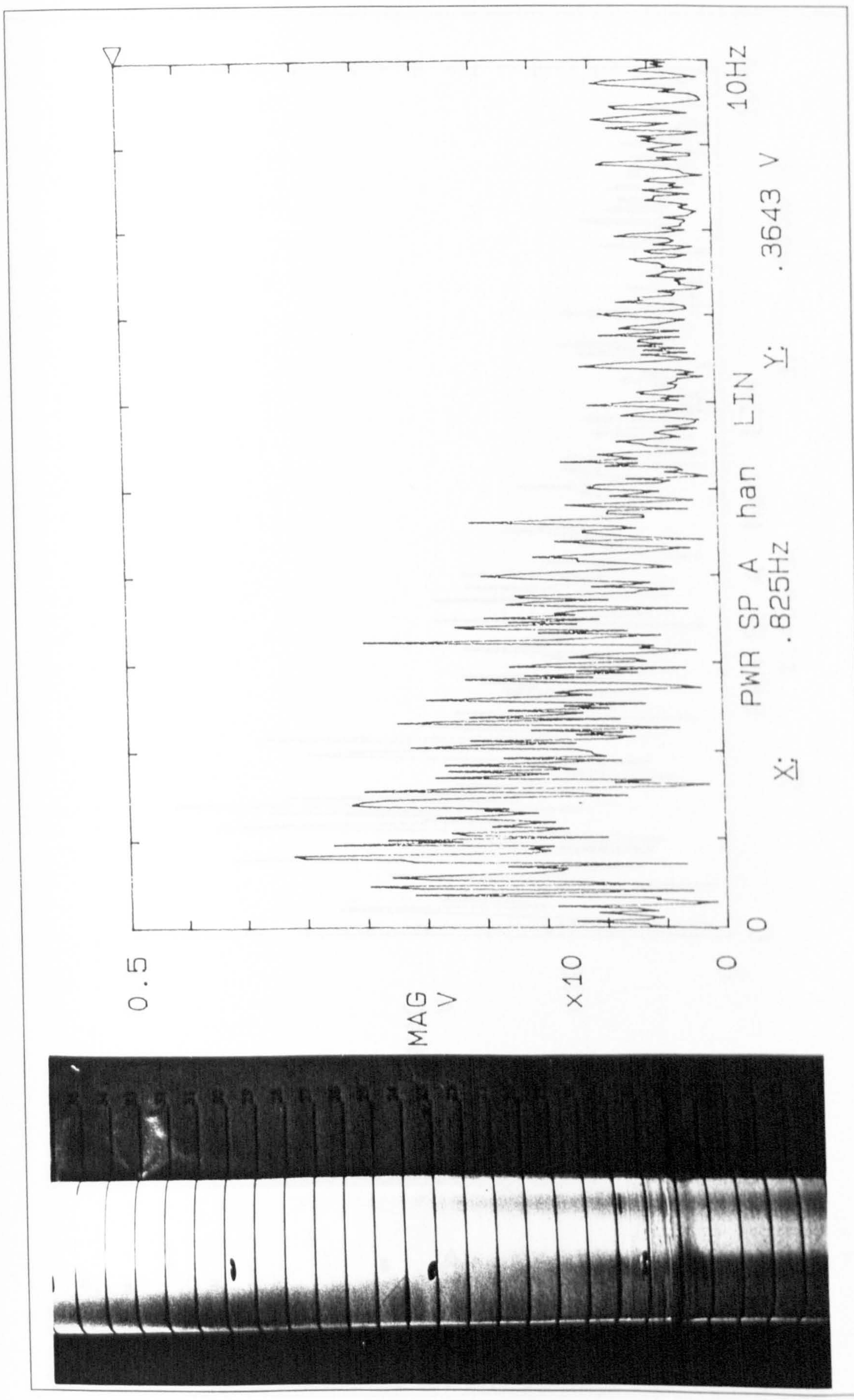

Figure 7.3 (Power spectra for a bubble velocity of 0.15 $^{m}/_{s}$)

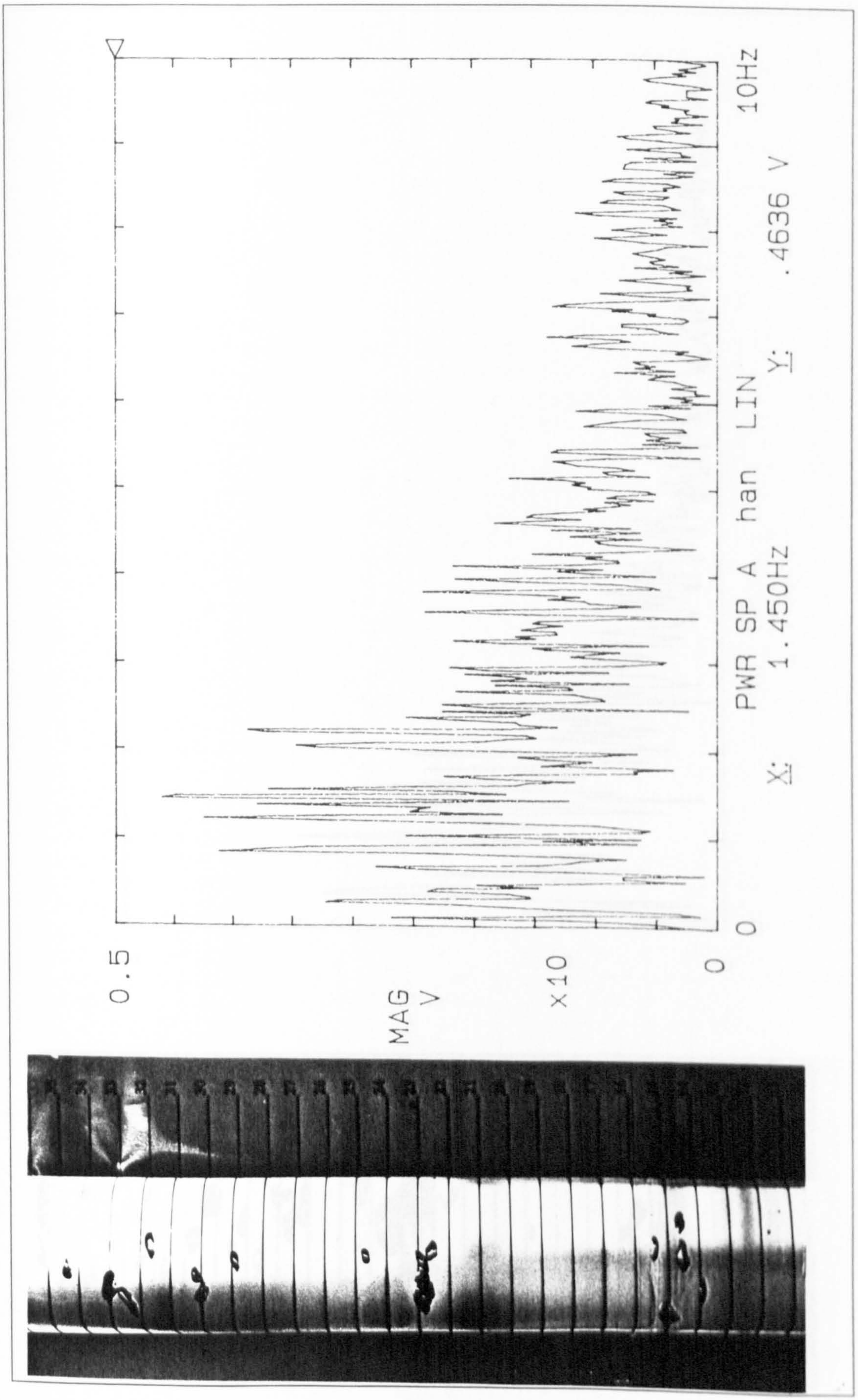

Figure 7.4 (Power spectra for a bubble velocity of 0.2 $^{m}/_{s}$)

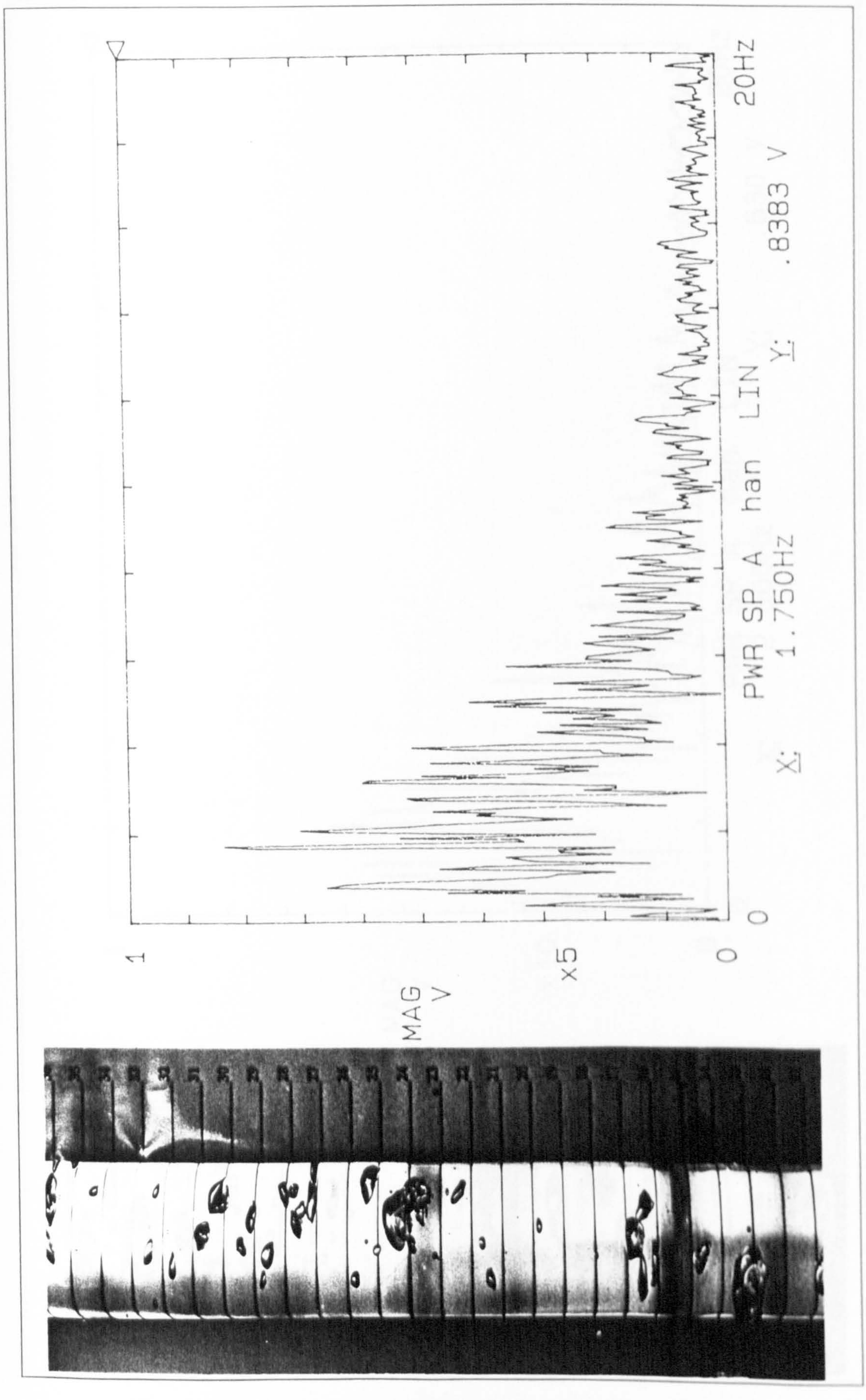

Figure 7.5 (Power spectra for a bubble velocity of 0.24 $^{m}/_{s}$)

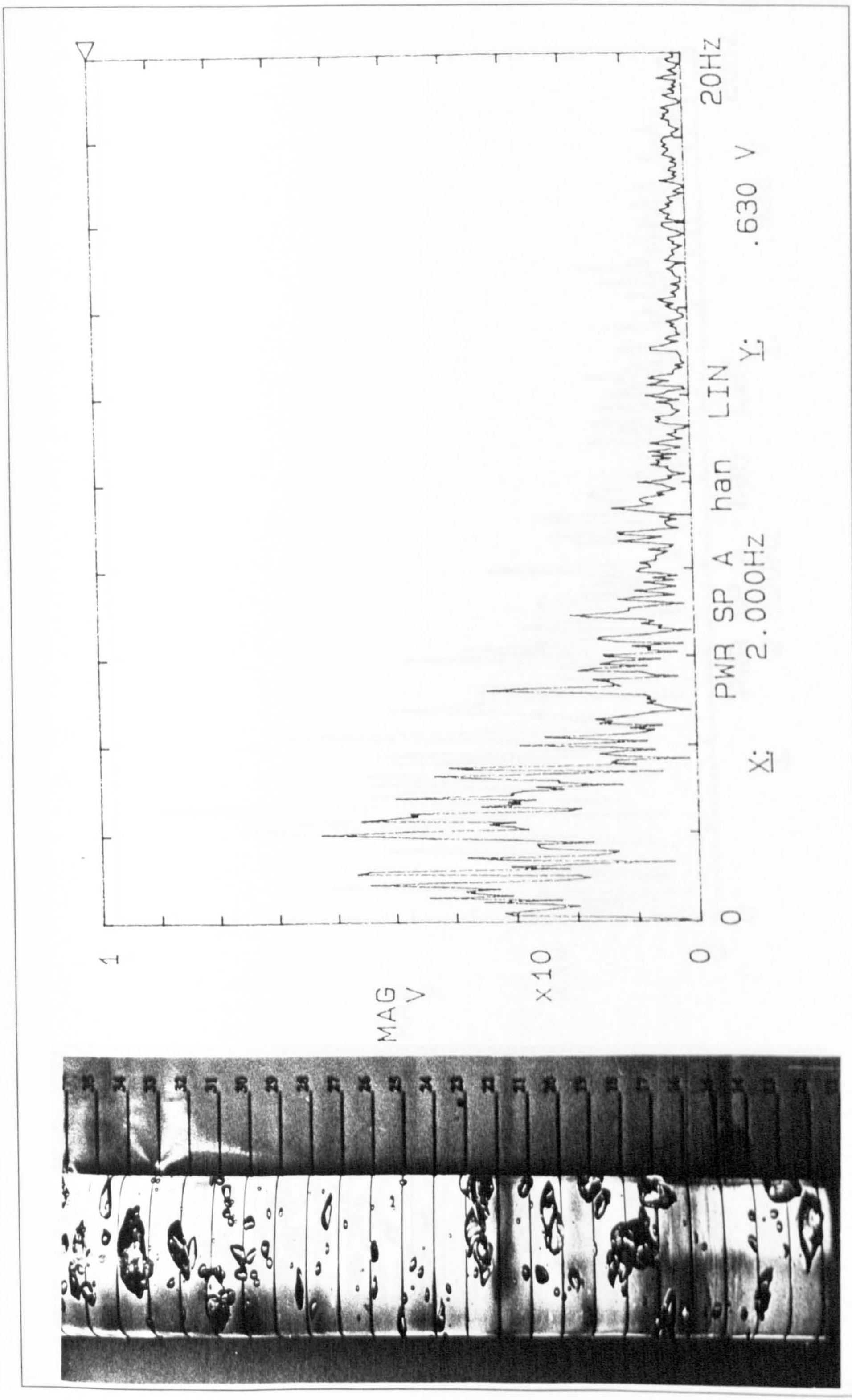

Figure 7.6 (Power spectra for a bubble velocity of 0.28 $^{m}/_{s}$)

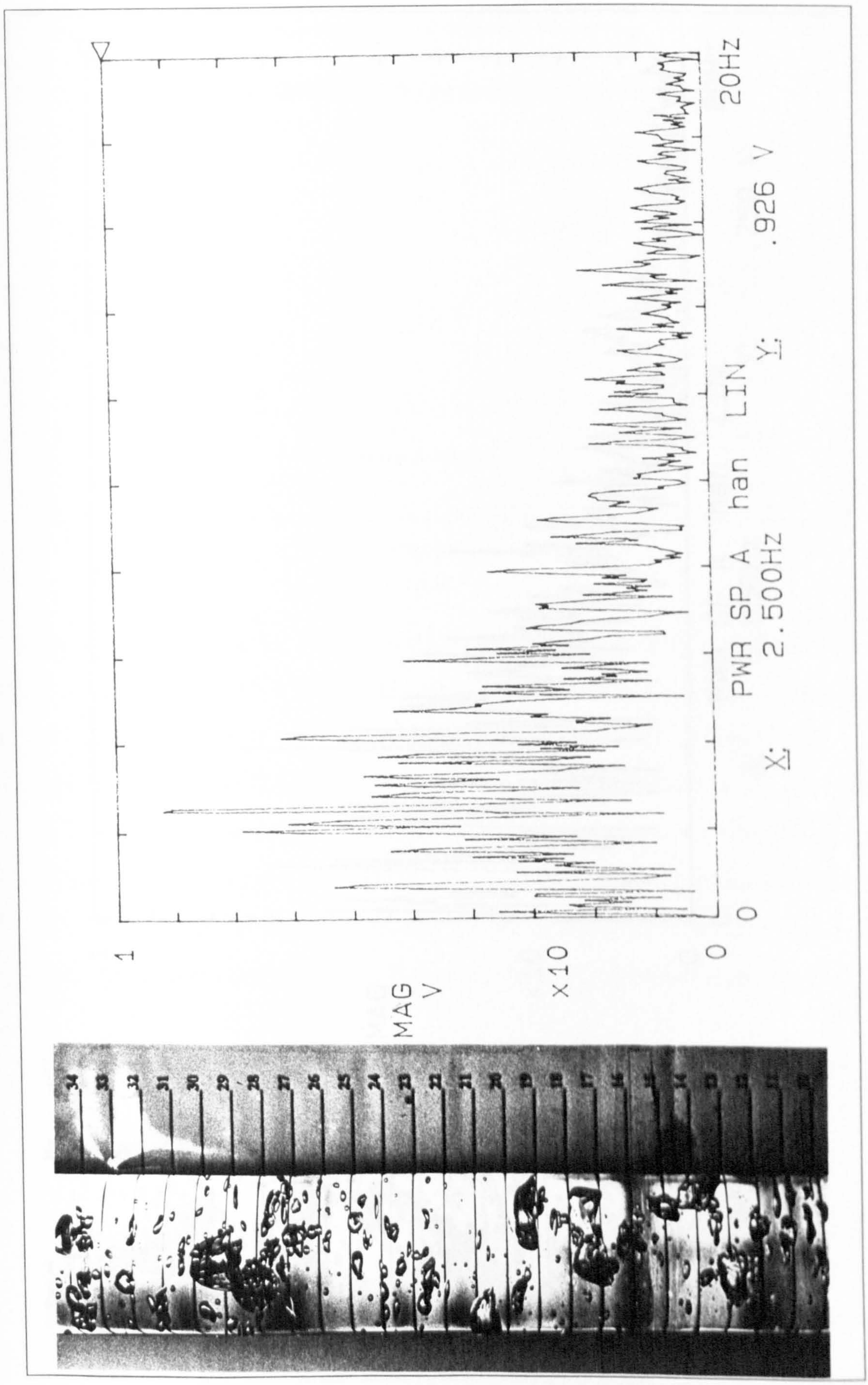

Figure 7.7 (Power spectra for a bubble velocity of 0.3 $^{m}/_{s}$)

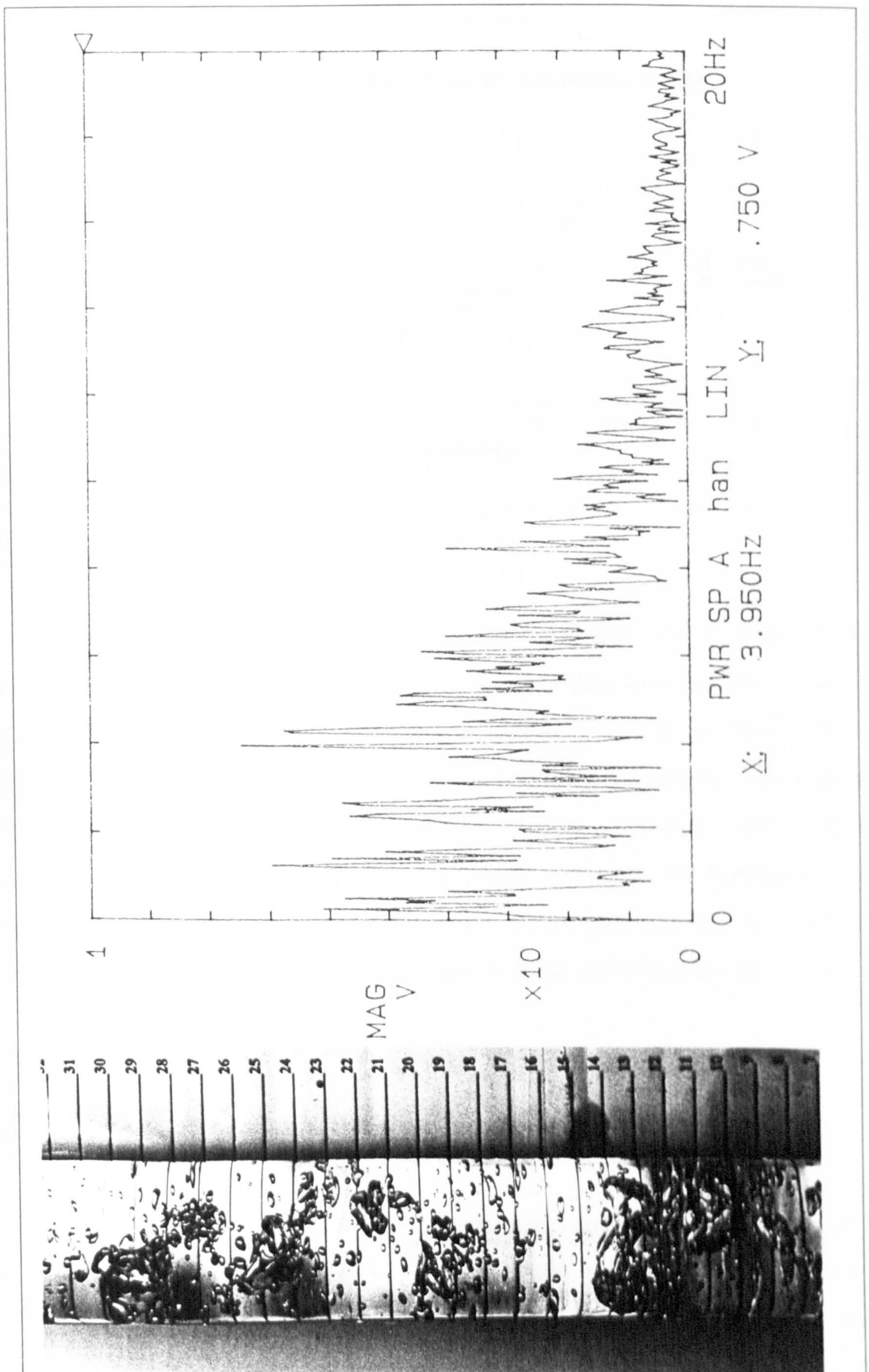

Figure 7.8 (Power spectra for a bubble velocity of 0.37 $^{m}/_{s}$)

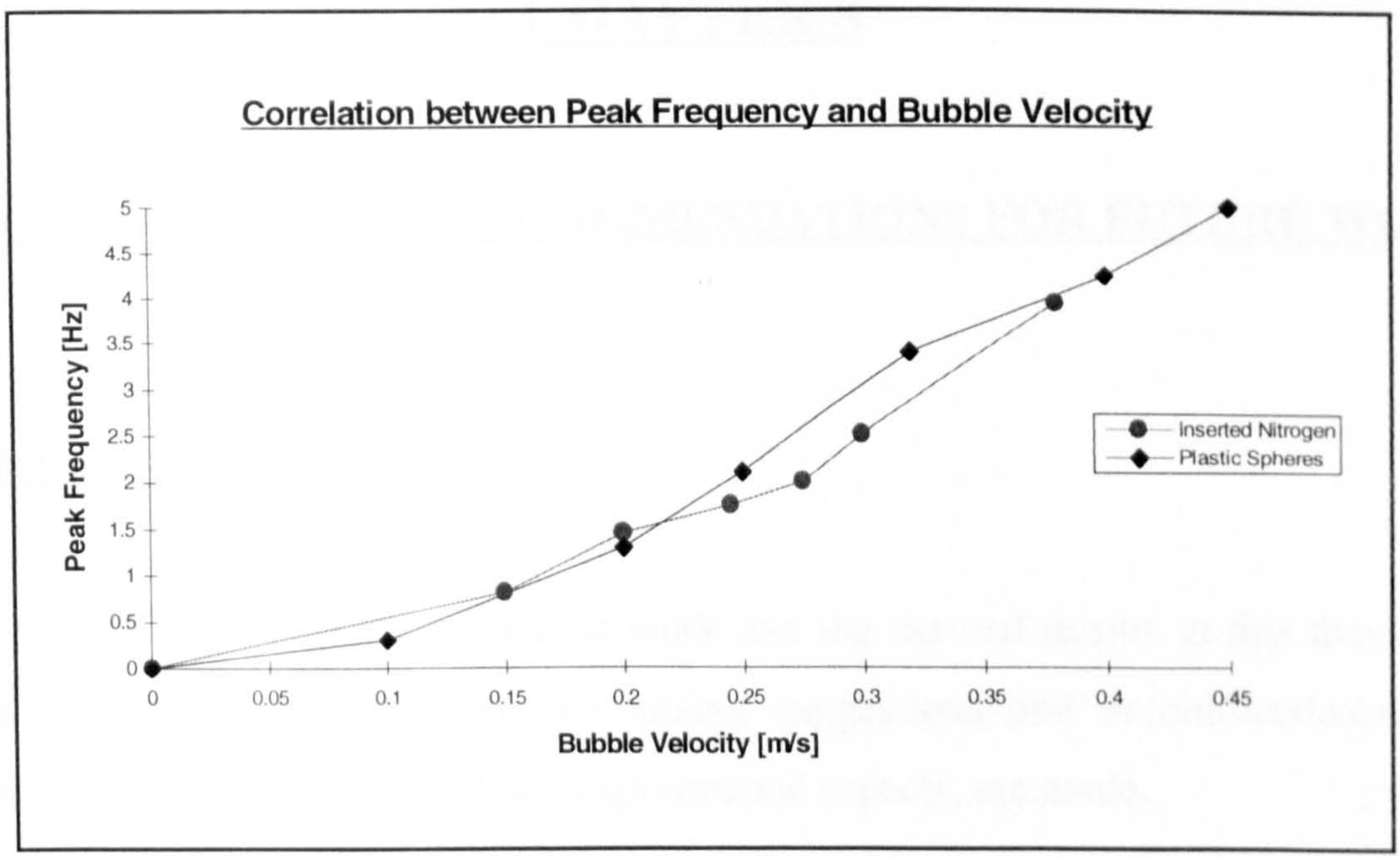

Figure 7.9

From equation 4.21 and the Figures 4.6 and 4.7 in chapter 4 it is expected that the power of the spectra is to increase with decreasing bubble spacing. This is the fact for very low bubble velocities and therefore gas bubbles which are inserted with a clear distance from each other (Figure 7.3 to 7.5). By analysing the results of the experiments in Figure 7.6 to 7.8 the power does not increase with decreasing bubble spacing. A clear reason for this occurrence could not be found. But a possible explanation could be that the gas bubbles for higher velocities are of different size and are much closer together, and in return this could alter the actual shape of the transformer signal.

7. 4 Summary

In this chapter experiments are conducted which examined the behaviour of the power spectra produced by gas bubbles of various speeds passing through the meter. The outcome of the experiments showed quantitatively the same response as the results in chapter 6. Because of the relatively high discontinuous noise level within the signal a more distinctive and stable power spectra could not be achieved.

CHAPTER 8

8 CONCLUSIONS AND RECOMMENDATIONS FOR FUTURE WORK

8.1 Introduction

This chapter rounds up the conducted work and the derived results in this thesis, and gives final conclusions. Furthermore arising suggestions and recommendations for future work, both on theoretical and experimental aspects, are made.

8.2 Conclusions of work

(i) A theoretical model is developed that investigated the behaviour of the quadrature component of an electromagnetic flowmeter that arises when a bubble (modelled in the form of a dipole) passes through the meter. The cause of such a signal is due to the fact that a bubble passing through the meter would unbalance existing eddy currents. The model predicted a signal with a distinctive shape. It also predicted that the magnitude of the signal is dependent on the magnetic field strength, excitation frequency, bubble size and bubble position. All influencing factors have a linear effect on the signal magnitude apart from bubble diameter which is cubed. The magnitude of the signal does not depend on the velocity of the bubble.

(ii) An investigation shows that when using large area electrodes for signal detection the position of maximum transformer signal does slightly change with the circumferencial position of the bubble in the pipe section.

(iii) A numerical investigation of this transformer effect is made by using the Finite Element Methods software package ANSYS. In a first attempt a dipole is modelled in order to predict and verify the transformer signal of concern. It is found that the shape of the signal is identical to analytical results and the signal magnitude altered by 30%. In a second step a bubble is modelled in form of spheres of different diameters. The results for the transformer signal for identical bubble diameter are virtually the same as the dipole modelled results.

(iv) A theoretical frequency analysis of the transformer signal generated by a bubble passing through the meter is performed. Fast fourier transforms are carried out on a set of signals arising when successive bubbles with certain separations are moving through the meter with various velocities. It is found that the peak frequency is directly proportional to the velocity of the bubbles. As higher the bubble velocity the higher the peak frequency.

(v) In a further investigation it is proved that the transformer signal for 1500 *Hz* excitation frequency does not distort the resulting transformer signal.

(vi) Although this work is trying to make use of the transformer signal, a brief investigation is carried out to see the effect of the second phase on the flow signal. A calculation predicted a negligible effect on the flow signal. In the actual experiments this prediction is verified when no voltage is detected on the flow signal.

(vii) For experiments carried out, the expected shape of the transformer signal is recorded. A comparison of peak signals between numerical and experimental solutions (for bubble diameters of 15 *mm*) indicated a good agreement. A slight overshoot of the signal is noticed before it approached zero value. This unexpected effect is thought to be due to asymmetric adjustment of the electrodes onto the flow conduit. Unfortunately a careful readjustment did not remove this effect.

(viii) The frequency analysis carried out on the experiments (that used beads fixed on a very thin fishing line and injected nitrogen bubbles) showed similar qualitative results as predicted in the theoretical simulation. A dependence of bubble velocity and peak frequency on the power spectra is obvious. Unfortunately a linear dependency between these two factors could not be achieved. A relatively high level of introduced noise onto the power spectra impaired the quality of the power spectra.

8.3 Recommendations for future work

This work laid the basis for the development of an electromagnetic flowmeter for two-phase flow measurement of insulating fluids. With regards to further work to develop and improve this method, suggestions are given below.

(i) In order to improve the quality of the power spectrum a method that would lead to a significant reduction in noise would be beneficial. Because noise is mainly introduced due to charge separation, coming from the moving bubble, noise reduction would be a difficult task.

(ii) An increase in bubble velocity (possibly up to 3 *m/s*) would be desirable to complete the relationship between peak frequency and bubble velocity over a wider range.

(iii) Eventually an investigation and tests of this method in a real two-phase flow (with a dielectric main phase and gaseous second phase) situation should be carried out. For testing this meter, the extraction of velocity information for each flow phase should be considered.

(iv) A further analytical or numerical investigation of end-effects and their implication on the transformer signal would be of use.

(v) For real two-phase flow conditions the bubble separation can be very small. This can be seen in flow regimes photographed and shown in Figures 7.3 to 7.6. Often two or even more bubbles move at the same axial position. This occurrence would obviously affect the transformer signal, both in magnitude and shape. An overlapping effect can be expected. To understand these issues and possible consequences a theoretical examination could yield to vital information.

(vi) To obtain a more precise result for the transformer signal, a more in depth investigation of the eddy current field should be considered.

(vii) Because of occurring minor phase shifts due to electrostatic pick-up on the coils, a method of accurate metering these phase shifts would provide an exact adjustment of the lock-in amplifier. This would avoid even very small leakage of the transformer signal in to the flow signal.

REFERENCES

[1] Faraday M. (1832)
Experimental researches in electricity
Phil. Tran. Roy. Soc. (London)

[2] Williams E.J. (1930)
The induction of e.m.f.'s in amoving liquid by a magnetic field and its application to an investigation of the flow of liquids
Proc. Phys. Soc., Vol. 42

[3] Fabre P. (1932)
Use of induced e.m.f.'s for recording speed variations of liquid conductors, A new blood flow measurement without palette
C.R. Acad. Sci., Paris, Vol. 194

[4] Kolin A. (1936)
An A.C. induction flowmeter for measurement of blood flow in intact blood vessels.
Proc. Soc. Exp. Biol., NY 1941 Vol. 46

[5] Denison A.B. et al. (1955)
A square wave electromagnetic flowmeter for application to intact blood vessels
Circ. Res., Vol. 3

[6] Yanof H.M. and Salz P. (1960)
A trapezodial-wave electromagnetic blood flowmeter
USAEC Report UCRL-9204

[7] Shercliff J.A. (1962)
The Theory of Electromagnetic Flow-Measurement
Cambridge University Press

[8] Bevir M.K. (1970)
The Theory of induced Electromagnetic Flowmeters
PhD-Thesis Warwick University

[9] Ketelsen B. (1964)
Nach dem Induktionsprinzip arbeitende Stroemungsmesseinrichtung
Deutsches Patentamt, Auslegeschrift 1 295 223

[10] Hemp J. (1975)
Improved magnetic field for an electromagnetic flowmeter with point electrodes
J. Phys. D: Appl. Phys., Vol. 8

[11] Al-Kahazraji and Baker R.C. (1979)
Analysis of the performance of three large-electrode electromagnetic flowmeters
J. Phys. D: Appl. Phys., Vol. 12

[12] O'Sullivan V.T. and Wyatt D.G. (1983)
Computation of electromagnetic flowmeter charactreistics from magnetic field data: III. Rectiliniar weight functions
J. Phys. D: Appl. Phys., Vol. 16

[13] Al-Kahazraji Y.A. (1979)
Electromagnetic flowmeters with large electrodes
Phd Thesis, London University

[14] Cox T.J. and Wyatt D.G. (1984)
An electromagnetic flowmeter with insulated electrodes of large area

J. Phys. E: Instrum., Vol 17

[15] Hemp J. (1990)
Theory of Eddy Currents in Electromagnetic Flowmeters
J. Phys. D: Appl. Phys., Vol. 24

[16] Baker R.C. (1968)
Solutions of electromagnetic flowmeter equation for cylindrical geometries
Brit. J. Appl. Phys. (J. Phys. D), Ser. 2, Vol. 1

[17] Cushing V. (1952)
Induction Flowmeter
Rev. Sci. Instr., Vol. 29, Nr. 8

[18] Cushing V. (1958)
Induction Flowmeter
Rev. Sci. Instr. Vol. 29, Nr. 8

[19] Cushing V. (1963)
Magnetoelectric Flowmeter
Rev. Sci. Instr., Vol. 35, Nr. 4

[20] Cushing V. (1965)
Electromagnetic Flowmeter
Rev. Sci. Instr., Vol.36, Nr.8

[21] Hentschel R. (1973)
Ueber induktive Durchflussmessung mischleitender und isolierender Fluessigkeiten
Dissertation, Techn. Universitaet Hannover

[22] Al-Rabeh R.H., Baker R.C., Hemp J. (1978)
Induction flow-measurment theory for poorly conducting fluids
Proc. R. Soc. A., Vol. 361

[23] Al-Rabeh R.H. (1981)
The theory and performance of electromagnetic flowmeters
PhD Thesis, London University

[24] Codazzi D. and Mioque J.Y. (1986)
Electromagnetic flowmeter with capacitive signal pick-off
Etudes et Fabrication Dowell Schlumberger

[25] Barnes D.C. (1991)
Design and testing of electromagnetic flowmeter for use within dielectric fluids
Schlumberger internal report

[26] Amare T. (1994)
Electromagnetic Flowmeter for Dielectric Liquids
PhD Thesis, Cranfield University

[27] Heineman J.B., Marchaterre J.F., and Mehta S. (1963)
Electromagnetic Flowmeters for Void Fraction Measurement in Two-Phase Flow
Rev. Sci. Instr., Vol. 34, Nr. 4

[28] Hori M., Kobori T., Ouchi V. (1966)
Method for measuring void fraction by Electromagnetic Flowmeters
JAERI (Japan Atomic Energy Research Institute) - 1111

[29] Bernier R.N., Brennen C.E. (1983)
Use of the Electromagnetic Flowmeter in two-phase flow
Int. J. Multiphase Flow Vol.9, No.3

[30] Velt I.D. et al
Correlation Technique for Flow Rate Measurement of Electroconductive Fluids and two-phase media and device for its Implementation
Patent No. 30 01 82

[31] Krafft R. (1993)
Electromagnetic flowmeters in multiphase flows
PhD Thesis, Cranfield University

[32] Abramowitz M.A. & Stegun I.A. (1964)
Handbook of Mathematical Functions
U.S. Department of Commerce, National Bureau of Standards, Appl. Math. Series 55, Dover, New York

[33] Durcan L.P. (1997)
Electromagnetic flowmeters for insulating fluids
PhD Thesis, Cranfield University, to be submitted

[34] Horowitz and Hill (1980)
The art of electronics
Cambridge University Press

[35] Terman F.E. (1948)
Radio engineer's handbook

Appendix A

Flow chart for potential difference accross electrodes

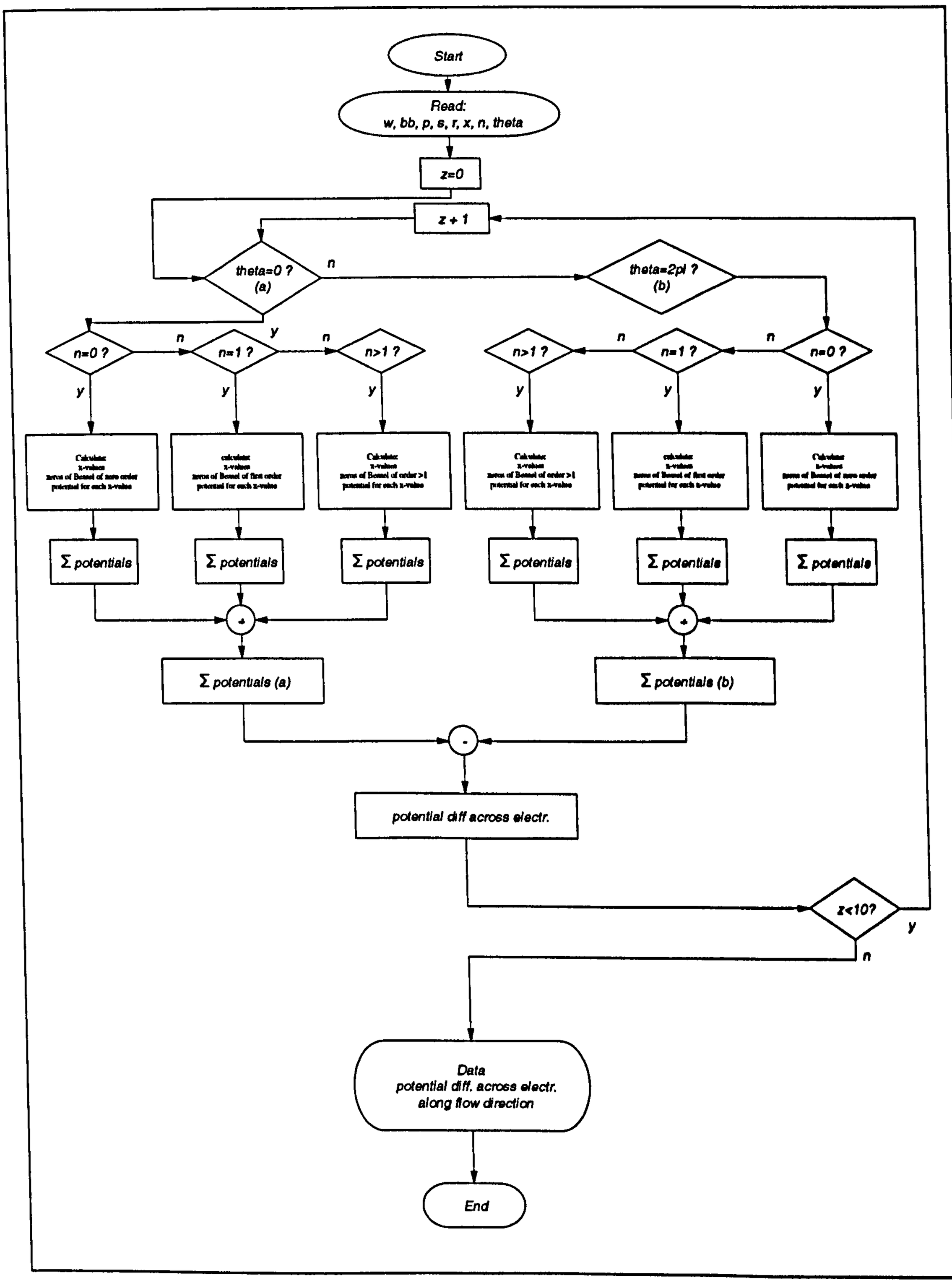

Flow chart to calculate zeros of determinant

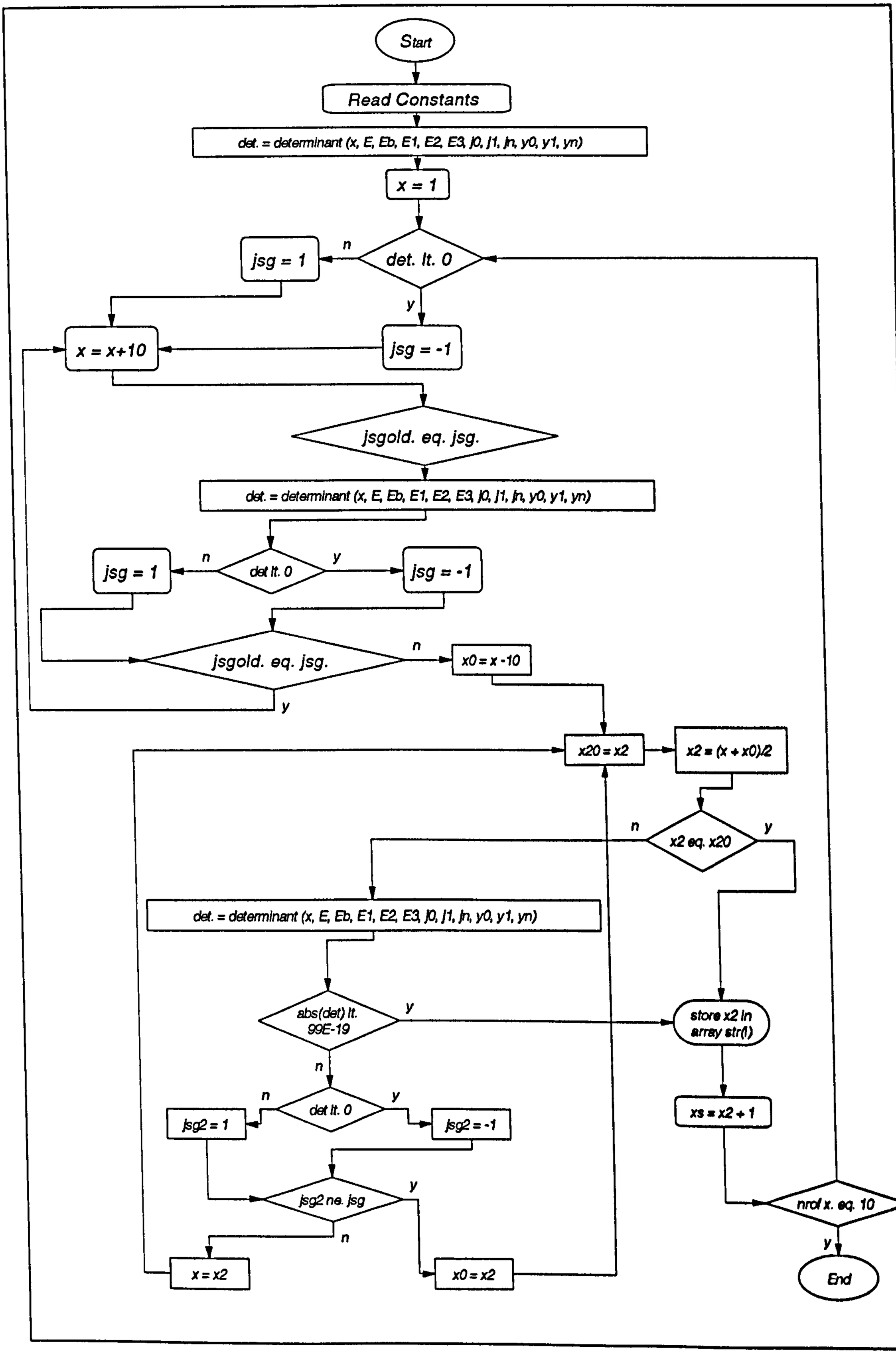

<u>Determinant calulated with 'MS Maple'</u>

```
X:=array([[a,-a,-b,0,0],[0,c,d,-c,-d],[0,0,0,c,f],[E1*g,-E2*g,-E2*b,0,0],[0,E2*i,E2*j,
-E3*i,-E3*j]]);
```

$$X := \begin{bmatrix} a & -a & -b & 0 & 0 \\ 0 & c & d & -c & -d \\ 0 & 0 & 0 & e & f \\ E1\,g & -E2\,g & -E2\,h & 0 & 0 \\ 0 & E2\,i & E2\,j & -E3\,i & -E3\,j \end{bmatrix}$$

```
det(X);
```

$$\begin{aligned} &-a\,c\,E2\,h\,e\,E3\,j + a\,c\,E2\,h\,f\,E3\,i + a\,E2\,g\,d\,e\,E3\,j \\ &- a\,E2\,g\,d\,f\,E3\,i + a\,E2^2\,g\,j\,c\,f - a\,E2^2\,g\,j\,d\,e \\ &- a\,E2^2\,i\,h\,c\,f + a\,E2^2\,i\,h\,d\,e - E1\,g\,a\,d\,e\,E3\,j \\ &+ E1\,g\,a\,d\,f\,E3\,i - E1\,g\,a\,E2\,j\,c\,f \\ &+ E1\,g\,a\,E2\,j\,d\,e + E1\,g\,b\,c\,e\,E3\,j \\ &- E1\,g\,b\,c\,f\,E3\,i + E1\,g\,E2\,i\,b\,c\,f \\ &- E1\,g\,E2\,i\,b\,d\,e \end{aligned}$$

APPENDIX B

Calculations for bandpass filter

All calculations refer to, Electronic Filter Design Handbook, Williams.

The corresponding poles of the normalized low-pass filter are found in table 12-1 as follows: $\alpha = -0.5000$ $\beta = \pm 0.8660$

$= 1.000$

The bandpass pole transformation is performed in the following manner:

$$C = \alpha^2 + \beta^2 = 1$$

$$D = \frac{2\alpha}{Q_{bp}} = 0.297$$

$$E = \frac{C}{Q_{bp}^2} + 4 = 4.088$$

$$G = \sqrt{E^2 + 4D^2} = 4.131$$

$$Q = \sqrt{\frac{E+G}{2D^2}} = 3.7198$$

$$M = \frac{\alpha Q}{Q_{bp}} 1.011$$

$$W = M + \sqrt{M^2 - 1} = 1.033$$

$$f_{r\alpha} = \frac{f_0}{W} = 1.438kHz$$

$$f_{rb} = Wf_0 = 1.536kHz$$

The following design equations for the element values can be obtained:

$$R = \frac{1}{2\pi f_r C} = R_2 = R_3$$

$$R_1 = QR$$

The capacity C and the recistors $R_4 = R_5$ are arbitrary and were chosen as $C = 0.1\ \mu F$ and $R_4 = R_5 = 10\ kHz$.

The obtained values for the first stage (n=1):

$f_r = f_{ra} = 1.438\ kHz$

$R = 1100\ \Omega$

$R_1 = 8400\ \Omega$

The obtained values for the second stage (n=2):

$f_r = f_{rb} = 1.536\ kHz$

$R = 1040\ \Omega$

$R_1 = 7860\ \Omega$

The obtained values for the third stage (n=3):

$f_r = f_0 = 1.486\ kHz$

$R = 1070\ \Omega$

$R_1 = 4014\ \Omega$